Doctoral theses at NTNU, 2020:137

Jian Meng Jiao

Si-based phase change materials in thermal energy storage systems

Doctoral thesis

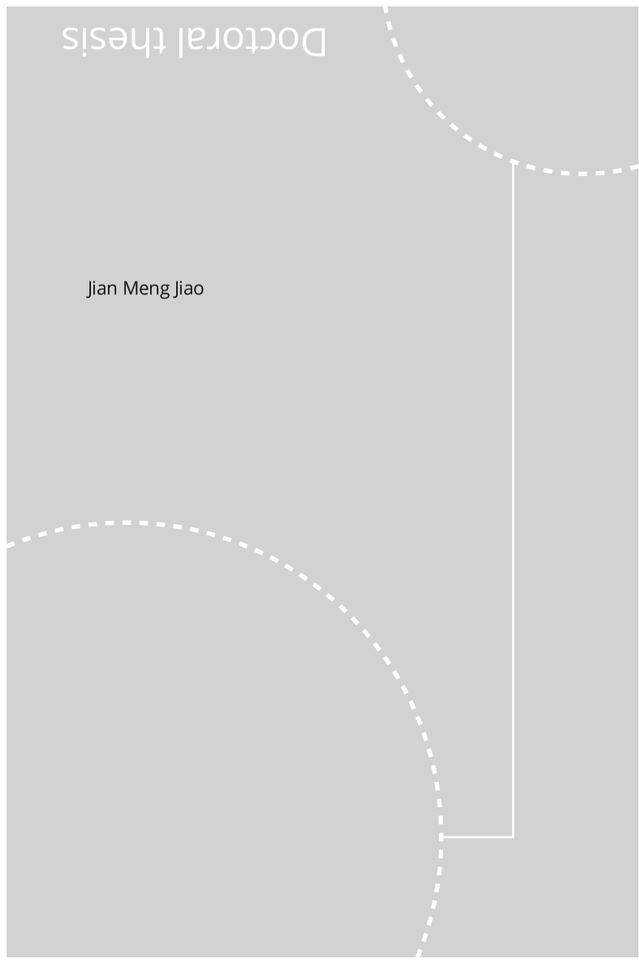

Jian Meng Jiao

ISBN 978-82-326-4622-7 (printed ver.)
ISBN 978-82-326-4623-4 (electronic ver.)
ISSN 1503-8181

NTNU
Norwegian University of
Science and Technology

Doctoral theses at NTNU, 2020:137

NTNU
Norwegian University of Science and Technology
Thesis for the Degree of
Philosophiae Doctor
Faculty of Natural Sciences
Department of Materials Science and Engineering

NTNU
Norwegian University of
Science and Technology

Jian Meng Jiao

Si-based phase change materials in thermal energy storage systems

Thesis for the Degree of Philosophiae Doctor

Trondheim, May 2020

Norwegian University of Science and Technology
Faculty of Natural Sciences
Department of Materials Science and Engineering

NTNU
Norwegian University of
Science and Technology

NTNU
Norwegian University of Science and Technology

Thesis for the Degree of Philosophiae Doctor

Faculty of Natural Sciences
Department of Materials Science and Engineering

ISBN 978-82-326-4622-7 (printed ver.)
ISBN 978-82-326-4623-4 (electronic ver.)
ISSN 1503-8181

Doctoral theses at NTNU, 2020:137

Printed by NTNU Grafisk senter

Preface

This thesis is submitted to NTNU, the Norwegian University of Science and Technology, as partial fulfillment of the requirements for the degree of Philosophiae Doctor. The work has been carried out at the Department of Material Science and Engineering between March 2017 and March 2020, including a two weeks stay at Foundry Research Institute, Cracow, Poland for the wetting tests of Fe-26Si-9B alloy on graphite substrate from 10th of February 2019 to 22th of February 2019. The work has been carried out under the supervision by Prof. Merete Tangstad and associate Prof. Jafar Safarian. The funding was provided by the Horizon 2020 through the project Amadeus (grant number 737054).

The main aim of the present research work was to investigate the Si-based phase change materials and a selection of proper container material for the selected phase change material. Collaboration with two master's projects and a summer job project was also part of the thesis work. The sole responsibility for the content of this thesis lies with the author.

Trondheim April 2020

Jian Meng Jiao

Acknowledgment

I would like to express my sincere gratitude to all the people who have supported and helped me in my three years Ph.D period. I am grateful to be part of the SiManti group.

First and foremost, I would like to thank my main supervisor Prof. Merete Tangstad for offering me this opportunity to gain knowledge and experience in the field of metallurgy. I am impressed by her broad knowledge in metallurgy, especially in Si and Mn areas. Whenever I encounter problems in my project, you always give me professional guidance, showing me how to make study serve the practical purpose. In daily life, you give a lot of care to my family, which I appreciate very much. It is my pleasure and luck to meet you.

I would also like to thank my co-supervisor Associate Prof. Jafar Safarian for his valuable advice and support. I have gained fruitful knowledge from the discussions with him. In particular, his efficient and careful revisions of the monography accelerated the process of my Ph.D work. A big thanks must also be given to Bettina Grorud, Kathrine Sellevoll, Caroline Sindland, and Sethulakshmy Jayakumari for working with the same project. In addition, many thanks for Kai Tang (SINTEF) for teaching me the FactSage software and helping me to create some phase diagrams and graphs presented in this monography.

The financial support from the European Union's Horizon 2020 is much appreciated. I am very grateful to have had the opportunity to meet partners from other universities in Europe. A special thanks to Prof. Natalia Sobczak and Dr. Wojciech Polkowski at the Center for High Temperature Studies, Foundry Research Institute in Cracow, Poland. They made it possible for me to spend two weeks finishing the wetting tests with Fe-26Si-9B alloy on a graphite substrate.

I would like to thank the SiManTi group and Prof. Gabriella Tranell, Ragnhild Aune, and Leiv Kolbeinsen. It provides an excellent platform to share your work with people, and you can always get useful feedback from them. I appreciate the organized activities in the group, such as SiManTi trip, ginger baking, summer barbecue, etc..

Great gratitude should be given to Ivar Andre Ødegård, Jonas Einan Gjøvik, Tine Eikevik, Pei Na Kui, Trygve Lindahl Schanche, Torid Krogstad, Yingda Yu, Morten Peder Raanes, Per Erik Vullum, Sarina Bao, and Dmitriy Slizovskiy for the technical supports with the experimental works and sample observations. Equal gratitude should be given to Elin Kaasen, Vidar Broholm, and Hilde Nordø.

Special thanks to David Dominikus Eide Brennhaugen, Azof Fabian, Are Bergin, Vincent Canaguier, Karin Fjeldstad Jusnes, Hamideh Kaffash, Arman Hoseinpur Kermani, Mengyi Zhu, Xiang Li, Fei Li, and Yan Ma. Thank you for providing support in my Ph.D period.

I want to thank my parents for supporting me in any situation without any expectations.

Finally, I thank my wife, Jiali, who has been with me in job and sorrow in Trondheim.

Acknowledgment

Abstract

The main aim of this dissertation is to develop new phase change materials (PCMs) for high temperature energy storage in thermal energy storage (TES) devices, with special focus on Si-based PCMs due to silicon's the high latent heat of fusion, high thermal conductivity, moderate melting point, abundance on earth, and low cost. The questions are, however, what kind of Si-based alloy can be used as PCM and what kind of refractory material can be used as PCM container at high temperatures. In order to comply with these objectives, experimental studies were carried out to investigate the thermodynamic properties of the selected PCMs and the interaction between PCMs and potential refractory materials. Ultimately, the results were used to decide the most suitable PCM and the most compatible refractory material.

First, Si-B alloys were selected as the potential PCMs, due to the high latent heat of fusion of B. In addition, Si has a high volume expansion going from liquid to solid, and the volume change is expected to decrease with the addition of B. The challenge is to find the optimal B content for Si-B alloy as the PCM. For this purpose, the effect of B content on the phase formation in Si-B alloys were investigated, in which alloys with 2-11 mass % B were heated to 1450 ^{o}C, 1550 ^{o}C, 1650 ^{o}C, and 1750 ^{o}C, respectively. Moreover, the effect of B on volume change and heat of fusion in Si-B alloys were calculated theoretically. Microstructural analyses showed that phase formations were changed with the increase of B content in Si-B alloys, and, it was proved that volume change was minimally decreased with the increase of the B content, and around 25 mass % B must be added to obtain no volume change during solidification. Moreover, the sum of heat of fusion is increased with the increase of B content, while Si-3.25B eutectic alloy possessed the highest heat of fusion per unit volume.

In order to find the most compatible refractory material for Si-B alloys, the interaction between graphite, Si_3N_4, and hexagonal BN (h-BN) and Si-B alloys were investigated. Using graphite showed that carbides were introduced to Si-B alloys. Carbides layers were formed at the interface between the Si-B alloys and the graphite, in which a single SiC layer was transformed to SiC and B_4C layers with the increase of B content. The C solubilities were measured in Si-B alloys, in which alloys with 2, 3.25, and 5 mass % B were melted in the graphite and SiC crucibles in the temperature range 1450-1750 ^{o}C, and it was found C solubility is increased with the increase of the B content. When Si_3N_4 was used as the container for Si-B alloys with the B addition of 2-11 mass % at 1750 ^{o}C, the cross-sectional images and micro-analyses showed that BN precipitates were formed in Si-B alloys and a BN layer was formed at the interface. However, the amount of BN precipitate was negligible. The wetting behavior was investigated in Si-3.25B/Si_3N_4 system under 10^{-4} atm, and a contact angle of 134^{o} showed non-wetting behavior between the alloy and the crucible material. When using a h-BN container, the wetting tests of Si-3.25B alloy were performed in a sessile drop furnace at temperatures below 1450 ^{o}C under 10^{-4} atm, and non-wetting behavior was observed. Microstructural analyses showed that no new phases are formed in the Si-3.25B alloy, neither at the interface. However, the relationship between partial equilibrium pressure of N_2 and BN decomposition recommended that it is better to use BN in high N_2 partial pressure. The study of Si-B alloys and the interaction between Si-B alloys and graphite, Si_3N_4, and h-BN definitively answers the question regarding the optimal B content in Si-B alloys and the most compatible refractory material. It is suggested that Si-3.25B alloy is used as the PCM and Si_3N_4 refractory material is used as the container. The advantage of the eutectic Si-3.25B alloy is that it will

have a high enthalpy change over a small temperature area. If Si_3N_4 is used as a crucible, no carbide phases will be formed in the alloy. Si_3N_4 is also a resistant material towards the alloy, and relatively cheap compared h-BN.

Secondly, Fe-26Si-9B alloy was selected as the potential PCM. The third element of Fe was added to Si-B based alloy aiming to decrease the volume change of Si-B alloys upon solidification. The main goal was to determine the chemical stability of the formed phase during thermal cycles, liquidus temperature, volume change, and value of the latent heat of fusion. In this regard, Fe-26Si-9B alloy was subjected to 1-12 temperature cycles between 1100 ºC and 1300 ºC in Si_3N_4 crucible under Ar. Microstructural analyses showed that FeSi, FeB, $FeSiB_3$, and SiB_6 were formed in the alloy, in which FeSi + $FeSiB_3$ constituted the eutectic structure, and TEM analyses confirmed that $FeSiB_3$ was a new ternary phase in Fe-Si-B system. Moreover, the formed phases were not changed with the increase of thermal cycles. Differential scanning calorimetry (DSC) tests of the Fe-26Si-9B alloys were performed in the temperature range from 25 °C to 1450 °C. DSC curves showed that solidus temperature was ~ 1223 ºC and liquidus temperature was ~ 1254 ºC in the heating step. Hence, Fe-26Si-9B alloy was believed not to be a eutectic alloy, while the eutectic composition was calculated to be 61 mass % Fe, 29 mass % Si, and 10 mass % B based on the formed morphology in the Fe-26Si-9B alloy. It was also found that the Fe-26Si-9B alloy slightly shrunk during cooling.

The interaction between Fe-26Si-9B alloy and graphite, Al_2O_3, Si_3N_4, and h-BN were also investigated, aiming to find the most compatible refractory material. Using graphite as the substrate under different atmospheres (Ar, 10^{-4} atm, 10^{-5} atm, and 10^{-9} atm), it was observed that carbides were formed at the top of the Fe-26Si-9B alloy and carbide layers were formed at the surface, especially at high pressures. Interestingly, the penetration of liquid alloy into graphite was insignificant. Moreover, the alloy wets graphite with contact angle of 31º-48º under four different atmospheres. For Al_2O_3 testing, the DSC and wetting tests were performed. Microstructural analyses showed that no Al-based phases were formed in Fe-26Si-9B alloy and no new layer was formed at the interface. However, Al might be dissolved into the other phases in the Fe-26Si-9B alloy. The formed oxides at the metal surface and the oscillation phenomenon also proved that oxygen was dissolved into Fe-26Si-9B alloy, due to little Al_2O_3 dissolution. Si_3N_4 and h-BN were also tested by sessile drop approach under 10^{-4} atm. Microscopic analyses showed that no nitride phases was formed in Fe-26Si-9B alloy and no new layers were formed at the interface between Fe-26Si-9B alloy and Si_3N_4 and h-BN. High N_2 partial pressure was recommended in the use of h-BN in the case of its decomposition. In conclusion, Fe-26Si-9B alloy is a desirable PCM, and graphite and Si_3N_4 were the most compatible refractory materials to be used as container for Fe-26Si-9B alloy.

Finally, Cr-43Si-5B alloy was selected as a potential PCM. Thermal cycle experiments were performed in a resistance furnace, in which Cr-43Si-5B alloy was charged to graphite crucible and subjected to 4 thermal cycles in temperature range 1314-1514 ºC. Micro-analyses showed that $CrSi_2$, CrB_2, Cr_3B_4, and Si were formed in Cr-43Si-5B alloy. However, the eutectic structure was not found in the solidified alloy. Moreover, substantial pores existed in Cr-43Si-5B alloy after experiments, which would affect its thermal conductivity. Therefore, Cr-43Si-5B alloy was not recommended to be the PCM in the TES systems.

Contents

List of Tables

List of Figures

1. Introduction

Climate change increases the risk of global catastrophe. With increasing temperature, the possibility of more droughts and more forest fires will occur. Moreover, a higher temperature will bring more rain and snowfall. The world scientists agreed that it was urgent to act against climate change in the first Climate Conference in 1979. Then, the Rio Summit in 1992, the Kyoto Protocol in 1997, and the Paris Agreement in 2015 had made a similar agreement on the decrease of greenhouse gas emissions. However, global warming becomes more and more serious. Recently, Australian wildfires have caught our eyes. The serious wildfires had resulted in more than 2,200 homes destroyed and ~10.7 million hectares burned until the 10th of January, 2020 [1]. In addition, the annual temperature rise in Svalbard was 4 ^{o}C between 1971-2017 [2], which had increased the snowmelt and rain floods. More seriously, climate change could increase such disasters three times as common by the end of the century [3].

It is urgent to curb climate change, and hence clean energy should largely replace high-carbon fossil fuels. In November of 2019, Ripple et al. [4] published a paper titled 'World Scientists' Warning of a Climate Emergency'. He claimed that for the safety of people and environment, massive energy efficiency and conservation practices should be implemented and fossil fuels should be replaced by low-carbon renewables and other cleaner sources of energy. Due to climate emergency, solar photovoltaic (PV), wind power, hydropower, bio-power, geothermal, ocean power, and concentrated solar power (CSP) are recognized as the new technologies to produce clean energy. **Figure 1-1** shows the annual additions of renewable power capacity in the period of 2012-2018 [5]. The grey line represents the total renewable power and the columns represent the capacity produced by each technology. It is seen that an estimated total of 181 Gigawatts (GW) was installed worldwide in 2018. From 2012-2018, the power generation from renewable energy increased steadily, especially for solar PV technology. However, the energy production, from wind and sun, is not continuous, and it is neither controllable. In the matter that energy is not produced at the time it is consumed, it is necessary to develop sustainable and cheaper energy storage units to store energy between the time of production and usage. In this regard, Thermal Energy Storage (TES) is developed as one of the main technologies to store energy due to its ability to solve the mismatch between energy supply and energy usage. TES stores energy by heating or cooling a material. The stored energy will then be used for heating or cooling applications and power generation. If material that is storing energy going through a phase change, it is called phase change material (PCM). When using TES systems, the produced clean energy can be stored and reused by the industries and residences, and hence it alleviates global warming.

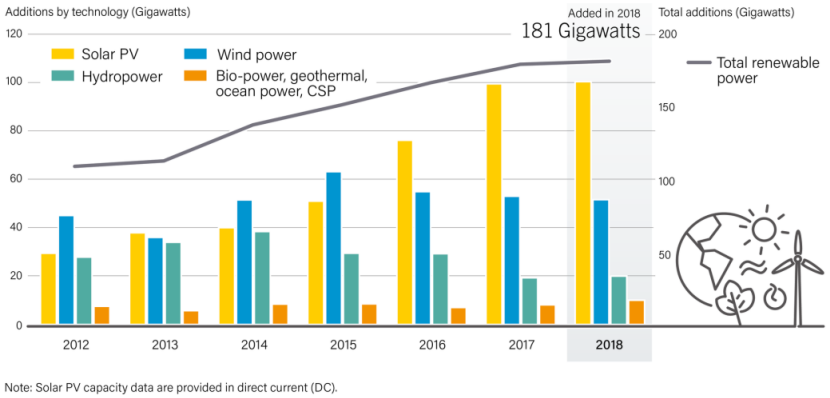

Figure 1-1 Annual additions of renewable power capacity, by technology and total, 2012-2018. [5]

1.1. Phase Change Materials

PCMs store and release energy by phase changes, from solid to liquid, solid to gas, liquid to gas, and solid to solid. Typically, the solid-liquid phase transformation plays a vital role in many TES systems and the energy storage ability of PCMs depends on the enthalpy changes of materials with temperature change. As shown in **Figure 1-2**, PCM can store energy in the form of sensible and latent heat. With the temperature increasing from T_1 to T_m in a solid state, it absorbs energy in the form of sensible heat, ΔH_s. Then, at the melting temperature of T_m, it reaches to the solid-liquid coexistence stage, in which energy is stored in the form of latent heat of fusion, ΔH_m with respect to the constant temperature. Energy is increased by the value of ΔH_l when temperature further increases to T_2 in a liquid state. Vice verse, PCM releases energy during cooling.

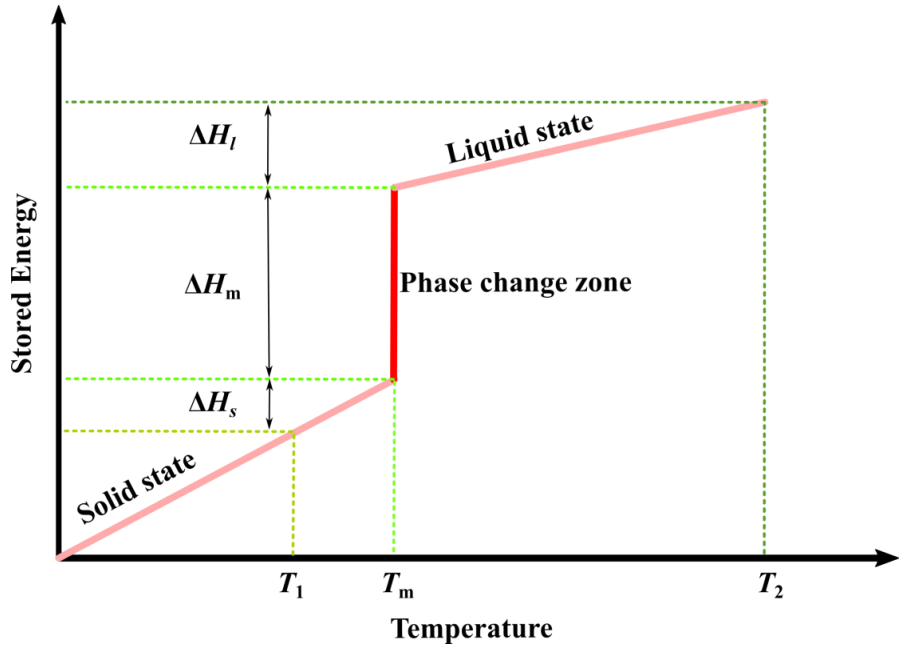

Figure 1-2 Energy change in the phase change materials during phase change in the melting/solidification process.

Considering the thermodynamic, kinetic, chemical and economical aspects, the following properties are proposed to be the basic requirements for PCMs [6], [7].

- A desirable melting/solidification temperature
- High specific heat capacity, latent heat of fusion and density
- Insignificant supercooling
- Small volume change in a thermal cycle process
- High thermal conductivity
- Congruent or eutectic melting
- Chemical stability
- Compatibility with PCM container
- Non-poisonous, abundant, and cheap
- Flame and fire safety

Three types of PCMs are presented in **Figure 1-3**, which includes organic, inorganic, and eutectic materials. Organic PCM is classified into paraffin and non-paraffin compounds. These materials are generally non-corrosive, cheap, clean, and abundant. However, the disadvantage is low thermal conductivity, low storage density, and flammability in the application of the TES systems. Next, the inorganic PCM is classified into salt hydrates and metals. These materials always have a relatively high storage density and a high thermal conductivity compared to organic PCMs. However, salt hydrates always have supercooling in the solidification process, strong corrosion with metals, phase segregation, and thermal instability, which impedes their applications. The last type of PCMs is the eutectic materials, which combine organic and inorganic to make a mixture of components. The advantage of eutectic

PCMs is the high storage density and their sharp melting temperatures [8]. However, limited data on their properties are found in the literature.

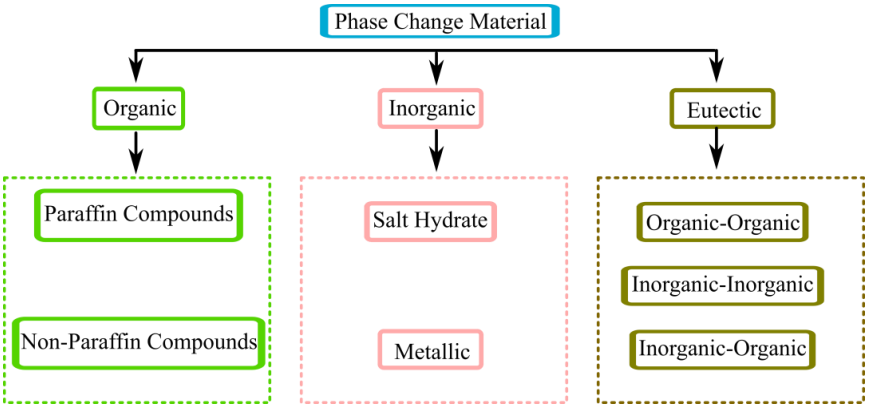

Figure 1-3 Classification of phase change materials.[8]

Inorganic and eutectic metals are proposed to store energy in industrial processes. **Figure 1-4** shows the relationship between the latent heat of the potential PCMs and their melting temperatures [9]. It indicates that Si (1230 kWh/m^3) and B (2680 kWh/m^3) have the highest fusion latent heat compared to other metals and salt hydrates. Hence, in 2015, Matthew [10] was the first to use pure Si as PCM to develop a solar thermal propulsion system for micro-satellites. However, as the high volume expansion of Si, it led to the PCM container breakage during solidification. On the other hand, B has an extremely high melting temperature and high price, limiting its application, even though it has the highest latent heat. It shows that there are still many technical problems to be solved in using pure Si and B as PCMs. Hence, in 2016, Datas et al. [9] proposed to use Si-B alloys as new PCMs. In the opinion of the authors, the addition of B to Si could reduce the volume expansion of pure Si and simultaneously improve the alloy's latent heat of fusion. This could make it possible to use Si-B alloys as PCMs in TES systems.

A new research project, Amadeus, was launched by seven European partners [11] in 2017. It was funded by the European Commission, Horizon 2020, aiming to develop new generation materials with latent heat in the range of 1000-2000 kWh/m^3 and solid state devices for high temperature energy storage and conversion in TES system. The new generation PCMs should have the ability to store energy well beyond 1000 °C, which is much higher compared to the mark of ~600 °C by the current state of the art TES systems. **Figure 1-5** shows the sketch of the TES proposed in the Amadeus project. In the charge cycle, any kind of energy (electricity, concentrated sunlight, and waste heat energy, etc.) will be employed for melting PCM at temperatures up to 2000 °C, in which energy will be stored in the form of sensible and latent heat. Therefore, high working temperature is desired. Then, in the discharge cycle, the stored energy is transferred to a hybrid thermionic photovoltaic device, which directly produces electricity based on the direct emission of electrons and photons through a vacuum space at high temperatures [12]. As shown in **Figure 1-5**, two parts are both investigated in the Amadeus project: heat storage at high temperatures and energy conversion.

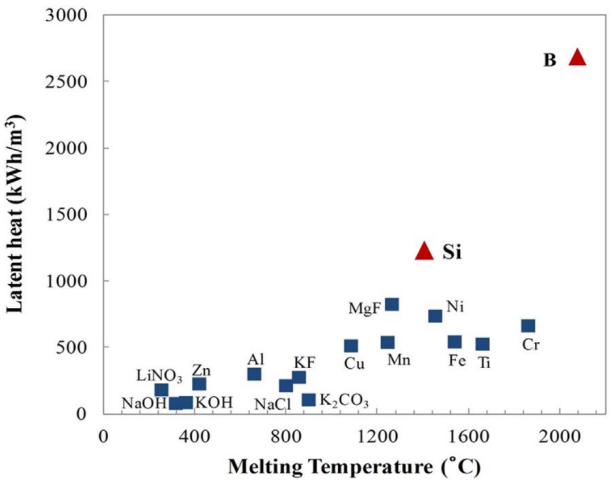

Figure 1-4 Latent heat of fusion of different materials as a function of the melting temperature. [9]

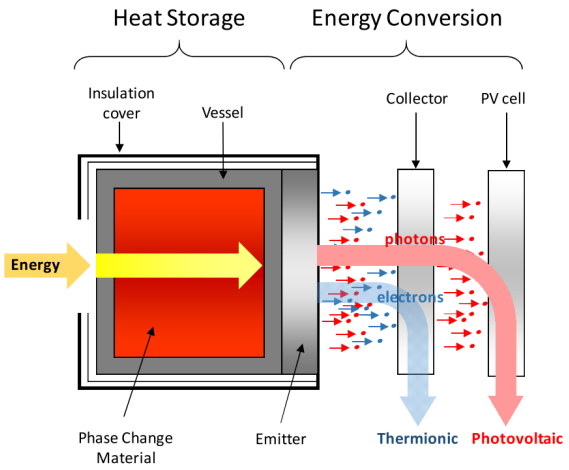

Figure 1-5 Sketch of the proposed Amadeus storage system. [11]

As one of the seven partners in the Amadeus project, NTNU is responsible for finding the most desirable materials as new PCMs in TES systems. Moreover, NTNU in cooperation with Foundry Research Institute (FRI) will determine the compatible refractory materials for PCM containers. The goal of this Ph.D project is hence to develop new Si-B based PCMs as well as find suitable container materials for PCMs.

The first task in the project is to investigate new PCMs. As described earlier, Si and B have the highest latent heat per volume compared to other potential materials (**Figure 1-4**). Hence, the project will investigate Si-B and X-Si-B ternary alloys as new PCMs, in which X represents the third element added to Si-B alloy. At present, Cu, Fe, and Cr are considered to be added to the Si-B based alloys to make a new ternary eutectic alloy. Their eutectic chemical compositions, melting points, and values of the latent heat of fusion are therefore calculated by FactSage based on the FTlite database, which is presented in

Figure 1-6. Moreover, some literature data about using the eutectic alloys as PCMs are summarized in figure [13]. As TES system typically will be a stationary unit, the volume would be more important than the mass, and hence the latent heat in kJ/cm^3 is given in the figure. Compared with the reported eutectic alloys, Si-3.25B, Cr-43Si-5B, and Fe-26Si-9B eutectic alloys have higher values of the latent heat of fusion and melting points than other reported eutectic alloys. Moreover, the melting temperature meets the requirement of high temperature (>1000ºC) energy storage in the Amadeus project [11]. In this regard, Si-3.25B, Fe-26Si-9B, and Cr-43Si-5B eutectic alloys will be investigated in this project.

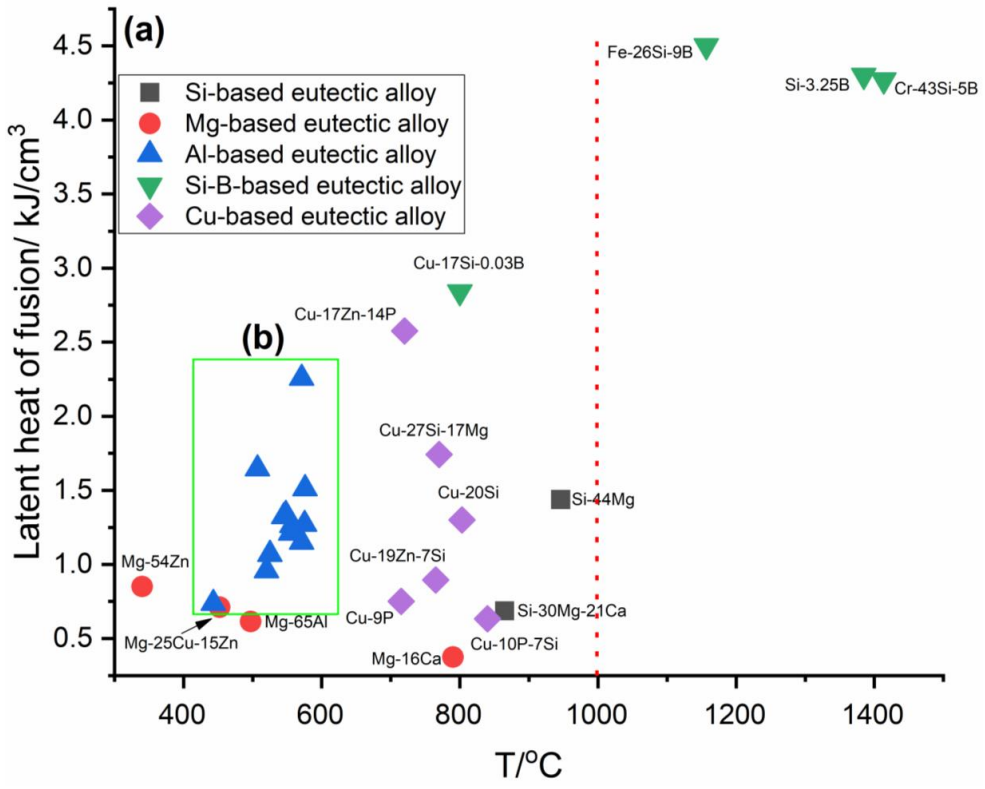

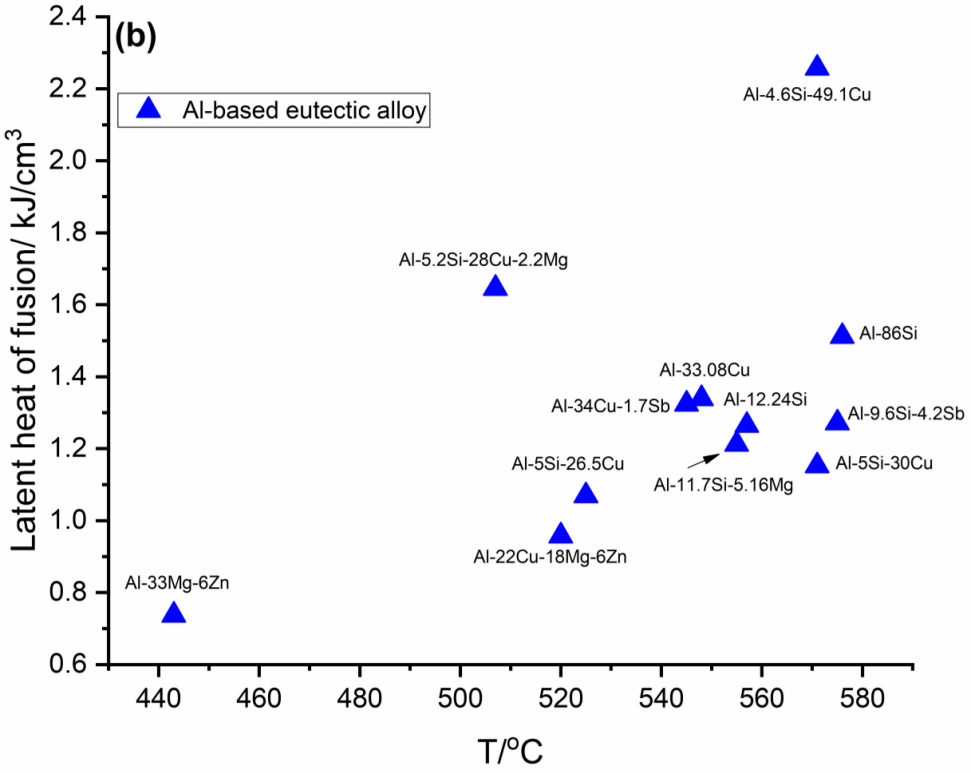

Figure 1-6 The latent heat of alloys with melting temperature.

The second task is to find suitable PCM container materials. In the application of new PCMs for long-term energy storage at temperatures up to 2000 ºC, of particular concern is the selection of a compatible refractory as the PCM container. It is critical to experimentally and theoretically investigate the interfacial reactivity between new PCMs and refractory materials at high temperatures. This task will focus on determining the thermodynamic properties when exposed to carbide-, nitride- and oxide-refractory materials. Moreover, the solubility limits of impurities (C, O, N, etc.) in new PCMs are also of interest after interaction with the selected refractory materials. Three types of ceramics have been widely investigated as a potential refractory material for Si and Si-based alloys [14].

1. Ionocovalent oxides such as Al_2O_3.
2. Graphite. It will form a SiC barrier layer between the liquid Si-based alloy and graphite.
3. Predominantly covalent ceramics such as Si_3N_4, SiC, and BN.

Hence, these three types of ceramics will be tested with the selected PCMs in our project. Finally, the best suitable refractory material will be proposed to build the PCM container.

1.2. Thesis outline

The main goal of this doctoral work is to find suitable high temperature PCMs and compatible refractory materials for PCM containers in the Amadeus TES system. Si-B, Fe-26Si-9B, and Cr-43Si-5B alloys are chosen as the potential PCMs to be investigated. Correspondingly, graphite, SiC, Al_2O_3, Si_3N_4, and h-BN refractory materials will be tested. The potential PCM should have a desirable melting/solidification temperature, a stable phase transformation during the heating/cooling process, and a comparable PCM container. Hence the focus will be set on the formed phases in new PCMs, the melting temperatures for new PCMs, the interaction between new PCMs and the selected refractory materials, the containment content in the PCMs after reacting with the selected refractory materials, and the wetting properties of new PCMs on various refractory materials.

This thesis is divided into six chapters to describe and discuss the experimental results from the three years Ph.D. In chapter 2, the fundamental theoretical knowledge will be summarized. Insights on the thermodynamic properties of Si-B, Fe-Si-B, Cr-Si-B alloys, and their subsystems are provided. In the last part, wetting behavior of different PCM alloys on graphite, Al_2O_3, Si_3N_4, and h-BN refractory materials are reviewed.

The experimental procedures are presented in chapter 3. The raw materials and the apparatus used in the experiments will be described in detail. Then, the phase formation experiments in Si-B alloys, the extraction experiments for measuring the C solubility in Si-B alloys, the preparation of Fe-26Si-9B and Cr-43Si-5B alloys, the thermal cycle experiments of Fe-26Si-9B alloy in Si_3N_4 crucibles, the wetting tests, and the DSC experiments are provided. The database used in the modeling software and the characterization techniques used will be explained.

In Chapter 4, the results will be given from the research of Si-B, Fe-26Si-9B, and Cr-43Si-5B alloys. In order to ensure the thesis continuity, some results obtained from the master students of Grorud [15] and Sellevoll [16] and the summer job student of Sindland [17] are included in this part. These MSc theses and the summer job were cosupervised by the present author. In Si-B alloys part, the thesis focuses on how B addition will influence the formed phases in Si-B alloys, C solubility in Si-B alloys, and the interaction between Si-B alloys and graphite. In Fe-26Si-9B alloy part, the determination of the new phase ($FeSiB_3$) produced in the alloys will be described. Then, the stability of the Si_3N_4 crucible under several thermal cycles is verified. Moreover, the DSC results are included in this part. In Cr-43Si-5B alloy part, the primary experimental results are reported. Furthermore, the wetting process of the three different alloys on various substrates are shown in each part.

Moving to chapter 5, it discusses the experimental results combined with the modeling results. The findings are compared with related studies. Finally, the main results are summarized and the future work based on the present works is recommended in Chapter 6.

2. Theoretical background

2.1. Si-B-C system and its subsystems

The following section will give an overview of the Si-B-C system and its subsystems. Si-B alloy is proposed as one of the potential PCMs to store energy in TES systems. It is essential to know the fundamental thermodynamic properties of the Si-B system, like the fusion enthalpy. The total enthalpy is dependent on the phases present, and the phases formed during solidification may also affect the heat conductivity in the PCM during charging and discharging. Hence, this chapter will focus on the phase formation in the Si-B alloys and the activity coefficients of B in liquid Si. Graphite is used as a potential refractory material to store Si-B alloy. The system will then be changed from Si-B to Si-B-C. Hence, the C solubility in the Si-B alloys and the formation of SiC layer between Si-B alloys and graphite are reviewed based on the findings from previous studies.

2.1.1. The Si-B system

Si-B system has been widely investigated. The Si-B binary phase diagram is re-evaluated by FactSage based on the FTlite database, as shown in **Figure 2-1**a, in which the X-axis is expressed as the mass fraction of B. It is well known that SiB_3, SiB_6, and SiB_n are the intermediate phases formed in the Si-B system.

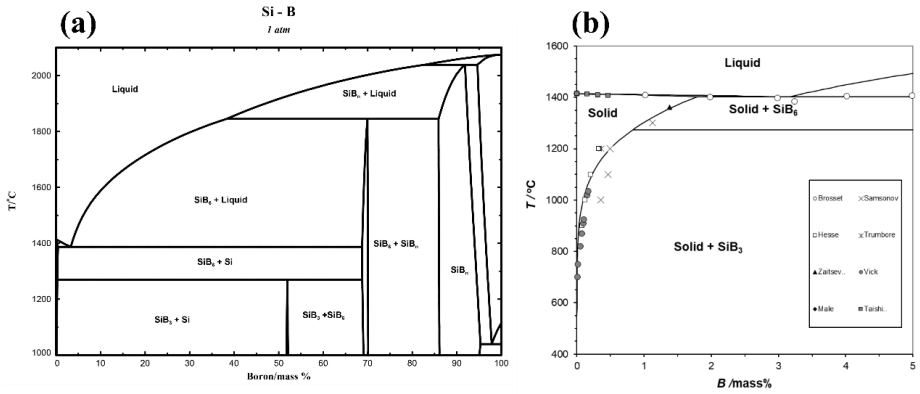

Figure 2-1 (a) Si-B binary phase diagram (FTlite database); (b) Phase equilibria in the Si-rich Si-B system, modeled by Tang. [18]

Si is a hard and brittle crystalline solid with a density of 2.33 g/cm^3 in solid state and 2.58 g/cm^3 in liquid state at the melting point (1414 ºC) [19]. In the phase transformation process from solid to liquid state, it can absorb a large amount of energy due to its high value of fusion enthalpy (1793 J/g, 4.3kJ/cm^3) [19]–[21].

The density of liquid Si was measured by Rhim et al. [22]. As shown in **Figure 2-2**, it is expressed by the following equation:

$$\rho(T) = 2.58 - 1.59(T - T_m) - 1.15(T - T_m)^2 \qquad (1350 - 1850\ K) \qquad 2.1$$

Where T_m represents the melting temperature of Si in this work (1414 ºC).

Therefore, the volume expansion concerning the melting temperature can be expressed.

$$V(T)/V_m = 1 + 6.18\times10^{-5}(T - T_m) + 4.72\times10^{-8}(T - T_m)^2 \qquad (1350 - 1850\ K) \qquad 2.2$$

Where V_m represents the volume of Si at the melting point in this work.

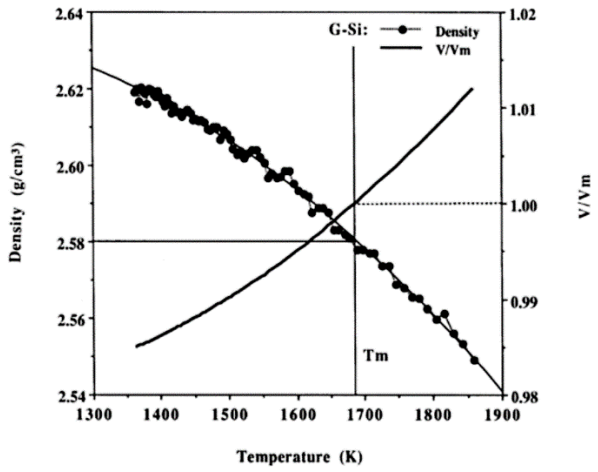

Figure 2-2 The density and volume expansion of liquid Si as a function of temperature in the temperature range 1027-1627 ºC [22].

The phase equilibria in Si-rich Si-B system was reviewed by Tang et al. [18], as shown in **Figure 2-1**b. The experimental results are somewhat conflicting. In 1963, the solubility of B in the solid Si was investigated by Samsonov et al. [23]. The solubility was estimated to be 1.3 mass % B at 1300 ºC by the analysis of the Si lattice parameter. Then, Olesinski et al. [24] summarized the work by Hesse in 1968 that the solubility of B in Si solid solution was determined by the electrical conductivity method, ranging from 0.08 mass % at 900 ºC to 0.33 mass % at 1200 ºC. One year later, Vick et al. [25] measured the B solubility in the range 0.012-0.18 mass % in the solid Si at 700-1151 ºC. It is close to the value of Hesse. In 1980, the B solid solubility was reported that it was increased from 0.01 mass % to 0.1 mass % when the temperature increased from 800 ºC to 1000 ºC. In 1984, Olesinski et al. [24] took into account the data from Samsonov et al. [23] and Hesse. The maximum solid solubility of B was estimated to be ~ 1.2 mass % at 1385 ºC. Considering all the experimental data in **Figure 2-1**b, it shows that the B solid solubility is negligible at temperatures lower than 800 ºC. [18]

SiB_3 is a solid solution with a homogeneity range 52.9-58.7 mass.% B [24]. The density is 2.52 g/cm^3 and SiB_3 is not stable above 1270 ºC [26]. Some publications [26], [27] also show that SiB_3 phase is identified as SiB_4, which may be caused by its homogeneity range. Once the temperature is decreased to 1270 ºC, SiB_3 is produced resulting from the peritectoid reaction, Si(ss) + SiB_6 → 2SiB_3. At

temperatures lower 1270 °C, Si(ss) is in equilibrium with SiB_3 at B content lower than 58.7 mass %. Otherwise, it equilibrates with SiB_6 in the B range 58.7-70 mass %.

SiB_6 is a black irregular crystal with a density of 2.47 g/cm^3 [26]. Thermal analysis reveals that SiB_6 decomposes in a peritectic reaction at 1850 °C and forms a liquid of 42 mass% B and SiB_n phase [24]. SiB_6 also has a narrow homogeneity range with a B content of 69-70.5 mass % [28]. Olesinski et al. [24] regarded it as a stoichiometric phase in the assessed Si-B phase diagram. Si(ss) is in equilibrium with SiB_6 in the temperature range 1270-1385 °C. A eutectic reaction occurs at 1385 °C, in which Liquid → Si(ss) + SiB_6, and hence above 1385 °C, SiB_6 is in equilibrium with liquid Si-B alloy.

SiB_n is a B-rich solid phase with a homogeneity range of 87.2-96.2 mass % B at 1600 °C [29]. SiB_n is confirmed to be a stable, solid, and rhombohedral phase [24]. Giese et al. [30] identified the value of '*n*' to be 14 through X-ray diffraction. Moreover, Armas et al. [29] gave the value of '*n*' in the range of 14-40 at 1427 °C and 15-40 at 1527 °C based on the activity of Si. A peritectic reaction occurs at 2020 °C, Liquid + B(ss) → SiB_n.

An overview of the invariant reactions that happen in the Si-B system is given in **Table 2-1**. The thermodynamic parameters of Si-B alloy are shown in **Table 2-2** and **Table 2-3**.

Table 2-1 Invariant reaction occurs in the Si-B system [24].

Reaction	Type	*T*/°C
Liquid + B → SiB_n	Peritectic	2020
Liquid + SiB_n → SiB_6	Peritectic	1850
Liquid → Si + SiB_6	Eutectic	1385
Si(ss) + SiB_6 → SiB_3	Peritectoid	1270
Liquid → Si	Congruent	1414
Liquid → B	Congruent	2092

Table 2-2 Thermodynamic parameters in Si-B system.

Phase	T_m/°C[24]	V_m(cm^3/mol)	ΔH_m (J/g)	ρ, g/cm^3
Si	1414	12.05(s) [19] 10.89(l) [22]	1793 [19]–[21]	2.33(s) [19] 2.58 (l) [22]
B	2092	4.64(s) [19] 5.32(l) [19]	4610 [31], [32] 2020[20]	2.37(s) [19] 2.08(l) [19]
SiB_3	1270	-	-	2.52 [26]
SiB_6	1850	37.6[26]	-	2.47 [26]

Table 2-3 Thermodynamic functions of the formation of intermediate phases.

Phase	*T*/°C	ΔH_f, (J/g)
SiB_3	25	-105.74 [32]
SiB_6	25	-69.61 [32]
	1484	-1589 ± 80 [33]
	1527	-1296 ± 514[29]
SiB_n	1496(n=15.67)	-1032± 116[33]
	1527(n=15)	-1134 ± 481[29]

Activity coefficients of B in Si

Many of the works on the activity coefficients of B in solid and liquid Si for an infinite dilute solution have been done, aiming to remove B from Si, like, e.g. in producing Si for solar cells. In this section, previous studies of the activity coefficients of B in solid and liquid Si are summarized and reviewed.

In 1994, Noguchi et al. [34] investigated the thermodynamics of B in liquid Si by the equilibrium reaction between liquid Si and solid BN under N_2 at 1450-1650 ºC. The temperature dependence of the dilute activity coefficient of B in liquid Si was expressed as follows.

$$\log \gamma_B^o = -11100/T + 5.82 \qquad (1723-1923K) \qquad 2.3$$

In 1998, Tanahashi et al. [35] measured the dilute activity coefficient and its self-interaction coefficient of B by equilibrating liquid Si-B alloy with solid BN and/or solid Si_3N_4 at 1450 ºC and 1500 ºC. The values $\ln\gamma_B^o$ were determined to be 2.5 ± 0.2 at 1450 ºC and 2.3 ± 0.2 at 1500 ºC. Corresponding to the self-interaction coefficient of B, the values ε_B^B were calculated to be -164 ± 8 at 1450 ºC and -105 ± 8 at 1500 ºC.

In 2003, Inoue et al. [36] determined the infinite activity coefficient of B in liquid Si relative to pure solid-state at 1450 ºC. In his experiments, ~ 2 g of liquid Si-B-Ca alloy with a piece of h-BN was placed in a Si_3N_4 crucible. The charged Si_3N_4 crucible was then placed in an Al_2O_3 holder and equilibrated at 1450 ºC for 40 h under N_2-10%H_2. The value $\ln\gamma_B^o$ was calculated to be 2.27 ± 0.2 at 1450 ºC, which corresponded well to the result of Tanahashi et al. [35].

In 2005, Yoshikawa et al.[37] studied the dilute activity coefficient of B in liquid Si by equilibrating liquid Si with Si_3N_4 and BN in a SiC electric resistance furnace. The sample was held for 6-16 h at 1420 ºC and 1500 ºC under N_2-10%H_2. The following equation is obtained based on the experimental results.

$$\log \gamma_B^o = 289(\pm 450)/T + 1.19(\pm 0.25) \qquad (1693-1923K) \qquad 2.4$$

In 2015, Khajavi et al. [38] investigated the effect of B removal from Si by solvent refining using Si-20Fe alloy (mass %). The self-interaction parameters of B (ε_B^B) were measured to be -96 ± 12 at 1310 ºC, -111 ± 28 at 1260 ºC, and -159 ± 45 at 1210 ºC. The activity coefficient of B in solid Si is expressed as follows.

$$\log \gamma_{\text{B in solid Si}}^o = 16317(\pm 282)/T - 7.06(\pm 0.18) \qquad (1483-1583K) \qquad 2.5$$

In 2019, Chen et al. [39] summarized the activity coefficients of B in solid and liquid Si. They fitted the dilute activity coefficients of B in liquid Si and solid Si from the literature of [35]–[38]. The relationship between the activity coefficient of B and temperature is expressed as follows. It should be noted that the data from Noguchi et al. [34] was ignored due to the significant deviation from other researchers'data.

$$\log \gamma_B^o = 17450/T - 8.15 \qquad (1173-1923K) \qquad 2.6$$

The activity coefficient of B in Si discussed in this section is summarized in **Figure 2-3**.

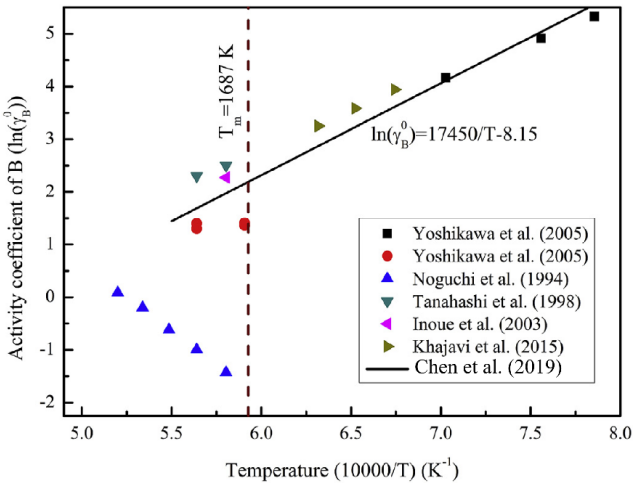

Figure 2-3 Summary of the dilute activity coefficient of B in Si from literature data [39].

2.1.2. The Si-C system

The Si-C binary phase diagram is calculated by FactSage 7.2 based on the FTlite database, as shown in **Figure 2-4a**. It involves three solid phases: Si(ss), SiC, and C(ss), a peritectic reaction at 2764 °C: Liquid + C(ss) → SiC(s), and a eutectic reaction at 1414 °C: Liquid → Si(ss) + SiC(s). SiC exists in two modifications below the peritectic temperature: α-SiC and β-SiC. β-SiC is stable at lower temperatures and it is transformed into α-SiC at high temperatures [40].

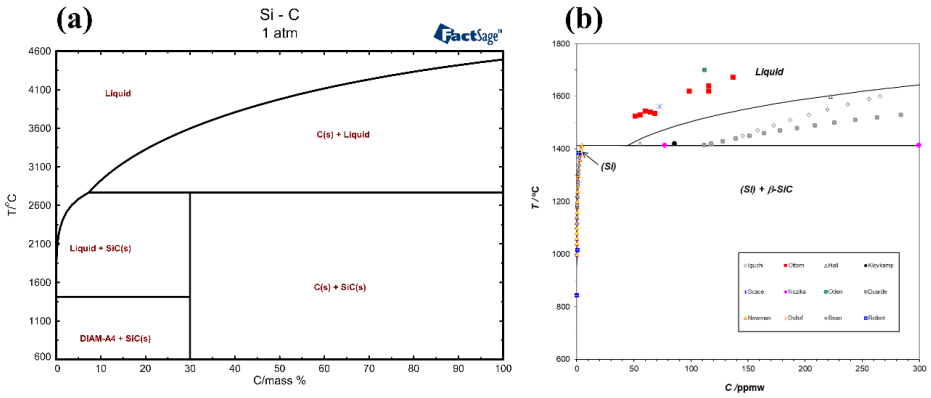

Figure 2-4 (a) Si-C binary phase diagram (FTlite database); (b) Phase equilibria in the Si-rich Si-C system, modeled by Tang [18]

C solubility in Si

Graphite is usually chosen as a refractory material for building a crucible because of ease of machining, high-temperature stability, and moderate ease of purification. When Si melts in a graphite crucible, a continuous SiC layer is produced at the interface due to the reaction between the liquid Si and graphite. Simultaneously, liquid Si may penetrate graphite crucible and C will be dissolved into the liquid Si [41]. The C solubility in the Si-rich Si-C system was reviewed by Tang et al. [18], as shown in **Figure 2-4b**. In the following part, the research of C solubility in liquid Si is summarized.

In 1958, Hall [42] equilibrated 50-200 mg SiC with 5g liquid Si in a fused quartz container under Ar. C solubilities were measured by weighing the mass loss of SiC crystals. The C solubilities were obtained to be 222 ppmm at 1520 ºC, 556 ppmm at 1600 ºC, and 1885 ppmm at 1725 ºC. Then, a solubility of 61 ppmm was determined at the melting point based on his published equation. The results were argued by Scace et al. [43] that the C might be oxidized by quartz crucible and left the melt as CO or CO_2 gas, leading to overestimating the C content in the liquid Si.

In 1959, Scace et al. [43] charged 0.5g Si into a graphite container. The container was closed by a graphite end plug, kept 1.5-2 min at the desired temperatures under Ar, and then quenched. The solubility of C in the liquid Si was measured by the ratio of the SiC mass and the total sample mass. The C solubility was determined to be 23 ppmm at 1412 °C. Scace et al. [43] assumed that all of the C was precipitated as SiC within the Si phase during solidification. Olesinski et al. [24] pointed out that these assumptions might not be valid due to the SiC would be formed at the existing SiC layer during solidification. It would lead to underestimating the C solubility in the liquid Si.

In 1970, Nozaki [44] used a bar of Si coated with an aqueous solution of C. The Si bar had been melted and solidified at different growth rates using the floating zone method. The content of C just before the appearance of SiC, was determined by the use of charged particle activation analysis. The C solubility in solid Si was determined to be 3 ppmm at the melting point. The equilibrium distribution coefficient of C was found to be 0.07 ± 0.01. Hence, the C solubility in liquid silicon was calculated to be 42 ppmm at the melting point.

In the same year, Bean et al. [45] annealed single crystals of Si in the temperature range 600-1350 ºC by using infrared measurements, aiming to find the relationship between C solubility in solid Si and temperature. The C solubility in solid Si was found to be increased from 0.2 ppmm at 1140 ºC to 1.9 ppmm at 1340 ºC.

In 1987, Oden et al. [46] used an internally sealed crucible to determine the C solubility in liquid Si at an increment of 150 ºC in temperature range 1700-2150 ºC. Samples for C analyses were recovered from the crucible by removing the crucible and 0.065 cm of the outer surface of the metal by diamond grinding. Subsequently, the C was analyzed by the combustion method using a Leco infrared analyzer. The results are shown in **Figure 2-5**. The C solubility increased from 112 ppmm (0.026 at. %) at 1700 ºC to 2862 ppmm (0.667 at.%) at 2150 ºC.

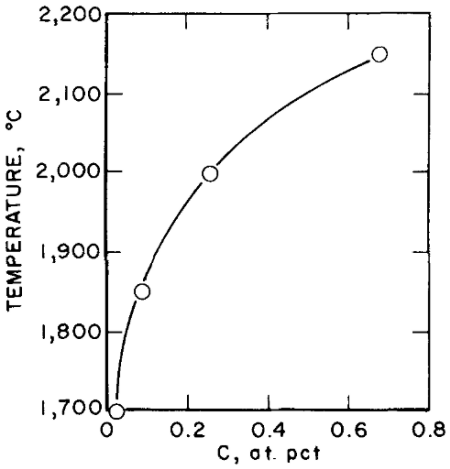

Figure 2-5 C solubility in liquid Si in the temperatures range 1700-2150 °C. [46]

In 1993, Ottem [47] investigated the C solubility in liquid Si in temperatures range 1420-1640 °C. A Leco analyzer was used to measure the C content in the rapidly quenched samples. The results are shown in **Figure 2-6**. It is known that the C solubility increased with the increase of temperature. The function of the C solubility with temperature is expressed as follows.

$$C_c / mass\% = 3359 \cdot \exp\left(-22417 / T\right) \qquad (1693-1913K) \qquad 2.7$$

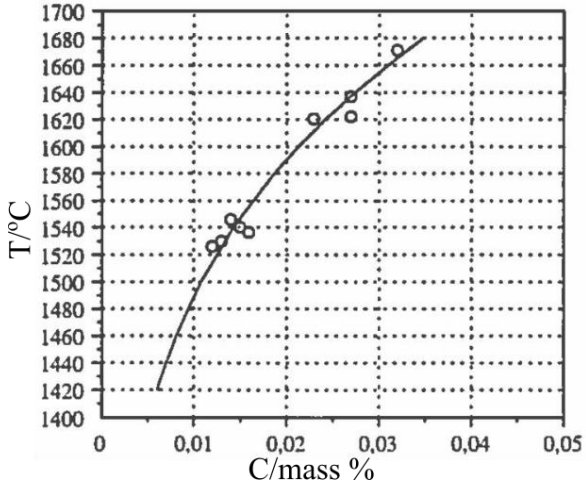

Figure 2-6 C solubility in the liquid Si in the temperatures range 1420-1640 °C. 9 points represent the measured C content in the liquid Si [47]

In 1997, Yanaba *et al.* [48] equilibrated liquid Si with SiC at 1450-1600 °C under Ar-CO flow gas. The C content of the quenched sample was measured by the combustion method using a Leco infrared analyzer. 79 ppm mass of the C solubility was calculated at the melting temperature based on the following equation:

$$\log(C_c / mass\%) = 3.63 - 9660/T \qquad (1723-1873K) \qquad 2.8$$

In 1999, Durand et al. [49] published a literature review, critically assessing the available literature for direct measurements of the solubility of C in solid and liquid Si. They found a solubility limit of ~ 112 ppm mass at the Si melting point and 3.86 ppm mass at the solid state. The distribution coefficient value of 0.0345 was lower than the previous values [44], [50]. The derived value of C solubility at the melting point was believed to be overestimated. In 2000, Durand and Duby found that the presence of the third element slightly increased the C solubility in a liquid and solid-state. The distribution coefficient was, however, unaffected by the third element [51].

In 2009, Dalaker [52] placed Si in a graphite crucible and held for a period at various temperatures. The sample was extracted using a quartz tube at each holding temperature. The value of 65 ppmm at the melting point was measured by the combustion method using a Leco infrared analyzer.

The C solubilities in liquid Si are summarized in **Figure 2-7**.

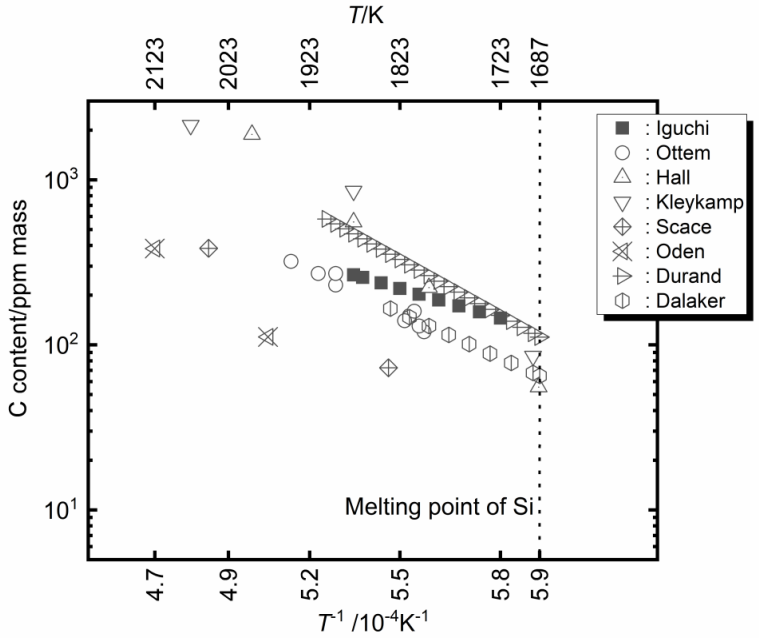

Figure 2-7 Summary of the literature data on the solubility of C in the liquid Si. [42], [43], [46], [47], [49], [52]–[54]

The formation of SiC layer between Si and graphite

A SiC layer is formed by the reaction between Si and graphite. In the use of graphite as a crucible in the processing of Si, the formed SiC layer can play the role of barrier coating between liquid Si and graphite and further affect the lifetime of the graphite crucible. In general, two SiC layers are produced in the reaction process, layer I and layer II, as shown in **Figure 2-13** [55]. It should be noted that the layer II may also be formed in the solidification process. In the following, the measured thickness of

the SiC layer is the sum of the layer I and layer II.

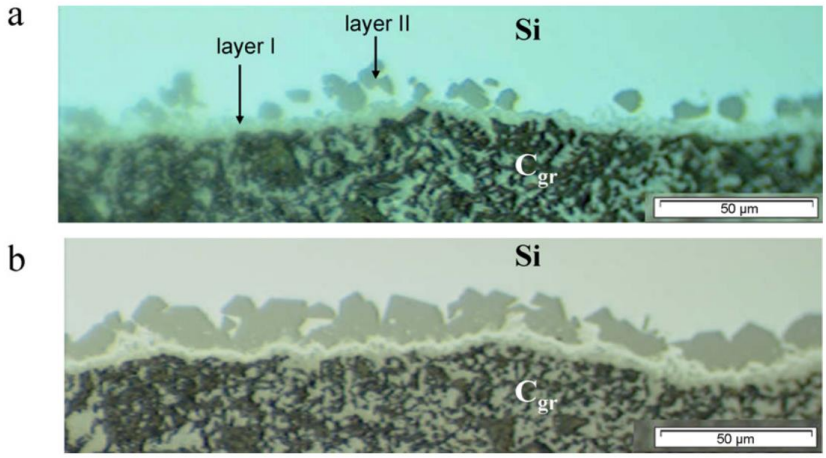

Figure 2-8 Layer between Si and graphite. (a) T = 1430 °C, t = 10min; (b) T = 1430 °C, t = 20min. [55]

In 1995, Deike et al. [56]concluded that layer I was a mixture of SiC and free Si, and layer II consisted of big compact crystals. It is found that a SiC layer was formed within 1h reaction time with an attained average layer thickness of ~ 19 µm and it increased to 26 µm after 48 h at 1500 °C.

In 2003, Favre et al. [57] studied the reaction between liquid Si and polycrystalline graphite by two siliconizing processes, progressive siliconizing and direct siliconizing. In the progressive siliconizing process, the Si powder was put in the graphite crucible and heated to 1600 °C with a heating rate of 5 °C/min and then held for 5 to 180 min under Ar flow. In the direct siliconizing process, the Si powder was set in an Al_2O_3 crucible. Then, it was heated to 1600 °C and held for 30 min to make the Si melt homogeneous. The Al_2O_3 crucible was then rotated, allowing the liquid Si to flow out to the graphite substrate. The temperature was kept constant for different reaction times from 1 to 150 min and then quenched to 1200 °C. The measured results of the formed SiC layer thickness is shown in **Figure 2-9**. It is found that the average thickness of SiC was ~ 12 µm after 180 min at 1600 °C for the progressive siliconizing process and ~ 18 µm after 60 min at 1600 °C for the direct siliconizing process. The thickness of the SiC layer was independent of time. This also shows that a SiC layer produced at low temperatures will protect the graphite from further reaction.

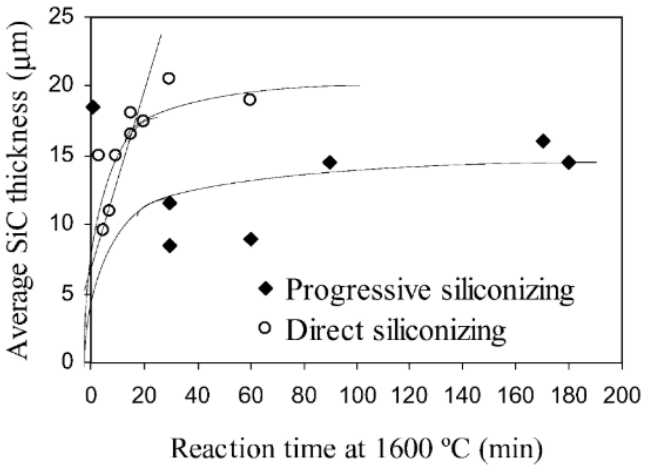

Figure 2-9 Thickness of the SiC layer as a function of the reaction time for 'progressive' and 'direct' siliconizing of graphite at 1600 ºC. [57]

In 2012, Voytovych et al. [55] investigated the reaction between graphite and liquid Si at 1412-1600 ºC. **Figure 2-10** showed the average thickness of the SiC layer for different holding time using two different graphite. It is found that the thickness of the SiC layer was hardly increased with time or with temperature. It was a good agreement with Favre et al.[57]. Hence, three stages were proposed by Voytovych et al. as follows.

1. At t < 1 min, the SiC layer was formed by a nucleation and growth process. Liquid Si could infiltrate the present SiC layer to solid C.
2. At the period 1 to ~ 20 min, the SiC layer was grown rapidly to a thickness of 15-20 μm. It was caused by liquid state diffusion.
3. At longer times, the SiC layer was impervious to liquid Si.

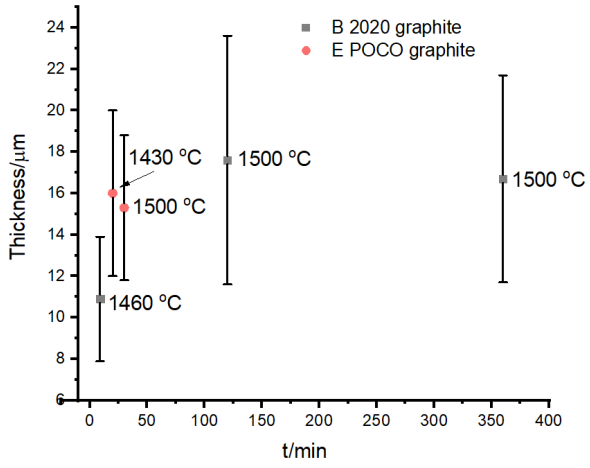

Figure 2-10 Effect of temperature and time on the total thickness of the SiC layer. Adapted from [55].

In 2017, Grorud [58] investigated the effect of the thermal cycles on the formation of the SiC layer between liquid Si and graphite. Liquid Si was subjected to 5 and 10 heating cycles in the temperature range 1430-1550 ºC after 1 h holding time at 1550 ºC. The results are shown in **Figure 2-11**. It is seen that the thickness of SiC layer was in a wide range between 8 and 70 µm.

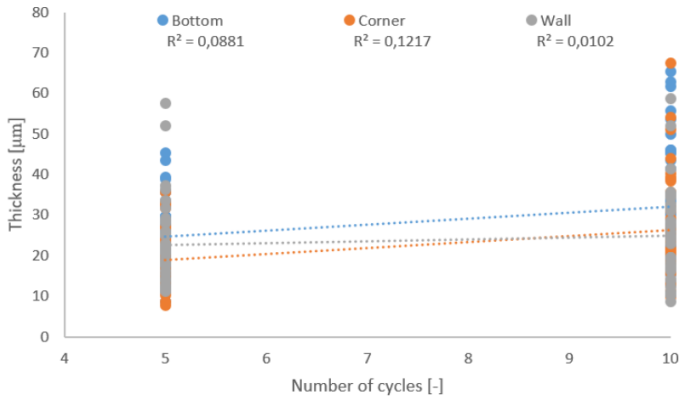

Figure 2-11 Thickness of the SiC layer as a function of thermal cycles in the bottom, corner, and wall three different areas. [58]

In 2019, Arman et al. [59] investigated the interaction of Si with graphite at high temperatures under Ar flow. The cross-section of the sample was analyzed after holding 1 h at 1500 ºC and 1800 ºC, as shown in **Figure 2-12**. Comparing the SiC layer formed at 1500 ºC and 1800 ºC, it is found that the SiC layer was not continuous at high temperatures. Hence, Arman et al. [59] regarded that SiC layer acted better as a passive layer at lower temperatures.

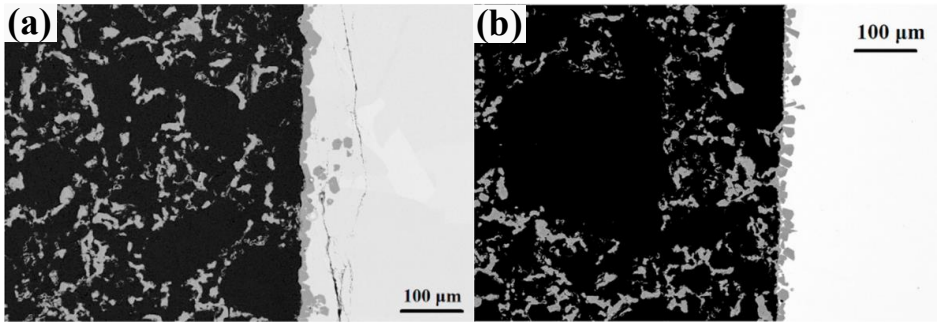

Figure 2-12 SEM images of the graphite crucible after holding Si melt for 1h. (a) 1500 ºC; (b) 1800 ºC. [59]

2.1.3. The B-C system

The calculated B-C phase diagram is presented in **Figure 2-13**. One phase exists in the system, boron carbide ($B_{4+\delta}C$), that has a C range in 8.8-20 at.% with a density of 2.42-2.52 g/cm^3. $B_{4+\delta}C$ is used in refractory, abrasive powders, coatings, nuclear applications due to its high melting point, high thermal stability, high hardness, and low density [60]. In 2018, the microstructure of B-rich $B_{4+\delta}C$ was observed

by Xie et al. [61]. It is found that $B_{4.2}C$ was transformed to $B_{5.6}C$, and then to $B_{7.6}C$ with the B addition. Besides, the hardness of $B_{4+\delta}C$ was reduced by the increase of B content. According to Seifert and Aldinger [62], $B_{4+\delta}C$ was also found as (B_4C), $B_{13}C_{2\pm x}$ or $B_{12}(B,C)_3$. The invariant reaction in the B-C binary system is given in **Table 2-4**.

Table 2-4 Invariant reaction occurs in the B-C binary system [63].

Reaction	Type	*T*/°C
liquid → B_4C	Congruent	2452.4
liquid → B_4C + graphite	Eutectic	2390.4
liquid + B_4C → βB	Peritectic	2102.9

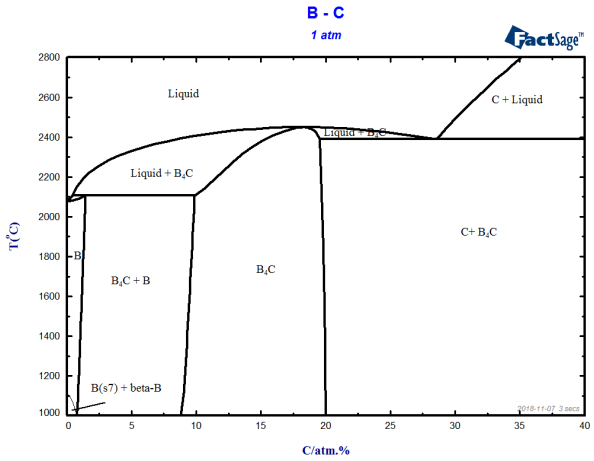

Figure 2-13 B-C phase diagram calculated in FactSage (FTlite database).

2.1.4. The Si-B-C system

The projection of Si-B-C system is shown in **Figure 2-14**. No stable ternary phase has been reported. Several invariant points are shown in **Figure 2-14**-**Figure 2-16**. Point 1-3 show the peritectic reactions, $Liquid_1$ + (C) → SiC + B_4C at 2290 °C, $Liquid_2$ + SiB_n → B_4C + SiB_6 at 2008 °C, and $Liquid_3$ + SiC → B_4C + Si(ss) at 1398 °C (**Figure 2-15**). Point 4-6 are presented in the Si-B-1C phase diagram (**Figure 2-16**), where C content is 1 mass %. The relevant reaction in Si-B-C system is listed in **Table 2-5**.

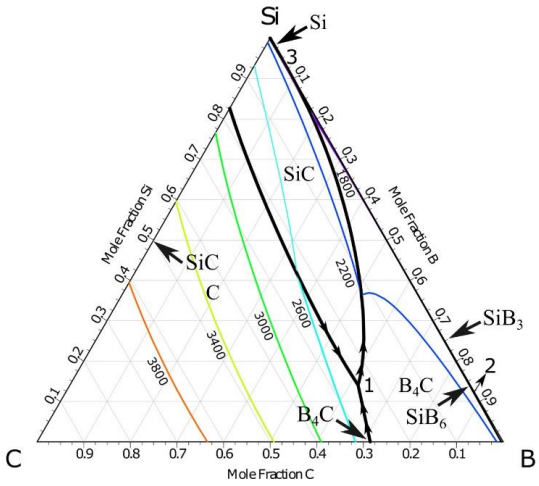

Figure 2-14 The projection of the Si-B-C system at 1300-3800 ºC (FactSage FTlite).

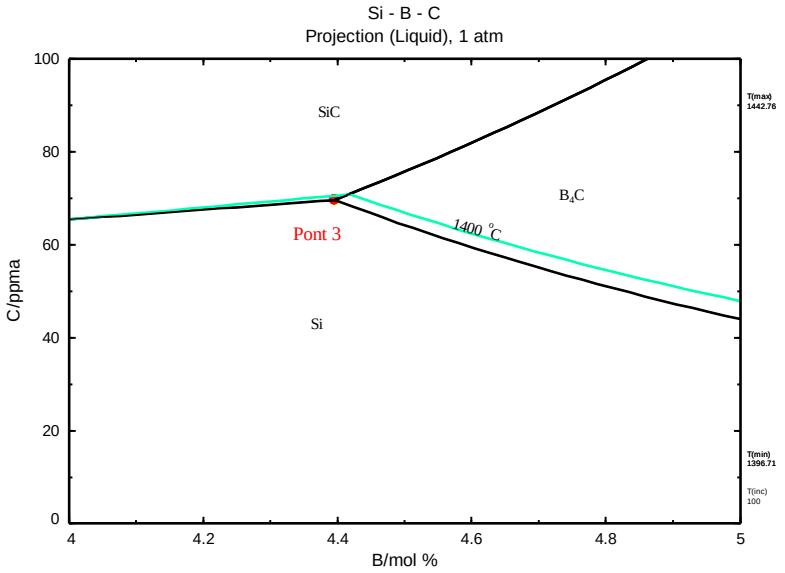

Figure 2-15 The projection of the Si-B-C system in the magnified Si part, the red point represents point 3.

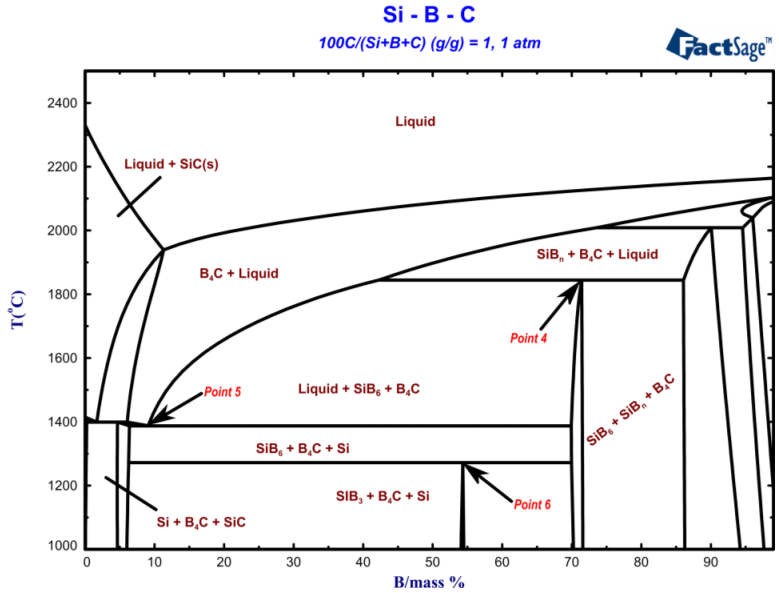

Figure 2-16 Isoplethal cross-section of the Si-B-1C phase diagram calculated by FactSage.

Table 2-5 Invariant reaction occurs in Si-B-C system.

T(°C)	Equilibrium reaction
2290 (Point 1)	$liquid + C \rightarrow B_4C + SiC$
2008 (Pont 2)	$liquid + B \rightarrow B_4C + SiB_n$
1398 (Point 3)	$liquid + SiC \rightarrow B_4C + Si$
1850(Point 4)	$liquid + SiB_n \rightarrow SiB_6 + B_4C$
1387(Point 5)	$liquid \rightarrow Si + SiB_6 + B_4C$
1272(Point 6)	$Si + SiB_6 \rightarrow SiB_3 + B_4C$

The effect of B on C solubility in Si-B alloys

In the use of graphite as a PCM container for Si-B alloys, the effect of B on C solubility in liquid Si-B alloys should be considered.

In 1998, Yanaba *et al.* [48] measured the C solubility in liquid Si-B alloys by equilibrating liquid alloy with SiC in the temperatures range 1450-1550 °C. The experimental results show that C solubility was increased with B addition at B content lower than 3 mass %, as shown in **Figure 2-17**. The relationship between the C solubility and B content was obtained using the analytical values at different temperatures.

1450 °C: $$\log(C_c / mass.\%) = -1.95 + 0.0836[C_B / mass.\%] \quad (2.9)$$

1500 °C: $$\log(C_c / mass.\%) = -1.83 + 0.0706[C_B / mass.\%] \quad (2.10)$$

1550 °C: $\log(C_c / mass.\%) = -1.68 + 0.0648[C_B / mass.\%]$ 2.11

1600 °C: $\log(C_c / mass.\%) = -1.51 + 0.0544[C_B / mass.\%]$ 2.12

The temperature dependence of the interaction parameter in the Si-B-C system was expressed as follows.

$$e_C^B = 0.267 - 6.02 \times 10^2 / T \quad (\mathrm{T} = 1723\text{-}1873\mathrm{K}) \qquad 2.13$$

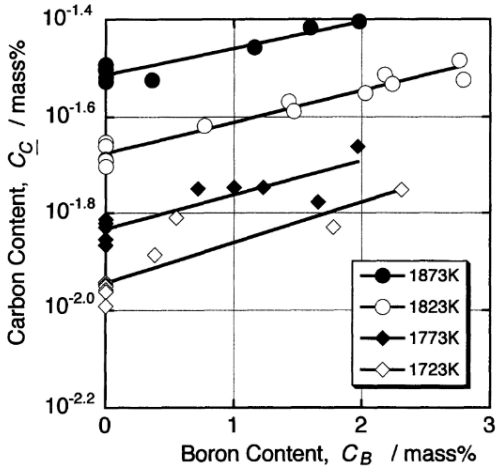

Figure 2-17 Effect of B content on C solubility in liquid Si-B alloys. [48]

In 2009, Dalaker [52] equilibrated liquid Si-B alloys with SiC to investigate C solubility in the temperatures range 1414-1559 °C under Ar. The Si-B alloy was charged into a high-density graphite crucible (Tanso IG-610). It was then heated in a resistance furnace. For the experiments with B additions, a holding time of 4 h was used to facilitate B dissolution. The samples were extracted at different temperatures during one experimental run. The results are shown in **Figure 2-18**. An equation is derived describing the solubility as a function of B content and temperature:

$$\log(C_c(T,B)) = 0.9240 - 8623.4/T - (0 - 0.2 + 3.87 \times 10^{-5} T) C_B \qquad 2.14$$

Where T is in the range 1687-1832K and C_B is in the range 0-2 mass%.

The corresponding B-C interaction coefficient is expressed as follow:

$$e_C^B = -0.20 + 3.87 \times 10^{-5} T \quad (\mathrm{T} = 1687\text{-}1823\mathrm{K}) \qquad 2.15$$

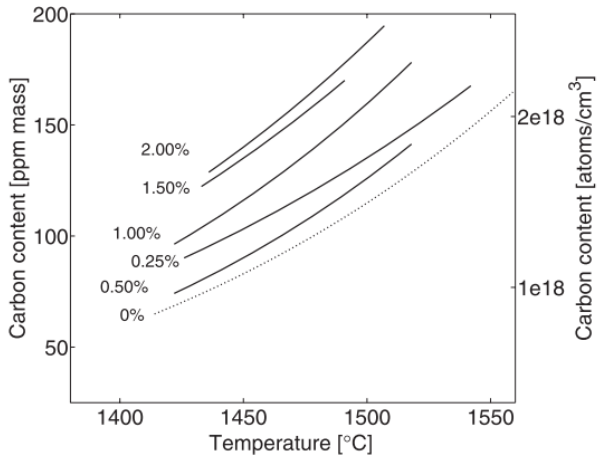

Figure 2-18 C solubility as a function of *T* for different B additions. The dashed curve indicates pure Si. [52]

In conclusion, C solubility increased with B addition within 0-3 mass % in the liquid Si-B alloys in temperatures lower than 1559 ºC. The negative value of the interaction coefficient of B-C shows that B and C have high interaction energy.

The formation of SiC layer between Si-B alloy and graphite

Grorud [58] conducted the experiments of Si-3.25B alloys in the dense graphite crucible. The charged Si-B eutectic alloys were subjected to various thermal cycles in temperatures range 1430-1550 ºC under Ar flow. It is seen from **Figure 2-19** that a single SiC layer was formed between the Si-3.25B alloy and graphite.

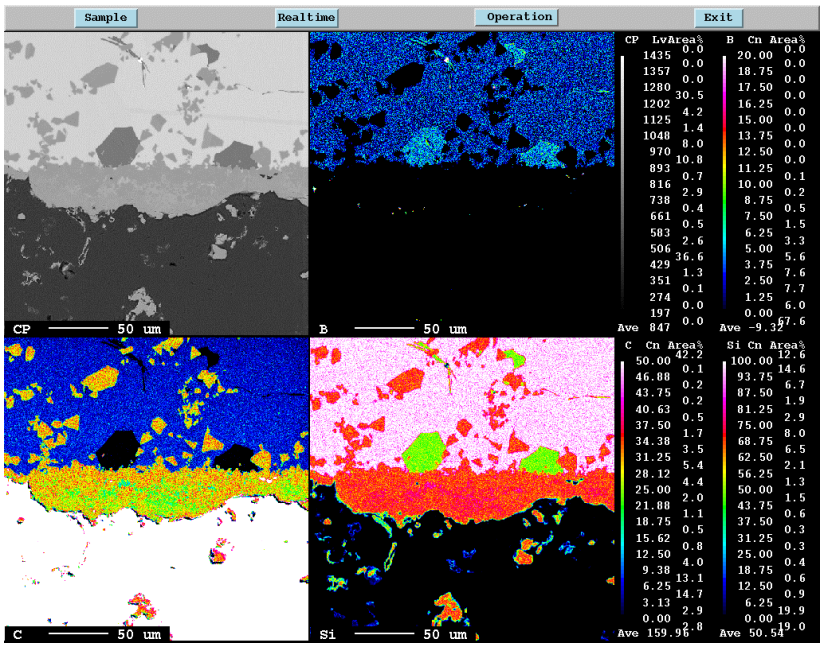

Figure 2-19 Element mapping in the bottom surface between Si-3.25B alloy and graphite. The Si-3.25B/graphite had been subjected to 1550 °C for 48 h. [58]

The average value of the thickness of the SiC layer as a function of thermal cycles is shown in **Figure 2-20**. It was observed that the thickness of the formed SiC layer was independent of the thermal cycles. The thickness was in the range 12-45 μm at three positions of graphite crucible. Besides, the relationship between the average thickness of the SiC layer and holding time was investigated, as shown in **Figure 2-21**. It shows that the thickness of the SiC layer was constant within the first 3h reaction time (maximum 40 μm). It, however, slightly increased to 60 μm after holding 48 h.

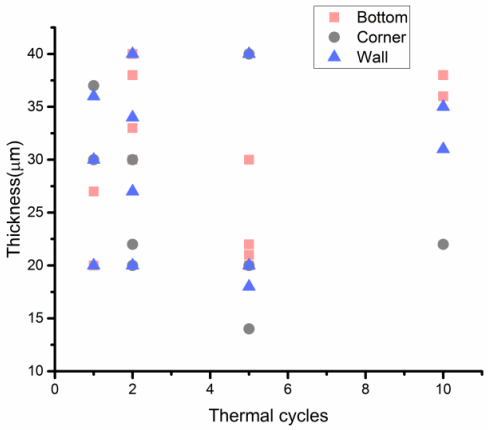

Figure 2-20 The SiC thickness of the Si-3.2B melts into the graphite crucible as a function of thermal cycles. [58]

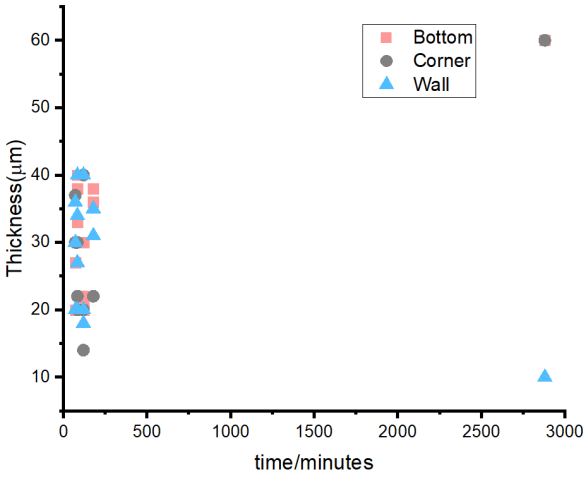

Figure 2-21 The SiC thickness of Si-3.25B alloy with graphite as a function of time. [58]

2.2. The Fe-Si-B system and its subsystems

2.2.1. The Fe-Si system

Figure 2-22 shows the Fe-Si binary phase diagram based on experimental data [64]. In the Fe rich part, the formed phases are complex. It involves low temperature magnetic, αFe/α'FeSi and α'FeSi/ $\alpha''$$Fe_3Si$ transition. Fe_2Si, FeSi, and Fe_3Si_7 silicides with a small homogeneity range melt congruently in the Fe-Si system. It is worth noting that Fe_3Si_7 is a form of $FeSi_2$ at high temperatures [65]. Kai et al. [66] reassessed the Si-rich part in Fe-Si system. The calculated Si-rich part phase diagram is shown in **Figure 2-23**b, where the position of $FeSi_2$ phase was substituting the Fe_3Si_7. In addition, the Fe solubility was also evaluated (**Figure 2-23**a). It shows that the maximum Fe solubility was 0.42 ppmm at 1346 ºC in the Fe-Si system.

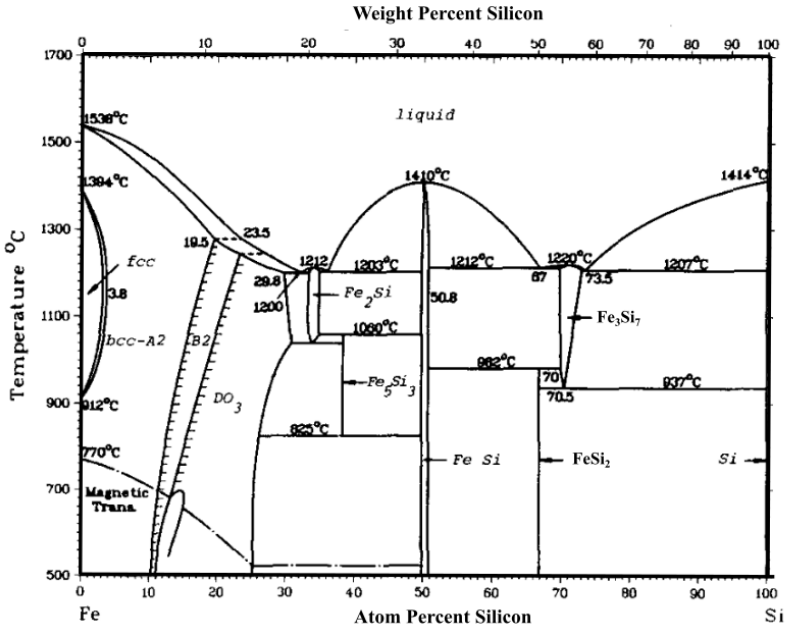

Figure 2-22 Fe-Si binary phase diagram.

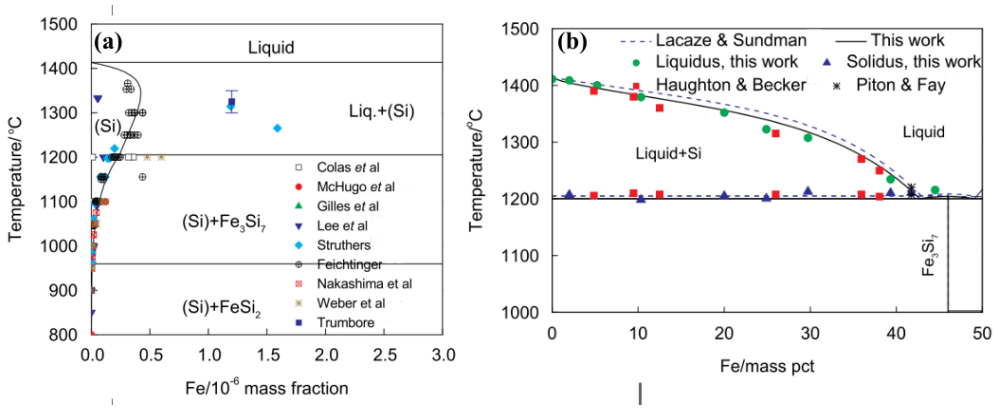

Figure 2-23 (a) Calculated Fe solubility in solid Si; (b) calculated Fe-Si phase diagram in Si-rich part. [66]

2.2.2. The Fe-B system

The Fe-B binary phase diagram is shown in Figure 2-24 [67]. Two intermediate phases, Fe_2B and FeB, are formed in the Fe-B binary system. Fe_2B is formed peritectically at 1409 °C. FeB is a homogeneous phase with a range of 1 at.% [63]. The B solubility in the Fe solid solution is very low. Hence, the invariant reactions of liquid + δFe → γFe and γFe → Fe_2B + αFe are close to the transition temperature

for δFe → γFe (1394.5 ºC) and γFe → αFe (911.8 ºC) [67]. Six invariant reactions occur in the Fe-B system, which is given in **Table 2-6**.

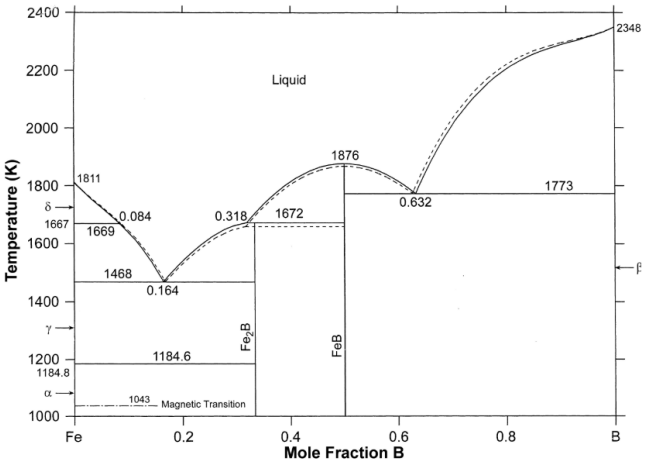

Figure 2-24 Fe-B binary phase diagram [67].

Table 2-6 Invariant reaction occurs in Fe-B system [63].

Reaction	Type	*T*/ºC
liquid → FeB	congruent	1633
liquid → FeB + βB	eutectic	1509.1
FeB + liquid → Fe_2B	peritectic	1409
liquid + δFe → γFe	peritectic	1394.7
liquid → Fe_2B + γFe	eutectic	1172.3
γFe → Fe_2B + αFe	eutectoid	911.7

2.2.3. The Fe-Si-B system

The isothermal section of Fe-Si-B system at 1000 ºC is shown in **Figure 2-25** [68]. Three ternary compound phases exist in the system: τ_1 (Fe_5SiB_2), τ_2 ($Fe_{4.7}Si_2B$), and τ_3 ($Fe_2Si_{0.4}B_{0.6}$). The crystal structures of these phases had been determined by Aronsson et al. [69]. However, the microstructures of the ternary phases have not been found in the literature. Neamţu et al. [70] determined the phases formed in the $Fe_{75}Si_{20}B_5$ alloy after DSC experiments. According to the Fe-Si-B system in **Figure 2-25**, τ_3 ($Fe_2Si_{0.4}B_{0.6}$) would be formed in the Fe-11.6Si-1.1B ($Fe_{75}Si_{20}B_5$ in at. %) alloy. However, only Fe_3Si and Fe_2B were determined by XRD analysis. Tong et al. [71] investigated the structure and properties of nanocrystalline Fe-5.3Si-3B ($Fe_{78}Si_9B_{13}$ in at. %) alloy. The formed phases were determined to be α-Fe(Si) solid solution and Fe_2B by XRD analysis. It corresponds well to the Fe-Si-B system in **Figure 2-25**.

In 2004, Tokunaga et al. [72] investigated the thermodynamic properties of Fe-Si-B system based on

the sublattice model. Furthermore, the results were evaluated by combining the experimental results from DSC with literature data. The Fe-Si-B master alloys with different compositions were used to perform the DSC experiments. The peak temperatures of the Fe-Si-B alloys were obtained during heating, as shown in **Table 2-7**. Then, the calculated isopleths at the 65 mol% Fe (**Figure 2-26**a), 10 mol% B (**Figure 2-26**b), and 10 mol% Si (**Figure 2-26**c) sections were compared with the DSC results separately. It is seen from **Figure 2-26**b and c that the peak temperature did not correspond to the calculated liquidus temperatures. Other DSC results were in good agreement with the calculated results. Moreover, it is found that the liquidus temperatures from Nagumo et al. [73] were lower than their calculated and DSC results. Tokunaga et al. [72] explained this deviation by the supercooling since the results from Nagumo et al. [73] were determined from the cooling curves of the melts in the DSC tests.

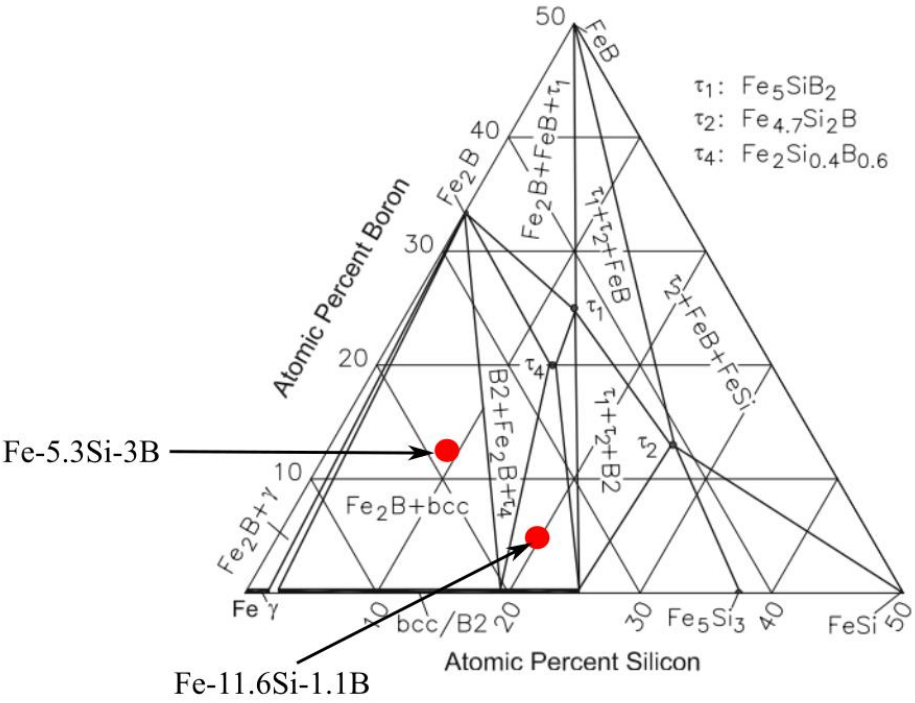

Figure 2-25 Fe-Si-B isothermal section at 1000 °C [68], calculated based on [72].

Table 2-7 Experimental results of Fe-Si-B ternary alloys determined by DSC on heating. [72]

Alloy composition (mol%)			Peak temperature (°C)			
Fe	**Si**	**B**				
80	10	10	1162			
70	20	10	1117	1121	1141	
65	25	10	1101	1112	1146	
60	30	10	1099	1164	1171	
52	38	10	1176			
70	10	20	1129	1266		
65	10	25	1115	1119	1211	1309
60	10	30	1120	1223	1380	
52	10	38	1162			
65	30	5	1153	1120	1127	1159
65	20	15	1102	1111	1200	
65	15	20	1115	1120	1231	
65	5	30	1119	1125	1273	1359

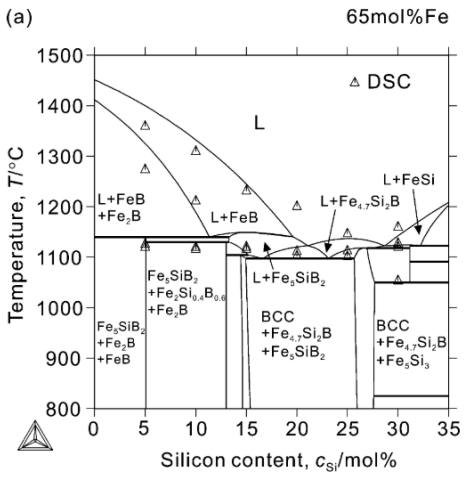

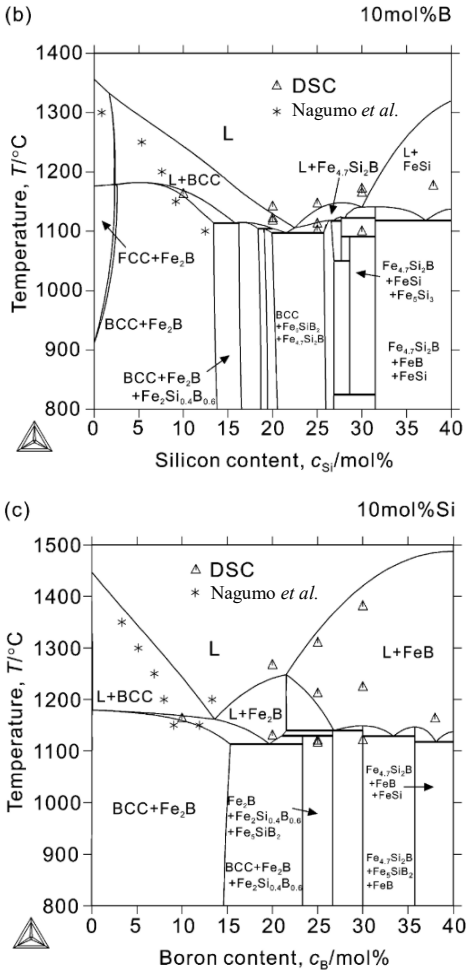

Figure 2-26 Calculated isopleths of the Fe-Si-B system at: (a) 65 mol% Fe; (b) 10 mol% B; (c) 10 mol% Si sections. [72]

In 2013, Poletti et al. [65] improved the thermodynamic description of the Fe-Si-B system by the Calphad method. Some DSC experiments were carried out to the transformation temperature in different Fe-Si-B alloys. The results were shown in **Table 2-8**. It is found that the calculated results had a better agreement with the DSC data from Tokunaga et al. [72].

Table 2-8 Experimental DSC data of the Fe-Si-B (heating rate 10 K/min). [65]

Alloy composition (mol%)			Transformation	T(°C)
Fe	Si	B		
78	2	20	Eutectic	1166
			Liquidus	1289
80	5	15	Melting	1168.5
80	7.5	12.5	Eutectic	1144
			Liquidus	1272
80	10	10	Eutectic	1148
			Liquidus	1236

These investigations of the Fe-Si-B system focuses on the Fe rich part where the content of Fe is higher than 50 at. %. No experimental data has been published in the Fe range of 0-50 at. %.

2.3. The Cr-Si-B system and its subsystems

2.3.1. The Cr-Si system

Figure 2-27 shows the Cr-Si phase diagram [74]. Four phases are formed in the Cr-Si system: Cr_3Si, Cr_5Si_3, CrSi, and $CrSi_2$. Cr_3Si melts congruently at 1780 °C. β-Cr_5Si_3 is regarded as Cr_3Si_2 in the earlier study and melts congruently at 1666 °C, and then is transformed to α- Cr_5Si_3 at 1488 °C [74]. Chen et al., however, argued that β-Cr_5Si_3 melts incongruently into liquid + Cr_3Si at 1659 °C [75]. CrSi decomposes at 1424 °C caused by the following reaction, CrSi → Cr_5Si_3 + liquid. $CrSi_2$ melts congruently at 1439 °C. Moreover, the maximum Si solubility in Cr solid solution ($Cr_{(ss)}$) is ~ 9.5 at.% at 1705 °C. The maximum Cr in Si solid solution ($Si_{(ss)}$) is ~ 8×10^{-6} at.% at 1305 °C [76].

The relevant invariant reactions are summarized in Table 2-9.

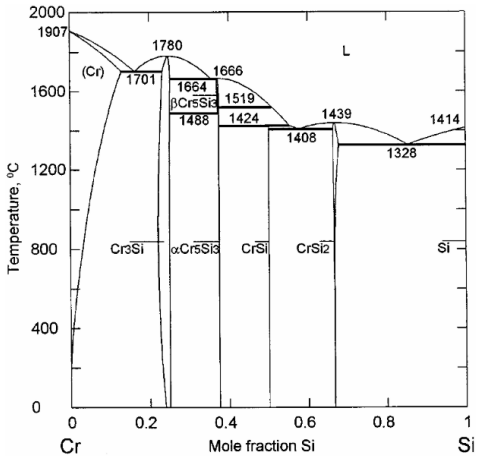

Figure 2-27 Cr-Si binary phase diagram [74].

Table 2-9 Invariant reaction occurs in Cr-Si system [63].

Reaction	Type	*T*/°C
liquid → Cr_3Si	Congruent	1776.9
liquid → $Cr_{(ss)}$ + Cr_3Si	Eutectic	1674.5
liquid → Cr_5Si_3	Congruent	1678
liquid → Cr_5Si_3 + Cr_3Si	Eutectic	1677
liquid → Cr_2Si	Congruent	1467.9
Cr_5Si_3 + liquid→ CrSi	Peritectic	1445.5
liquid → Cr_2Si + CrSi	Eutectic	1435.9
liquid → Cr_2Si + $Si_{(ss)}$	Eutectic	1333.7

2.3.2. The Cr-B system

The Cr-B phase diagram is proposed by Liao et al. [77] based on literature data, as shown in **Figure 2-28**. Six phases exist in the system: Cr_2B, Cr_5B_3, CrB, Cr_3B_4, CrB_2, and CrB_4. Besides, Cr_4B, Cr_3B_2, and CrB_6 have been reported, but these phases are not included in the Cr-Si phase diagram due to their uncertain existence. The B solubility in Cr(ss) was ~ 0.7 at.% at 1200 °C. The Cr solubility in B(ss) was ~ 2 at.% at 1830 °C. The relevant invariant reactions in the Cr-B system are summarized in **Table 2-10** [77].

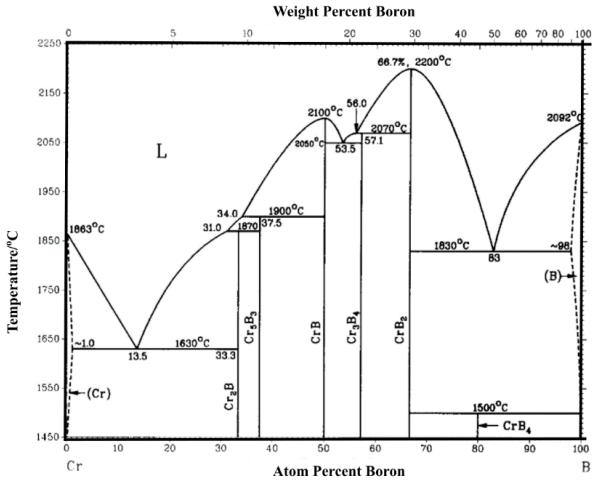

Figure 2-28 Calculated phase diagram for the Cr-B system [77].

Table 2-10 Invariant reactions in the Cr-B system [77].

Reaction	Type	*T*/°C
liquid → CrB_2	congruent	2200
liquid → CrB	congruent	2100
liquid + CrB_2 → Cr_3B_4	peritectic	2070
liquid → Cr_3B_4 + CrB	eutectic	2050
liquid + CrB → Cr_5B_3	peritectic	1900
liquid → CrB_2 + βB	eutectic	1830
Cr_5B_3 + liquid → Cr_2B	peritectic	1870
liquid → Cr_2B + bcc	eutectic	1630
βB + CrB_2 → CrB_4	peritectoid	1500

2.4. Wetting

2.4.1. The principle of wettability

Wettability is determined by the force balance between adhesive and cohesive forces between the liquid and solid surfaces. It is defined as the degree of wetting and characterized by the contact angle, θ, formed at the gas-liquid-solid interface (**Figure 2-29**) [78]. The relationship between the contact angle and the surface tension is described by Young's Equation:

$$\cos\theta = \frac{\gamma_{sg} - \gamma_{sl}}{\gamma_{lg}} \qquad 2.16$$

Where θ is the contact angle, γ_{lg} is the surface tension between liquid and gas phases, γ_{sg} is the surface tension between solid and gas phases, and γ_{sl} is the surface tension between solid and liquid phases. The contact angle of 90° is a threshold value. If $\theta > 90°$, adhesional wetting occurs. If $\theta_{con} < 90°$, immersional wetting occurs [79]. It should be noted that Young's equation can only be used in a smooth, flat, and rigid interface between solid and liquid.

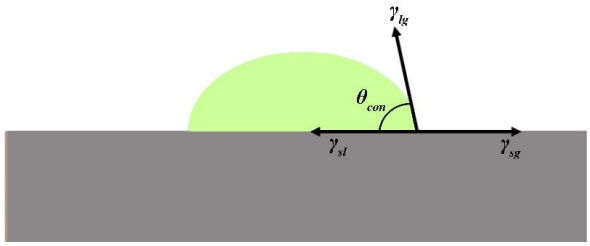

Figure 2-29 Schematic illustration of wetting angle.

When the metal/ceramic system is reactive wetting, the wetting behavior is governed by the interfacial reaction. Some reactions further lead to the formation of a continuous layer between the metal and ceramic.

2.4.2. Wettability properties of Si-B system

Wettability properties of liquid Si on graphite substrate

Wettability of liquid Si on graphite has been widely investigated. SiC is formed at the interface in the reaction of liquid Si with graphite. Hence, wetting is governed by the local chemical reaction at the triple line. The contact angle decreases with time and liquid Si spreads on the surface of graphite.

In 1975, Whalen et al. [80] studied the wetting of liquid Si on pyrolytic graphite under 1.3×10^{-7} atm at 1502 °C. A slight dependence of wetting on crystal orientation was detected. The equilibrium contact angle was measured to be ~10° with the formed SiC.

In 1995, Li et al. [81] investigated the wetting and infiltration of liquid Si on graphite. The experiments were conducted in a sessile drop furnace under Ar at 1430 °C. The melting process was shown in **Figure 2-30**. Once at 1414 °C, Si started to melt (**Figure 2-30**b), then spread on the substrate during melting (**Figure 2-30**c), and was completely melted after 1.5 min (**Figure 2-30**d). Subsequently, the contact angle decreased rapidly with time (**Figure 2-30**e) and stabilized at low value after ~ 10 min (**Figure 2-30**f). Moreover, the results showed that the surface roughness would enhance the wetting.

The vertical and lateral penetration depth to graphite was measured by Li et al. [81]. As shown in **Figure 2-31**, the vertical penetration depth was noted by H and the lateral penetration depth was noted by D. According to the function of the penetration depth with the equilibrium contact angles (**Figure 2-32**), the vertical penetration depth was independent of the contact angles but increased with porosity of the graphite material. The lateral penetration depth decreased with the increasing of contact angles.

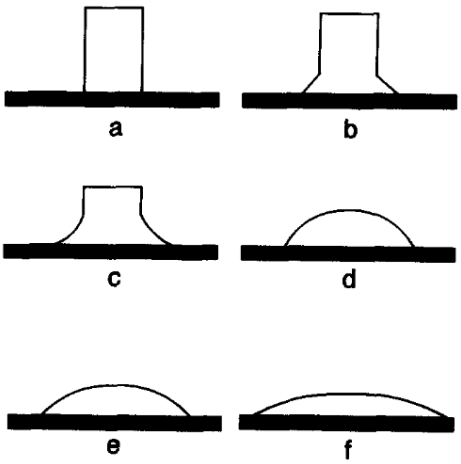

Figure 2-30 Schematic representation of the melting process of Si and its spreading on the graphite substrate. (a) before melting; (b) start of melting; (c) during melting; (d) complete melting; (e) during spreading; (f) stabilization. [81]

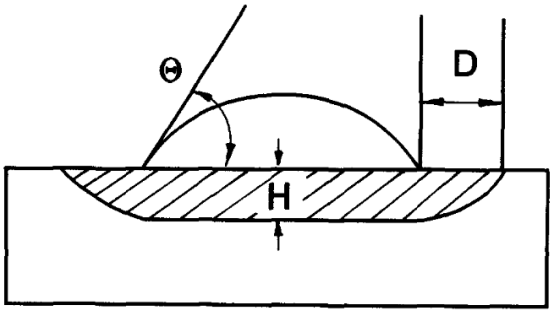

Figure 2-31 Schematic representation of the cross-section of the Si/graphite interface. θ is the equilibrium contact angle, H is he vertical penetration depth, and D is the lateral penetration depth. [81]

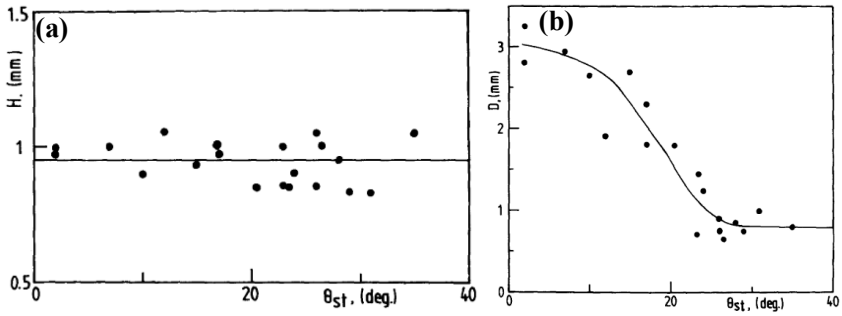

Figure 2-32 The penetration depth as a function of the equilibrium contact angles. (a) vertical penetration depth, (b) lateral penetration depth. [81]

In 2005, Dezellus et al. [82] studied the wettability of C materials by liquid Si at 1430 °C under a vacuum of 10^{-10} atm by using the dispensed drop variant of the sessile drop technique. Two different C materials of vitreous C and pseudo-monocrystalline graphite were used in the experiments. It is found that spreading occurred in two main steps, as shown in **Figure 2-33**. In the beginning, the liquid Si/C interface was non-reactive that the contact angle θ_0 was characteristic of Van der Waals interactions. In the second step, the contact angle θ_F was characterized by the chemical interaction at the liquid Si/C interface. The spreading kinetics were coupled to the reaction of SiC at the triple line.

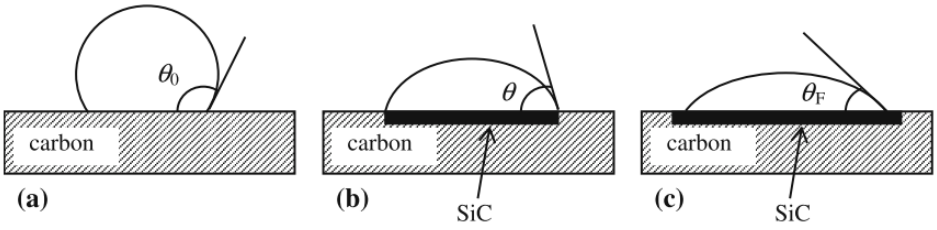

Figure 2-33 Schematic representation of the 'Reaction Product Control' model. For Si on C, the initial contact angle θ_0 is the contact angle on the unreacted carbon substrate surface, while the final contact angle θ_F is on SiC. [14]

In 2010, Ciftja et al. [83] reported the wettability and infiltration of liquid Si on five different graphite materials under Ar by a sessile drop method. The properties of the graphite materials are listed in **Table 2-11**. The results showed that the main factor affecting the penetration depth of liquid Si in graphite was the average pore size (**Figure 2-34**). It correlated with the work done by White et al. [84] and Israel et al. [85]. It was no clear the dependence of penetration depth with graphite density and porosity. **Figure 2-35** shows that the final contact angle with SiC decreased with the increase of surface roughness. It is a good agreement with Li et al. [81].

Table 2-11 The properties of the graphite substrates used in the experiments. [83]

Substrate	Average Pore Diameter, μm	Porosity, Pct	Bulk Density, g/cm^3
IG11	2.5	18.3	1.742
ISEM3	2.72	13.4	1.858
ISO88	0.66	12.1	1.885
SIC-6	3.2	12.7	1.849
IG610	2.6	12.8	1.814

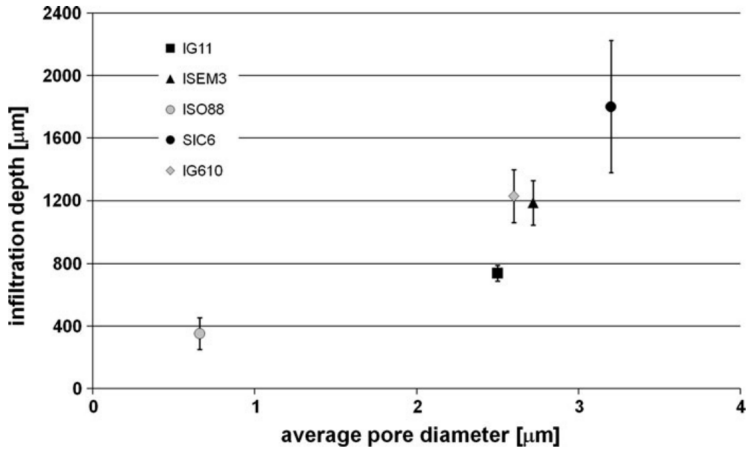

Figure 2-34 The function of penetration depth of liquid Si with the average pore diameter of the graphite substrates. [83]

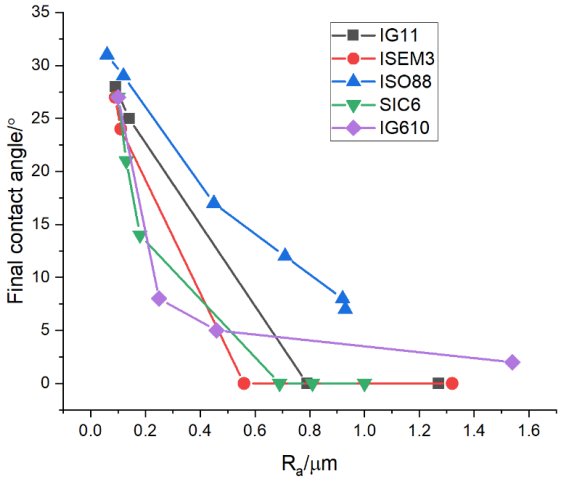

Figure 2-35 The function of the final contact angle with the roughness of the different graphite substrates. [83]

In 2012, White et al. [84] investigated the melting behavior of Si in contact with different grades of graphite in a sessile drop furnace. It was found that the heating rate strongly influenced the wetting

behavior of Si on graphite under Ar. The author believed that it was caused by the formation of SiC through the gas-solid reaction at less than the liquidus temperature of Si. It further altered the surface properties of the graphite.

In 2019, Naikade et al. [86] measured the contact angle of liquid Si on vitreous C under 5×10^{-8} atm. The contact angle was measured at 1500 °C, as shown in **Figure 2-36**, where two images were captured at 50 min interval. It was observed that the droplet's height decreased with the holding time increasing. However, the diameter of the droplet remained constant. It indicates that the volume of the droplet was reduced in the wetting process, which was caused by the evaporation of Si.

The summary of the contact angles of liquid Si on graphite substrates is listed in **Table 2-12**.

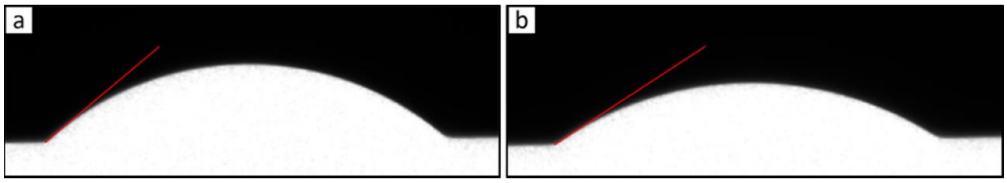

Figure 2-36 Si droplet on vitreous carbon at 1500 °C under 5×10^{-8} atm. (a) t = 0; (b) t = 50 min.

Table 2-12 Summary of the contact angle of liquid Si on graphite. θ_0 represents the contact angle between liquid Si and graphite, θ_F represents the contact angle between liquid Si and SiC.

Authors	θ_0/°	θ_F/°	T/°C	Atmosphere	Ra(μm)	Porosity (%)	Average pore diameter(μm)
Li et al. [81]	~18	3	1430	Ar	3.18		
	~48	35			0.005		
Dezellus et al. [82]	146	35-40	1430	10^{-10} atm			
Whalen et al. [80]	23	10	1502	1.3×10^{-7} atm			
Ciftja et al. [83]	~100	0	1600	Ar	1.27	18	2.5
	~95	~30			0.09		
Israel et al. [85]	~90	~12	1460	Ar	0.77	15	2.3
Casado et al. [87]	23.6	0	1424	Ar	4.83	17	9.32

Wettability properties of liquid Si on Si_3N_4 substrate

Si_3N_4 is one of the potential refractory materials for the production of solar-grade Si. The wettability property of liquid Si on Si_3N_4 is vital for successful development of the technology. Consequently, it has been widely studied by researchers. However, the equilibrium contact angles from literature are scattered and in the range 0-85°. In 1973, Champion et al. [88] investigated the wetting of polycrystalline Si_3N_4 at 1500 °C under 1.3×10^{-8} atm. The final contact angle of liquid Si on Si_3N_4 was obtained to be less than 40°. In 1975, Whalen et al. [84] measured the contact angle of liquid Si and Si-0.39B on hot-pressed Si_3N_4 under 1.3×10^{-7} atm. It is found that the wetting was affected significantly

by temperature. The value of the final contact angle for Si was 43° at 1427 °C and 10° at 1482 °C. For Si-0.39B, it was changed to 48° at 1427 °C and 8° at 1482 °C. In 1986, Maeda et al. [89] studied the contact angle and reaction between liquid Si and hot-pressed Si_3N_4 (no binder) at temperatures over 1412 °C under inert gas. A final contact angle of 51° was measured. In 2004, Yuan et al. [90] investigated the wettability property of liquid Si on sintered Si_3N_4 substrate at 1420 °C under Ar. The evolution of the measured contact angle with time was shown in **Figure 2-37**. It was found that the initial contact angle was 89°. It had a slight decrease with time and kept at 85° after 15 min.

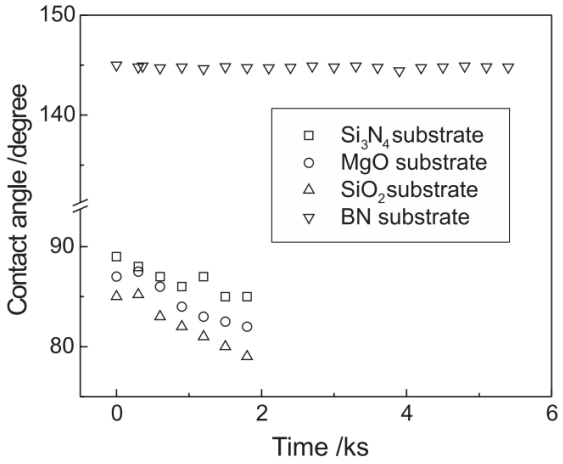

Figure 2-37 The contact angles of liquid Si on Si_3N_4, MgO, SiO_2, and BN substrates at 1420 °C under Ar, the partial pressure of oxygen was 10^{-20}-10^{-21} atm. [90]

It is known that a thick oxynitride (SiO_xN_y) layer is formed when Si_3N_4 is in contact with oxygen. The composition of oxynitride varied over a broad range, depending on the oxygen content. The oxynitride layer would be eliminated in contact with Si. The reaction is expressed as follows.

$$4SiO_xN_y + [3y + 4(x-1)]Si \leftrightarrow ySi_3N_4 + 4xSiO \qquad 2.17$$

SiO gas was formed in the reaction between Si and oxynitride layers. Hence, in 1992, the influence of oxygen partial pressure on the wetting behavior of liquid Si on Si_3N_4 was investigated by Li et al. [91]. The contact angle was measured at 1450 °C under Ar. **Figure 2-38** shows the function of the contact angle with the partial pressure of oxygen in the Si/Si_3N_4 system. The results showed that the contact angle decreased sharply from 180° to 53° at the oxygen pressure of ~ 10^{-9} atm, then kept constant at ~ 48° in the oxygen pressure range 5×10^{-19}-10^{-9} atm, and decreased with decreasing of oxygen pressure in the range 3.4×10^{-24}-5×10^{-19} atm. The contact angle of 0 was considered to be the actual contact angle of liquid Si on Si_3N_4. However, Drevet et al. [92] disagreed that the value of 0 was probably caused by the decomposition of Si_3N_4. It demonstrated that the pressure of oxygen in the system significantly affected the value of contact angles.

Figure 2-38 also represented the equilibrium oxygen pressure of Si/SiO_2 at 1450 °C (5.0×10^{-19} atm). Hence, SiO_2 would be formed at $p(O_2) > 5.0\times10^{-19}$ atm. However, the complete passive SiO_2 on the surface of liquid Si was possible only at $p(O_2) > 2.0\times10^{-2}$ atm at 1450 °C due to the reaction of Si and SiO_2 leading to the formation of SiO gas.

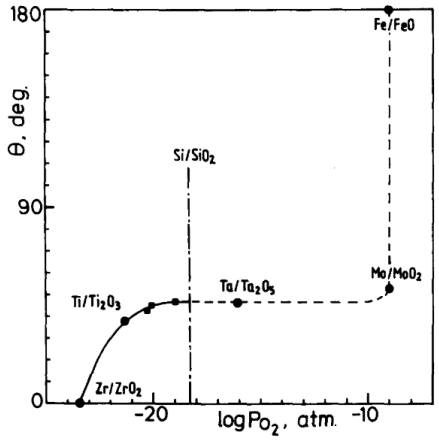

Figure 2-38 The function of the contact angle with the partial pressure of oxygen in the Si/Si_3N_4 system at 1450 ºC. [91]

In 2009, Drevet et al. [92] studied the wetting of Si_3N_4 by liquid Si by the sessile drop method. The Si_3N_4 substrate was sintered using Y_2O_3 and Al_2O_3 (both 6 mass %) with an average roughness of 70nm. The contact angle was measured at 1430 ºC under Ar, as shown in **Figure 2-39**. It is found that the contact angle decreased with time, from the initial value of 82º to a final value of 49º. The value of 82º was regarded as the contact angle of liquid Si on SiO_2 and the value of 49º was considered to be the contact angle of Si on Si_3N_4. The effect of the partial pressure of oxygen on wettability results was checked under an oxygen pressure of 10^{-19} atm. The results did not differ significantly.

The summary of the contact angles of liquid Si on Si_3N_4 substrates is listed in **Table 2-13**.

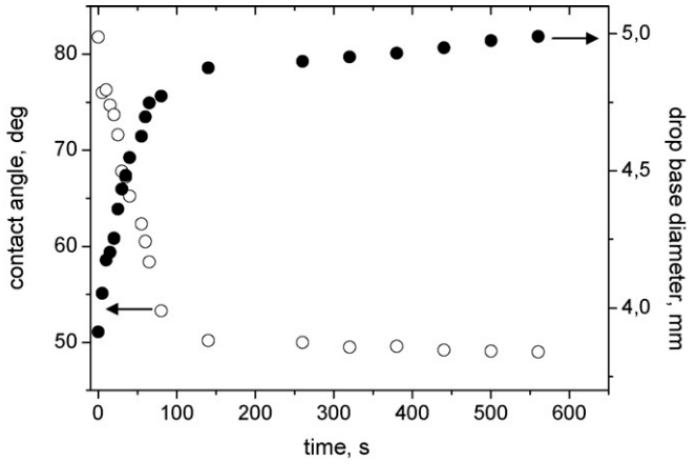

Figure 2-39 The function of contact angle and drop base diameter with time in Si/ Si_3N_4 system at 1430 ºC. [92]

Table 2-13 Summary of the contact angles of liquid Si on Si_3N_4.

Authors	Atmosphere/atm	angle/°	*T*/°C	Si_3N_4
Champion et al. [88]	1.3×10^{-8}	>40	1500	Polycrystalline
Whalen et al. [84]	1.3×10^{-7}	43	1427	Hot pressed
		10	1482	
Maeda et al. [89]	inert gas	51	1412	Hot pressed
Yuan et al. [90]	Ar($P(O_2)=10^{-20}$)	85	1420	Sintered
Li et al. [91]	Ar($P(O_2)=3.4\times10^{-24}$)	0	1450	Sintered
	Ar($P(O_2)=9.0\times10^{-17}$)	48		
Drevet et al. [92]	Ar	49	1430	Sintered

Wettability properties of liquid Si and Si-B alloy on BN substrate

BN exists in two modifications: hexagonal and cubic BN. Most wetting results of liquid Si on BN are obtained with the h-BN substrate. The wettability behavior of BN by liquid Si has been studied and the contact angle values are in the range 90°-145° at 1420-1500 °C. However, the scattered values are measured at various conditions (roughness of substrate surface, type and content of impurities in the Si/BN system, and the partial pressure of oxygen).

In 1973, Champion et al. [88] investigated the wetting of pyrolytic BN at 1500 °C under 1.3×10^{-8} atm. The value of the contact angle was measured to be 105°.

In 1986, Maeda et al. [89] investigated the wettability behavior of liquid Si on hot-pressed BN (no binder) at temperatures over 1412 °C under inert gas. The contact angle was obtained to be 122.5°. It is found that the solidified droplet was separated from BN without adhesion.

In 2004, Yuan et al. [90] investigated the wettability property of liquid Si on pyrolytic BN (99.5 mass %) at 1420 °C under Ar. The measured contact angles in the Si/BN system are shown in **Figure 2-37**. It was found that the contact angle was independent of time at oxygen partial pressures ranging from 10^{-20}-10^{-21} atm. The value of 144° was obtained. EPMA analyses for the cross-section of the Si/BN interface was shown in **Figure 2-40**. It is found that a discontinuous Si_3N_4 layer (below 20 μm) was formed and it has the function of preventing the further dissolution of BN into the liquid Si.

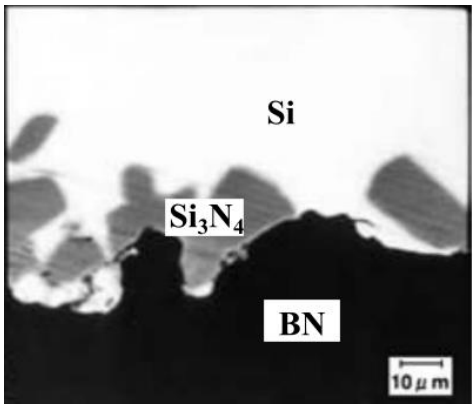

Figure 2-40 EPMA analyses of Si/BN cross-section at 1420 °C after 1 h. [90]

In 2009, Drevet et al. [92]studied the wetting of pyrolytic BN by liquid Si at 1430 °C under Ar. The results are presented in **Figure 2-41**. The initial contact angle was 133° and decreased to 117° after 10 min, and then kept constant. Moreover, an average thickness of ~ 10 μm Si_3N_4 layer was observed, as shown in **Figure 2-42**. Hence, the initial value of 133° was regarded as the contact angle of Si with BN and the final value of 117° was regarded as the contact angle of Si with Si_3N_4. However, the measured final contact value of Si with Si_3N_4 was 49° at the same condition [92]. It is much lower than 117°. The author gave a possible explanation that the weak reaction between Si and BN, leading to the B saturation of liquid Si well before the equilibrium contact angle on the Si_3N_4 layer.

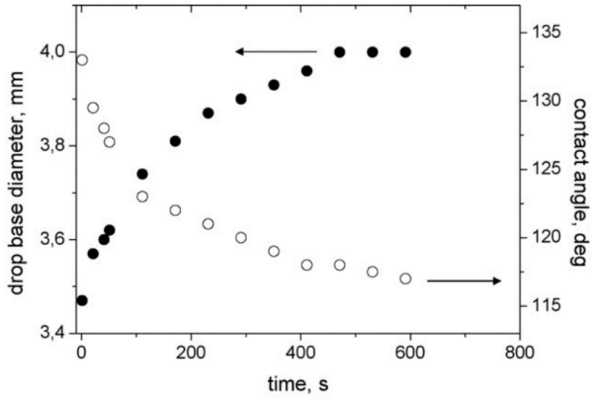

Figure 2-41 The function of contact angle and drop base diameter with time in the Si/BN system at 1430 °C. [92]

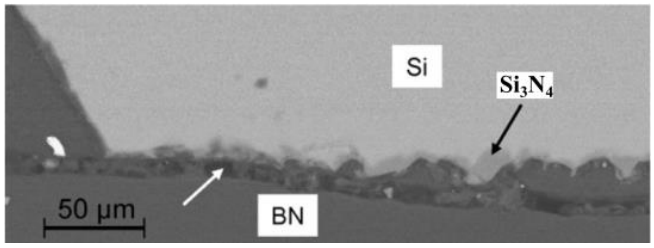

Figure 2-42 The interface between Si and BN, the write arrow indicates the crack. [92]

In 2017, Polkowski et al. [93] investigated the wetting behavior of liquid Si with h-BN substrate at temperatures up to 1750 °C under static Ar. The contact angle of 90 ± 5° was obtained at 1750 °C. The wetting behavior in the Si/h-BN system was controlled by the substrate dissolution and reprecipitation mechanism. However, SiC was observed at the interface instead of Si_3N_4 (Figure 2-43). Polkowski et al. [93] explained that it might be caused by C pollution in the h-BN substrate.

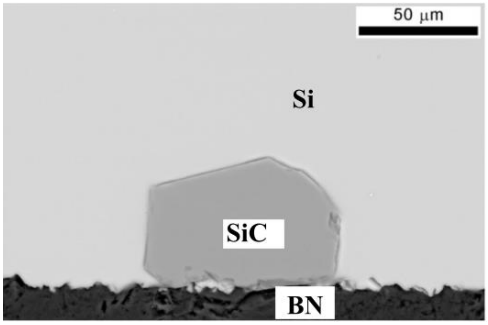

Figure 2-43 The interface between Si droplet and h-BN. [93]

In 2019, Polkowski et al. [94] investigated the wetting of h-BN by liquid Si upon the melting/solidification process. The Si/h-BN was introduced to a sessile drop furnace subjected to 15 thermal cycles in the temperature range 1300-1450 °C under static Ar. It is seen from Figure 2-44 that the contact angle was higher than 90° for the whole process and an abrupt increase was observed in the 10th cycle. The variation of the contact angle with the number of cycle was explained by the regrown platelets that altered the surface morphology, smoothness, and flatness in each thermal cycle.

Polkowski et al. [95] also studied the effect of B on the wetting of h-BN by liquid Si-B alloys. Si-1B, Si-3.2B, and Si-5.7B (mass %) alloy were used in the sessile drop experiments under static Ar at temperatures up to 1750 °C. The recorded images of Si and Si-B alloys on h-BN are presented in Figure 2-45, and the relevant measured contact angles are listed in Table 2-14. It shows that the contact angle in Si-B/h-BN was higher than Si/h-BN system. Polkowski et al. [95] proposed that the addition of B suppressed the dissolution of h-BN to liquid Si.

The summary of the contact angles of liquid Si on BN substrates is listed in Table 2-15.

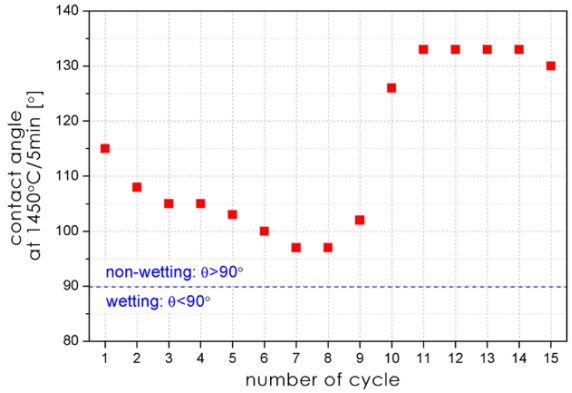

Figure 2-44 The relationship between the average contact angle value and the thermal cycle on the h-BN substrate. [94]

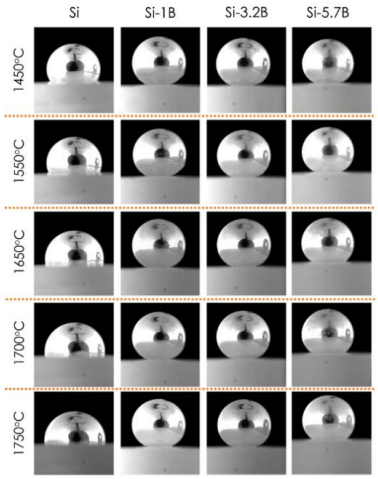

Figure 2-45 Images of Si-B/h-BN sessile drop couples in situ recorded during the high-temperature tests. [95]

Table 2-14 Contact angle values measured by the sessile drop method for Si and Si-B alloys on the h-BN substrate. [96]

	Si/h-BN	**Si-1B/h-BN**	**Si-3.2B/h-BN**	**Si-5.7B/h-BN**
T/°C	contact angle values after 5 min test, θ/°			
1450	115	147	146	145
1550	97	150	144	143
1650	94	150	147	136
1700	92	152	150	134
1750	90	151	151	131

Table 2-15 Summary of the contact angles of liquid Si on BN.

Authors	Atmosphere	angle	T	BN
Champion et al. [88]	1.3×10^{-8} atm	105	1500	pyrolytic
Maeda et al. [89]	inert gas	122.5	1412	hot pressed
Yuan et al. [90]	Ar	144	1420	pyrolytic
Drevet et al. [92]	Ar	117	1430	pyrolytic
Polkowski et al. [93]	Ar	90	1750	sintered

2.4.3. Wettability properties of Fe-Si-B system

Fe-26Si-9B alloy is proposed to be one of the potential PCMs in our research. To successfully introduce the Fe-26Si-9B alloy into reality, a proper selection of reliable refractory materials for the PCM container is essential. Hence, the wetting behaviors of Fe-Si-B alloy on graphite, Al_2O_3, Si_3N_4, and h-BN are reviewed. As Fe and Si are the main elements in the Fe-Si-B alloy, the following literature review focuses on the wettability properties of Fe, Fe-Si, and Fe-Si-B alloys on the refractory materials.

Wettability properties of liquid Fe, Fe-Si, and Fe-Si-B alloy on graphite substrate

The wetting behavior of Fe on graphite has been studied by several researchers [97]–[100]. These studies show that good wetting exists in the Fe/graphite system under different atmospheres. The final contact angles are in the range 0-66°.

In 1954, the wettability and adherence in the Fe/graphite system were investigated by the sessile drop method. The contact angle of liquid Fe on the electrode grade graphite was measured at 1550 °C under different atmospheres, which was 0° under 6.6×10^{-9} atm, 37° under H_2, and 51° under He [97].

In 1998, Wu et al. [98] studied the interfacial phenomena by measuring the contact angle of liquid Fe on solid graphite at 1600 °C under Ar. **Figure 2-46**a shows the influence of C on the initial and equilibrium contact angle of liquid Fe on graphite. It is seen that the initial contact angle increased with the increase of C content. The final contact angle was, however, slightly affected by C content. In addition, **Figure 2-46**b shows that the contact angle decreased with time, while the final contact angles were not changed with the C content.

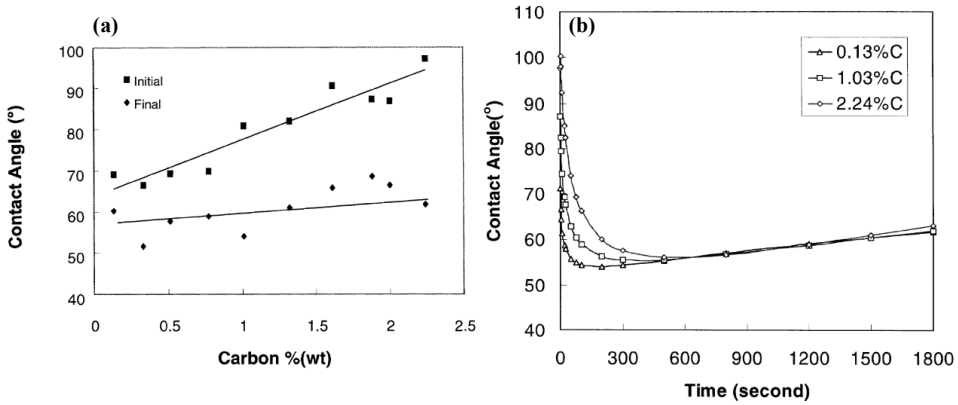

Figure 2-46 (a) Influence of C content on the contact angle of liquid Fe on graphite substrate; (b) the function of contact angle with time. It is noted that sulfur was less than 0.02 mass %.

In the same year, Sun et al. [99] investigated the C dissolution into liquid Fe and Fe alloys. The Fe cylinder was placed on a graphite base in an electric resistance furnace under Ar. Then, the contact angle was measured in the heating process. The contact angle of a sample of initial 0 mass % C was 66° at 1300 °C, 60° at 1400 °C, and 59° at 1500 °C. When the initial C content was increased to 4.8 mass %, the contact angle was increased to 110° at 1300 °C, 120° at 1400 °C, and 118° at 1500 °C.

In 2003, Zhao et al. [101] investigated the C dissolution from the graphite substrate to liquid Fe at 1600 °C under Ar. The measured initial contact angle was 64°, decreased to 38° after 9 min, and kept constant after 45 min. The final C saturation was 5.62 mass %.

The wetting behavior is moved from Fe/graphite system to Fe-Si/graphite system. In 1973, Champion et al. [88] investigated the wetting of SiC by Fe-33Si at 1500 °C and Fe-56Si (mass %) at 1450 °C under 1.3×10^{-8} atm. The values of contact angle of them were measured to be less than 40°.

In 2006, Rubio et al. [102] studied the dynamic wetting of graphite and SiC by ferrosilicon alloys containing 25, 74, and 98.5 mass % Si at 1550 °C under purified Ar. The synthetic graphite plate (Clifftonite) and 85 mass % SiC (85%SiC-15%Si) were used in the sessile drop experiment without more information. The contact angle with time for the three ferrosilicon alloys on graphite is shown in **Figure 2-47**, and on SiC is shown in **Figure 2-48**. It shows that the final contact angle of Fe-74Si and Fe-98.5Si on graphite was 0. The contact angle of Fe-25Si on graphite was, however, 70° after 19.5 min. It is seen from **Figure 2-48** that the final contact angle of SiC was 12° by Fe-98.5Si, 31° by Fe-74Si, and 38° by Fe-25Si. The results indicated that the dynamic wetting was strongly dependent on the rate of formation of SiC at the interface between ferrosilicon and graphite. According to the XRD results, the SiC layer was formed at the interface between Fe-25Si and graphite. Hence, it was expected that the contact angle was close to 38° in the Fe-25Si/graphite system after 30 min. However, the contact angle remained steady at 70°, which was not explained.

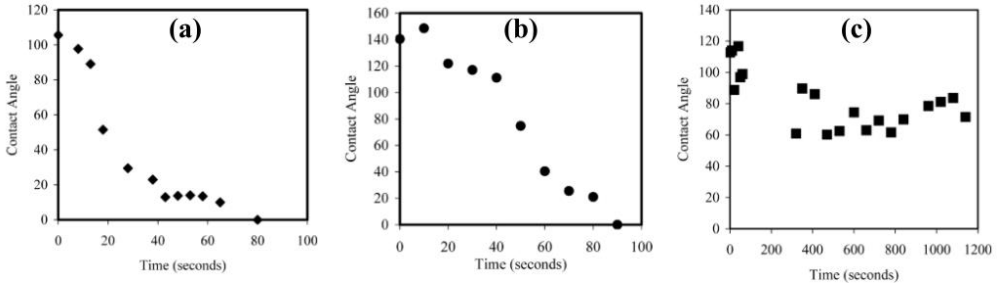

Figure 2-47 Dynamic wetting of ferrosilicon on synthetic graphite. (a) Si 98.5%, (b) FeSi 74%, (c) FeSi 25%

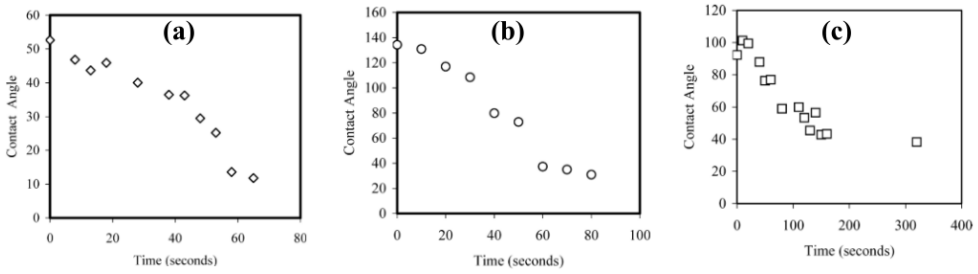

Figure 2-48 Dynamic wetting of ferrosilicon on SiC. (a) Si 98.5%; (b) FeSi 74%; (c) FeSi 25%.

In 2016, Gao et al. [103] studied the contact angle of liquid Fe-5.3Si-3B alloy on the SiC substrate in a vacuum atmosphere by the sessile drop method. The author did not provide the value of the vacuum. The final contact angle of liquid Fe-5.3Si-3B alloy on SiC was ~ 100º at 1150-1360 ºC under vacuum. $B_{13}C_2$ phase was detected by XRD that was caused by the reaction between Fe-5.3Si-3B alloy and SiC.

In 2018, Grorud et al. [15] under the supervision of the present author, investigated the wetting behavior of Fe-26Si-9B alloy on a graphite substrate under 10^{-4} atm. The images of the Fe-26Si-9B on graphite substrate during the heating process are shown in **Figure 2-49**. When the temperature reached to 1220 ºC, the sample started to melt, as shown in the white dotted circle. The final contact angle with SiC was measured to be 31º at 1550 ºC.

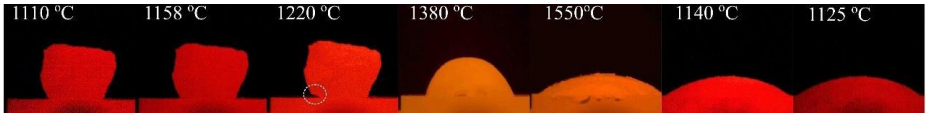

Figure 2-49 Images of Fe-26Si-9B on graphite substrates under 10^{-4} atm.

Wettability properties of liquid Fe, Fe-Si, and Fe-Si-B alloy on Al_2O_3 substrate

The wetting behavior of Fe-based alloy on Al_2O_3 is affected by the atmosphere, oxygen pressure, carbon content, and temperature.

In 1954, the wettability of liquid Fe on Al_2O_3 substrate was investigated by the sessile drop method at 1550 ºC. The final contact angle was measured to be 121.4º under H_2 and 128.7º under He [97].

In 1973, Champion et al. [88]investigated the wetting of Al_2O_3 by Fe-33Si at 1500 ºC and Fe-56Si (mass %) at 1450 ºC under 1.3×10^{-8} atm. The values of contact angle were measured to be 85º with Fe-33Si and 90º with Fe-56Si.

In 1992, Jimbo et al. [104] measured the contact angle of Fe-C alloys on the Al_2O_3 substrate at 1450 ºC and 1550 ºC under a CO_2/CO gas atmosphere. The function of the contact angle with C content is shown in **Figure 2-50**. It is seen that the value of the contact angle decreased as a function of C content at constant temperature and increased at constant C content as temperature decreased. The contact angle of pure liquid Fe with Al_2O_3 was measured to be 124º at 1450 ºC at a low oxygen potential of 9 ppm.

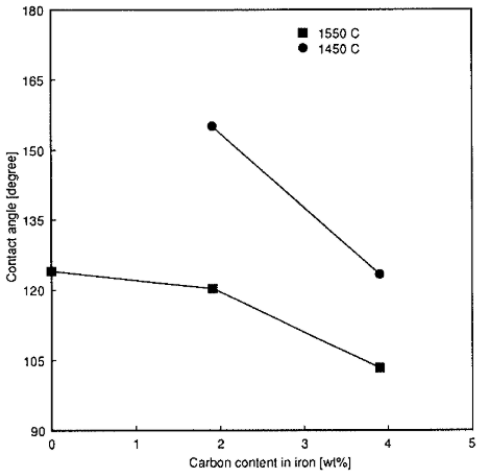

Figure 2-50 Contact angle between Fe-C alloy as a function of C content. [104]

In the same year, Nakashima et al. [105] studied the effect of oxygen on the wetting of liquid Fe on the Al_2O_3 substrate at 1600 ºC under different atmospheres. It is seen from **Figure 2-51**a that the final contact angle was in the range 100-140º. The value of the contact angle was strongly affected by the atmosphere and the purity of the Al_2O_3. The effect of oxygen on the contact angle of liquid Fe on Al_2O_3 was presented in **Figure 2-51**b. The results showed that the contact angle increased with the increase of the oxygen content in the range of less than 0.01 %, while it was decreased with the increase of oxygen content at oxygen content higher than 0.01 %.

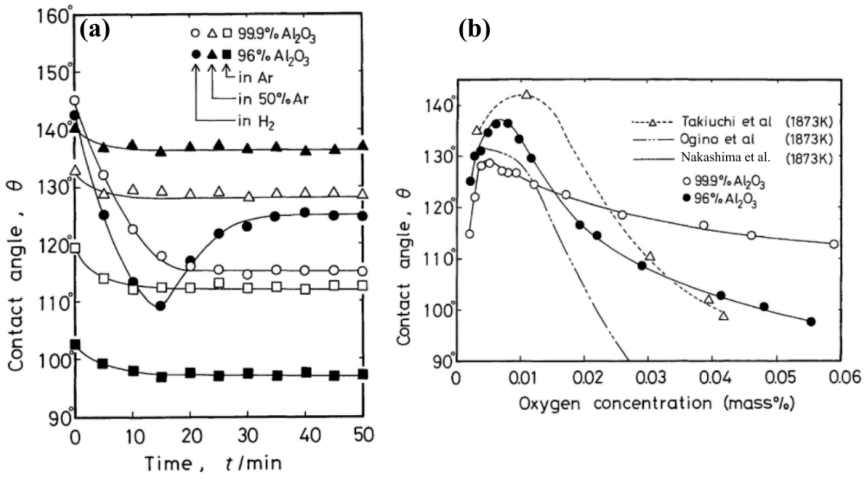

Figure 2-51 (a) Change of contact angle of liquid Fe with time at 1600 ºC; (b) effect of oxygen on the contact angle of liquid Fe at 1600 ºC. [105]

In 2003, Zhao et al. [101] measured the contact angle of liquid Fe on Al_2O_3 (99.8%) at 1600 ºC under Ar. The contact angle was obtained to be 125º and independent of time. The oxygen was calculated to be low. The value of the contact angle was in good agreement with Nakashima et al. [105] and Jimbo et al. [104].

In 2018, Yan et al. [106] investigated the wettability of liquid steel in contact with Al_2O_3. The C and O content in the steel was 0.39 mass % and 0.003 mass %, respectively. The wetting experiments were performed in sessile drop furnace under a flow Ar with the oxygen content of less than 2 ppm. The contact angles were measured at 1500 ºC, 1510 ºC, and 1520 ºC, as shown in **Figure 2-52**. It is seen that the final contact angle was ~ 127º at 1500 ºC, ~ 125º at 1510 ºC, and ~ 124º at 1520 ºC.

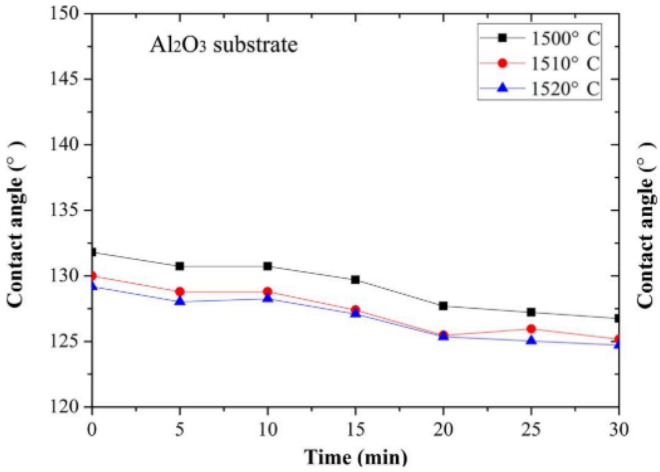

Figure 2-52 The function of contact angle with time on Al_2O_3 substrate at 1500, 1510, and 1520 ºC. [106]

In 2016, the contact angle of liquid Fe-5.3Si-3B alloy on the Al_2O_3 substrate was studied in a vacuum

atmosphere by the sessile drop method [103]. It was found that the final contact angle decreased with temperature from 142° at 1160 °C to 116° at 1360 °C. The Fe_2AlB phase was detected by XRD, produced from the reaction between the Fe-5.3Si-3B alloy and Al_2O_3.

In 2018, Grorud et al. [15] studied the wetting behavior of Fe-26Si-9B alloy on Al_2O_3 substrates under 10^{-4} atm, as shown in **Figure 2-53**. In Al_2O_3-1, the sample started to melt at 1219 °C and was completely melted at 1354 °C. The final contact angle was measured to be 124 °. In Al_2O_3-2, it started to melt at 1220 °C and was completely melted at ~ 1250 °C. The final contact angle was 120 °.

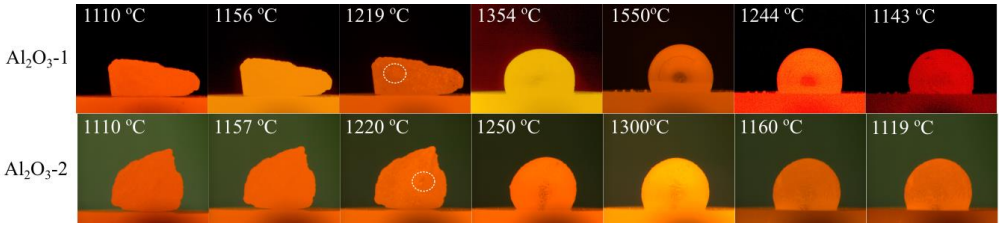

Figure 2-53 Images of Fe-26Si-9B on Al_2O_3 substrates under 10^{-4} atm. [15]

Wettability properties of liquid Fe, Fe-Si, and Fe-Si-B alloy on Si_3N_4 and BN substrate

In 1966, Yasinskaya et al. [107] studied the wetting of liquid Fe on Si_3N_4 and BN substrates at the melting temperature under an Ar atmosphere or a vacuum of 1.3×10^{-5}-1.3×10^{-7} atm. The contact angles were measured after 15 min after complete melting. It was found that the contact angle was 112° in Fe/BN system and 90° in Fe/Si_3N_4 system.

In 1973, Champion et al. [88] investigated the wetting of Si_3N_4 and BN substrates by Fe-33Si and Fe-56Si (mass %) under 1.3×10^{-8} atm. The measured contact angle was 76° in Fe-33Si/ Si_3N_4 system at 1500 °C, 66° in Fe-33Si/BN system at 1550 °C, 66° in Fe-56Si/ Si_3N_4 system at 1450 °C, and 82° in Fe-56Si/BN system at 1500 °C. Fe-33Si and Fe-56Si alloys showed good wetting behaviors on both Si_3N_4 and BN substrates.

In 2016, the contact angle of liquid Fe-5.3Si-3B alloy on BN substrates was studied by sessile drop method under different atmospheres (Ar, N_2, and vacuum) [103]. The final contact angles were measured after keeping the melt at the testing temperature for 30 min. The results were shown in **Figure 2-54**. The contact angle of liquid Fe-5.3Si-3B alloy on BN decreased slightly with increasing temperature. The value was in the range of 140-147° at 1160-1360 °C under vacuum and 136-150° at 1160-1410 °C under Ar. The droplets in the N_2 atmosphere had irregular oval shapes, even though the temperature was much higher than the melting point. Hence, the contact angle was difficult to measure. The reaction product of Si_3N_4 at the interface was detected by XRD and was confirmed by SEM-EDS results. It shows that the wetting process of Fe-5.3Si-3B alloy on BN belonged to reactive wetting.

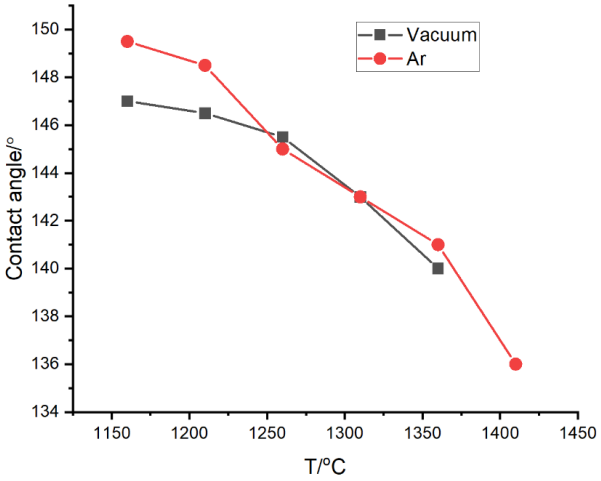

Figure 2-54 The function of contact angle with temperature on BN substrate under vacuum and Ar. [103]

3. Experimental details and model description

In this chapter, raw materials, equipment, and procedures used in the experiments are described in detail. Si, B, Fe, and Cr were used to make Si-B, Fe-26Si-9B, and Cr-43Si-5B alloys, in which numbers show the mass % of the element. Graphite, SiC, Al_2O_3, Si_3N_4, and h-BN were chosen to be the potential refractory materials and were also the PCM containers to be investigated in this research.

The experiments were performed in induction and resistance furnaces. The wetting tests were carried out in the sessile drop furnaces. Moreover, the latent heat of fusion and liquidus temperature of the potential PCMs were measured by the DSC method.

Scanning electron microscopy with energy dispersive spectroscopy (SEM-EDS) and electron probe micro-analysis (EPMA) with wavelength dispersive X-ray spectroscopy (WDS) technology were used to study the microstructures in the solidified PCMs and used to determine the phase compositions quantitatively or semi-quantitatively. X-ray diffraction (XRD) and transmission electron microscopy (TEM) were applied to determine the phases in the Fe-26Si-9B alloys. Inductively coupled plasma mass spectrometry (ICP-MS) and Leco instruments were used to analyze the chemical composition of the materials quantitatively.

Some work was also done by MSc students as a part of the Amadeus project [15]–[17], [58], [108]. The students were co-supervised by the author, and some of the analyses and materials were done by the author. To get the full knowledge, the work from these works will hence be included in the thesis while referenced.

3.1. Materials

3.1.1. Raw materials

Si, B, Fe, and Cr were used in the experiments to make the Si-B, Fe-26Si-9B, and Cr-43Si-5B alloys. For simplicity, solar grade Si (SG-Si) was supplied from the Sintef industry, made from a fluidized bed reactor (FBR) process in the United States. 99.9 mass % B was supplied from two Chinese companies, ZhongNuo Advanced Material Technology Co., Ltd (B-1) and Shanghai Aladdin Biochemical Technology Co., Ltd (B-2, B105883). Alfa Aesar provided the 99 mass % Fe (00737) and Cr (10147). The content of the impurities in the B powder was determined using ICP-MS at NTNU, as shown in **Table 3-1**. The content of the main contaminants in the Fe and Cr metals were provided by Alfa Aesar, as shown in **Table 3-2**.

It is seen from **Table 3-1** that the B content is ~ 92.3 mass % in B-1. It contains 6.3 mass % Zr and 1.3 mass % Fe, which is much lower than the shown purity of 99.9 mass %. Hence, it was used for the

preliminary experiments to investigate the phases formed in the Si-B alloys at 1450-1750 ºC. The B content is ~ 99.97 mass % in B-2 and was used in the rest of the experiments.

Argon (Ar) was used in the experiments as a protective gas with a purity of 99.999 %.

Table 3-1 Chemical composition of the B powder analyzed at NTNU. [ppm mass]

	Zr	W	Pb	Mg	Al	Si	Cr	Mn	Fe	Ni	Cu	Sr
B-1	62935	42	0	120	664	-	30	53	12797	15	3	0.5
B-2	29	0	0	2	51	16	11	1	211	2	0.15	0.01

Table 3-2 Chemical composition of the Fe and Cr powder supplied by Alfa Aesar. [mass %]

Metal	O_2	Mn	Si	P	C	S	Al	Fe
Fe	0.35	0.18	0.09	0.016	0.01	0.01	-	-
Cr	-	-	0.02	0.003	0.0185	0.0086	0.02	0.22

3.1.2. Fe-26Si-9B, Cr-43Si-5B, and Si-3.25B master alloys

The Fe-26Si-9B and Cr-43Si-5B master alloys were produced in an induction furnace before the thermal cycling experiments [15]–[17]. Once, the Fe/Cr, Si, and B raw materials were placed in an Al_2O_3 crucible (A-1), the charged Al_2O_3 crucible would be moved to a larger graphite crucible (G-1). The mixed raw materials were heated to 1700 ºC under Ar flow. At this point, a holding time of 15-60 min was used to completely melt and make the sample homogeneous. Finally, the solidified master alloy was crushed into pieces for the thermal cycling experiments and wettability experiments. The chemical compositions of the Fe-26Si-9B and the Cr-43Si-5B master alloys were determined using ICP-MS. The measured, normalized, and nominal contents of Si, Fe, Cr, B, Al, and Mn are summarized in **Table 3-3** and **Table 3-4**. The Fe-26Si-9B master alloys produced were labeled as Fe-Si-B-1, Fe-Si-B-2, and Fe-Si-B-3. Moreover, the O (oxygen) solubility in the Fe-Si-B master alloys was measured using Leco ON836 infrared combustion [108]. It is found that the O content was in the range 8-31 ppm mass in the Fe-Si-B-3 master alloy and 30 ppm mass in the Fe-Si-B-1 master alloy.

Table 3-3 Chemical composition of the Fe-Si-B master alloy analyzed by ICP-MS. [mass %]

Sample		Si	Fe	B	Al	Mn
Fe-Si-B-1	Measured	26.68	56.47	8.11	0.067	0.21
	Normalized	29.15	61.69	8.86	0.073	0.23
Fe-Si-B-2	Measured	27.87	66.45	9.54	0.18	0.23
	Normalized	26.73	63.72	9.15	0.17	0.22
Fe-Si-B-3	Measured	25.65	63.33	8.47	0.18	0.23
	Normalized	26.08	64.39	8.61	0.17	0.22
	Nominal composition	26.38	64.27	9.35	0	0

Table 3-4 Chemical composition of the Cr-Si-B master alloy analyzed by ICP-MS. [mass %] [17]

Sample		Si	Cr	B	Al	Mn
Cr-Si-B	Measured	40	50	4.7	0.11	0.0004
	Normalized	42.19	52.74	4.96	0.12	0.0004
	Nominal composition	43.05	52.22	4.73	0	0

Si-3.25B master alloy was taken from the sample extraction experiment, which will be described in subsection 3.4. Si-3.25B master alloy was prepared for the wetting tests.

3.1.3. Refractory materials

Graphite crucible was supplied by Svenska Tanso AB. It is machined from a block of isostatically pressed graphite with several good properties, such as high reliability, ultra-heat resistance, good electrical conductivity, high thermal conductivity (140 $W/m^{-1}\cdot K^{-1}$), low porosity (10%), and good chemical resistance. Two sizes of graphite were used in the experiments, G-1 and G-2. G-1 was used for extraction experiments, aiming to investigate the C solubility in the liquid Si and Si-B alloys. Moreover, it was treated as a holder to support other crucibles in the induction furnace. G-2 was applied to investigate the phase formation and interaction between PCMs and graphite at various temperatures.

Al_2O_3 crucible was made by Coors Tek™. The ultra-pure Al_2O_3 was used as a raw material in the production of the crucible. It exhibited high hardness and strong inertness. However, the operating temperature should be lower than 1750 °C. The type of A-1 Al_2O_3 crucible was used to produce the Fe-26Si-9B and Cr-43Si-5B master alloys at high temperatures.

Si_3N_4 was supplied by Steuler Solar Technology AS. The Si_3N_4 crucible was made of very pure reaction bonded Si_3N_4 for use in solar and semiconductor Si industry. The thermal conductivity was 12 $W/m^{-1}\cdot K^{-1}$ and the thermal expansion was 3.3×10^{-6} $°C^{-1}$. Si_3N_4 (S-1) was used to investigate its stability as a PCM container at high temperatures.

h-BN was made by Fuzhou creative new materials development Co., Ltd. It can be used at temperatures up to 2100 °C under an inert atmosphere. No adhesion, no pollution and long serve life were observed by the company. The thermal conductivity was reported to be 35 $W/m^{-1}\cdot K^{-1}$ at 25 °C. The thermal expansion was 1.5×10^{-6} $°C^{-1}$ in the temperature range 25-1200 °C. h-BN crucible (B-1) was used in the wetting tests.

The dimensions of the crucibles used in the experiments are summarized in Table 3-5. It should be noted that refractory materials from G-3, G-4, A-2, S-3, and SiC-2 were used as substrates in the wetting tests, in which G-4 was supplied from Sintef.

Some properties were provided by the refractory company. They are listed in Table 3-6.

Table 3-5 The dimensions for the refractory materials used in the experiments. [mm]

	Name	Height	Diameter	Wall thickness
Graphite (IG-15)	G-1	150	85	7.5
	G-2	34	22	3.5
	G-3	5	20	Substrate
Graphite (SINTEF)	G-4	3	10	Substrate
Al_2O_3	A-1	105	59	2
	A-2	3	10	Substrate
Si_3N_4	S-1	34	26 (top) 22 (bottom)	4
	S-2	3	10	Substrate
h-BN	B-2	3	10	Substrate
SiC	SiC-1	120	60	5
	SiC-2	4	9	Substrate

Table 3-6 The physical properties of graphite and alumina crucibles.

Crucible	Property	Value	Unit
Graphite (IG-15)	Density	1.9	g/cm^3
	Cumulative pore volume	0.052	m^3/g
	Open porosity	10	vol %
	Radius of average open pores	1.4	μm
	Thermal conductivity	140	W/(m·K)
Al_2O_3	Purity	99.8	%
	Operating temperature range	<1750	°C
	Permeability	Gas tight	-
	Water absorption	None	-
Si_3N_4	Density	2.6	g/cm^3
	Porosity	12	%
	Thermal expansion	3.3×10^{-6}	/°C
	Thermal conductivity	12	W/(m K)
h-BN	Density	1.6	g/cm^3
	Thermal expansion (25-1200 °C)	1.5×10^{-6}	/°C
	Thermal conductivity at 20 °C	35	W/mK
	Purity	>99.7	%

3.2. Induction and resistance furnace

3.2.1. Induction furnace

Figure 3-1a, **b** shows the induction furnace used in the experiments and the sketch. The furnace has a maximum power of 30 kW, in which 5kW to 8kW corresponds to the temperatures range of 1450-1750 °C in the experimental process. It can be used at temperatures up to 2000 °C. However, the

recommended maximum operating temperature should be lower than 1800 ºC. The vacuum can reach below 1.3×10^{-5} atm in the furnace chamber. As the heat is employed by eddy's currents, it causes a continuous stirring in the molten alloys assuring proper mixing.

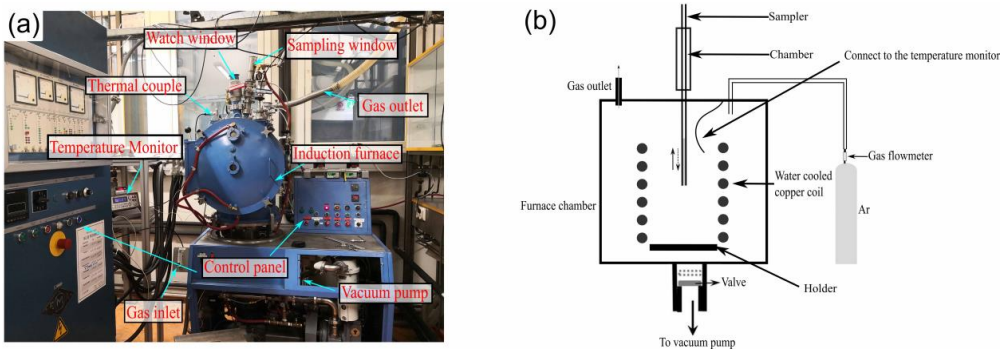

Figure 3-1 (a) Induction furnace and affiliated parts; (b) sketch of the induction furnace.

3.2.2. Resistance furnace

Two vertical graphite tube resistance furnaces were used in the experiments, which is named as TF-2 and TF-3. The set-up of TF-2 is shown in **Figure 3-2** and the schematic figure is presented in **Figure 3-3**. The heat is supplied by resistive heating and the recommended maximum temperature is below 1700 ºC. Hence, the applied temperature program lower than 1600 ºC is acceptable. Moreover, the temperature was measured by the C-type thermocouple and the B type thermocouple was used to control the furnace. Grorud [58] used pure copper (Cu) as the reference material to calibrate the thermocouple and the difference of less than 2 ºC was acceptable. The temperature variation was within the accuracy level for the C-type thermocouple.

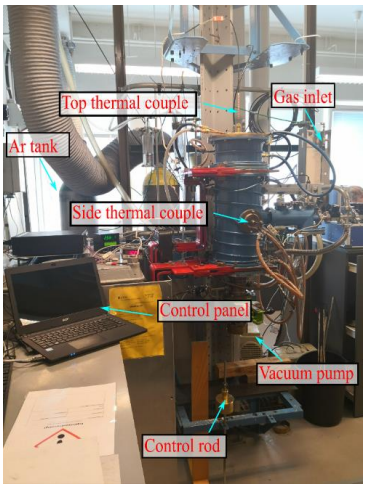

Figure 3-2 Resistance furnace (TF-2) and affiliated parts

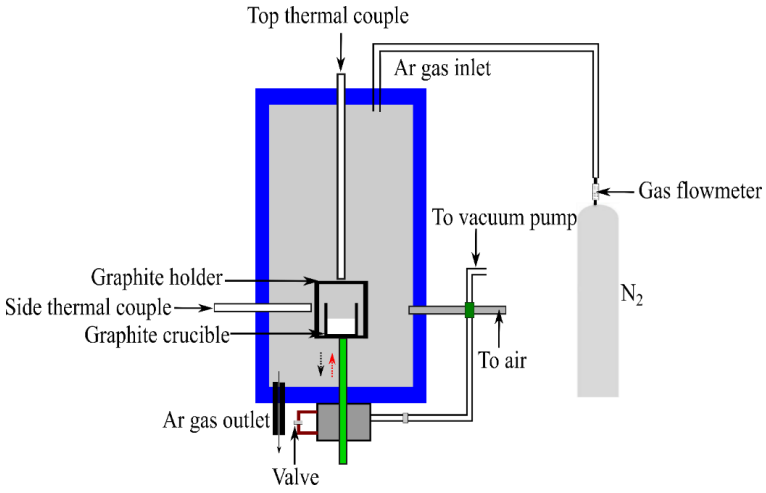

Figure 3-3 Schematic of the resistance vertical graphite tube furnace (TF-2) [109].

The set-up of TF-3 is shown in **Figure 3-4** and the sketch is presented in **Figure 3-5** [110]. The heating mechanism is the same as TF-2. However, only the top thermocouple (C-type) was used to detect the temperature inside the TF-3 furnace, which was in contact with the top side of the graphite holder (as shown in **Figure 3-5**). The samples were placed at the bottom of the graphite holder. The distance is ~ 50 mm from the bottom of the crucible to the top of the graphite holder. Hence, temperature correction should be made before experiments. Sellevoll [108]found that the temperature on the top position was 19.5 ºC higher than the bottom position where the samples were located during experiments. Therefore, the temperature program was set 19.5 ºC higher in order to get the correct temperature at the bottom position.

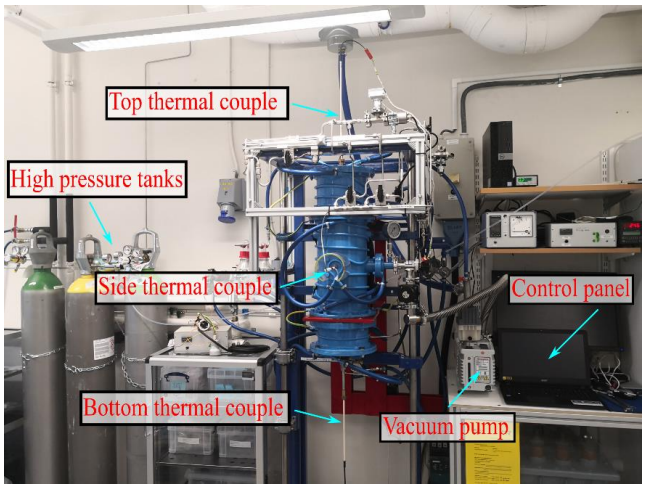

Figure 3-4 Resistance furnace (TF-3) and affiliated parts

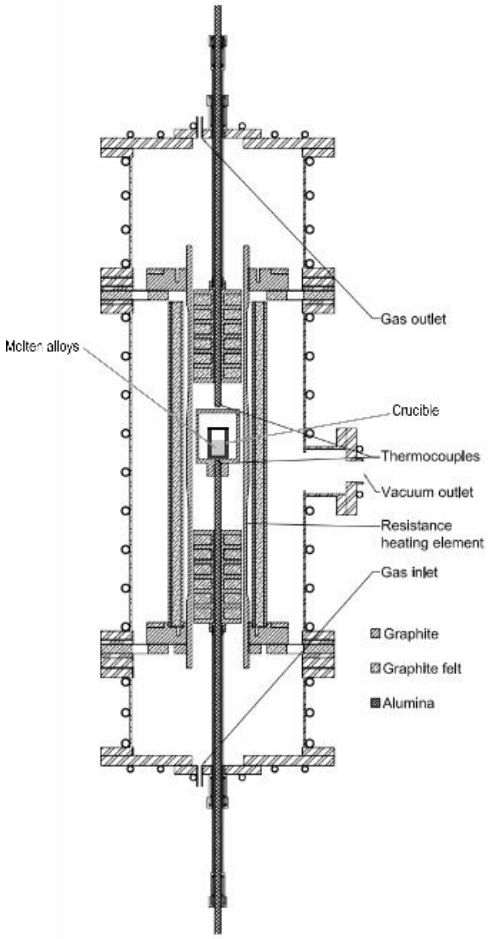

Figure 3-5 Sketch of the resistance furnace (TF-3) used in the experiments [110].

3.3. Phase formation experiments

3.3.1. The experiments of Si-B alloys in induction furnace

The goal of the experiments was to determine how the phases would develop as the Si-B alloys would react with graphite or Si_3N_4 crucible. All the experiments were performed in the induction furnace. **Figure 3-6** shows the schematic illustration of the experiments. In a large graphite crucible (G-1), two holes were drilled at the top of the graphite wall to fix a graphite thermowell using a molybdenum wire. Then, an Al_2O_3 tube was inserted into the graphite thermowell to prevent the thermal couple directly

touching the graphite. 4 g Si-B powder mixtures with various B additions were placed into four small graphite crucibles (G-2) and covered with a graphite lid. The four charged G-2 crucibles were placed at the bottom of the G-1crucible. Finally, the G-1 crucible was fixed to the center position of the copper coil.

When the Si_3N_4 (S-1) was used in the furnace, 6 g Si-B mixtures with the addition of 2, 5, 8, and 11 mass % B were charged to four S-1 crucibles, respectively. Then, the S-1 crucibles were placed at the bottom of the large graphite crucible. It should be noted that no lid was covered at the top of the Si_3N_4 crucibles.

As the furnace started, the chamber was evacuated to 1.3×10^{-5} atm before the Ar gas filled the chamber. Three cycles of vacuum and Ar filling were essential to confirm that the air was extracted. Then, a continuous flow of Ar was kept through the furnace chamber, bottom in and top out. Next, the furnace was heated to the set temperature. At this point, a holding time of 2 h was used to facilitate the B dissolution. In the next segment, the liquid Si-B alloys started to solidify with an average cooling rate of ~50 ºC/min. After complete solidification, the temperature is decreased slowly and reduced to 50 ºC within 90 min. A typical temperature profile is shown in **Figure 3-7**.

An overview of all the small scale experiments performed in the induction furnace is listed in **Table 3-7**.

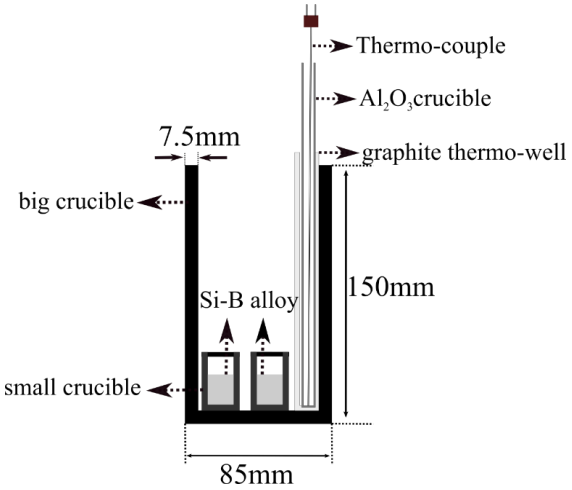

Figure 3-6 Schematic illustration about the small scale experiments.

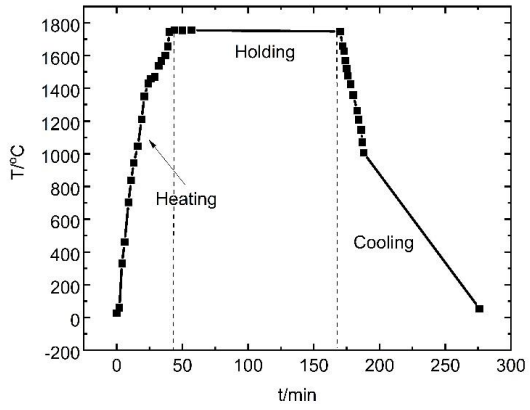

Figure 3-7 Typical temperature profile for the small scale experiments in an induction furnace.

Table 3-7 Overview of experiments performed in the small scale experiments for Si-B alloys. G-2 graphite crucibles and S-1 Si_3N_4 crucibles were used in the experiments.

Experiment No.	Temperature (°C)	B addition (mass %)	Holding time/h	Repetitions*
C-1	1650	0	2	1
C-2	1450	2	2	3
C-3	1550	2	2	3
C-4	1650	2	2	3
C-5	1750	2	2	3
C-6	1450	5	2	3
C-7	1550	5	2	3
C-8	1650	5	2	3
C-9	1750	5	2	3
C-10	1450	8	2	3
C-11	1550	8	2	3
C-12	1650	8	2	3
C-13	1750	8	2	3
C-14	1450	11	2	3
C-15	1550	11	2	3
C-16	1650	11	2	3
C-17	1750	11	2	3
C-18	1650	15	2	1
C-19	1750	15	2	1
C-20	1650	25	2	1
C-21	1750	25	2	1
S-22	1750	2	2	1
S-23	1750	5	2	1
S-24	1750	8	2	1
S-25	1750	11	2	1

***: parallel tests for the melting of the Si-B mixtures in the induction furnace.**

3.3.2. The remelt of Si-B master alloys in resistance furnace (TF-2)

In order to check the stability of Si-B master alloys in the graphite crucible, the Si-5B and Si-8B master alloys made in graphite crucibles were then melted in graphite crucibles in the resistance furnace (TF-2). As shown in **Figure 3-3**, the graphite holder can be moved up and down in the chamber using the control rod. In the beginning, the charged graphite crucible was placed at the bottom of the graphite holder and was fixed in the small chamber outside of the furnace. Then, the furnace was heated to 1450/1550 °C. At this point, the charged graphite was pushed to the furnace chamber from the bottom of the furnace. An abrupt temperature decrease was observed in this process, as shown in **Figure 3-8**. Subsequently, a holding time of 2 h was used to equilibrate the master alloy and graphite. Then, the graphite holder was dragged back to the small chamber under Ar. **Figure 3-8** shows a typical temperature profile at 1550 °C. The overview of the experiments is listed in **Table 3-8**.

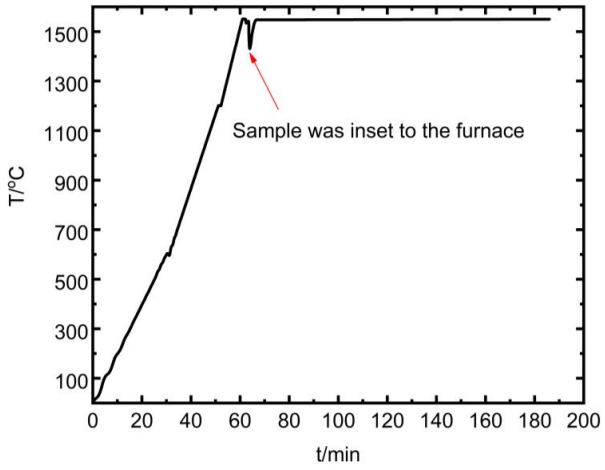

Figure 3-8 Typical temperature profile for the experiments in the resistance furnace (TF-2).

Table 3-8 Overview of remelting Si-B master alloys in the resistance furnace (TF-2).

Experiment No.	Temperature (°C)	Master alloy	Holding time/h	Crucible
C-26	1450	Si-5B	2	G-2
C-27	1550	Si-5B	2	G-2
C-28	1450	Si-8B	2	G-2
C-29	1550	Si-8B	2	G-2

3.4. C solubility in liquid Si-B alloys

Graphite is proposed to be used as the refractory material for PCM containers in TES systems. The liquid Si-B alloys would undergo long-term melting/solidification cycles for absorbing and releasing

energy. Hence, C would be dissolved to liquid Si-B alloy to form a C-saturated Si-B alloy. Therefore, the investigation of C solubility in Si-B alloys is essential to successfully apply Si-B alloys in the graphite container at high temperatures. In this regard, C solubility in liquid Si-B alloys was measured in the experiments.

The experiments were carried out in an induction furnace, as shown in **Figure 3-9**. Two different crucibles were used in the experiments, dense graphite (G-1) and SiC, in order to verify the reliability of the experimental data. In the experiments, 200-300 g Si-B mixtures with 0-5 mass % B were charged to the crucible. The start of the induction furnace was described earlier. Once the furnace temperature reached 1450 °C, a holding time of 3 h was used to facilitate the B dissolution and make a homogeneous liquid Si-B alloy. Then, a quartz tube was used to extract the liquid Si-B alloy. The quartz tube was fed into the furnace, down through the hole from the sampling window and into the liquid Si-B alloy (**Figure 3-1**). Then the C-saturated liquid Si-B alloy was sucked up by the use of a syringe. The quartz tube with 0.8-1.2 g of liquid Si-B sample was extracted. This process should be fast, as the quartz will be softened and can break at high temperatures. After the sample was extracted at 1450 °C, the liquid Si-B alloy was heated to 1550 °C within 2 min. Another 1h holding time was used at 1550 °C, and then the liquid Si-B alloy was extracted. The operations at 1650 °C and 1750 °C were the same as the process at 1550 °C.

When using SiC crucibles, the extraction experiments were carried out in the liquid Si-B alloys with the B additions of 2 and 3.25 mass %. The extraction temperatures were increased to 1450 °C, 1500 °C, 1550 °C, 1600 °C, and 1650 °C.

The temperature profile for the Si-B alloy extraction in one experimental run is shown in **Figure 3-10**. The grey circles represent the extraction point and the black squares represent the recorded temperatures in one extraction experiment. One of the extracted Si-2B samples is presented in **Figure 3-11**a. **Figure 3-11**b shows the image of the interface between the Si-5B alloy and quartz tube. It is seen that no reaction occurs between the Si-5B alloy and quartz tube. Moreover, Si(ss), SiB_3, and B_4C phases were detected in the Si-5B alloy. Hence, B was completely dissolved into the Si-5B alloys in the extraction process. The overview of the experiments is listed in **Table 3-9**.

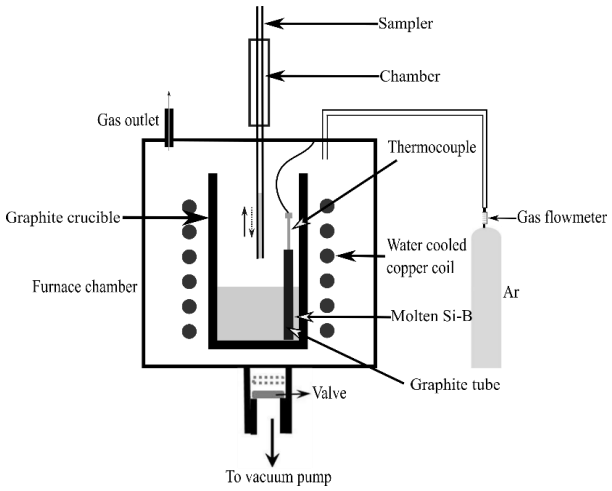

Figure 3-9 Schematic illustration about the C extraction experiments in an induction furnace.

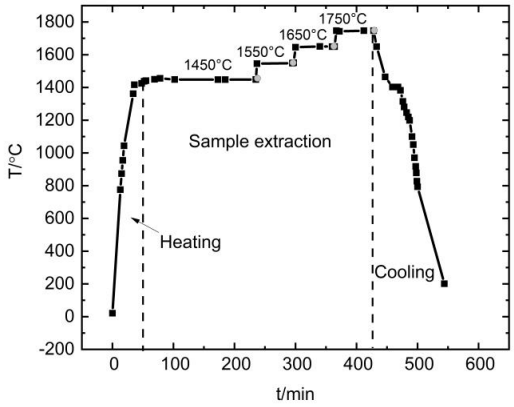

Figure 3-10 Typical temperature profile for the C extraction experiments in an induction furnace, the grey points represent the extraction time.

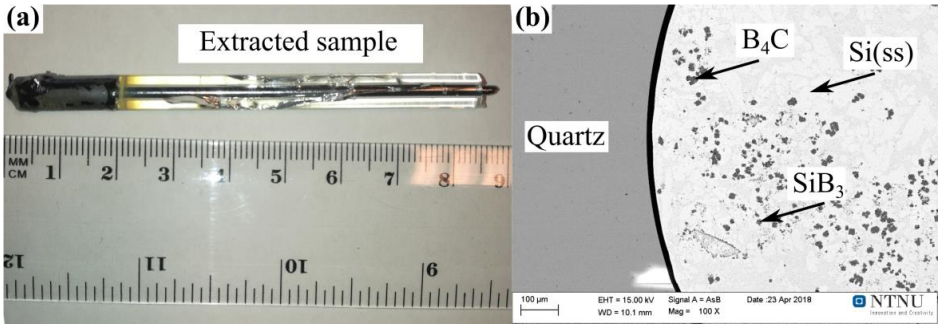

Figure 3-11 (a) The solidified extracted samples from molten Si-B alloys using quartz tube; (b) SEM image of the Si-5B alloy extracted at 1750 °C.

Table 3-9 Overview of C extraction experiments in molten Si-B alloys.

Experiment No.	Temperature (°C)	B addition (mass %)	Holding time/h	Crucible	Repetitions
C-30	1450-1750	0	6	G-2	2
C-31	1450-1750	2	6	G-2	3
C-32	1450-1750	3.25	6	G-2	1
C-33	1450-1750	5	6	G-2	2
C-34	1450-1750	2	7	SiC	1
C-35	1450-1750	3.25	7	SiC	1

3.5. The use of Fe-26Si-9B master alloys in Si_3N_4 crucible

In our group, the long term thermal cycle experiments had been investigated in the graphite crucible with Si-3.25B alloy by Grorud [58] and with Fe-26Si-9B master alloy by Grorud [58], Sindland [17], and Sellevoll [16], all co-supervised by the present author. In this part, I will describe the additional thermal cycle experiments. The thermal cycle experiments of Fe-26Si-9B master alloys were preformed in Si_3N_4 (S-1) crucibles.

The resistance furnace (TF-3) were used in the thermal cycle experiments. 10 g Fe-26Si-9B master alloy was charged to the Si_3N_4 crucible. Then, the charged Si_3N_4 crucible was placed at the bottom of the graphite holder. Once the bottom lid of the furnace was opened, the graphite holder was fixed to the bracket that connected to the bottom lid. Next, the bottom lid was pushed back to the original position of the furnace and fixed using the bolt. Three times vacuum and filling Ar were performed to remove the residue oxygen in the furnace. Finally, a flow Ar was kept in the whole experimental process.

In the heating process, the furnace was heated to 1550 ºC with a heating rate of 60 ºC/min. Then, a holding time of 60 min was used to confirm the homogeneity of the liquid alloy. The temperature was decreased to 1100 ºC with a cooling rate of 60 ºC/min and the liquid alloy solidified in the cooling process. A holding time of 10 min was kept at 1100 ºC. Subsequently, the temperature was increased to 1300 ºC and the solidified alloy was melted again. A holding time of 10 min was also kept at 1300 ºC. The thermal cycle was done in this process. Presently, 1, 6, and 12 thermal cycles were performed in the Si_3N_4 crucible to investigate the interaction between the liquid Fe-26Si-9B alloy and Si_3N_4. The typical temperature profile is shown in **Figure 3-12**. The red cycles represent 1, 6, and 12 melting/solidification stop position. The overview of the experiments in Si_3N_4 crucible is listed in **Table 3-10**.

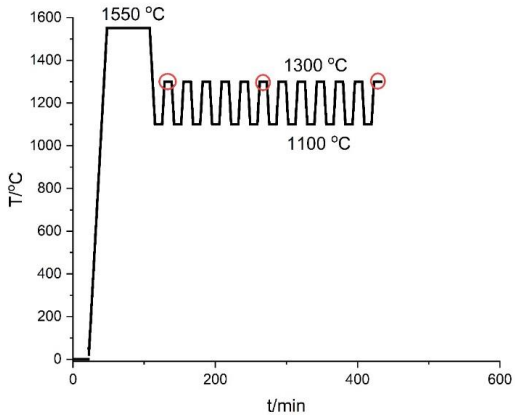

Figure 3-12 Typical temperature profile for the thermal cycle experiments in the resistance furnace.

Table 3-10 Overview of thermal cycle experiments of Fe-Si-B alloy in Si_3N_4 crucible in the resistance furnace (TF-3).

Experiment No.	Temperature (°C)	Master alloy	Cycles	Crucible
S-36	1100-1300	Fe-Si-B-2	1	S-1
S-37	1100-1300	Fe-Si-B-2	6	S-1
S-38	1100-1300	Fe-Si-B-2	12	S-1
S-39	1100-1300	Fe-Si-B-2	12	S-1

3.6. Wettability experiments

In order to apply PCMs to the energy storage system successfully, the selection of proper refractory material is important to build the PCM container. Suitable refractory material should meet several requirements.

1. The refractory material can be used at high temperatures.
2. The refractory material should defend against the molten PCM corrosion after long-term thermal cycles.
3. The refractory material should not pollute the molten PCM.

The sessile drop based method was carried out to determine the wettability properties of molten PCMs on different refractory materials. The potential PCMs are Si-3.25B, Fe-26Si-9B, and Cr-43Si-5B master alloys. The potential refractory materials are graphite, SiC, Si_3N_4, Al_2O_3, and h-BN substrates. Two different sessile drop furnaces were used in the wetting tests, which are named SDF-1 and SDF-2.

The sessile drop furnace of SDF-1 is shown in Figure 3-13. All the heated furnace parts are constructed of graphite. The maximum working temperature should be lower than 2400 °C. Hence, our running temperature lower than 1800 °C is reasonable. A firewire digital video camera is used to record the wetting process. The pyrometer and thermocouple are used to measure the temperature in the furnace. The contact angle of molten drop on a substrate can be measured and the softening and melting temperature of alloys can be observed based on the recorded pictures. The wetting tests performed under two conditions: a vacuum of 10^{-4} atm and inert Ar.

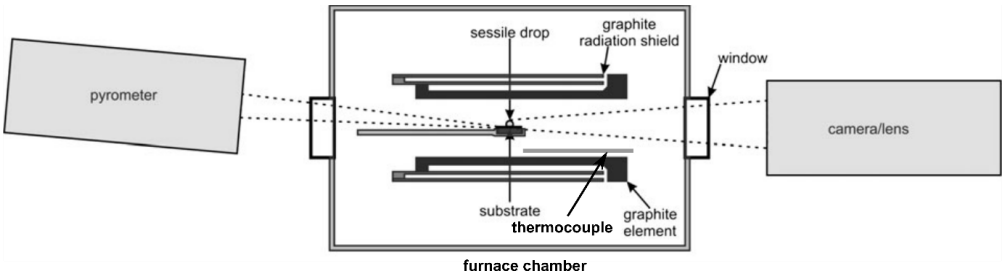

Figure 3-13 The schematics of the sessile drop furnace (SDF-1), adapted from [83].

The SDF-2 sessile drop furnace is located in the Foundry Research Institute (FRI) lab, Krakow. It is designed to perform high temperature wettability tests. The information of the SDF-2 can be obtained in detail from [111], as shown in Figure 3-14. The instrument equipped with tantalum (Ta) and

molybdenum (Mo) heaters gives a possibility of temperatures up to 2100 ºC. The images of the sample are recorded by using MC 1310 high-speed high-resolution camera with a rate of 100 frames per second. Then, the contact angle can be measured and a real-time movies can be prepared by the ASTRA2 special software (IENI-CNR, Italy). Moreover, it is possible to use different testing methods in the SDF-2, including sucking and drop pushing, contact heating, and capillary purification methods.

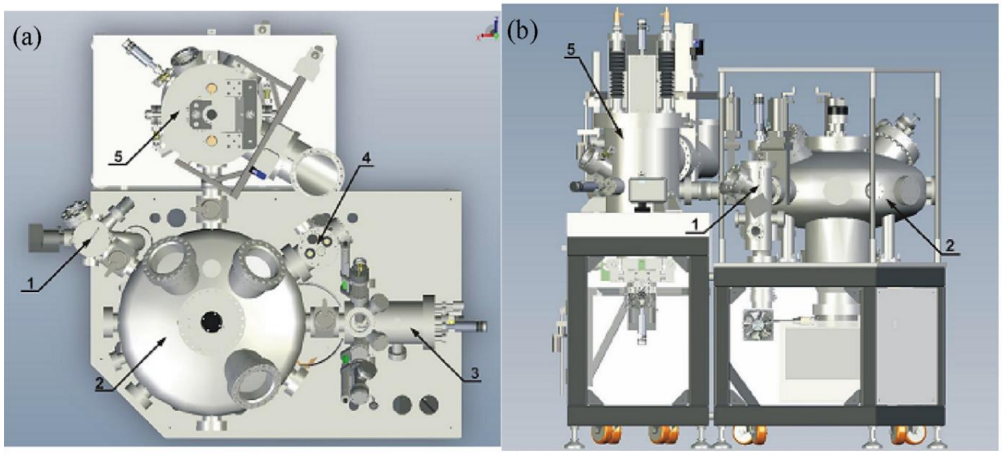

Figure 3-14 The schematics of the sessile drop furnace (SDF-2), taken from [111]. 1: vacuum chamber; 2: ultra high temperature chamber; 3: analytical chamber; 4: portable vacuum chamber; 5: experimental chamber.

3.6.1. Si-3.25B alloy

The Si-3.25B master alloy was produced in a graphite crucible. In the wetting test, a small piece of Si-3.25B master alloy particle was chosen and placed at the top of the substrate. Heating was performed in a vacuum of 10^{-4} atm or argon atmosphere to 1100 ºC in 4 min. Then, the temperature was increased to the set temperature with a slow heating rate (5-20 ºC/min). In the end, the furnace power was shut off and the sample was cooled to room temperature. Two different refractory materials were used as the substrates in the wetting test. It includes h-BN, Si_3N_4.

h-BN

The wetting tests of Si-3.25B master alloy on the h-BN substrate were carried out in the sessile drop furnace (SDF-1). It is known that the theoretical melting point of Si-3.25B eutectic alloy is 1385 ºC [24]. Hence, the maximum running temperature was programmed to be 1450 ºC. Two different experimental procedures were conducted in the furnace, as shown in **Figure 3-15**. In the first experiments, the Si-3.25B powder was shaped like a long cylinder and fixed at the top of the h-BN substrate. It was heated to 1300 ºC from 1100 ºC with a rate of 20 ºC/min under 10^{-4} atm. Then, the

heating rate was decreased to 5 °C/min to 1450 °C. The slow heating rate was used to accurately measure the liquidus temperature of the Si-3.25B particle (**Figure 3-15**a).

The temperature profile of the second wetting test on the h-BN is shown in **Figure 3-15**b. Three melting/solidification cycles were subjected to a temperature range of 1000-1450 °C under 10^{-4} atm, in order to investigate the reactivity in the Si-3.25B/h-BN system during thermal cycles. It is noted that the Si-3.25B master alloy was directly used in the experiment without pretreatment. In the first experiment, the melting temperature was observed to be ~ 1397 °C. Hence, a holding time of 5 min was used at 1400 °C. Then, the temperature continued to increase to 1450 °C. Then, the liquid Si-3.25B alloy was cooled to 1000 °C. After three cycles, the Si-3.25/h-BN couple was cooled to room temperature.

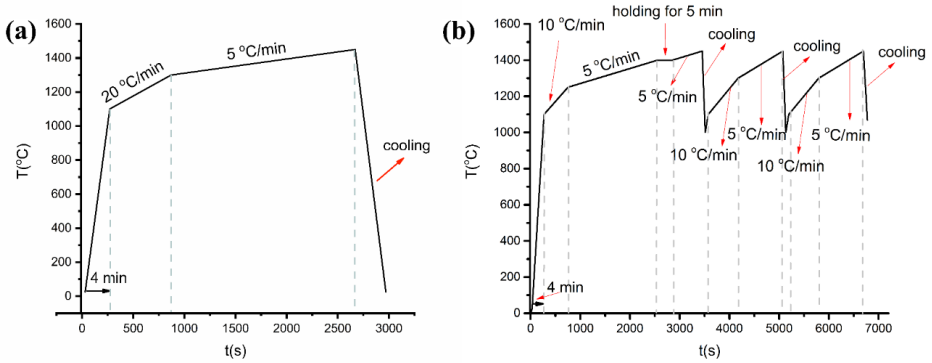

Figure 3-15 Temperature profile of Si-3.2B particles on BN substrates under 10^{-4} atm, (a) Si-3.25B powder on h-BN, (b) Si-3.25B particle on the h-BN subject to 3 thermal cycles.

Si_3N_4 substrate

The wetting behaviors of the Si-3.25B alloys on Si_3N_4 substrate was investigated in the SDF-1 under 10^{-4} atm. The temperature procedure is presented in **Figure 3-16**. A gradual increase to 1350 °C from 1100 °C with a heating rate of 20 °C /min, then 5 °C /min to 1400 °C. Next, the liquid Si-3.25B alloy was kept at 1400 °C for 10 min. In the end, the liquid Si-3.25B alloy was cooled to room temperature.

An overview of the wetting tests of Si-3.25B alloy on different substrates is listed in **Table 3-11**.

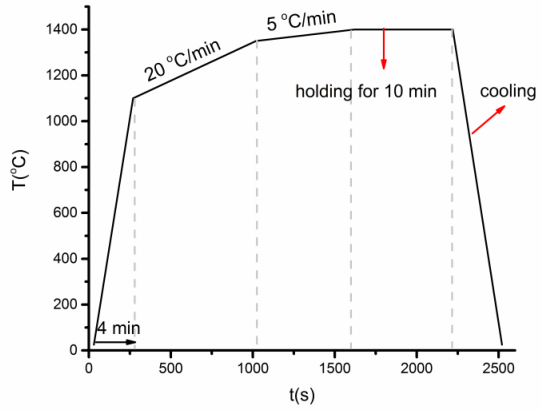

Figure 3-16 Temperature profile of Si-3.2B particles on Si_3N_4 substrate.

Table 3-11 Overview of the wetting tests of Si-3.25B alloy on h-BN and Si_3N_4.

Experiment No.	Substrate	Material	pretreatment	Cycles	Atmosphere	Furnace	T_{max}/°C
W-40	h-BN	powder	No	1	10^{-4} atm	SDF-1	1450
W-41	h-BN	particle	No	3	10^{-4} atm	SDF-1	1450
W-42	Si_3N_4	particle	No	1	10^{-4} atm	SDF-1	1400

3.6.2. Fe-26Si-9B alloy

The wettability properties of Fe-26Si-9B alloys on different refractory materials were investigated in the SDF-1 and SDF-2. Graphite, SiC, Al_2O_3, Si_3N_4, and h-BN refractory materials were used as the substrates in the wetting tests. The set up of the experiments is described as follows.

Graphite and SiC

The wetting tests of Fe-26Si-9B alloy on SiC and graphite were designed as follows .

1. The Fe-26Si-9B particle were etched in an HF, HNO_3, and ethanol (1:5:2) solution bath in 10 sec, rinsed with water and ethanol, and contained in ethanol before the experiments. The particle was then placed at the SiC and graphite substrate (G-4) and heated to 1250 °C under Ar, in which a holding time of 10 min was used at 1250 °C (**Figure 3-17**). However, both the particles on the SiC and graphite did not melt. Hence, the Fe-26Si-9B master alloy was heated to 1550 °C after holding of 10 min at 1250 °C on the SiC substrate. It aims to check whether Fe-26Si-9B particle would completely melt at higher temperatures (**Figure 3-18**).

2. The Fe-26Si-9B particle was milled to a powder. Hence, the oxide layer at the surface of the particle should be broken by the physical method. Then, the powder was shaped like a long cylinder and fixed at the top of the graphite (G-4). It was heated to 1450 °C under 10^{-4} atm. The heating rate was 5 °C/min from 1100 °C to 1250 °C, and then increased to 1450 °C with 10 °C/min. The temperature profile is shown in **Figure 3-19**.
3. The rest of the wetting tests were performed in the SDF-2 furnace, in order to examine the effect of various testing procedures and conditions on the interaction of Fe-26Si-9B alloy with graphite (G-3). For this purpose, four experiments were performed by using the sessile drop method coupled with the contact heating procedure and the capillary purification procedure (h-BN capillaries were used during these experiments). The Fe-26Si-9B particles were not pretreated before wetting tests. Besides, the graphite substrates were heated to 800 °C in a vacuum load lock to remove residue gas and water. Then, the heating was started after obtaining high vacuum (10^{-9} atm) or low vacuum (10^{-5} atm) level. The static argon (850-900 mbar) was introduced to the furnace at 800 °C. In each experiment, the Fe-26Si-9B drop was held for 5 min at 1250 °C, cooled down to 1100 °C, and then once again heated up and held for 5 min at 1250 °C. The double remelting was just to check if the native surface layer will be rebuild. The temperature profile is shown in **Figure 3-20**.

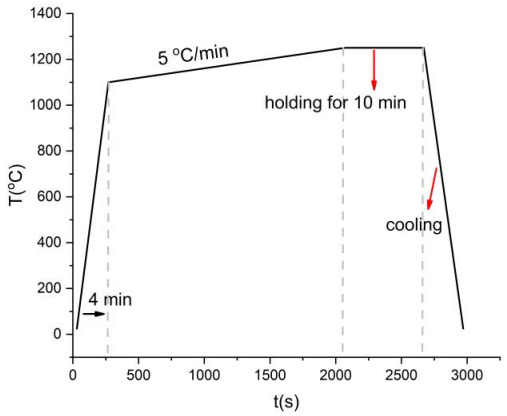

Figure 3-17 Temperature profile of Fe-26Si-9B particles on SiC and graphite substrates (G-4) under Ar (T_{max} = 1250 °C).

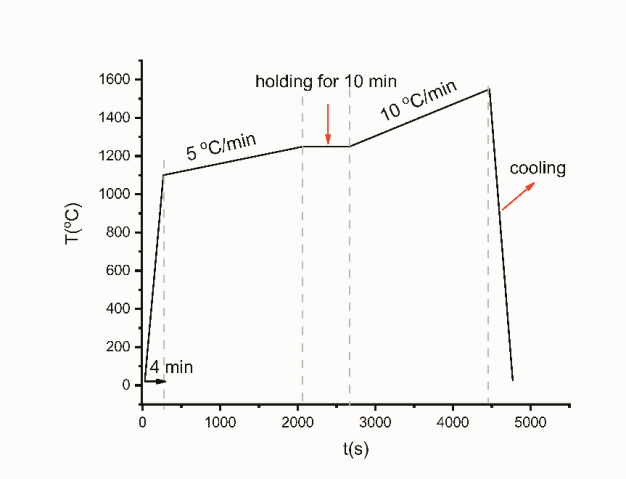

Figure 3-18 Temperature profile of Fe-26Si-9B particles on SiC substrate under Ar flow (T_{max} = 1550 °C).

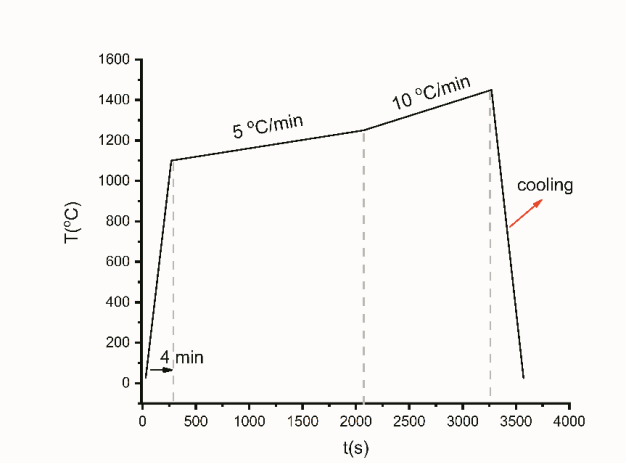

Figure 3-19 Temperature profile of Fe-26Si-9B particle on graphite substrate (G-4) under 10^{-4} atm.

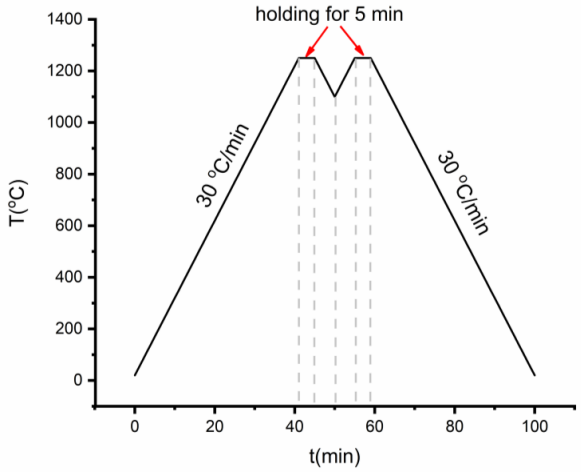

Figure 3-20 Temperature profile of the wettability test including 2 melting/solidification cycles in Fe-26Si-9B/graphite (G-3) system, the wetting tests were performed in SDF-2 furance in FRI under static Ar.

Al_2O_3

The Fe-26Si-9B powder was shaped like a long cylinder and fixed at the top of the Al_2O_3, the heating was started in a vacuum of 10^{-4} atm to 1250 ºC from 1100 ºC and the drop was held for 10 min. In the case of the Fe-26Si-9B alloy did not melt completely, it was continuously heated to 1350 ºC, then cooled to room temperature. The temperature profile is shown in **Figure 3-21**. It is worth noting that the Fe-26Si-9B alloy was not pretreated in the acid bath before experiments.

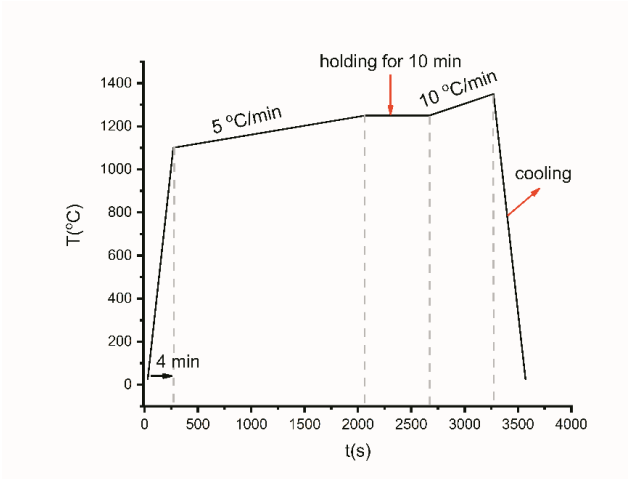

Figure 3-21 Temperature profile of Fe-26Si-9B powder on Al_2O_3 substrate under 10^{-4} atm.

Si_3N_4

The wetting test of Fe-26Si-9B alloy on Si_3N_4 substrate was performed in the SDF-1 under 10^{-4} atm. The Fe-26Si-9B particle was pretreated before the experiment. The particle coupled with Si_3N_4 was heated to 1200 ºC with a rate of 20 ºC /min from 1100 ºC under 10^{-4} atm, then increased to 1300 ºC with a rate of 5 ºC /min. A holding time of 5 min was used at 1300 ºC. Then, the temperature was increased to 1350 ºC with a rate of 10 ºC/min. After that, the Fe-26Si-9B/Si_3N_4 was cooled to room temperature, as shown in **Figure 3-22**.

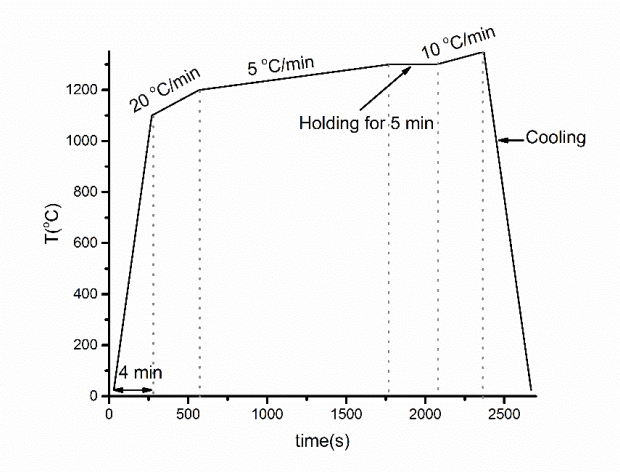

Figure 3-22 Temperature profile of Fe-26Si-9B particle on Si_3N_4 substrate under 10^{-4} atm.

h-BN

The wetting test of Fe-26Si-9B alloy on h-BN substrate was performed in SDF-1 under 10^{-4} atm. The Fe-26Si-9B particle was pretreated before the wetting test. In order to investigate the wettability and reaction between Fe-26Si-9B alloy and h-BN in the melting/solidification process, the temperature was gradually increased to 1350 ºC with a rate of 5 ºC/min from 1100 ºC, then, increased to 1550 ºC with a rate of 10 ºC/min, cooled to 1100 ºC, then increased to 1550 ºC with a rate of 10 ºC/min. After three thermal cycles, the Fe-26Si-9B/h-BN system was cooled to room temperature. The temperature profile is shown in **Figure 3-23**.

An overview of the wetting tests of Fe-26Si-9B alloy on different substrates is listed in **Table 3-12**.

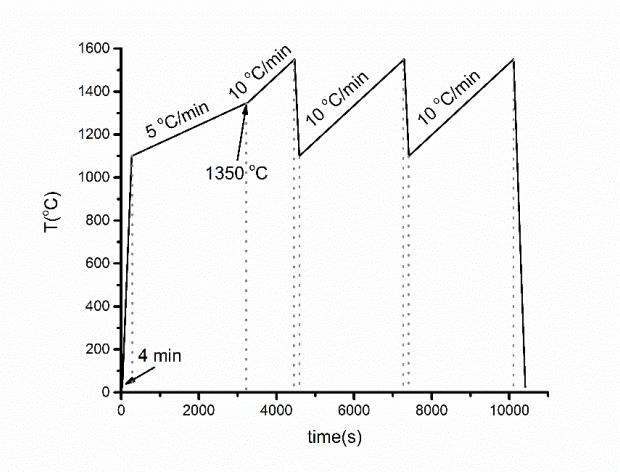

Figure 3-23 Temperature profile of Fe-Si-B particle on h-BN substrate under 10^{-4} atm.

Table 3-12 Overview of the wetting tests of Fe-26Si-9B alloy on different substrates.

Experiment No.	Substrate	Material	Pretre-atment	Cycles	Atmosphere	Furnace	T_{max}/°C
W-43	Graphite (G-4)	particle	Yes	1	Ar	SDF-1	1250
W-44	SiC	particle	Yes	1	Ar	SDF-1	1250
W-45	SiC	particle	Yes	1	Ar	SDF-1	1550
W-46	Graphite (G-4)	powder	No	1	10^{-4} atm	SDF-1	1450
W-47	Graphite (G-3)	particle	No	2	Ar	SDF-2	1250
W-48	Graphite (G-3)	particle	No	2	Ar	SDF-2	1250
W-49	Graphite (G-3)	particle	No	2	Ar	SDF-2	1250
W-50	Graphite (G-3)	particle	No	2	Ar	SDF-2	1250
W-51	Al_2O_3	powder	No	1	10^{-4} atm	SDF-1	1350
W-52	Si_3N_4	particle	Yes	1	10^{-4} atm	SDF-1	1350
W-53	h-BN	particle	Yes	3	10^{-4} atm	SDF-1	1550

3.7. DSC experiments

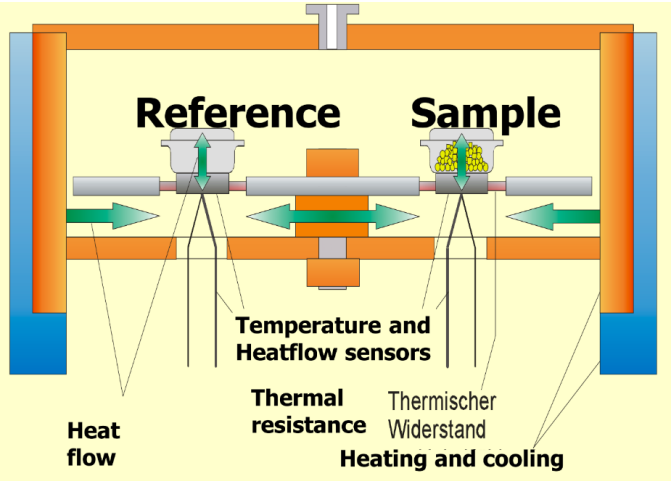

Figure 3-24 A schematic representation of the differential scanning calorimetry [112].

In this study, the DSC apparatus was applied for the experimental determination of the liquidus and solidus temperatures and the heat of phase transitions for Fe-26Si-9B alloys. It was carried out using a Netzsch STA 449F3 commercial calorimeter. As shown in **Figure 3-24**, the heat flow difference is quantitatively determined by measurement of the temperature difference of a defined thermal path between the sample and reference, where sample and reference are subject to the same temperature program. The estimation of values of critical temperatures and latent heat of fusion/latent heat of crystallization was done with a Netzsch Proteus Thermal Analysis software. The DSC tests were performed in the temperature range from 25 °C to 1450 °C under flow Ar/N_2 with a heating/cooling rate of 10 K/min. It is noted that three times vacuum and filling of Ar/N_2 (99.999%) were done before each experiments in order to completely remove the O_2 from the chamber. The mass of the alloy particle was in the range of 30-60 mg. The sample was placed in the Al_2O_3 crucible of GB399972 type (85 µl) produced by Netzsch. For the selected temperature range, sensitivity and temperature calibrations were made with five pure reference metals (In, Bi, Al, Au, Ni) using the same commercial Al_2O_3 crucibles and the same temperature profile under flow N_2. The temperature profile is shown in **Figure 3-25**.

An overview of the DSC experiments is listed in **Table 3-13**.

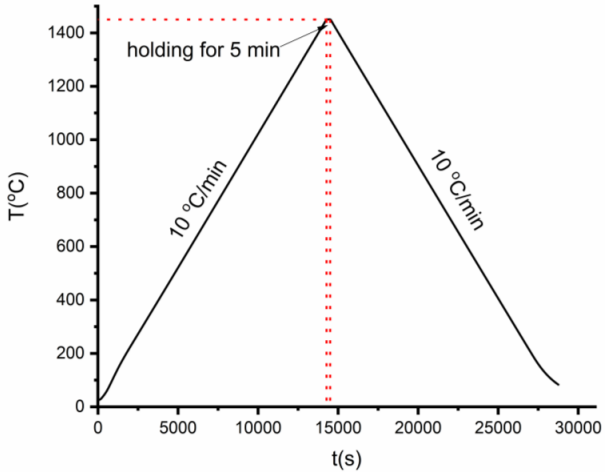

Figure 3-25 Applied Temperature profile for DSC experiments.

Table 3-13 Overview of the DTA and DSC experiments.

Experiment No.	Alloy	Crucible	Atmosphere	Furnace
DSC-54	Fe-26Si-9B	Al_2O_3	N_2	DSC
DSC-55	Fe-26Si-9B	Al_2O_3	N_2	DSC
DSC-56	Fe-26Si-9B	Al_2O_3	N_2	DSC
DSC-57	Fe-26Si-9B	Al_2O_3	Ar	DSC
DSC-58	Fe-26Si-9B	Al_2O_3	Ar	DSC
DSC-59	Fe-26Si-9B	Al_2O_3	Ar	DSC

3.8. FactSage software

In the investigation of PCMs and refractory materials, the fundamental thermodynamic data is vital to understand their behavior at high temperatures before experiments. However, the published literature relevant to our new alloys is scarce. Therefore, FactSage software is used in our research to predict thermodynamic properties.

FactSage is well known for its powerful computing systems in chemical thermodynamics based on its database. The evaluated databases for metals were developed by optimization of literature data using advanced modeling techniques. With FactSage you can calculate the conditions for multiphase, multicomponent equilibria, with a wide variety of tabular and graphical output modes, under a large range of constraints [113].

FactPS, FTlite, FSstel, and FSupsi databases were chosen to be used in the calculation process. Besides, some calculations were conducted by Kai Tang using the Sintef database [114]. The calculated results were used to explain the experimental phenomenons.

3.9. Characterization method

3.9.1. ICP-MS

Inductively coupled plasma mass spectrometry (ICP-MS) was used to analyze the impurity contents in the raw materials (pure Si, B, and Fe) and the chemical composition of the Si-B, Fe-26Si-9B, Fe-25Si-24B, and Cr-43Si-5B alloys after experiments. All the analyses were conducted by Senior Engineer Syverin Lierhagen, NTNU.

ICP-MS is a type of mass spectrometry which is capable of detecting metals and several non-metals at concentrations as low as one part per quadrillion on non-interfered low-background isotopes. In general, ICP-MS uses a sample in a solution, which presents the advantages of proper control over homogeneity and ease of calibration. It must be mentioned that to get the correct composition the whole sample must be dissolved. This is maybe also the main uncertainty of this process, as some black precipitate that can not be dissolved to the solution are found in the Si-B alloys, where the samples to be tested were digested in an acid mixture with 1.5 ml HNO_3 (69%) + 0.5 ml HF (40%).

3.9.2. SEM-EDS

Scanning electron microscopy with energy dispersive spectroscopy (SEM-EDS) can produce magnified images and in situ chemical information from virtually any type of specimen. Backscattered secondary electrons (BSE) are generated within the primary beam-sample interactive volume and are the two main signals used to form images. Therefore, SEM is the most commonly used detection method.

The samples should be treated before SEM observation. The samples were mounted in EpoFix cold-setting embedding resin and left for 12 h to harden. Then, the samples were ground and polished using the ATM Saphir 550 machine. Two different grinding discs, 220 grit Akasel diamond disc and Allegro 9 disc, and 2 different polishing cloths, 3 μm Akasel Daran cloth and 1 μm Akasel Napal cloth were used in this process. Next, the bottom and edge of the sample was wrapped in tin foil. In the end, the samples were coated with C and were placed in a thermotank chamber, where the temperature was held at 100 ^{o}C, aiming to remove the residue gas and water from the sample.

Zeiss Supra, 55VP and Zeiss Ultra, 55 limited Edition SEM machines were used to observe the microstructures in the samples. Both SE and BSE images were obtained in the analysis process. EDS was applied to determine the chemical composition in the samples by using the point, line scan, and mapping detection methods.

3.9.3. EPMA

Electron probe micro-analysis (EPMA) is an instrument to analyze the mass of elements in a phase, by irradiating electron beams onto the substance surface and measuring the characteristic x-ray that is generated. It is equipped with electron optics technology, x-ray spectrometry technology, system control, and data processing technology. It has evolved into an instrument that can handle the elemental analysis of sub-micron areas as well as observation, analysis, and image analysis for areas as large as 10 cm^2.

All the samples were coated with carbon on the surface before EPMA analysis, in order to ensure sufficient conductivity. Moreover, the hight of the samples should be lower than 1 cm. The JEOL JXA 8500 EPMA machine was used to produce the high-resolution mapping for Si, B, Fe, Cr, C, O, and N to observe the distribution of the elements in the alloys. Simultaneously, the chemical composition of the formed phases in the samples was determined by wavelength dispersive X-ray spectroscopy (WDS) technique. It should be noted that elements of B, C, and O are semi-quantitative detection. All the analyses were done by Morten Peder Raanes, NTNU.

3.9.4. Leco

In the Leco instrument for carbon analysis, the samples were combusted in a ceramic crucible in an induction furnace under an oxygen atmosphere, causing carbon to react and form carbon dioxide (CO_2). The CO_2 content is then measured by infrared spectroscopy (IR-spectroscopy). The necessary sample amount was at least 0.5g for each parallel analysis in the Leco instrument (Leco CS-200). All the samples were analyzed at SINTEF Molab. It is the total carbon that is measured, irrespective if it is as dissolved carbon or present in carbides like e.g., SiC and B_4C.

3.9.5. XRD

The phases produced in Fe-26Si-9B alloys were analyzed by the X-ray diffraction instrument (Bruker D8 A25 Davinci, Germany) with Cu Kα radiation, 35-105 deg diffraction angle, 0.013 deg step size. The diffraction peak patterns were analyzed using DIF-FRAC.EVA software (Bruker AXS GmbH, Karlsruhe, Germany) and the JCPSD-database PDF-4 + 2018 RDB.

3.9.6. Focused ion beam-scanning electron microscope (FIB-SEM)

In order to determine the new ternary compound $FeSiB_3$ crystal structure, a transmission electron microscopy analysis was conducted by Per Erik Vullum, Sintef. The TEM requires very thin samples (~

100 nm). Hence, a Helios G4 UX dual-beam focused ion beam-scanning electron microscope (FIB-SEM) was used to prepare the sample prior to the TEM analysis. At present, a cross-section sample was made by a standard lift-out technique. Moreover, coarse thinning was performed at 30 kV acceleration voltage for the Ga+ irons. Final thinning was performed at 5 and 2 kV to minimize surface damage on either side of the TEM lamella. The TEM preparation process is shown in **Figure 3-26**.

A carbon layer is deposited in situ in the FIB on top of the chosen region to protect the sample below. The Ga ion-beam is used to cut out/remove the material around the chosen region. When a tiny bridge is the only thing that still keeps the TEM lamella to the macroscopic sample, a tungsten "Easylift" needle is positioned next to the corner of the lamella and further welded to the lamella by deposition of carbon pad/weld. Once the lamella is welded to the "Easylift" needle, the bridge is sputtered away and the lamella is transferred and welded to a dedicated Cu half grid for TEM. Once welded on either side inside a trench in the Cu TEM grid, the lamella is thinned down to electron transparency (a thickness of around 100 nm). The present SE image shows the prepared cross-section. The dark contrast part is the $FeSiB_3$ phase.

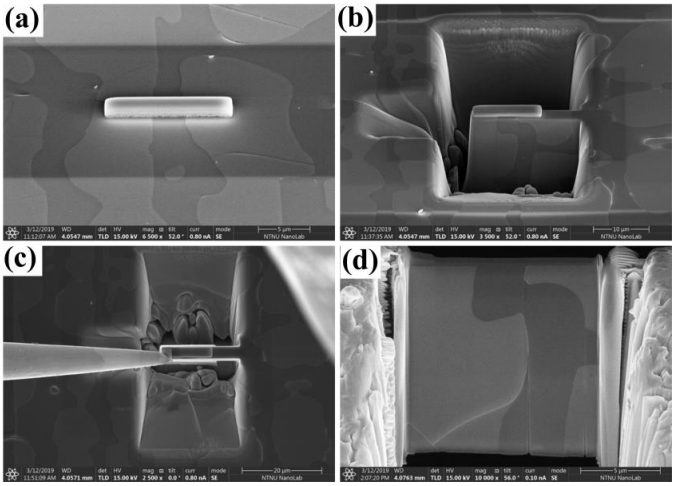

Figure 3-26 TEM sample preparation process in FIB-SEM.

3.9.7. TEM

TEM was performed with a double Cs aberration-corrected cold FEG ARM 200FC, operated at 200 kV. Element mapping was performed in scanning transmission electron microscopy (STEM) mode by simultaneous X-ray energy dispersive spectroscopy (EDS) and electron energy loss spectroscopy (EELS). EDS was acquired with a large solid angle (0.98 srad) Centurio silicon drift detector. Dual EELS was performed with a Quantum ER.

4. Results

The experimental results of the three potential PCMs (Si-B, Fe-26Si-9B, and Cr-43Si-5B alloys) are described in this chapter.

4.1. Si-B alloys

Si-B alloys are suggested as good metallic PCMs and alloys up to 11 mass % of B were experimentally investigated. In subsection 4.1.1, the phases formed in the Si-B alloys and the interaction between the Si-B alloys and graphite are presented. Then, the macro behavior of the graphite crucible after experiments are summarized in the second part. In subsection 4.1.2, the results about the interaction between the Si_3N_4 crucible and the Si-B alloys with the B addition of 2-11 mass % are investigated at 1750 ºC. In the last part, we summarize the wetting behavior of the Si-3.25B alloy on the Si_3N_4 and h-BN substrates at low pressure (10^{-4} atm).

4.1.1. Si-B alloys in the graphite crucible

Phase formation in the C-saturated Si-B alloys

The phases formed in the Si-B alloys after cooling were determined by combining the SEM and EPMA characterization. Si(ss), SiB_3, SiC, and B_4C were produced in the Si-B alloys. Images in **Figure 4-1** a-p represent the microstructures of the Si-B alloys in the graphite crucible, in which alloys with 2, 5, 8, and 11 mass % B were heated to 1450 ºC, 1550 ºC, 1650 ºC, and 1750 ºC, respectively, and 2h holding time was used at each temperature. It is seen that the microstructure in the Si-2B alloy is mainly Si(ss) and eutectic structure (Si + SiB_3). However, the B_4C phase was also detected in the Si-2B alloys (**Figure 4-18**). Hence, three phases were confirmed in the Si-2B alloys. Four phases were produced in the Si-5B, Si-8B, and Si-11B alloys: Si(ss), SiB_3, B_4C, and SiC. It was observed that SiB_3 was in the form of either large particles or eutectic structures. Some SiC particles were surrounded by B_4C, some were formed inside the SiB_3 large particles, and others were formed in the Si matrix. The phases formed in the Si-B alloys are dependent on the B content in the Si-B alloys. With the increase of B content, the amount of SiB_3 particles would be increased. Obviously, SiC and B_4C have been produced by introducing C from graphite. In addition, the formed phases did not vary much with varying temperatures at 1450-1750 ºC.

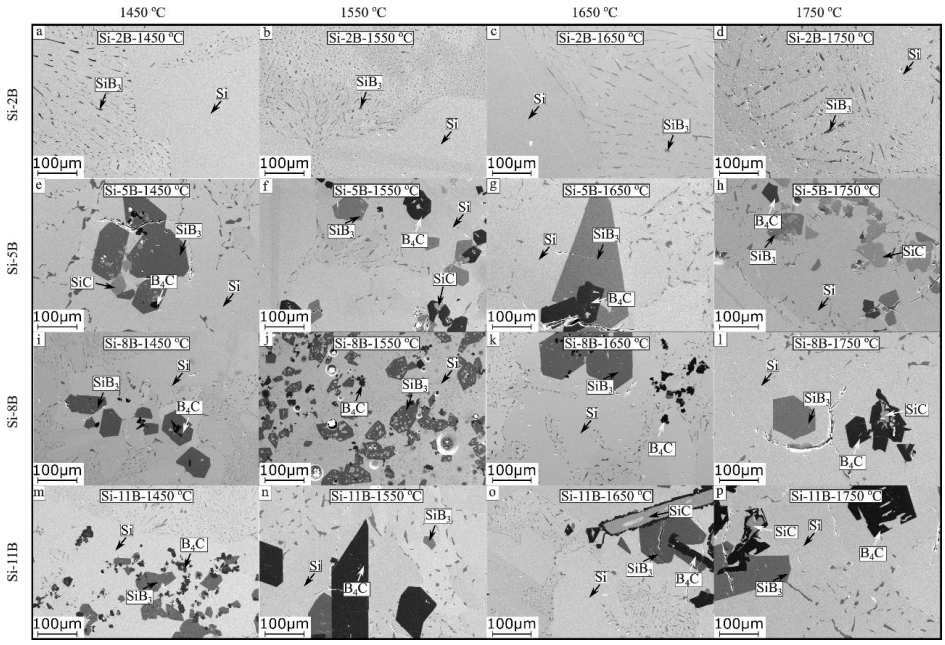

Figure 4-1 SEM images of the microstructures of samples Si-2B, Si-5B, Si-8B, and Si-11B alloys, keeping at 1450, 1550, 1650, and 1750 ºC for 2 h. (a-d) Si-2B alloys at 1450-1750 °C; (e-h) Si-5B alloys at 1450-1750 °C; (i-l) Si-8B alloys at 1450-1750 °C; (m-p) Si-11B alloys at 1450-1750 °C.

To further confirm the chemical composition of the formed phases in the Si-B alloys, the phases formed in the Si-5B alloy were quantitatively analyzed by WDS, as shown in **Figure 4-2**. 11 points in 4 different phase areas were analyzed. The results are listed in **Table 4-1**. Si(ss) (point 1-3), SiB_3 (point 4-6), SiC (point 7,8), and B_4C (point 9-11) were then determined based on their chemical compositions. The content of C was in the range of 7.2-8.3 at.% in the Si(ss) and was in the range of 5.8-6.1 at .% in the SiB_3, which is caused by the C coating for the EPMA analysis. The atomic ratio of Si and C was close to 1 in the SiC phases. Moreover, the atomic ratio of B and C was in the range of 4.33-4.82 in the B_4C phases, which is in accordance with the reported range of 4-10.4 [60]. The Si content was measured to be in the range 2.5-3.1 at. % in the B_4C phase. It is close to the measured value of 2.5 at. % Si by Telle [115]. Besides, the SiB_3 phases formed in the Si-B alloys were also analyzed by EDS. It is worth noting that the samples were not C coated before the EDS analysis. The relationship between the B content in the SiB_3 and the B addition in the Si-B alloys is depicted in **Figure 4-3**. The outliers varied in the range 38-59 at.%, which may be caused by the mixture of Si and SiB_3 phases. It is seen from the figure that the average B content was ~ 70 at.% in the SiB_3 phases, which is slightly lower than the reported value of 74.3-78.5 at.% [24]. The analyzed element contents were only used to confirm the phases formed in the Si-B alloys. It cannot be treated as the real chemical composition in the phases, due to the uncertainty of the analyses for the light elements of B and C by this method.

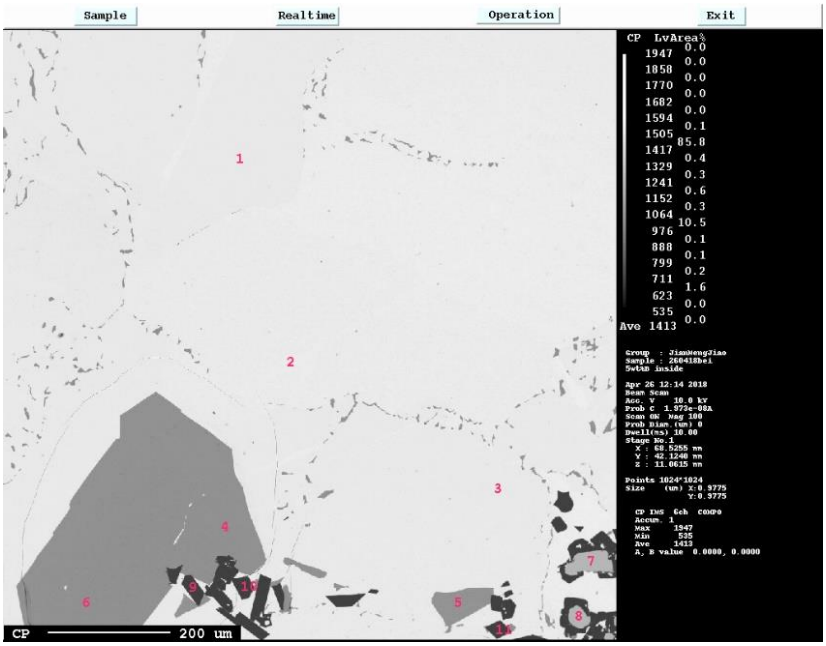

Figure 4-2 EPMA quantitative analysis of the Si-5B alloy in the big graphite crucible treated at 1450-1750 ºC.

Table 4-1 EPMA quantitative results of the Si-5B alloy. [at. %]

Point	Si	C	B	Compound
1	91.70	8.30	0.00	Si(ss)
2	92.73	7.27	0.00	Si(ss)
3	92.80	7.20	0.00	Si(ss)
4	28.22	6.14	65.64	SiB_3
5	27.95	5.75	66.29	SiB_3
6	27.86	5.89	66.19	SiB_3
7	48.22	50.90	0.00	SiC
8	48.19	51.05	0.00	SiC
9	3.10	17.94	78.40	B_4C
10	2.92	18.09	78.39	B_4C
11	2.52	16.28	78.42	B_4C

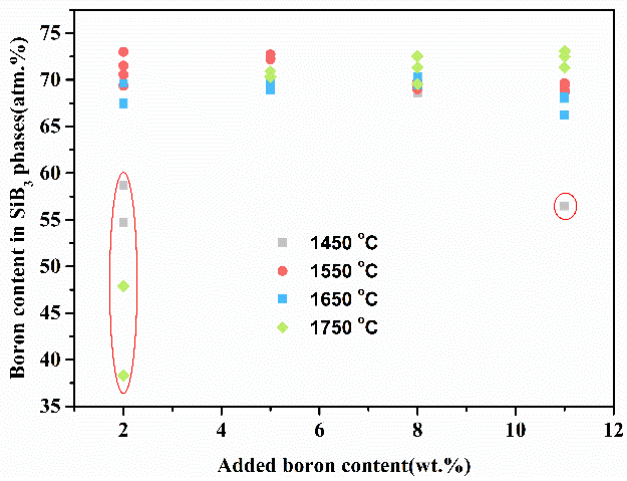

Figure 4-3 Results of the B content in the SiB_3 phases analyzed by SEM-EDS.

To further confirm the B distribution in the Si-B alloys, the EDS mapping technique was used in the Si-8B alloy. The elemental distributions of Si, B, and C are shown in **Figure 4-4**. Three phases were identified based on the grain morphology and contrast. It includes Si(ss) (bright regions), SiB_3 (grey grains), and B_4C (dark grains). It reveals that B was mainly distributed in the SiB_3 and B_4C particles, while C was accumulated in the B_4C particles.

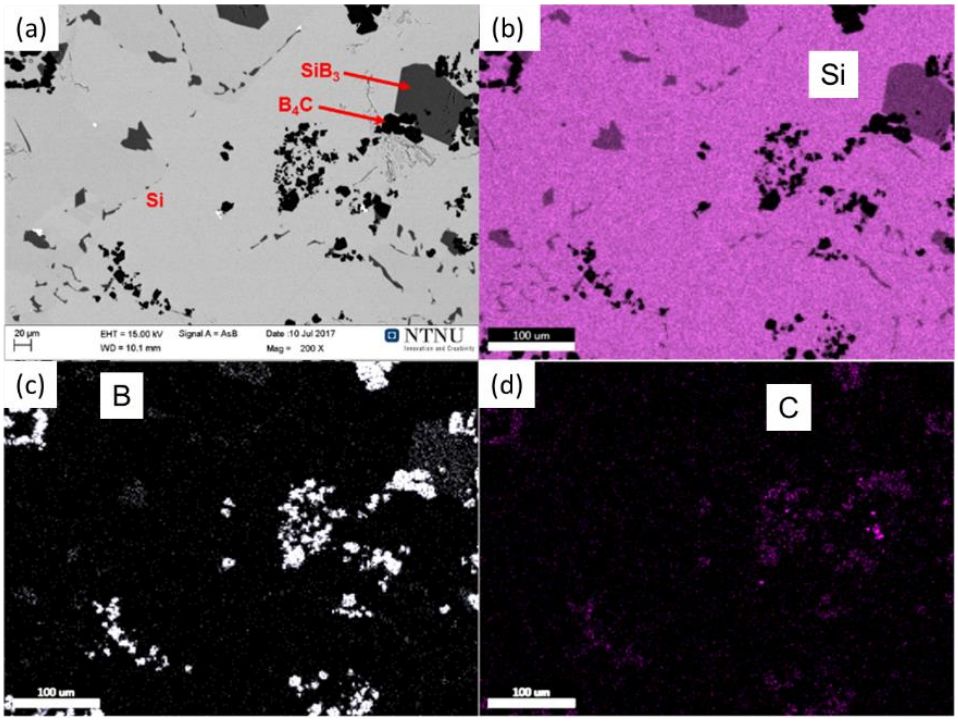

Figure 4-4 SEM micrographs and EDS maps of the Si-8B alloy at 1650 °C. (a) was captured by a secondary electron detector; (b-d) were EDS elemental maps of Si, B, and C, respectively.

Interaction between the Si-B alloys and graphite

The phases formed at the interface between Si-B alloys and graphite were investigated in the temperature range 1450-1750 °C. It is found that the SiC layer was formed when the B addition was lower than 5 mass %. The SiC and B_4C layers were formed at the interface when the B addition was higher than 5 mass %.

Figure 4-5 shows the SEM images for the phase distributions at the interface between the Si-B alloys and graphite. In the graphite body, two distinct phases are observed: graphite (black) and SiC (dark grey). A small quantity of the B_4C particles was, however, found by the EDS line scanning (**Figure 4-6**b). It is hence confirmed that Si and B (or the melt) would penetrate the graphite pores. At the interface, a continuous SiC layer was formed between the Si-2B alloy and graphite at 1450-1750 °C (**Figure 4-5**a-d). **Figure 4-6**b shows the line scan of the Si-2B alloy and graphite crucible at 1750 °C over its interface (**Figure 4-6**a). At the boundary between the metal matrix and the SiB_3 phase, there was a sharp decrease in the Si concentration, corresponding to an increase in the B concentration. At the boundary between the SiB_3 phase and SiC layer, the concentrations of Si and C were increased, and that of B was decreased. Moreover, Si and B contents were at a low level in the graphite. N and O were detected in extremely low contents in the whole area.

At the B contents higher than 5 mass %, as shown in **Figure 4-5** e-p, the SiC and B_4C layers were formed: the SiC close to the graphite and the B_4C close to the Si-B alloys. The SiC layer was formed by the reaction between the liquid Si and graphite, $Si(l) + C(s) \rightarrow SiC(s)$. The B_4C layer may be formed by the reaction between the B in liquid and SiC layer, $4SiC(s) + 4B(l) \rightarrow B_4C(s) + 4Si(l)$ or the reaction between the dissolved C and B components during solidification process, $\underline{C} + 4B(l) \rightarrow B_4C(s)$.

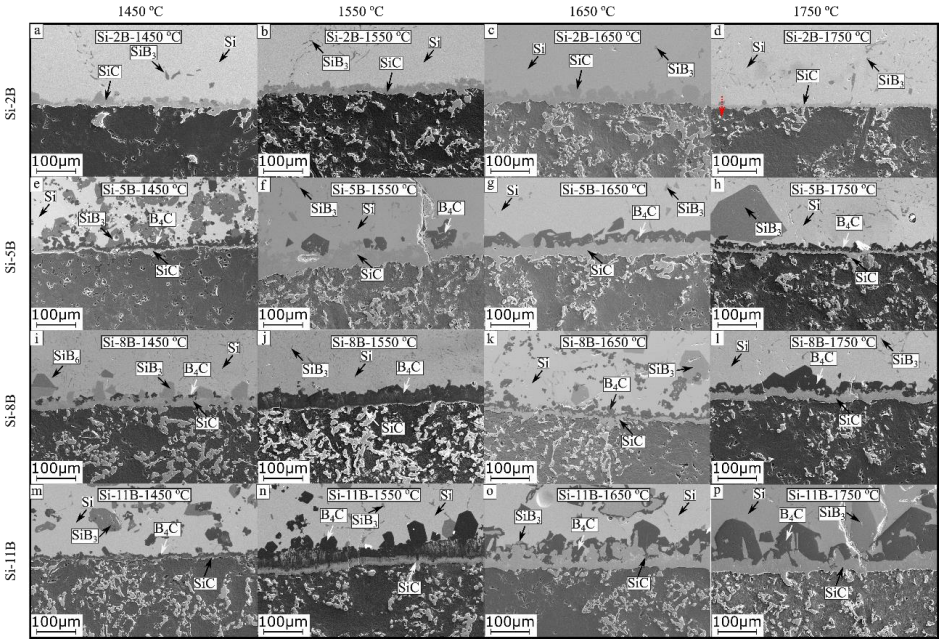

Figure 4-5 SEM images of the interface phase distributions between samples and graphite, the samples were kept at 1450, 1550, 1650, and 1750 °C for 2 h, respectively. The red dotted arrow represents the EDS line scan position. (a-d) Si-2B alloys at 1450-1750 °C; (e-h) Si-5B alloys at 1450-1750 °C; (i-l) Si-8B alloys at 1450-1750 °C; (m-p) Si-11B alloys at 1450-1750 °C.

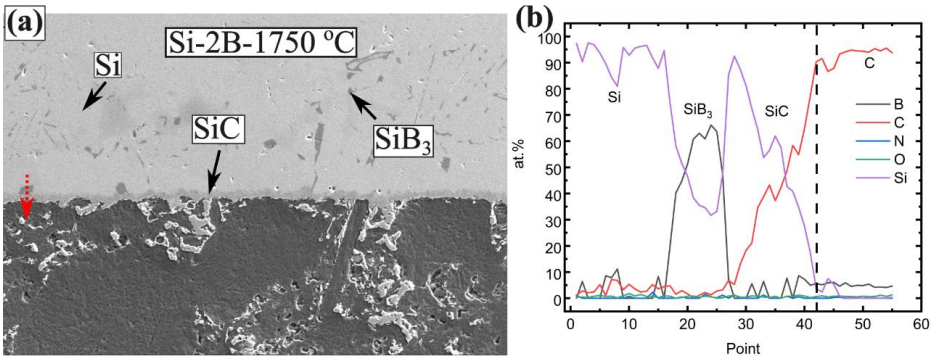

Figure 4-6 (a) Interface of the Si-2B alloy and graphite at 1750 °C ;(b) EDS line-scan of B, C, N, O, and Si across the interface between the Si-2B alloys and graphite at 1750 °C. The red arrow shows the line scan position.

In the extraction experiments, the graphite crucible was changed from G-1 to G-2, corresponding to a

diameter change from 22mm to 85mm. Moreover, the holding time was increased to 6 h in the temperature range 1450-1750 ºC. The phases produced at the interface is shown in **Figure 4-7**. It is found that the formed phase is SiC at the interface between the Si-2B and Si-3.25B alloys and graphite. Then, it was changed to the B_4C and SiC at the interface between the Si-5B alloy and graphite, and the SiC is on the graphite side and the B_4C is on the alloy side. It indicates that the formed phases were dependent on the B addition in the Si-B alloys and were independent of the holding time. In addition, large SiB_3 crystals were formed close to the SiC layer, while the eutectic structures and Si(ss) were formed in the Si-2B alloy close to the SiC layer and in the Si-5B alloy close to the B_4C layer. It is known that crystals are preferred to be formed at the interface during solidification, due to the rough surface available at the interface. With the increase of B content from 2 to 3.25 mass %, the size of the SiB_3 crystal was increased in the Si-3.25B alloys as observed by the microscopic study. However, in the Si-5B alloys, the B content was decreased close to the interface due to the formation of the B_4C layer. Hence, large SiB_3 crystals were more easily formed in the Si-3.25B alloys, compared to the higher B contents.

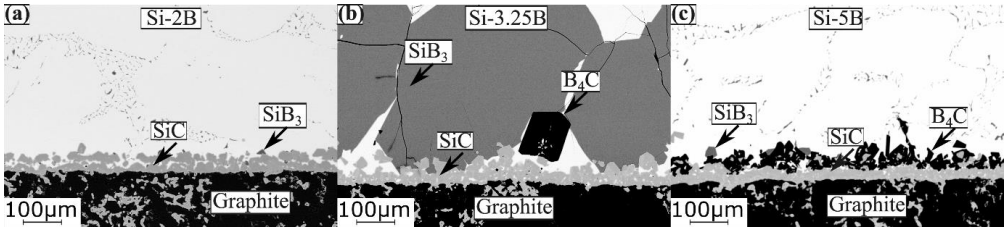

Figure 4-7 SEM images (BSE contrast) of the interphase phase distributions between Si-B alloys and graphite in the extraction experiments. (a) Si-2B; (b) Si-3.25B; (c) Si-5B.

Figure 4-8 shows the BSE image of the Si-5B alloy after the holding time of 6 h in the temperature range 1450-1750 ºC, along with the EPMA area maps depicting concentration distributions of B, C, and Si. It is seen that the B and Si were found in the graphite, attesting the B and Si penetrated from the liquid Si-B alloys to the graphite.

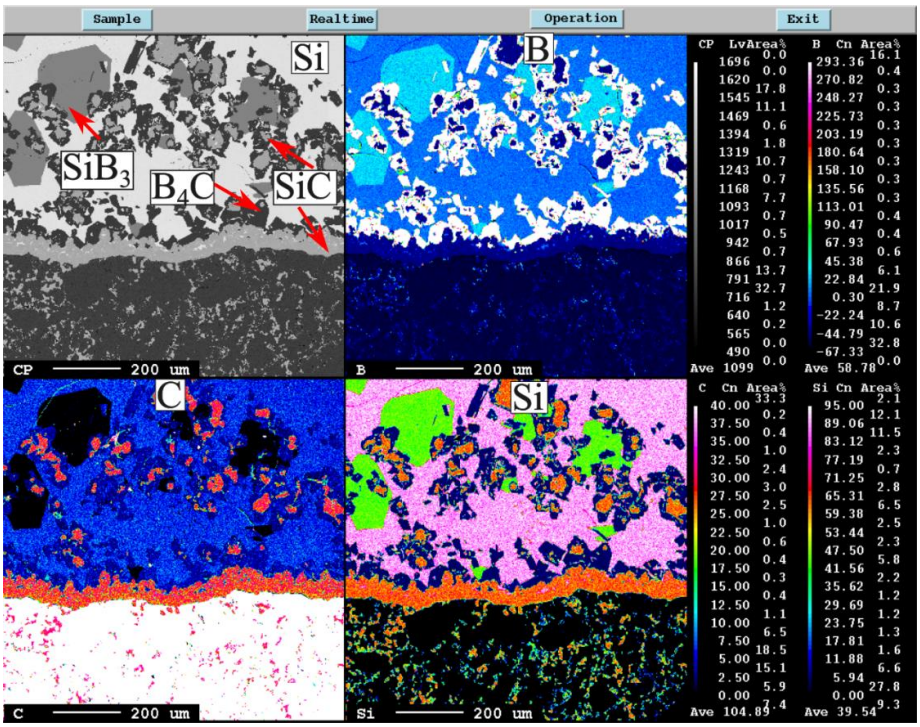

Figure 4-8 EPMA elemental map of Si-5B alloy after heating at 1450-1750 ºC for 6 hrs.

Figure 4-9-Figure 4-11 show the evolution of the average thickness of SiC and B_4C layers at the interface between the Si-B alloys and graphite. The average values with the standard deviations were taken from the two replicas, labeled as Exp-1 and Exp-2. It is worth noting that the experiments were under the same conditions. As seen in Figure 4-9 a-d, it shows the relationship between the thickness of SiC layer and the B addition in the Si-B alloys at 1450 ºC, 1550 ºC, 1650 ºC, and 1750 ºC, respectively. The red dotted lines show the boundary of the two different interfaces, in which at the left only a single SiC layer has been formed, and at the right the SiC + B_4C layers have been formed. Considering the single SiC layer, it has kept constant thickness in the temperature range1450-1650 ºC, which is ~ 25 µm. However, the thickness of the SiC layer was slightly decreased to ~ 12 µm at 1750 ºC. Considering the SiC and B_4C layers, the thickness of the SiC has been decreased at lower temperatures to 1550 ºC, and then has been increased to 1750 ºC with increasing the B content.

Figure 4-10 shows the relationship between the thickness of the B_4C layer and the B addition at different temperatures. It is seen that it remained constant at 1450 ºC and 1550 ºC, while it became thicker with the increasing B addition at 1650 ºC and 1750 ºC.

Figure 4-11 shows the thickness of the SiC/B_4C layer as a function of holding time. It is seen from Figure 4-11a that the SiC layer became slightly thicker with the longer holding time in the Si-2B alloy/graphite system. The thickness of SiC and B_4C layers were, however, in the same range for different holding times in the Si-5B/graphite system.

The measured thickness of the SiC layer was in the range of 4-48 µm. The measured thickness of the

B_4C layer was in the range of 8-65 µm. Grorud [58] investigated the interaction between the Si-3.25B alloy and graphite at 1450-1550 °C and the thickness of SiC was measured to be at the range of 10-80 µm after 1-48 h holding time. It is in good agreement with the measured values in this study.

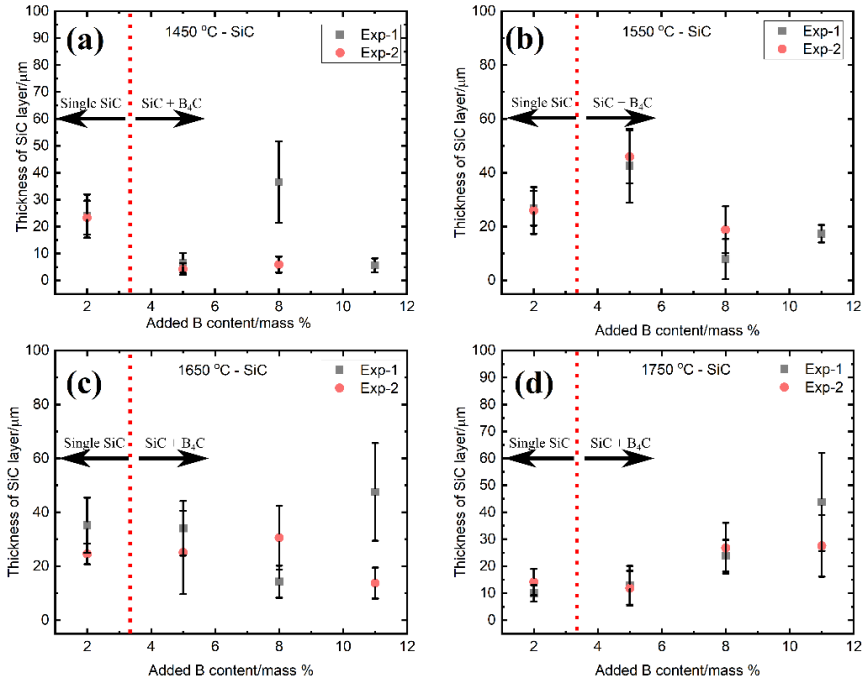

Figure 4-9 The thickness of the SiC layer as a function of the B addition at four different temperatures. (a) 1450 °C; (b) 1550 °C; (c) 1650 °C; (d) 1750 °C. Exp-1 and Exp-2 represent two different experiments in the same condition. The red dotted lines.

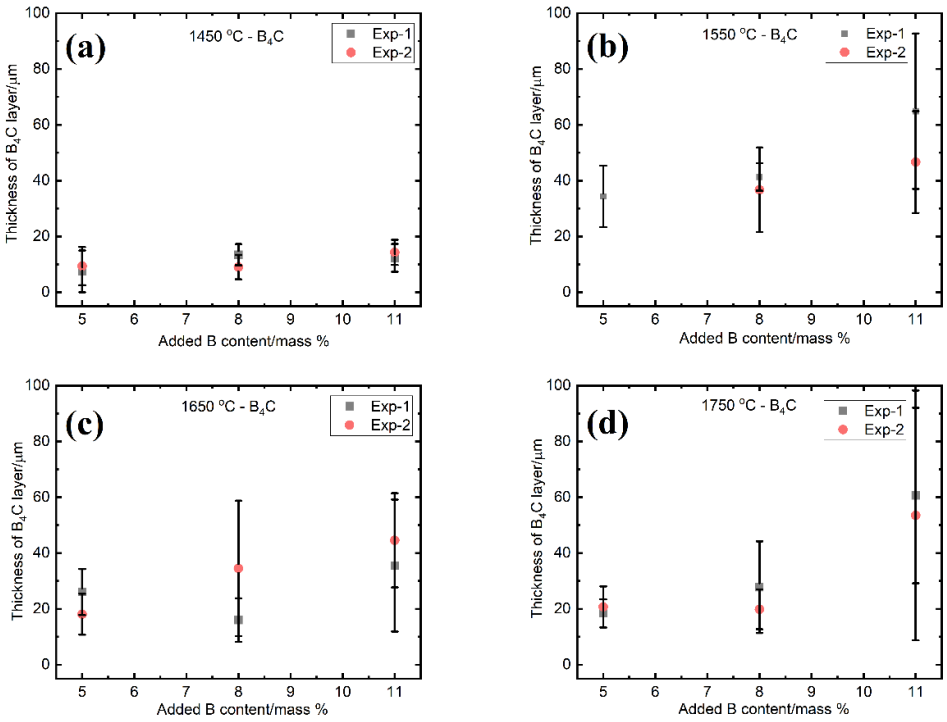

Figure 4-10 The thickness of the B_4C layer as a function of the B addition at four different temperatures. (a) 1450 °C; (b) 1550 °C; (c) 1650 °C; (d) 1750 °C. Exp-1 and Exp-2 represent two different experiments in the same condition.

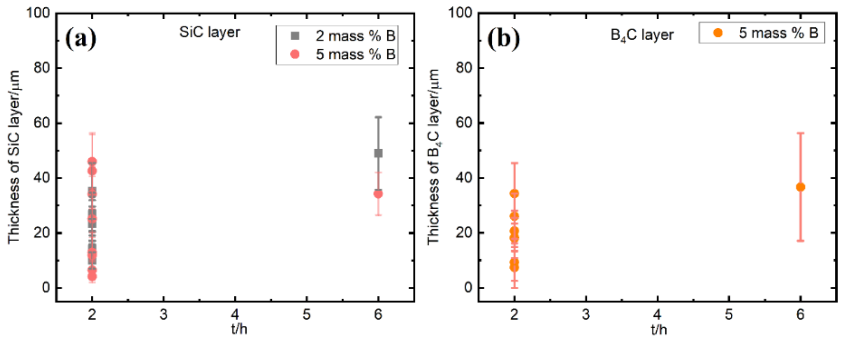

Figure 4-11 The thickness of the produced layer as a function of holding time at 1450-1750 °C, (a) SiC; (b) B_4C.

Macro behavior of Si-B alloys in graphite crucibles

Figure 4-12 shows the cross-section of the solidified Si-B alloys with the B addition of 0, 5, 15, and 25 mass %, which was subjected to 1650 °C for 2 h in the graphite crucible (G-1). The red lines represent

the original position of the Si and B mixtures. After the experiments, the solidified alloy samples were at the bottom of the graphite crucible. This is caused by the non-compact Si-B mixture powders and to a lesser extent, by the penetration of the liquid Si-B alloys to the graphite. Moreover, the Si-B alloys with 0-15 mass % B crept up on the wall of the graphite crucibles due to good wetting. However, the Si-25B alloy did not stick to the graphite wall after solidification.

The cross-sections of the Si-B alloys in the big graphite crucibles are presented in **Figure 4-13**. It is found that the graphite crucibles had cracked after solidification when 300 g Si-B mixture was charged (**Figure 4-13**a, b), while the graphite crucibles were not broken when the mass of the Si-B mixture was changed to 200g. The original position of the alloys does not change after experiments. It indicates that the loss of the Si-B alloys is negligible in the big crucibles. With larger crucibles, the area to volume ratio will affect two matters. Firstly, the gravity will compensate for a high wetting, and hence the melt will not move over the walls in the same extent. It is also expected not to be a problem in the final usage of the LHTES. Secondly, the lower area/volume ratio will to a minor extent change the final alloy composition, as less B is reacting with the crucible per volume unit to B_4C.

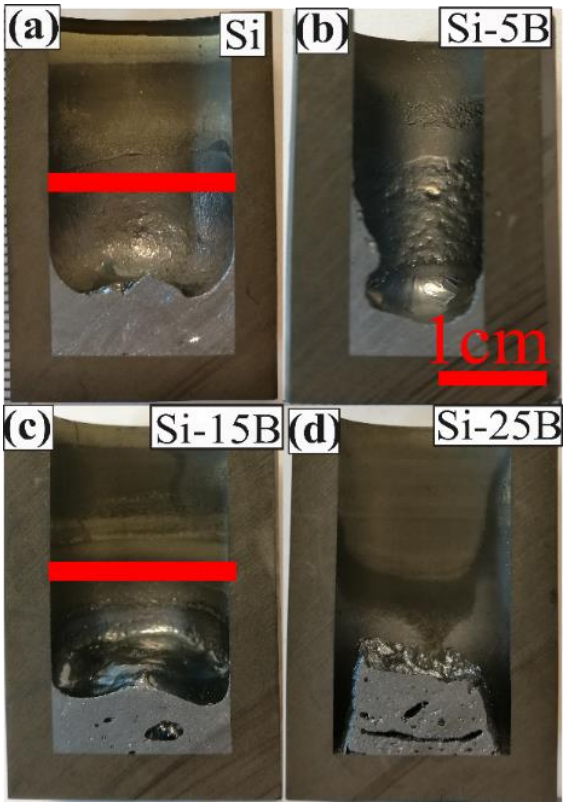

Figure 4-12 The cross-section of the Si-B alloys at 1650 °C. (a) pure Si; (b) Si-5B alloy; (c) Si-15B alloy; (d) Si-25B alloy.

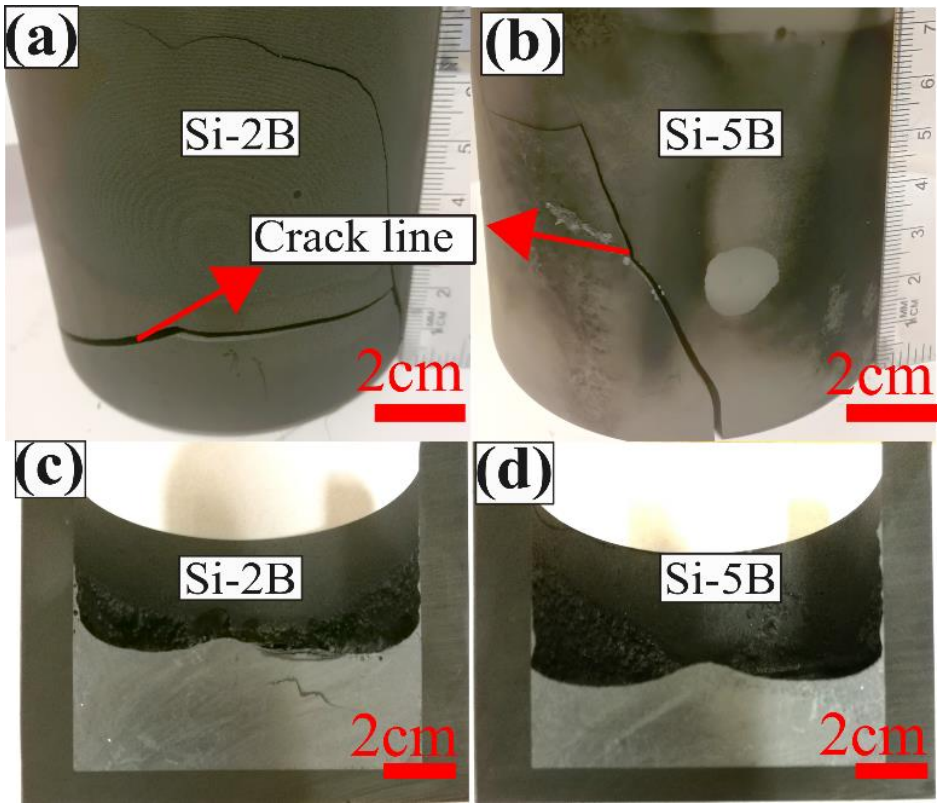

Figure 4-13 Si-B alloy in the big graphite crucible. (a)-(b) 300g; (c)-(d) 200g.

Re-melting of the Si-B master alloy in the graphite crucible

The master alloys of 5 and 8 mass % B were charged to a graphite crucible, then subjected to 1450 and 1550 °C for 2 h holding time in a resistance furnace. This was done to see if the mixed and pre-melted alloys would react with the graphite crucible in the same manner. **Figure 4-14**-**Figure 4-16** show the microstructures of the samples after re-melting of the Si-5B and Si-8B master alloys. It was found that Si(ss), SiB_3, B_4C, and SiC were formed in the center of the Si-B alloys. B_4C and SiC layers were produced in the interface between the Si-B alloys and graphite. It corresponds well with the phases formed in the Si-B alloys that were mixed. Due to the cooling rate is faster in the present experiments, the SiC layer seems to be two different layers, in which the light grey SiC layer was a mixture of the SiC and free Si and the grey SiC layer had larger compact crystals (as seen in **Figure 4-14**b). The two SiC layers were also earlier reported at the interface between Si and graphite [55] and the interface between Si-3.25B alloy and graphite [58].

The B_4C and SiC layers are formed at the interface between the Si-8B master alloys and graphite at 1450 °C and 1550 °C. It is seen from **Figure 4-15** and **Figure 4-16** that the thickness of SiC and B_4C is

thinning at 1450 ºC, which is in accordance with the results in the first melting experiment (**Figure 4-5** i). The liquidus temperature of the Si-8B alloy is ~ 1520 ºC, and hence the Si-8B alloy was not completely melted at 1450 ºC. Liquid Si-B phase and SiB_6 phases existed at 1450 ºC, which resulted to the decrease of B content in the liquid Si-B alloy. It further affected the formation of B_4C layer at 1450 ºC.

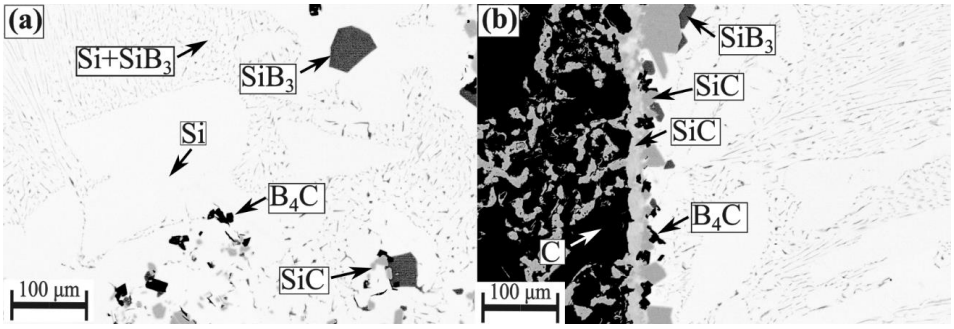

Figure 4-14 SEM images (BSE contrast) of the phase formation in the Si-5B alloy/graphite system. (a) in the center of the Si-5B alloy; (b) at the interface between the Si-5B alloy and graphite.

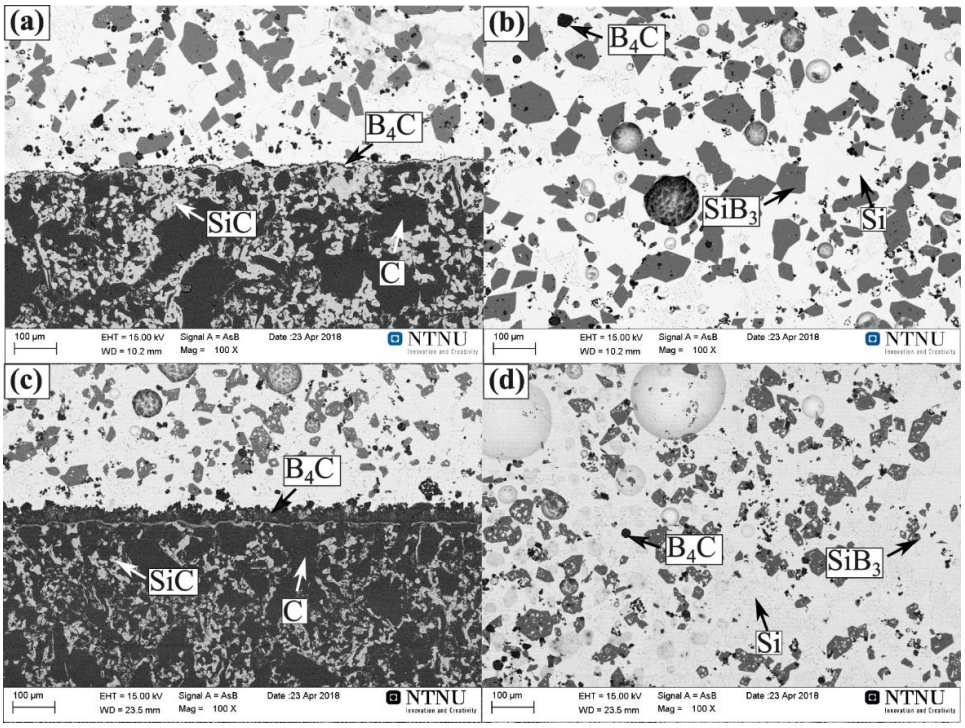

Figure 4-15 SEM images (BSE contrast) of the phasees in the Si-8B alloy/graphite system. (a) and (c) at the interface between the Si-8B master alloy and graphite at 1450 ºC and at 1550 ºC; (b) and (d) in the center of the Si-8B alloy at 1450 ºC and 1550 ºC.

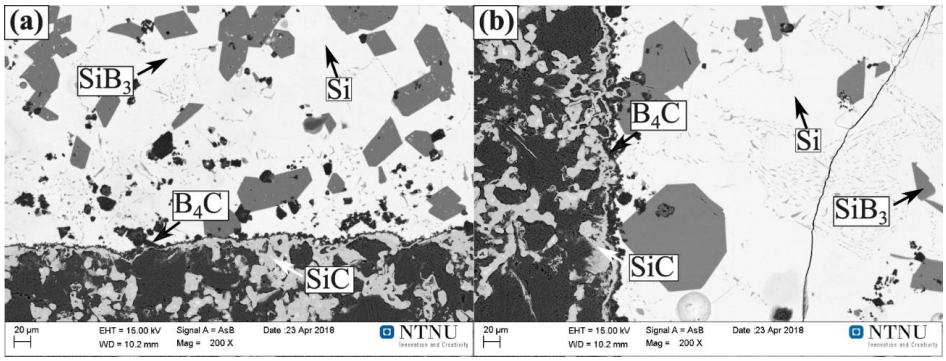

Figure 4-16 High magnification SEM images (BSE contrast) of the interface in the Si-8B alloy/graphite system at 1450 ºC. (a) horizontal position; (b) vertical position.

C solubility in liquid Si at 1450-1750 ºC

The results of the total C content in the liquid Si-B alloys are summarized in **Table 4-2**. HF represents the samples etched in the HF acid, and H_2O represents the samples just rinsed by the distilled water. It shows that the C solubilities are similar at the same temperature. Hence, the extracted C-saturated Si samples were not affected by the quartz and HF.

Figure 4-17 shows the function of the C solubility with various temperatures. The analyzed data is fitted to an Arrhenius function using the method of least squares at temperatures range between 1450 ºC and1750 ºC.

$$Cc(T) = 0.596 \cdot \exp\left(\frac{-16452}{T}\right) \ (T = 1723\text{-}2023\ K) \qquad 4.1$$

At the melting point of Si, the fitted equation gives a solubility of 34.7 ppm mass C in the liquid silicon.

Table 4-2 C solubility in the liquid Si. (ppm mass).

T/ºC	HF	H_2O
1450	40	50
	40	50
1550	80	70
	90	50
1650	90	90
	120	100
1750	190	180
	210	200

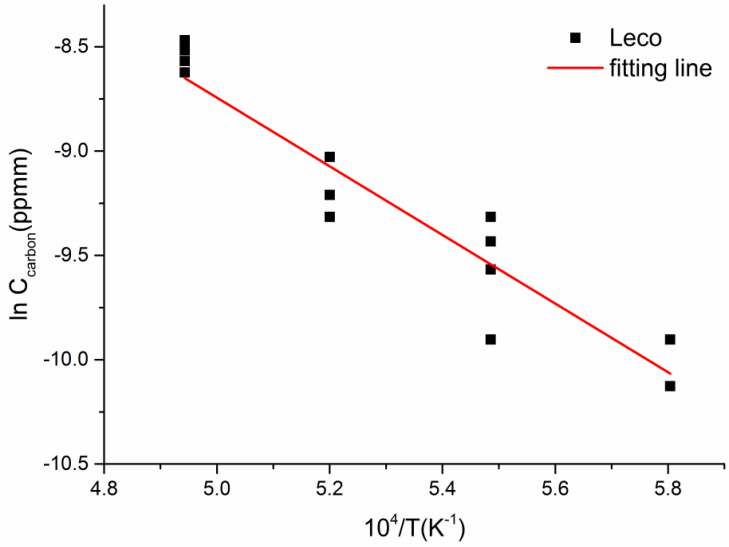

Figure 4-17 C concentration as a function of temperature. The experimental points are shown together with the plot of the fit Arrhenius equation.

C solubility in liquid Si-B alloys at 1450-1750 °C

Figure 4-18a shows the interface between the extracted Si-2B alloys and quartz tube at 1450 °C. It is found that no reaction happens between the sample and the quartz tube. Hence, it shows that the quartz would not pollute the extracted sample. **Figure 4-18**b-d show the microstructures of the extracted samples in 2, 3.25, and 5 mass % Si-B alloys. Si(ss), B_4C, and SiB_3 were produced in the solidified samples. The C was in the form of B_4C in the Si-B alloys in the B range of 2-5 mass %. The SiC was, however, not detected in the Si-B alloys. It shows that C might be completely formed to B_4C during cooling in the extraction process.

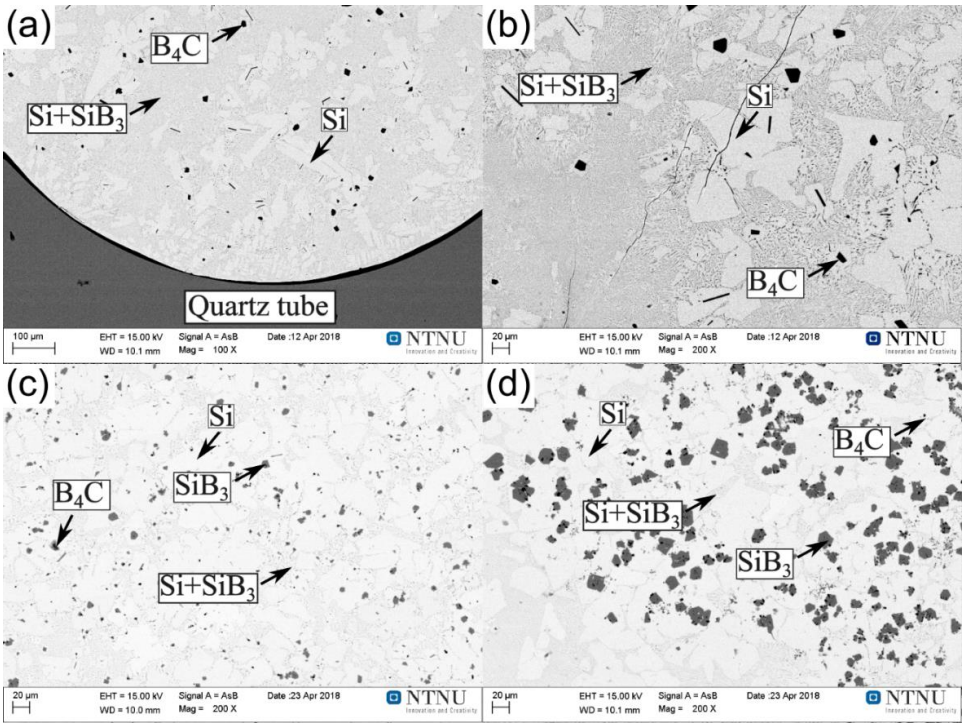

Figure 4-18 SEM picture of the extracted samples in the quartz tube. (a) the interface between the quartz tube and Si-2B alloys at 1450 ºC; (b) Si-2B alloy at 1450 ºC; (c) Si-3.25B alloy at 1650 ºC; (d) Si-5B alloy at 1750 ºC.

12 samples were extracted from the 2, 3.25, and 5 mass % B alloys in graphite crucibles in the temperature range 1450-1750 ºC. 10 samples were extracted from the Si-2B and Si-3.25B alloys in the SiC crucibles in the temperature range 1450-1700 ºC. For the 12 samples from the graphite crucibles, one part was sent to analyze the Si and B contents, and the measured B concentrations are shown in **Figure 4-19**. It is seen from **Figure 4-18**b-d that B was in the form of Si(ss), SiB_3, and B_4C in the extracted samples. In addition, B_4C cannot be digested by the $1.5HNO_3 + 0.5HF$ solution. Hence, the analyzed B content represents the B in Si(ss) and SiB_3.

Another part of the extracted samples from the graphite and 10 samples extracted from the SiC were sent to analyze the C content by the combustion method using a Leco infrared analyzer. The results are presented in **Figure 4-20**. It is seen from **Figure 4-18**b-d that C was in the form of Si(ss) and B_4C phases. The C solubility in the Si (ss) was reported to be in the range 3-24 ppm mass [44], [45], [116], which is much lower compared with the current measurements. Hence, the analyzed C content is assumed to be mainly from the B_4C phase. Therefore, the B content (C_{B1}) in the B_4C phase can be determined by the analyzed C content, while the B content (C_{B2}) in the Si(ss) solid solution and SiB_3 phase can be determined by the ICP-MS analysis. The retained B ((C_B)) in the Si-B alloys is the sum of the C_{B1} and C_{B2}, as shown in **Table 4-3**.

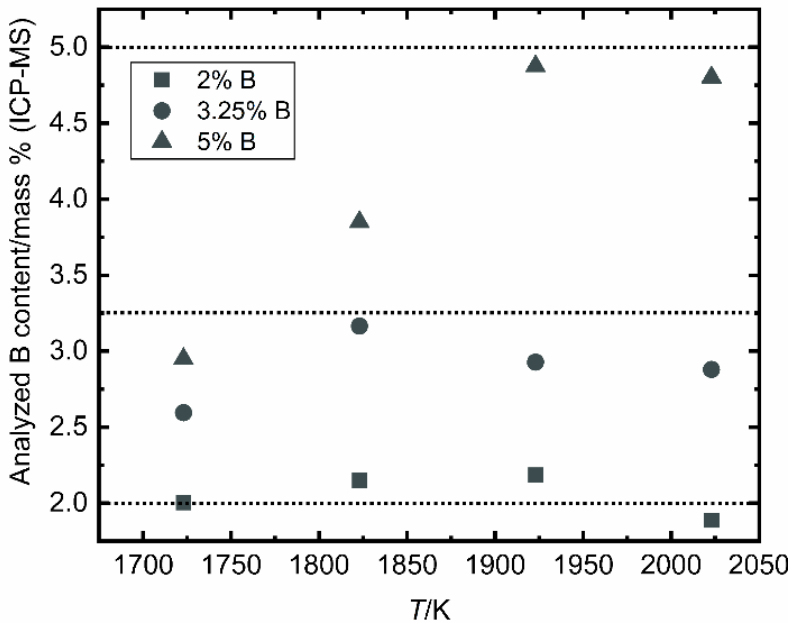

Figure 4-19 Analyzed values for B in the Si-B target alloys at temperatures 1723-2023 K, graphite is used as the crucible (the measurement of C_{B2}).

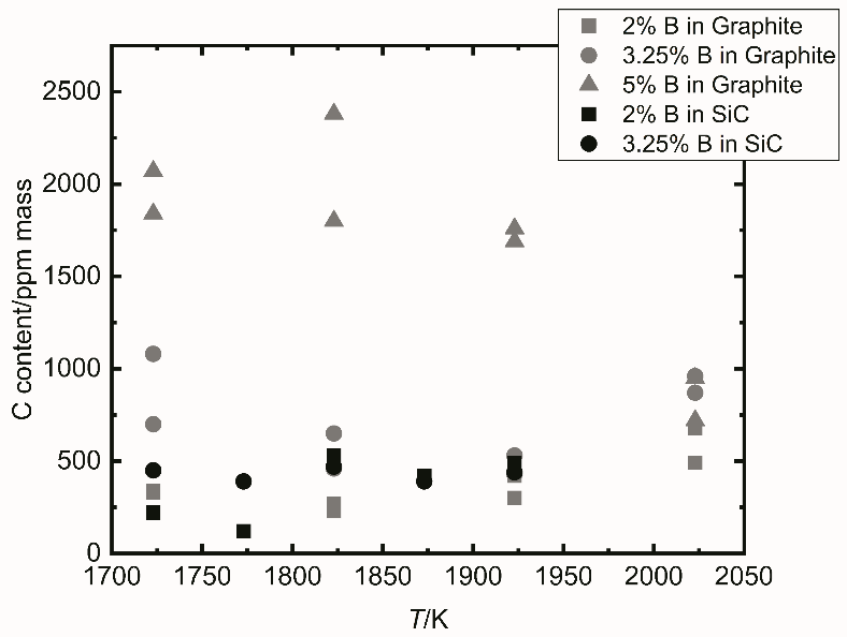

Figure 4-20 Analyzed values for C in the liquid Si-B target alloys at temperatures 1723-2023 K (the measurement of C_{B1}).

Table 4-3 The summary of the B and C content in Si-B alloys. The extraction experiments were conducted in the graphite crucibles. [mass %]

Sample-ID	C_{B1}	C_C	C_{B2}	C_B
2B-1450	1.95	0.03	0.12	2.07
2B-1550	2.15	0.03	0.09	2.24
2B-1650	2.18	0.04	0.13	2.32
2B-1750	1.89	0.06	0.21	2.10
3.25B-1450	2.60	0.09	0.32	2.92
3.25B-1550	3.17	0.06	0.20	3.37
3.25B-1650	2.93	0.05	0.17	3.10
3.25B-1750	2.88	0.09	0.33	3.21
5B-1450	2.95	0.20	0.71	3.66
5B-1550	3.85	0.21	0.76	4.61
5B-1650	4.88	0.17	0.63	5.50
5B-1750	4.80	0.17	0.61	5.41

4.1.2. The Si-B alloys in the Si_3N_4 crucible

Si_3N_4 is the second refractory material to be used as the PCM container for the Si-B alloys. The phases formed in the Si-B alloys and the interaction between the Si-B alloys and Si_3N_4 are the focus.

Phases formed in the Si-B alloys

The Si-B mixtures with the addition of 2, 5, 8, and 11 mass % B were charged to the Si_3N_4 crucibles and were subjected to 1750 ºC for 2 h. **Figure 4-21** a-d show the microstructures of the Si-B alloys after experiments. It is seen that Si(ss), SiB_3, and SiB_6 were formed in the Si-B alloys. SiC and B_4C were also detected in the Si-B alloys due to the C pollution.

The elemental distribution of Si, B, C, and N in the Si-8B alloy is shown in **Figure 4-22**. Three areas were identified based on phase morphology and contrast. It is easy to confirm that the bright region was Si(ss) and the grey particles were SiB_3. However, the dark phase was complex. It is seen from **Figure 4-22**c-e that C and N were accumulated on the bottom side of the dark grains, which was consisted of B_4C and BN phases. It seems like BN and B_4C were indistinguishable in **Figure 4-22**a. The top side of the dark grains looked like the pure B phase. However, the measured chemical composition was 82.9 at.% B and 14.2 % C in this area. The ratio of B/C was 5.8, which is in the range 4.3-12 for the B_4C phase [117]. Hence, the dark grain was believed to be B_4C.

To further confirm the BN phase in the Si-B alloys, the microstructures in the Si-8B alloy were shown

in a high magnification state. It is seen from **Figure 4-23** b that BN and B_4C show a similar morphology color in the Si-8B alloy, while it can be distinguished in a high contrast state, as shown in **Figure 4-23** c. Obviously, the BN phase was embedded in the SiB_6 phase.

Figure 4-24 shows the isothermal sections of the Si-B-Si_3N_4 system at 1000 °C and 1750 °C. The calculated phase diagrams show that no stable ternary phase was formed in the Si-B-Si_3N_4 system. It is consistent with the data provided by Seifert *et al.* [62]. It is seen from the isothermal section at 1750 °C (**Figure 4-24** b) that 2-11 mass % B alloys were in the BN + Liquid area. During solidification, the alloys were transferred to the SiB_3 + Si + BN area at 1000 °C (**Figure 4-24**a). The calculated results are in good agreement with our experimental results, regardless of the C pollution.

SiC and B_4C were detected in the Si-B alloys, which was not expected. In the experiments, the charged Si_3N_4 crucibles were placed at the bottom of the graphite crucible (G-2) under Ar flow. The presence of SiC and B_4C may hence be caused by the pollution from the graphite holder.

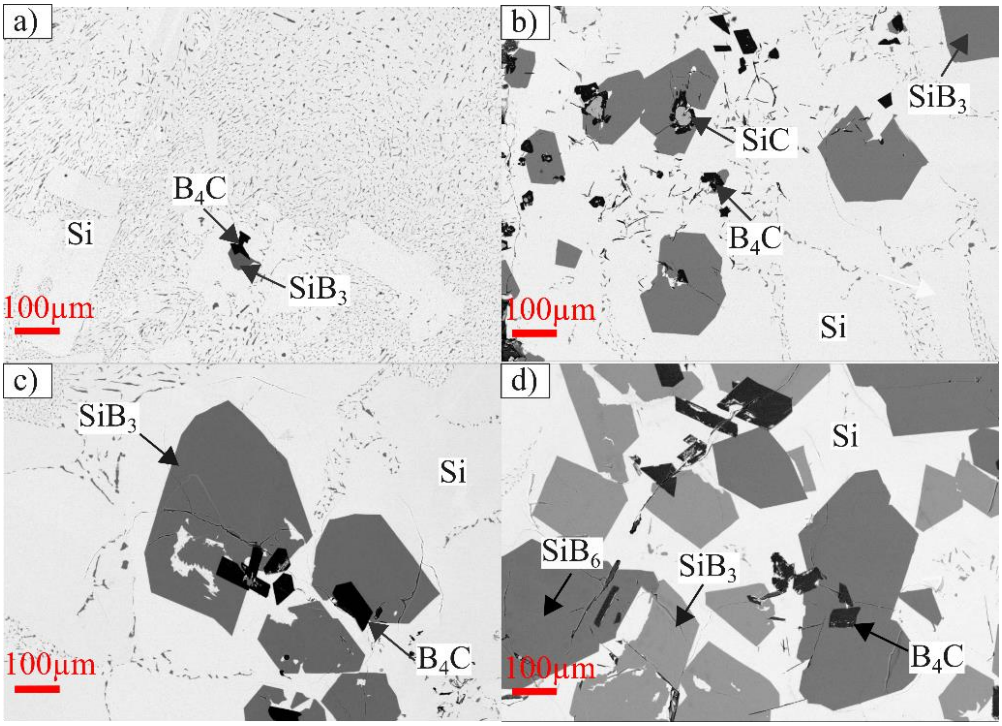

Figure 4-21 BSE Images of the center part of the Si-B alloys after solidification. (a) 2 mass % B; (b) 5 mass % B; (c) 8 mass % B; (d) 11 mass % B.

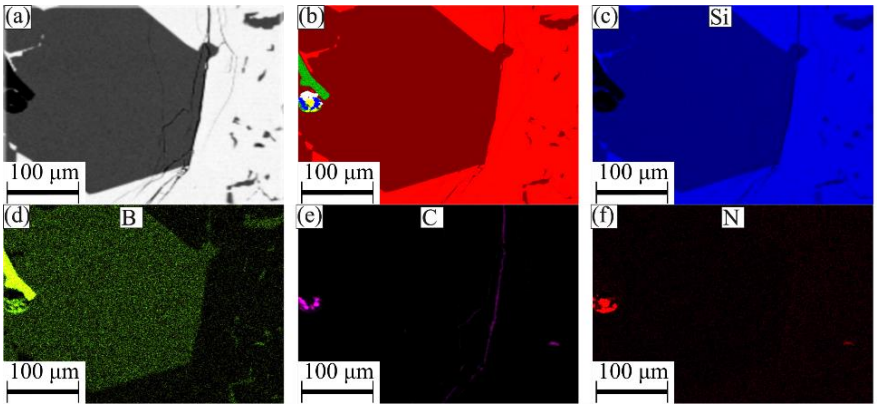

Figure 4-22 SEM micrographs and EDS maps of the Si-8B alloy in the Si_3N_4 crucible at 1750 °C. (a) was captured by a secondary electron detector; (b-e) were EDS elemental maps of silicon, boron, carbon, and nitrogen, respectively.

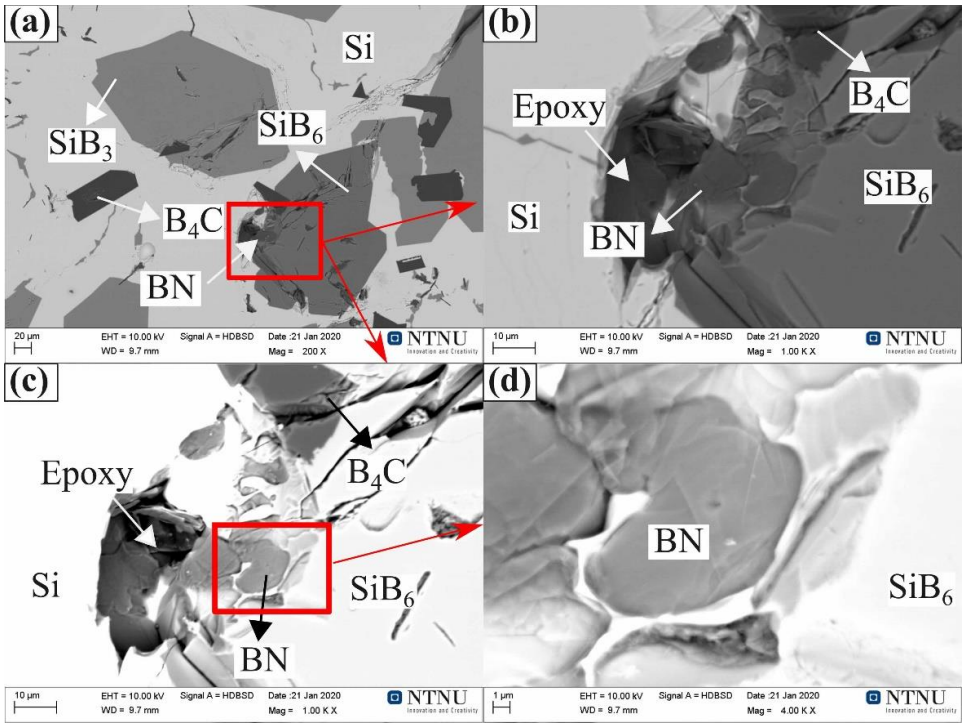

Figure 4-23 BSE Images of the Si-8B alloy after solidification. (a) 200X; (b) low contrast at 1000X; (c) high contrast at 1000X; (d) 4000X

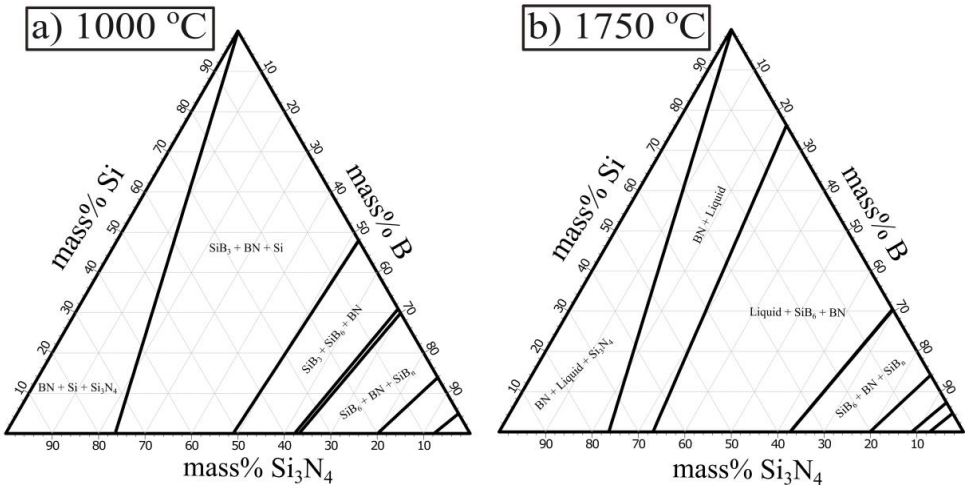

Figure 4-24 Calculated isothermal sections in the Si-B-Si_3N_4 system. (a) 1000 °C; (b) 1750 °C. Calculated with FactSage 7.2 based on FTlite database.

Interface phase formation between Si-B alloys and Si_3N_4 crucible

Figure 4-25 and **Figure 4-26** present the elemental distribution at the interface between the Si-8B alloy and Si_3N_4. For the B distribution mapping area, it is seen that the B content was higher in the Si_3N_4 area close to the interface. It indicates that a continuous BN layer was produced at the interface. The B elemental distribution shows that the liquid B would diffuse to the Si_3N_4 crucible and the diffusion depth was measured to be 247 μm. For the N, the results show that the N content was almost negligible in the Si-8B alloy. The formation of the BN layer can play the role of barrier coating between the Si-8B alloy and the Si_3N_4 crucible. It shows that Si_3N_4 is a potential refractory material as the PCM container in the thermal energy storage system.

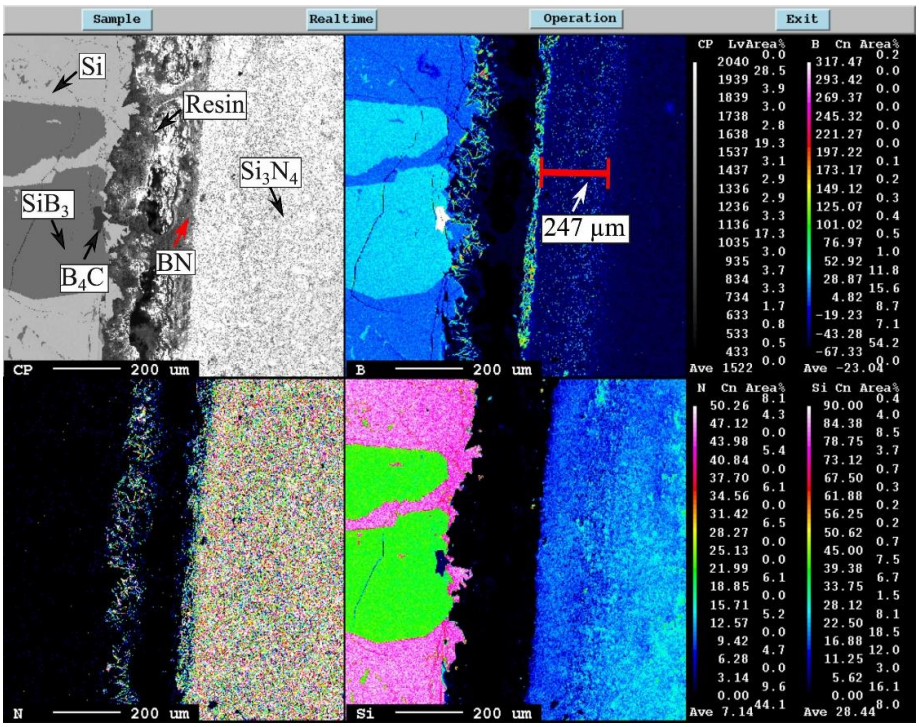

Figure 4-25 EPMA elemental map at the interface between the Si-8B alloy and Si3N4 crucible at low magnification.

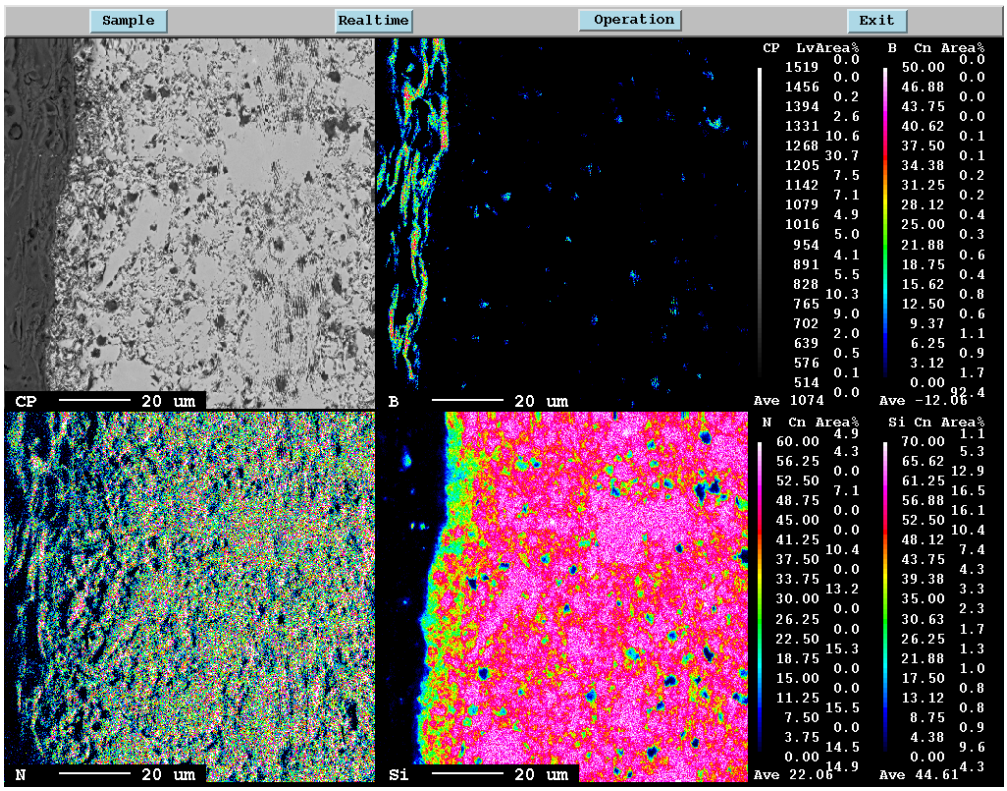

Figure 4-26 EPMA elemental map at the interface between the Si-8B alloy and Si3N4 crucible at high magnification.

4.1.3. Wetting tests of Si-B alloys on Si_3N_4 and h-BN substrates

Si_3N_4

Figure 4-27 describes the changing shape of the Si-3.25B particle during the melting/solidification process at 10^{-4} atm. At 1389 °C, the sample started to melt and was completely melted at 1400 °C. The onset temperature was close to the theoretical melting point of 1385 °C [24]. The recorded images show that the solidification started at 1318 °C and finished at ~ 1200 °C. The volume expansion was easily observed in the cooling process, by the final liquid flowing out at the left top of the solidified drop.

Figure 4-28 shows the contact angles of the Si-3.25B droplet as a function of time. The time of zero corresponds to the complete melting at 1400 °C. It is apparent from the figure that the initial contact angle was equal to 134 ± 1° and it was almost constant within the holding time of 80 s.

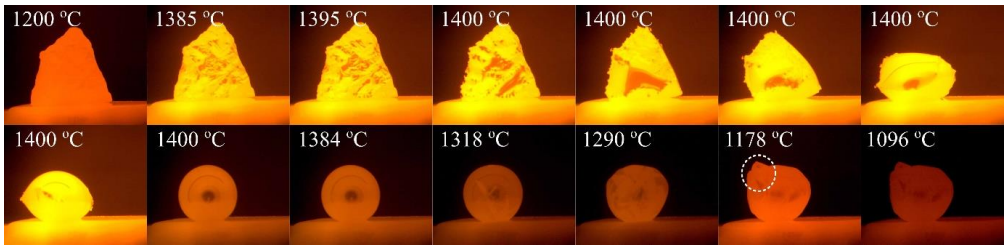

Figure 4-27 Wetting test of Si-3.25B alloy on Si_3N_4 substrate under 10^{-4} atm. White dotted circle represents the volume expansion of Si-3.25B alloy during solidification.

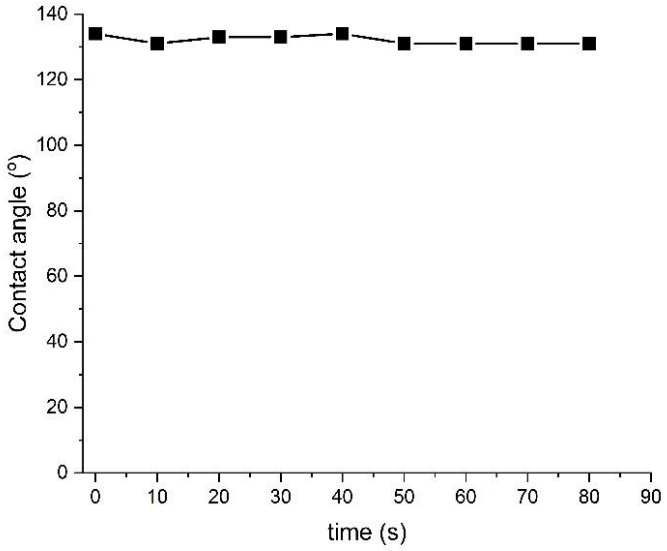

Figure 4-28 Contact angle as a function of time for a liquid Si-3.25B drop on Si_3N_4 substrate at 1400 °C.

h-BN

Figure 4-29 shows the wetting process of the Si-3.25B powder on the h-BN substrate under 10^{-4} atm. In the heating process, the Si-3.25B alloy started to melt at 1396 °C and was completely melted at 1397 °C. The contact angle was measured to be 120 °C at 1450 °C. However, the wetting of the liquid Si-3.25B alloy on the h-BN was changed with the increase of thermal cycles (**Figure 4-30**). It is seen that the Si-3.25B particle was completely melted at 1386 °C, close to the melting point in the first wetting test. In the thermal cycles, the equilibrium contact angle between the Si-3.25B drop and h-BN was measured at the steady-state. It was recorded that the contact angle was decreased from 135° (first cycle) to 85° (second cycle), and then, the contact angle was continuously decreased to ~ 63° in the third cycle. In addition, a wetting-to-dewetting transition of the Si-3.25B alloy was observed in the heating process

in the second and third cycles, as shown in **Figure 4-31**. The contact angle was increased from 85° to 90° in the second cycle and from 48° to 63° in the third cycle. Moreover, a slight variation of the liquid Si-3.25B alloy was observed in the heating step in the thermal cycle experiment. It indicates that the gas was released at the surface.

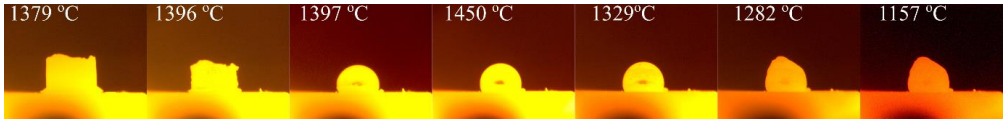

Figure 4-29 Wetting test images of Si-3.25B powder on the h-BN substrate for 1 thermal cycle under 10^{-4} atm.

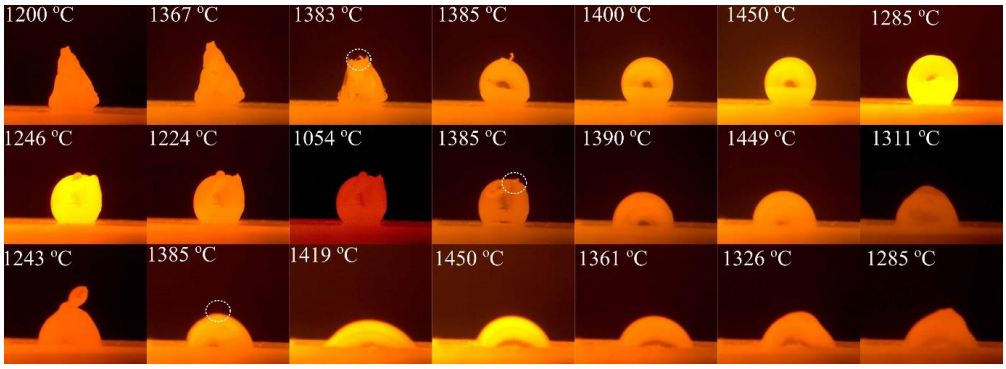

Figure 4-30 Wetting test images of Si-3.25B particle on the h-BN substrate for 3 thermal cycles under 10^{-4} atm.

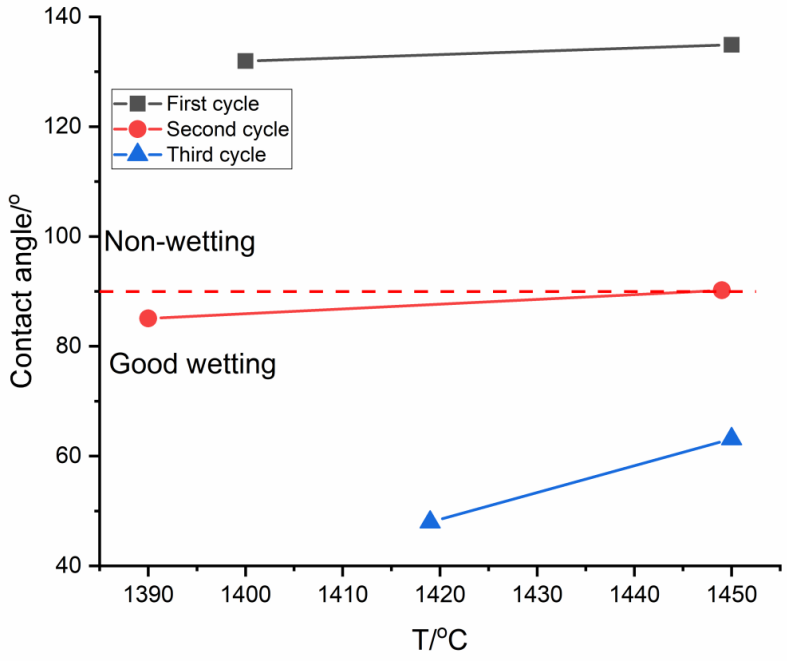

Figure 4-31 Contact angle as a function of temperature in the heating step. The red dashed line shows the position of 90°.

Figure 4-32 a-d show the cross-sectional interfacial areas in the Si-3.25B/h-BN system. It is seen that the Si(ss) and Si + SiB_3 eutectic structure was formed in the solidified Si-3.25B alloys (**Figure 4-32**b). SiB_3 particles were formed at the interface, in which it might be produced by the reaction of Si and B during solidification: Si(l) + B(l) → SiB_6, and the SiB_6 was then transformed to SiB_3 with the further cooling. It is worth noting that the Si-3.25B master alloy was produced in the graphite crucible, in which the liquid Si-3.25B alloy should be C-saturated. Hence, some SiC particles were formed in the area close to the three phases contact area and along the interface (**Figure 4-32** c and d).

The red rectangle area shows that a new interface formed in the dewetting zone area (**Figure 4-32** c). The elemental distribution of B, Si, O, N, and C was then taken in this area, as shown in **Figure 4-33**. It is seen from **Figure 4-33**a that four phases exist in the three-phase contact area: Si, h-BN, epoxy, and SiO_2. The SiO_2 phase was determined by the elemental distribution of the Si and O (**Figure 4-33** c and d), and it is on the substrate/gas interfacial area after the experiment. The wetting behavior of Si-3.25B alloy on h-BN changing from non-wetting to wetting might be caused by the formation of the SiO_2 layer, in which the reported contact angle was 85° between the liquid Si and SiO_2 at 1400 °C [90]. The oxygen present could be due to air leakage to the furnace.

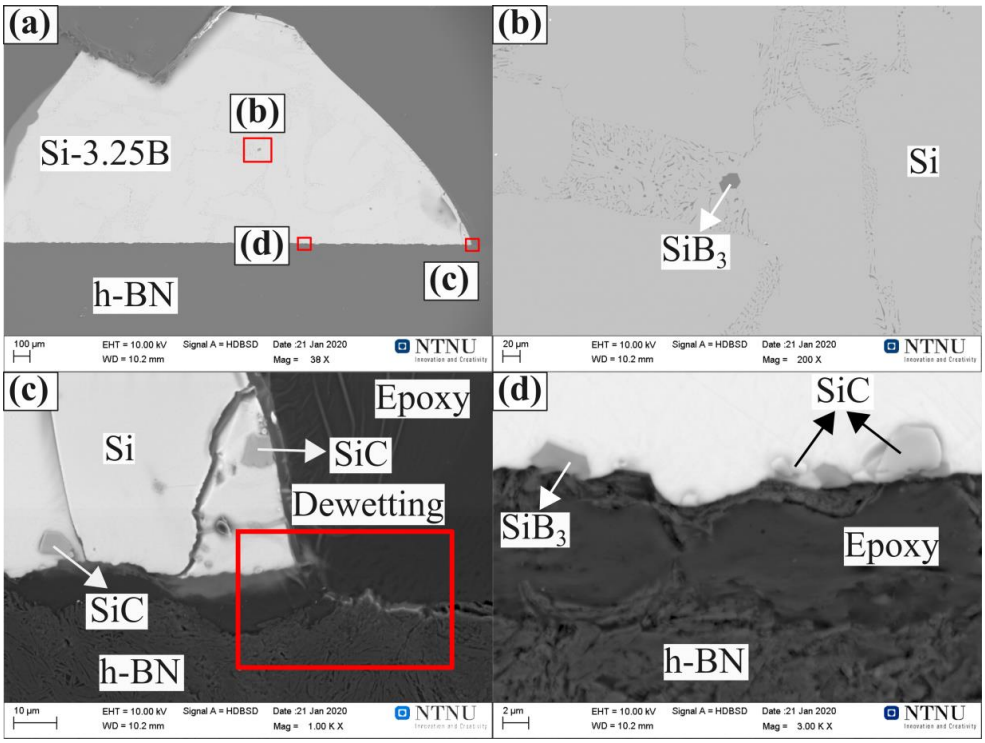

Figure 4-32 microstructures observed on the cross sectioned sample in the 3.25B/h-BN system. (a) an overall view, red rectangles show the magnification area; (b) enlarged areas showing SiB_3 and Si phases; (c) enlarged areas showing SiC particles in three-phase contact area, red rectangle shows the mapping area ; (d) enlarged area showing the SiB_3 and SiC particles at the interface.

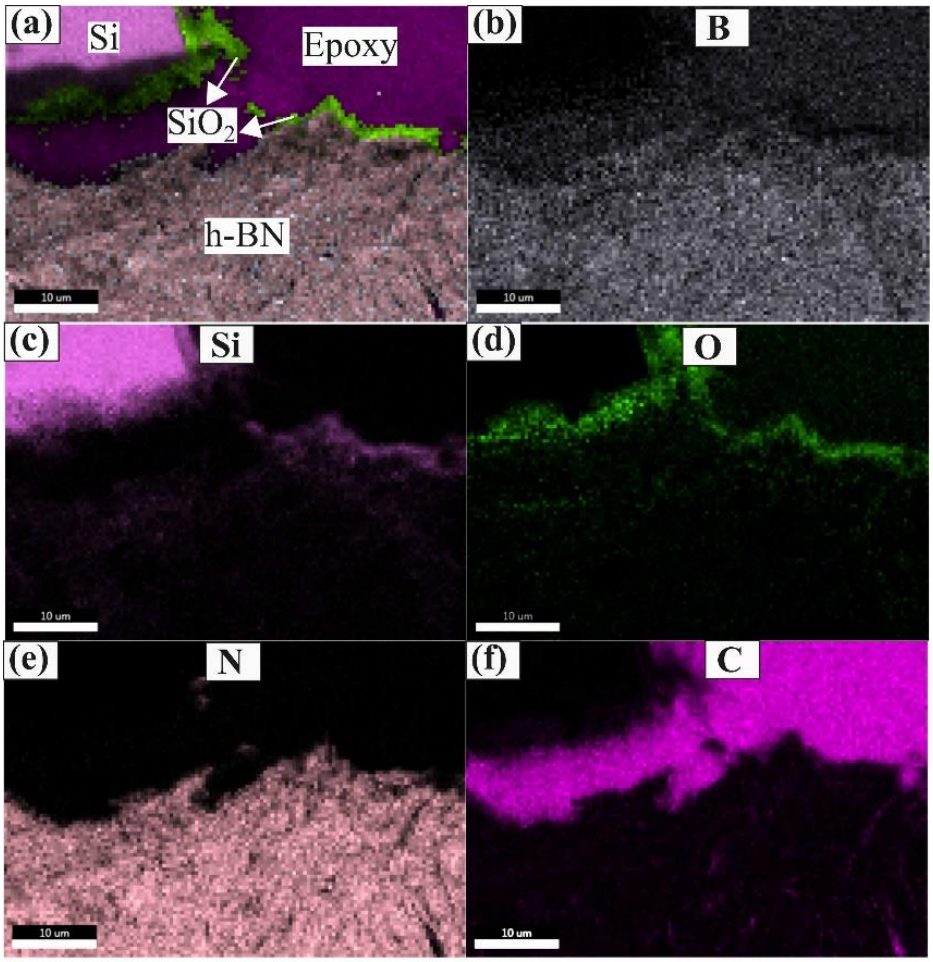

Figure 4-33 Elemental distribution in the three phases contact area: (a) phase distribution; (b) B; (c) Si; (d) O; (e) N; (f) C. The mapping area is shown in the red rectangle area in **Figure 4-32**c.

Volume change in the Si-3.25B alloys during solidification in the wetting tests

The relative area changes of the cross section of the Si-3.25B alloy was calculated based on the recorded images in the wetting tests during solidification. As shown in **Figure 4-34**, the grey squares and black triangles represent the measured area change relative to the area at the melting temperature. It should be noted that the measured melting temperature was in the range of 1386-1400 ºC in the wetting tests. Hence, the choice of the highest temperature (1400 ºC) should be more reasonable. It is seen that the calculated relative area change of Si-3.25B alloy was similar based on the wetting tests on Si_3N_4 and h-BN, in which the solidification process in the first cycle was used to measure the relative area change in the wetting test on h-BN (**Figure 4-30**).

To some extent, the area change represents the volume change in the wetting tests. The volume continued to increase in the liquid state, which might be caused by the supercooling in the solidification process. Then, it had a sharp increase in the period from the solidification onset to the solidification offset, corresponding to the volume expansion of 5.42 % in the wetting test on h-BN and of 7.1 % in the wetting test on Si_3N_4. Considering the whole solidification process, the maximum volume expansion was ~ 9 % from the liquidus point to the complete solidification. The main conclusion here is that the small amount of B addition to the alloy does not reduce the volume expansion significantly, compared to Si that has a volume expansion of 10% [22].

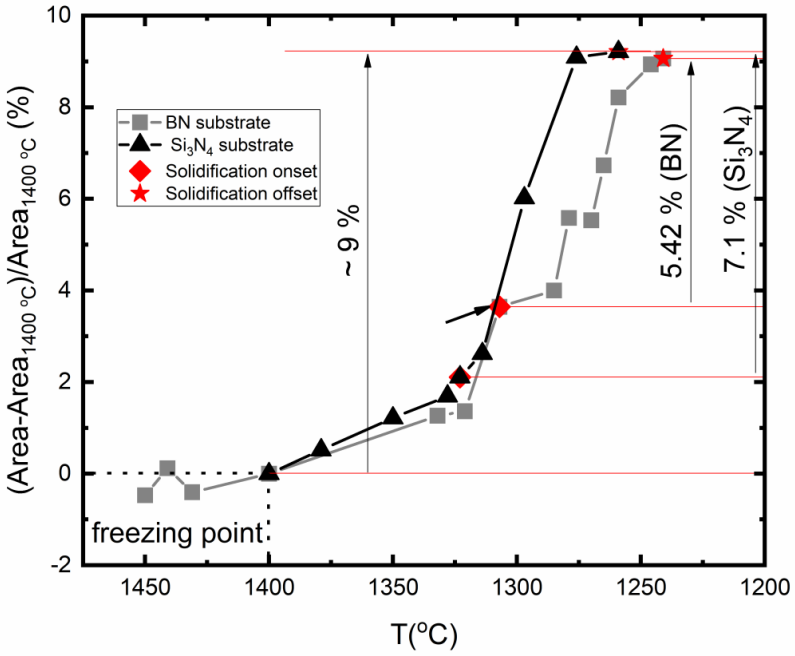

Figure 4-34 Relative area change of the Si-3.2B alloy on the BN and Si_3N_4 substrates.

4.2. Fe-26Si-9B alloy

Fe-26Si-9B eutectic alloy was another potential metallic PCM investigated in our group. In subsection 4.2.1, the results about the interaction of Fe-26Si-9B alloy with Si_3N_4 crucible are given, aiming to test the stability of Si_3N_4 crucible as the PCM container at high temperatures. Then, in the second subsection, the characterization results about the $FeSiB_3$ phase are provided by combining FBI-SEM and TEM technology. In subsection 4.2.3, the wetting behavior of Fe-26Si-9B eutectic alloy on various refractory

materials is presented under the low vacuum (10^{-4}, 10^{-5}, and 10^{-9} atm) and 1 bar Ar atmosphere. The refractory materials include graphite, SiC, Al_2O_3, Si_3N_4, and h-BN. In the last subsection, the DSC experiments of Fe-26Si-9B alloys are summarized.

4.2.1. Fe-26Si-9B alloy in Si_3N_4 crucibles

Phase formation in Fe-26Si-9B alloys

The interaction between the Fe-26Si-9B alloy and the Si_3N_4 crucible was investigated in a resistance furnace, in which the Fe-26Si-9B particles were subjected to 1, 6, and 12 thermal cycles in the temperature range 1100-1300 ºC. The phases formed in the Fe-26Si-9B alloys are shown in **Figure 4-35**. FeB, FeSi, SiB_6, and $FeSiB_3$ were observed in the bulk of the Fe-26Si-9B alloys. FeB was formed in the form of large crystals. However, FeSi and $FeSiB_3$ were in the form of eutectic structure. Compared with **Figure 4-35**a, b, and c, the formed phases were the same with the increasing thermal cycles. It shows good phase stability in the Fe-26Si-9B alloys in the repeated melting/solidification process. Moreover, no nitride phases were present in the alloys. It shows the possibility of using the Si_3N_4 material as the Fe-26Si-9B alloys' container at high temperatures.

Figure 4-36 shows the eutectic area in the Fe-26Si-9B alloy after 6 thermal cycles. The grey area represents the FeSi phase, and the black area represents the $FeSiB_3$ phase. Moreover, the phase amounts were calculated based on the obtained images: 40% $FeSiB_3$ and 60% FeSi in the low magnification (**Figure 4-36**a) and 44 % $FeSiB_3$ and 56% FeSi in the high magnification (**Figure 4-36**b).

Due to the C contamination in the preparation of the Fe-26Si-9B master alloys, some B_4C and SiC particles were observed at the top of the Fe-26Si-9B alloys after thermal cycles, as shown in **Figure 4-37**. It is seen that the SiC particles were decorated with the B_4C phases.

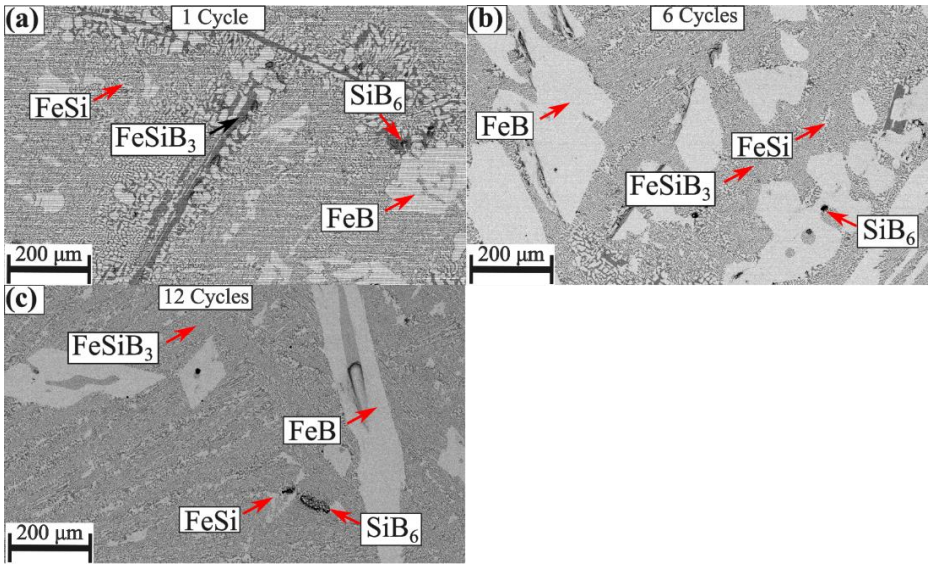

Figure 4-35 Images of the Fe-26Si-9B alloy after thermal cycle experiments. (a) one cycle; (b) six cycles; (c) twelve cycles.

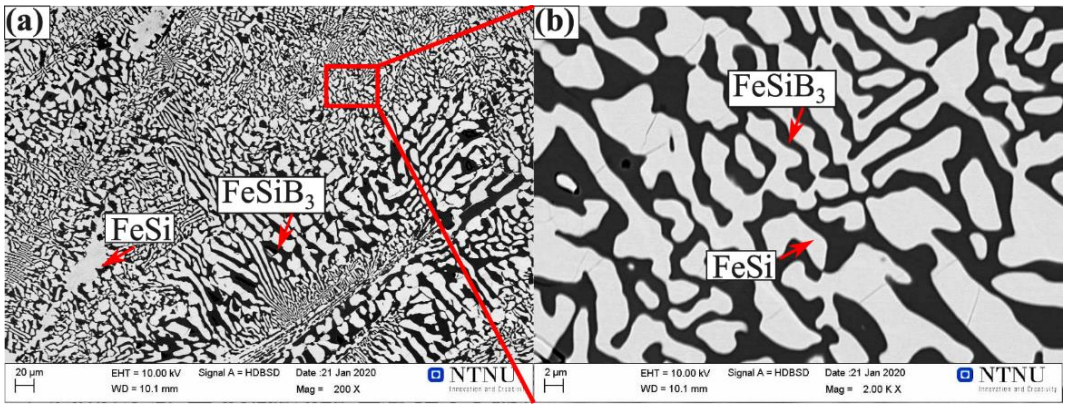

Figure 4-36 Images of eutectic area in the Fe-26Si-9B alloy after six thermal cycles. (a) 200X; (b) 2000X. Red rectangle area shows the magnification position.

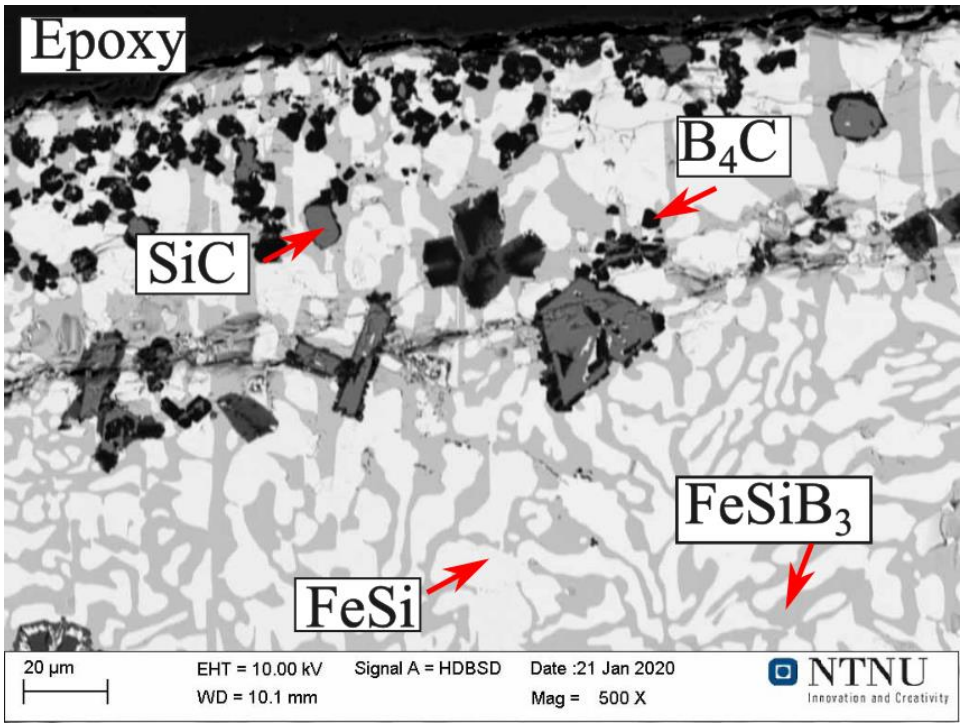

Figure 4-37 Image from the top of the solidified Fe-26Si-9B alloy after six thermal cycles.

Interface phase formation between Fe-Si-B alloys and Si_3N_4 crucible

Figure 4-38 and **Figure 4-39** show the distribution of the elements at the interface of the Fe-26Si-9B alloy/ Si_3N_4 crucible after 6 thermal cycles, in which Si, N, B, and Fe were analyzed, respectively. As seen in **Figure 4-38**, the left bright part shows the Fe-26Si-9B alloy. The right dark grey part shows the Si_3N_4 crucible wall. The dark area between the Fe-26Si-9B alloy and the Si_3N_4 crucible is epoxy. The Fe-26Si-9B alloy did not adhere to the Si_3N_4 crucible, which showed the non-wetting behavior between them. It is seen from the distribution of the elements that Fe and B were not detected in the Si_3N_4 crucible and nitride phases were not detected in the alloy. **Figure 4-40** shows the Si_3N_4 morphology close to the interface at the high magnification state. It is seen from **Figure 4-40**b that no new phase was formed in the Si_3N_4 crucible. The results show that Si_3N_4 is stable after the repeated melting/solidification process.

The phase evolution in the interaction of Fe-26Si-9B alloy with Si_3N_4 at 1550 ºC was predicted by FactSage 7.2 based on the FTlite database, as shown in **Figure 4-41**. The Y-axis represents the amounts of phases formed in the interaction between Fe-26Si-9B alloy and Si_3N_4. The X-axis represents the amount of Fe-26Si-9B alloy. It is seen that BN will be formed between Fe-26Si-9B alloy and Si_3N_4 at 1550 ºC. However, BN was not experimentally found in the Fe-26Si-9B alloy or at the interface.

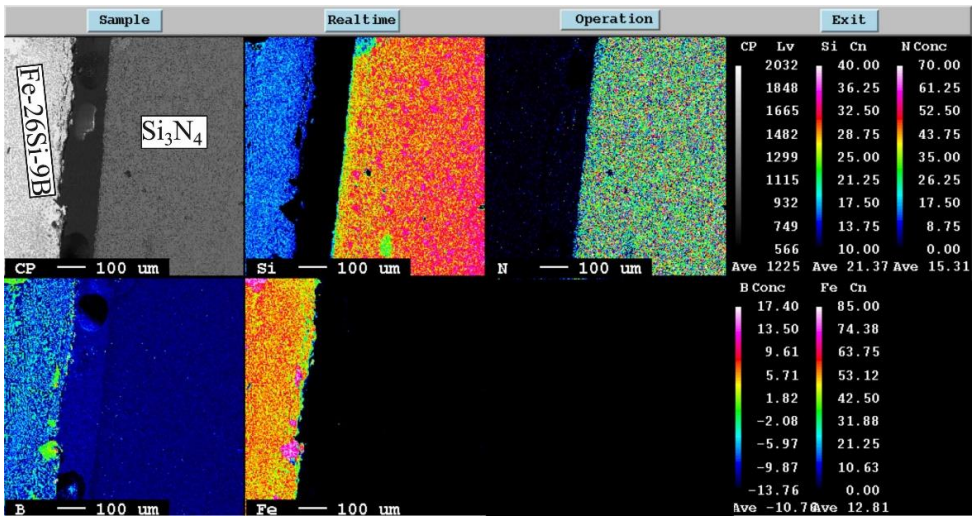

Figure 4-38 EPMA elemental map at the interface between Fe-Si-B alloy and the right Si_3N_4 crucible wall after six thermal cycles at 1100-1300 ºC

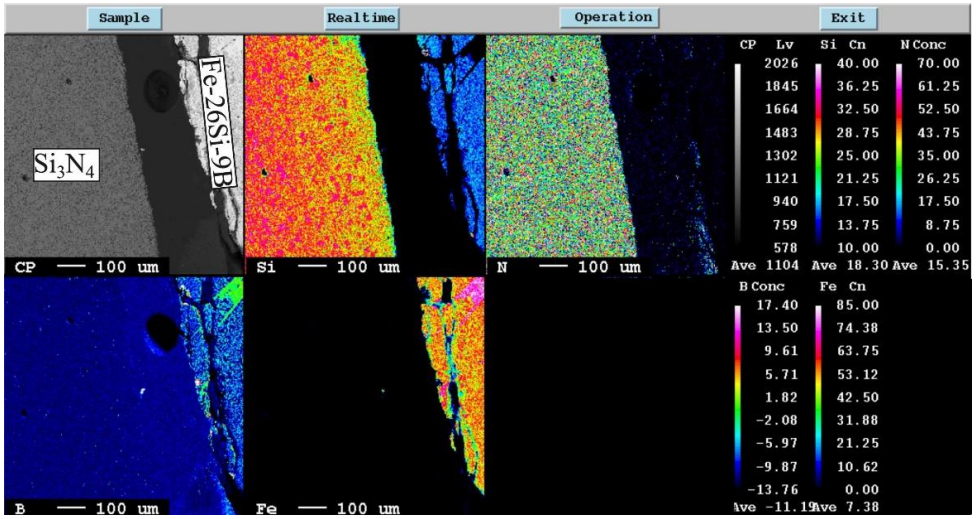

Figure 4-39 EPMA elemental map at the interface between Fe-Si-B alloy and the left Si_3N_4 crucible wall after six thermal cycles at 1100-1300 ºC

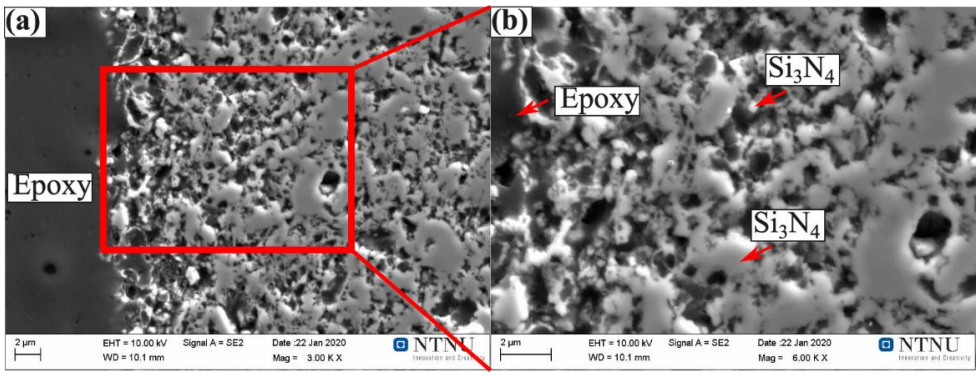

Figure 4-40 Images of the interface close to the Si_3N_4 part. (a) 3000X; (b) 6000X.

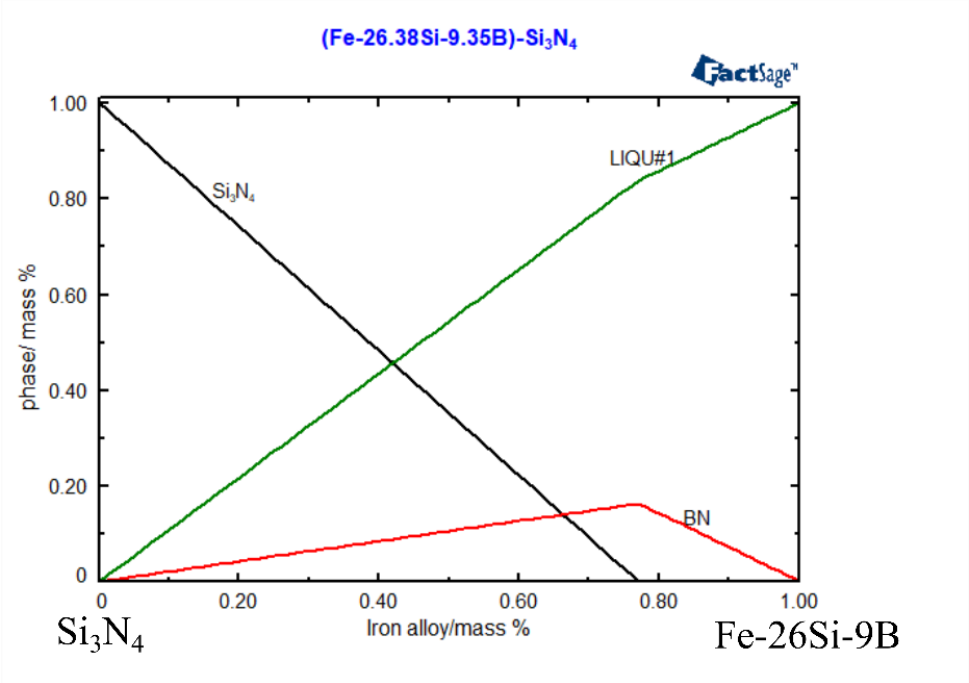

Figure 4-41 The evolution of the phase formation in the interaction of Fe-26Si-9B alloy with Si_3N_4 refractory material at 1550 °C. Calculated with FactSage 7.2 based on the FTlite database.

4.2.2. Characterization of the $FeSiB_3$ phase

The formed phases formed in the Fe-26Si-9B alloys were confirmed by XRD, as shown in **Figure 4-42**. It is worth noting that the samples were taken from the thermal cycle experiments in the graphite crucible, in which the thermal cycle and the temperature range was designed as 1–4 times at 1157 ± 20

°C and 1157 ± 100 °C [109]. It is seen from **Figure 4-42**a that FeB, FeSi, SiB_6, and B_4C phases were detected by XRD spectra. **Figure 4-42**b shows the expanded view of XRD spectra at the scan range of 47°–55°. Several XRD peaks were labeled by the red dotted rectangles. The phases presented by the XRD peaks were not found in the JCPSD-database PDF-4 + 2018 RDB. The unidentified peaks are believed to be the new ternary phase of $FeSiB_3$.

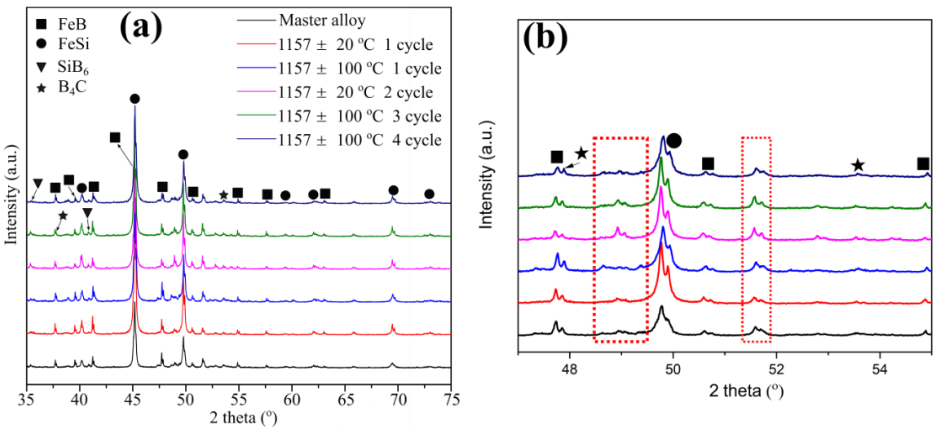

Figure 4-42 (a) XRD patterns of Fe-26.38Si-9.35B alloys with different temperature intervals and thermal cycles; (b) An expanded view of the XRD spectra at the scan range of 47–55°. The red dotted rectangle areas show the unidentified phases in the Fe-26Si-9B alloys.

To further confirm the new ternary phase of $FeSiB_3$, the crystalline structure of the $FeSiB_3$ phase was investigated by TEM. A dual-beam FIB-SEM was used to collect a TEM sample from the Fe-26Si-9B sample. **Figure 4-43** shows the microstructures of the Fe-26Si-9B alloy. The red lines show the position of the TEM lamella. The phases formed in the red line area were analyzed by EDS mapping in the FIB-SEM, as shown in **Figure 4-44**. The dark contrast phase shows only Fe and Si in the EDS spectra and with an atomic ratio of ~ 1:1 between Fe and Si. However, the dark contrast phase shows B in addition to Fe and Si, which indicates the $FeSiB_3$ ternary phase.

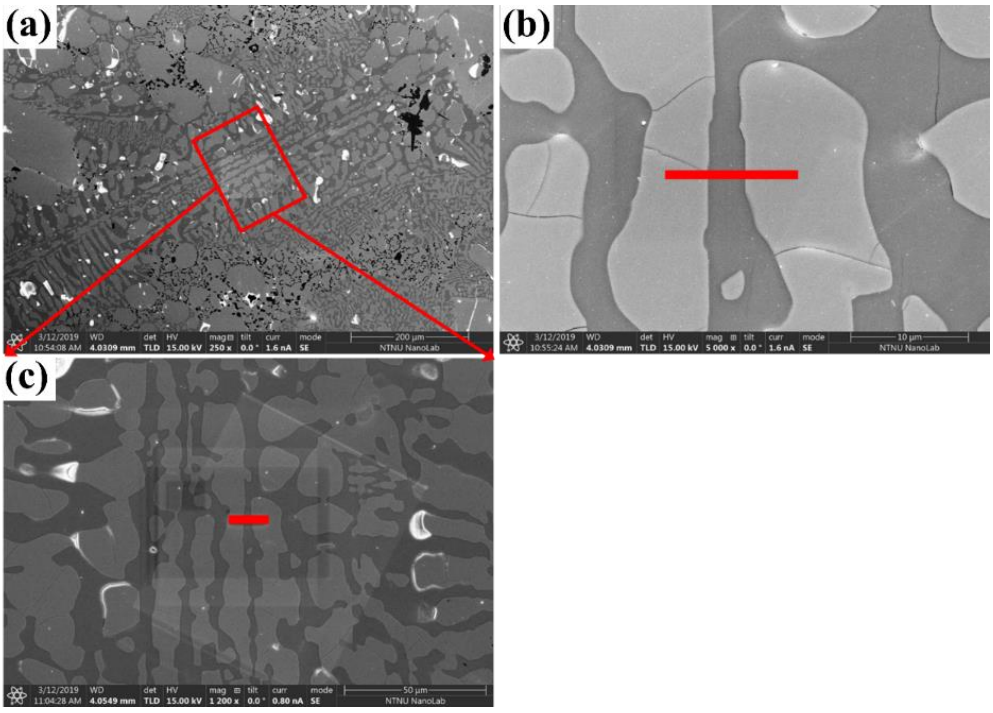

Figure 4-43 Images in the center part of the Fe-26Si-9B alloy. (a) 250X magnification; (b) 5000X magnification; (c) 1200X magnification. Red line shows the position of the TEM lamella.

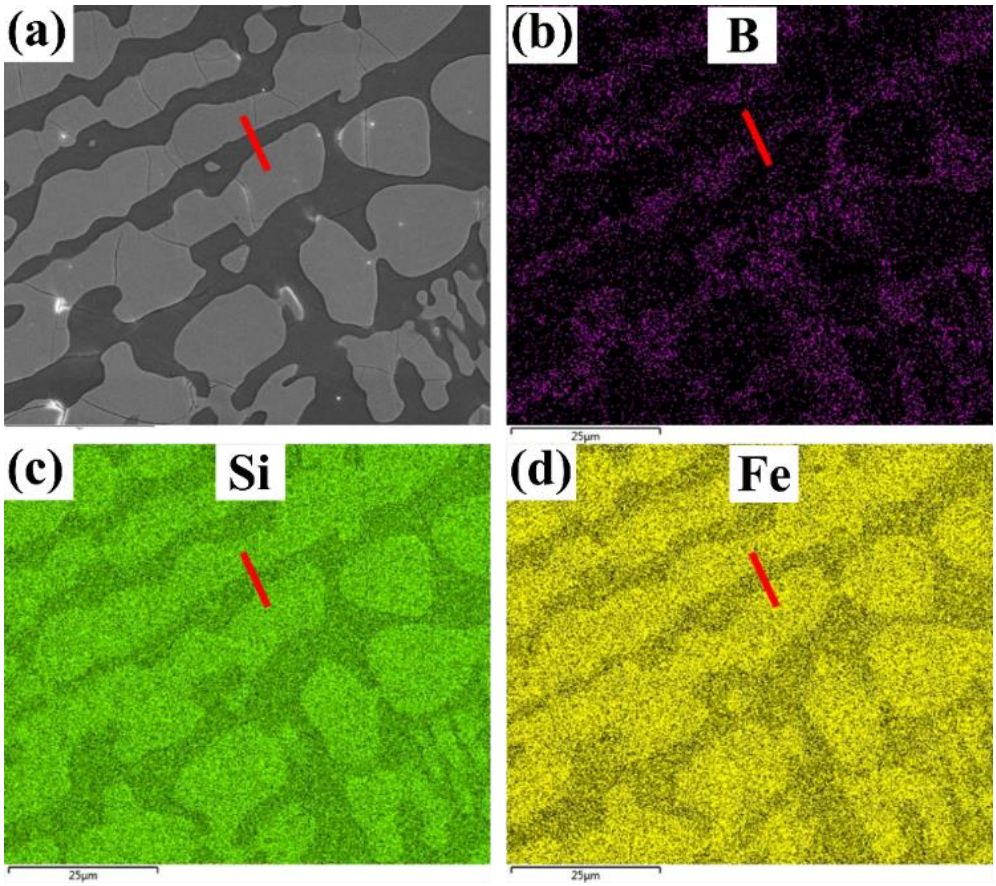

Figure 4-44 EDS mapping in the Fe-26Si-9B alloy by FIB-SEM. (a) BSE image; (b) B; (c) Si; (d) Fe.

Figure 4-45 shows the High Angle Annular Dark Field Scanning Transmission Electron Microscopy (HAADF-STEM) images obtained by TEM. The contrast by this imaging technique scales almost with Z^2, where Z represents an atomic number. Hence, phases with heavy elements give bright contrast, and light elements give a dark contrast. The B-rich phase, therefore, has dark contrast compared to the much brighter FeSi phase.

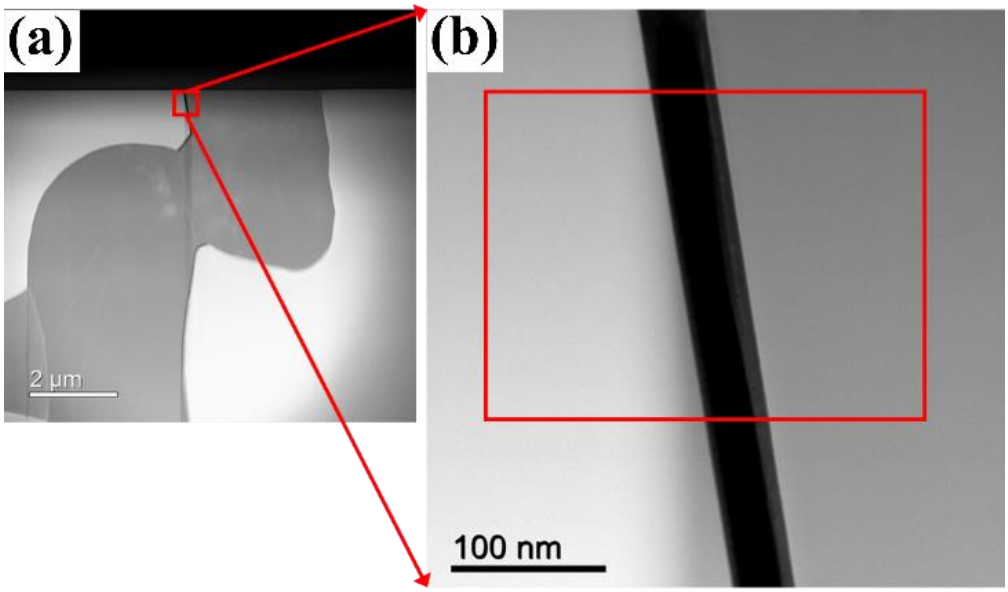

Figure 4-45 High Angle Annular Dark Field Scanning Transmission Electron Microscopy (HAADF-STEM) images. (a) low magnification; (b) high magnification.

Figure 4-46 shows the bright field (BF) TEM images. The red arrows point at low angle grain boundaries inside the $FeSiB_3$ phase. There are also a high number of dislocations in the $FeSiB_3$ phase and many cracks at the interface between the FeSi and the $FeSiB_3$.

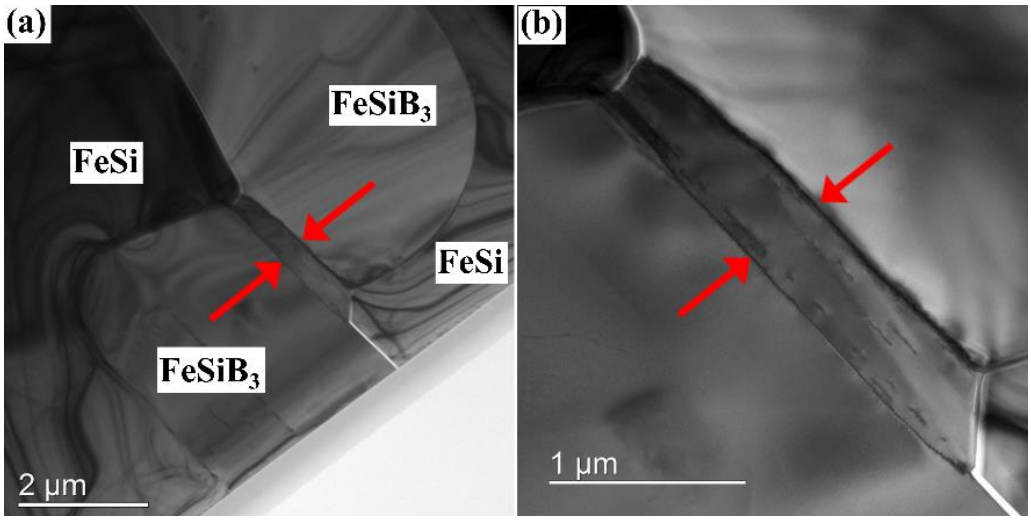

Figure 4-46 TEM images. (a) in low magnification; (b) in high magnification. Red arrows point at low angle grain boundaries inside the $FeSiB_3$ phase.

Figure 4-47 shows the electron diffraction patterns from the $FeSiB_3$ phase. It should be noted that the three $FeSiB_3$ phases have the same crystal structure (**Figure 4-46**a). The two-electron diffraction

patterns in **Figure 4-47**a and b are indexed according to an orthorhombic unit cell with the following unit cell parameters: a = 4.88 Å, b = 10.22 Å, and c = 5.91 Å, in which Å is a unit of length to 10^{-10} m. The electron diffraction pattern in **Figure 4-47**a is from the [001] zone axis. It means that the electron beam is parallel to the [001] direction. The electron diffraction pattern in **Figure 4-47**b is from the [$\bar{1}$ 01] zone axis. Both diffraction patterns are indexed with Miller indices for the central reflections.

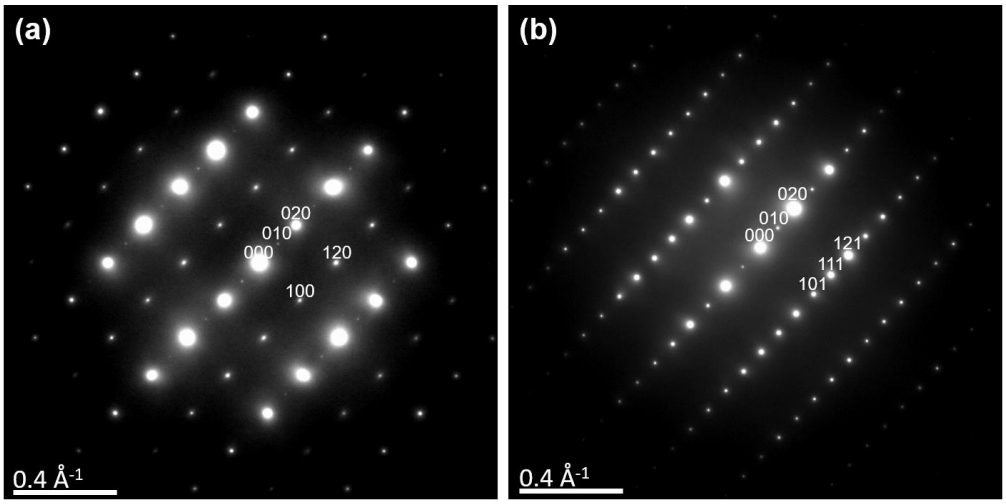

Figure 4-47 $FeSiB_3$ phase electron diffraction patterns. (a) [001]; (b) [$\bar{1}$ 01].

Figure 4-48 shows the electron diffraction patterns from the FeSi phase. The electron diffraction pattern in **Figure 4-48**a is from the [1$\bar{1}$0] zone axis. The electron diffraction pattern in **Figure 4-48**b is from the [1$\bar{1}\bar{1}$] zone axis. Both patterns are indexed according to a primitive cubic unit cell with the following lattice parameter: a = 4.48 Å. This is in good accordance with the published data [118].

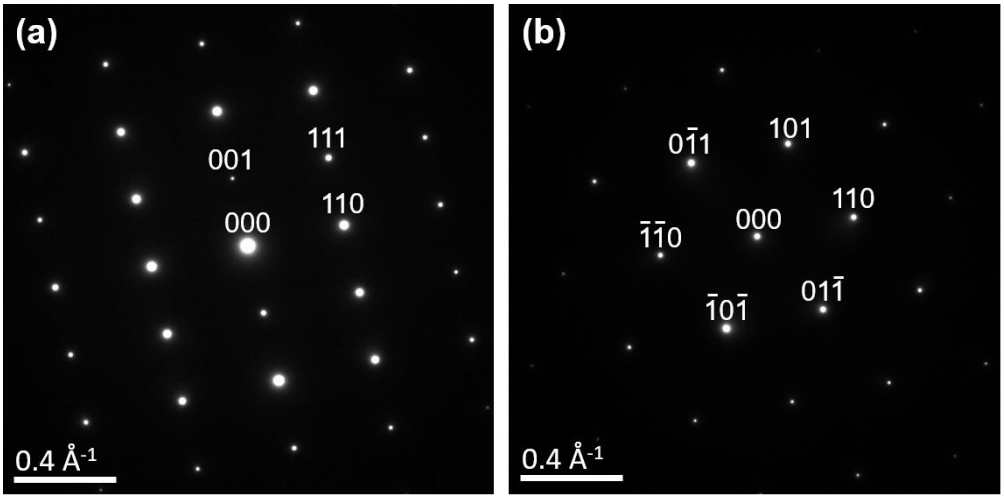

Figure 4-48 FeSi phase electron diffraction patterns. (a) [1$\bar{1}$0]; (b) [1$\bar{1}\bar{1}$].

4.2.3. Wetting of the Fe-26Si-9B alloys on the graphite, SiC, Al_2O_3, Si_3N_4, and h-BN substrates

In this part, the wetting behaviors of Fe-26Si-9B alloy on various refractory materials are summarized. Five refractory materials were used as the substrates in the wetting tests: graphite, SiC, Al_2O_3, Si_3N_4, and h-BN. The equilibrium contact angles of Fe-26Si-9B alloy on different substrates were measured based on the recorded images in the wetting test. The volume change of the Fe-26Si-9B alloys during solidification process was calculated. The surface morphologies of the droplets were observed by SEM. Moreover, the microstructures in the cross-section of the Fe-26Si-9B alloy/refractory material systems were studied by SEM and EPMA, aiming to investigate their interactions. Besides, four conditions were applied in the wetting experiments, under 1 bar Ar flow and the vacuum of 10^{-4}, 10^{-5}, and 10^{-9} atm.

Graphite and SiC

The wetting behavior of the Fe-26Si-9B alloy on the graphite substrate was investigated. Four wetting tests were performed in the SDF-2 furnace under various conditions at FRI (Krakow). It includes two procedures, contact heating and capillary purification heating, and two atmospheres, 10^{-5} and 10^{-9} atm. By using the contact heating technique, the Fe-26Si-9B particle was placed on the graphite substrate and then was heated up to 1250 ºC in the vacuum of 10^{-5} and 10^{-9} atm, in which the initial stage of the wetting process was absent or obscured by the melting process. The capillary purification heating technique is also named dispensed drop technique. It allows non-contact heating by squeezing the liquid Fe-26Si-9B alloy through a hole in a h-BN capillary, in which the processes of melting and spreading are separated and fully isothermal experiments are carried out. It should be noted that the vacuum was kept before 800 ºC in the heating process, and the static Ar was introduced to the furnace at the temperatures from 800 ºC and up to 1250 ºC.

Figure 4-49 shows the morphologies at the surface of the Fe-26Si-9B/graphite system after solidification under four conditions, in which the conditions are the contact heating process under 10^{-5} atm (**Figure 4-49**a), the capillary purification process under 10^{-5} atm (**Figure 4-49**b), the contact heating process under 10^{-9} atm (**Figure 4-49**c), and the capillary purification process under 10^{-9} atm (**Figure 4-49**d), respectively. It is seen that three distinct areas were observed in the SEM images: the surface of the Fe-26Si-9B alloy, the transition area, and the surface of the graphite substrate. Some crack lines existed on the surface of the Fe-26Si-9B alloys, while others separated the Fe-26Si-9B alloys and transition areas.

The phases formed on the surface of the Fe-26Si-9B/graphite couple were confirmed by the EDS point analysis, as shown in **Figure 4-50**a-d. The analyzed results show that the formed phases were the same in the transition areas, FeB, FeSi, and $FeSiB_3$. However, FeSi and SiB_3 covered the surface of the Fe-26Si-9B alloys.

Compared to the images in **Figure 4-49** and **Figure 4-50**. It seems that the heating process and the

vacuum level are independent of the morphologies and phases formed in the Fe-26Si-9B/graphite system. FeSi, FeB, $FeSiB_3$, and SiB_3 phases were formed at the surface of the Fe-26Si-9B alloy.

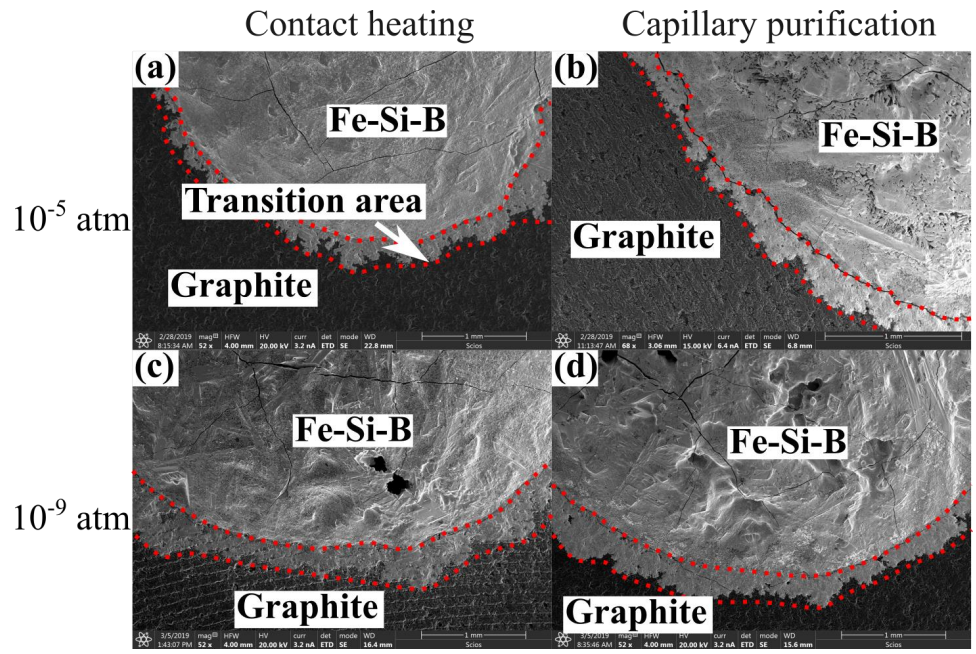

Figure 4-49 The surface of the Fe-26Si-9B/graphite system after solidification. (a) Contact heating, 10^{-5} atm; (b) Capillary purification, 10^{-5} atm; (c) Contact heating, 10^{-9} atm; (d) Capillary purification, 10^{-9} atm;

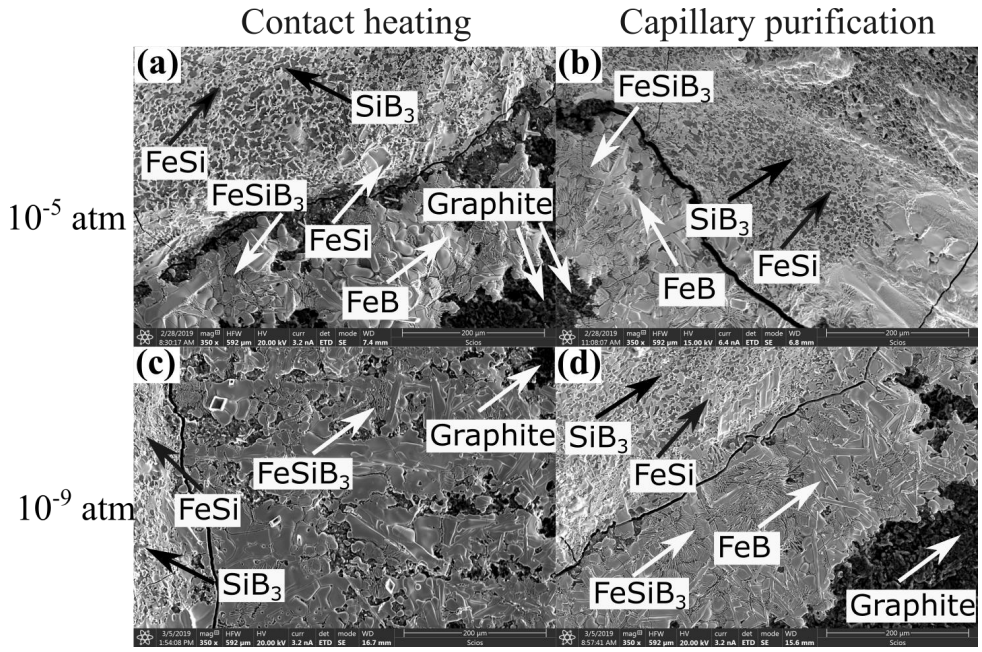

Figure 4-50 Phases formed at the surface in the Fe-26Si-9B/graphite system after solidification. (a) Contact heating, 10^{-5} atm; (b) Capillary purification, 10^{-5} atm; (c) Contact heating, 10^{-9} atm; (d) Capillary purification, 10^{-9} atm.

The elemental distributions at the interface were presented in **Figure 4-51** and **Figure 4-52**, in which the cross-sections of the Fe-26Si-9B/graphite system were obtained in the capillary purification and in the contact heating tests under 10^{-5} atm, respectively. It is seen that the Si, B, and Fe have slightly penetrated into the graphite substrate. The formed phases at the interface were confirmed based on the X-ray mapping and WDS point analysis. It is seen from **Figure 4-53**a that the FeSi, FeB, SiB_3, and $FeSiB_3$ were produced in the Fe-26Si-9B alloy, in which FeSi and FeB were not distinguished directly by color. The separate phases of FeSi and FeB are shown in **Figure 4-53**b in high contrast. It seems that FeSi and FeB were the precipitated phases during cooling, and the eutectic phases were FeSi and $FeSiB_3$. A continuous SiC layer was formed between the Fe-26Si-9B alloy and graphite. Moreover, FeB and SiC were formed in the graphite substrate. No oxide was formed in the Fe-26Si-9B alloy and in the graphite.

Figure 4-54 shows the images in the transition area of the Fe-26Si-9B in the contact heating test under 10^{-9} atm. It is seen from the high magnification image (**Figure 4-54**c) that the main phase was FeSi. FeB and SiB_3 in the transition area.

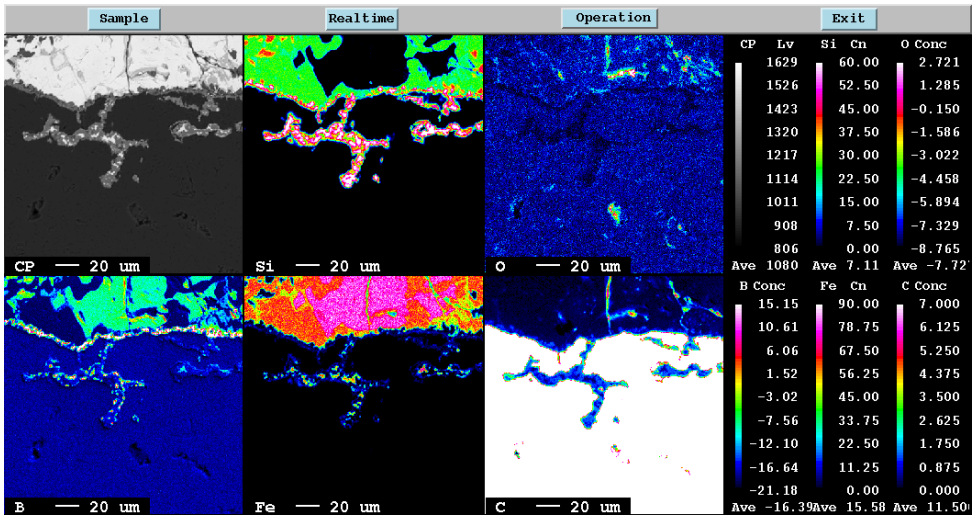

Figure 4-51 EPMA mapping image of the cross-section of the Fe-26Si-9B/graphite after solidification in the capillary purification test under 10^{-5} atm.

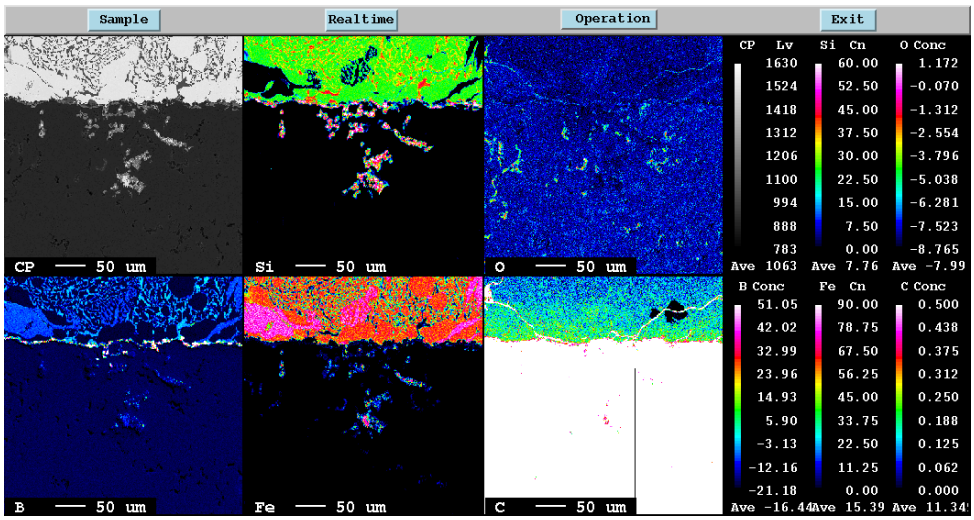

Figure 4-52 EPMA mapping image of the cross-section of the Fe-26Si-9B/graphite after solidification in the contact heating process under 10^{-5} atm.

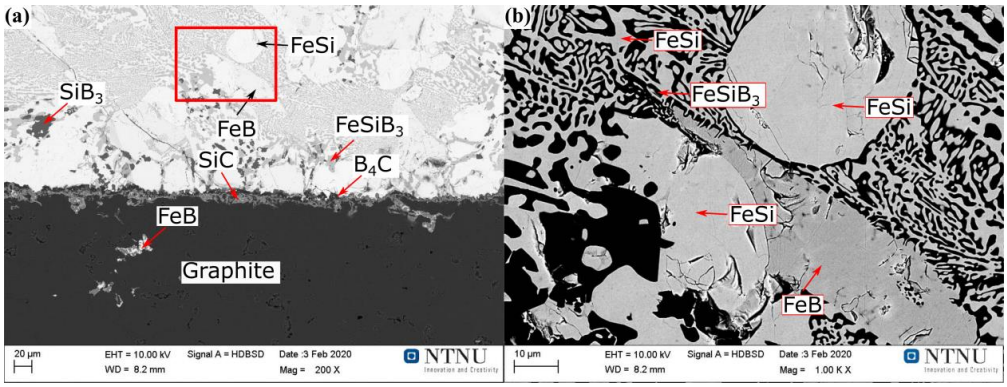

Figure 4-53 BSE images of the Fe-26Si-9B/graphite interfacial area after solidification in the contact heating process under 10^{-9} atm. (a) 200X; (b) 1000X.

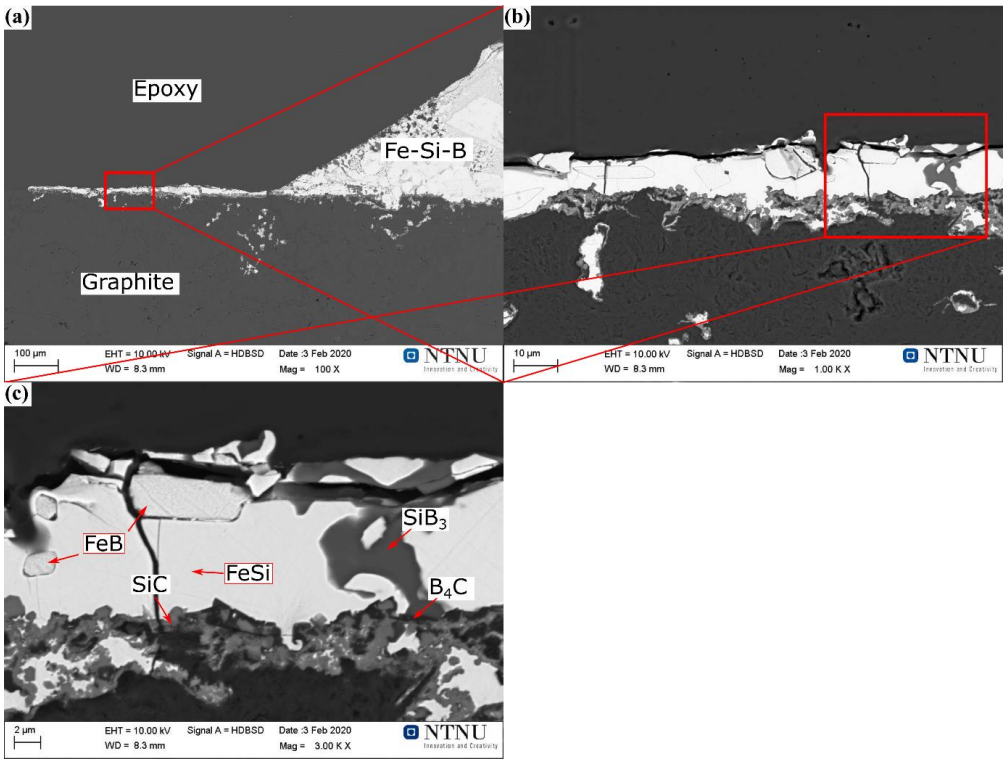

Figure 4-54 BSE images in the transition area of the Fe-26Si-9B in the contact heating process on the graphite under 10^{-9} atm. (a) 100X; (b) 1000X; (c) 3000X.

The vertical penetration depth to graphite was investigated based on the images taken from the three phases contact area in the Fe-26Si-9B/graphite system, as shown in **Figure 4-55**a-d. The red rectangle areas represent the lateral penetration area. However, the width of the lateral penetration from liquid Fe-26Si-9B alloy to graphite cannot be determined based on the image in the figure, due to the inconsistent width in the transition area (as shown in **Figure 4-49**). Moreover, the elemental distributions of Si, O, B, Fe, and C were analyzed in the area close to the three phases contact area, as shown in **Figure 4-56**-**Figure 4-59**. The EPMA mappings correspond well to the results in **Figure 4-51** and **Figure 4-52** that Si, B, and Fe penetrated to the graphite and spread on the surface of the graphite. However, the spread of the liquid Fe-26Si-9B alloy to the graphite surface was limited by the interfacial reaction in the heating process.

The maximum penetration depth of the liquid Fe-26Si-9B alloy into graphite in the transition and interface position is presented in **Figure 4-60**. It is seen that the penetration depth was similar in the interface and transition area under contact heating, which was lower than 100 µm. When it is transferred to the capillary purification process, the penetration depth in the interface area was higher than in the transition area. It shows that the capillary purification process would promote the penetration from the liquid Fe-26Si-9B alloy to the graphite at the interface. In addition, the penetration depth was independent of the degree of vacuum in the system.

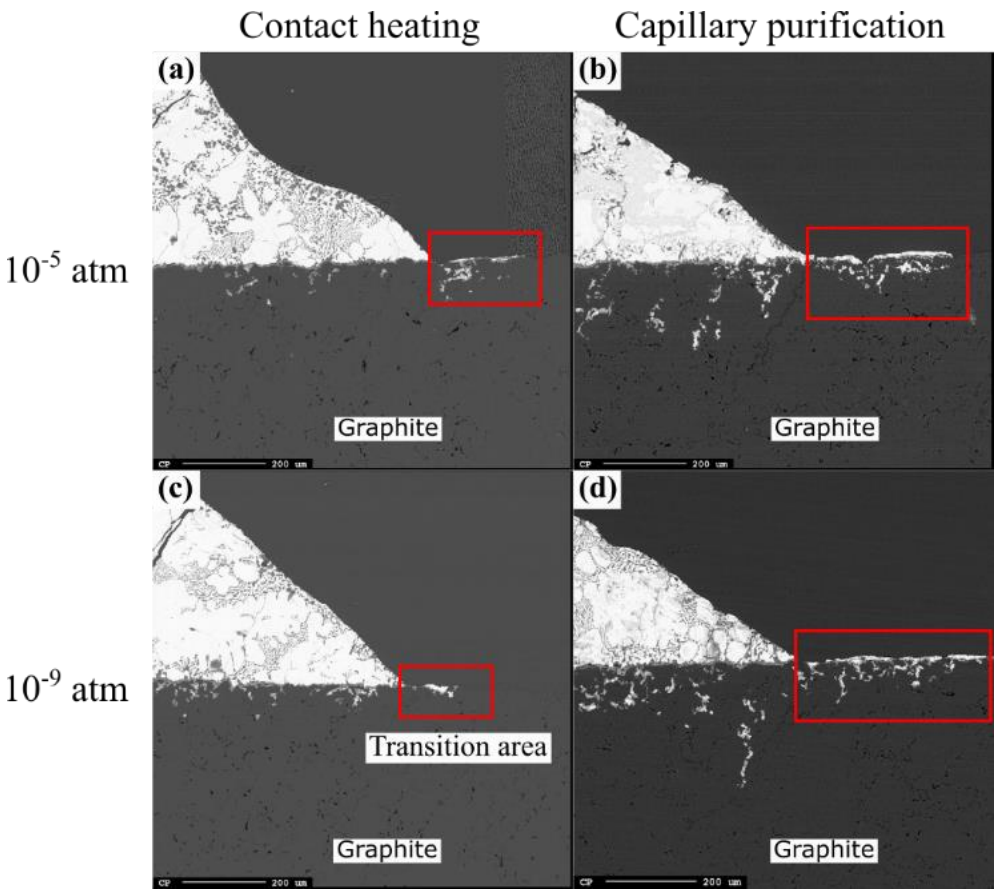

Figure 4-55 EPMA images of the cross-section of the Fe-26Si-9B/graphite. (a) Contact heating, 10^{-5} atm, (b) Capillary purification, 10^{-5} atm, (c) Contact heating, 10^{-9} atm, (d) Capillary purification, 10^{-9} atm.

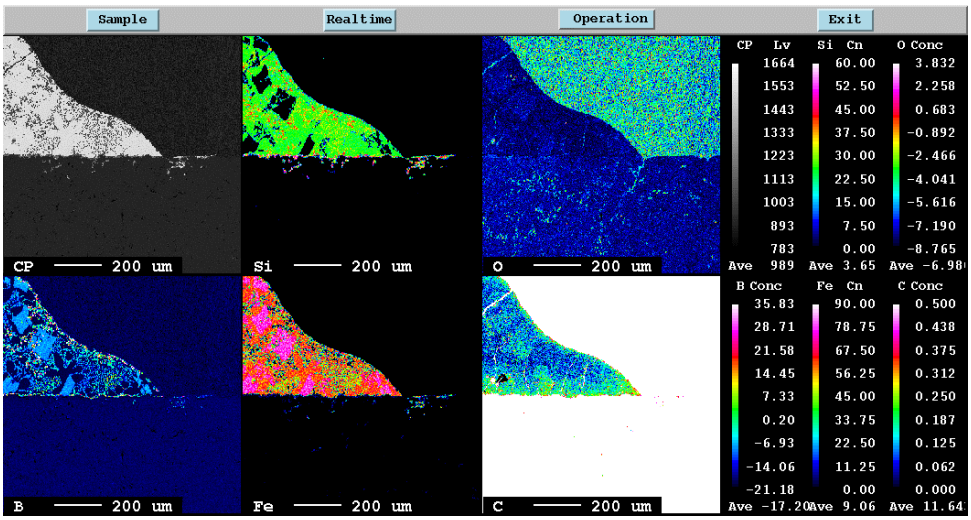

Figure 4-56 EPMA mapping image of the cross-section of the Fe-26Si-9B/graphite after solidification in the contact heating process under 10^{-5} atm.

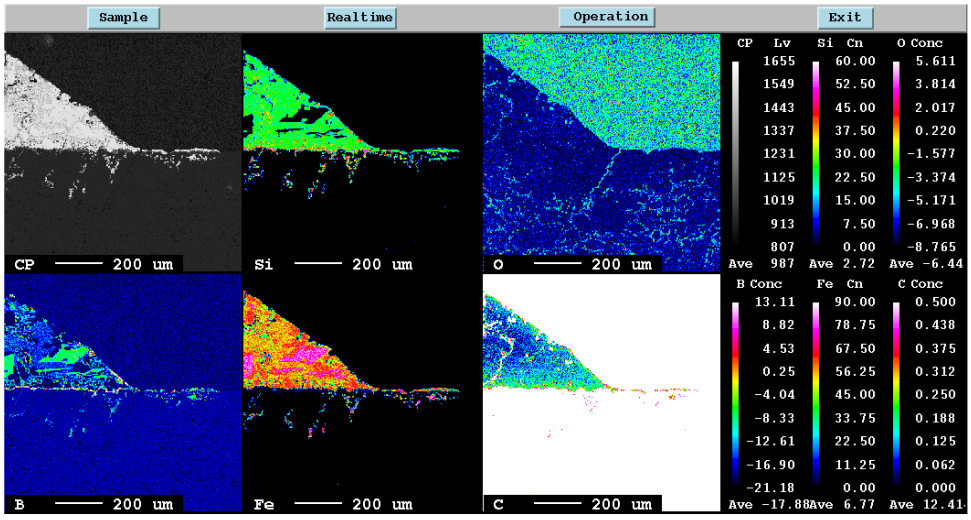

Figure 4-57 EPMA mapping image of the cross-section of the Fe-26Si-9B/graphite after solidification in the capillary purification process under 10^{-5} atm.

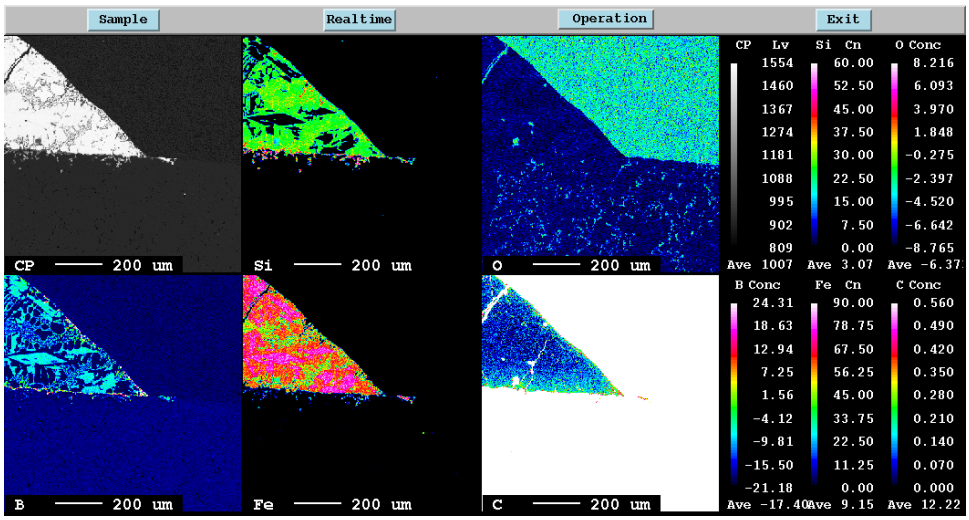

Figure 4-58 EPMA mapping image of the cross-section of the Fe-26Si-9B/graphite after solidification in the contact heating process under 10^{-9} atm.

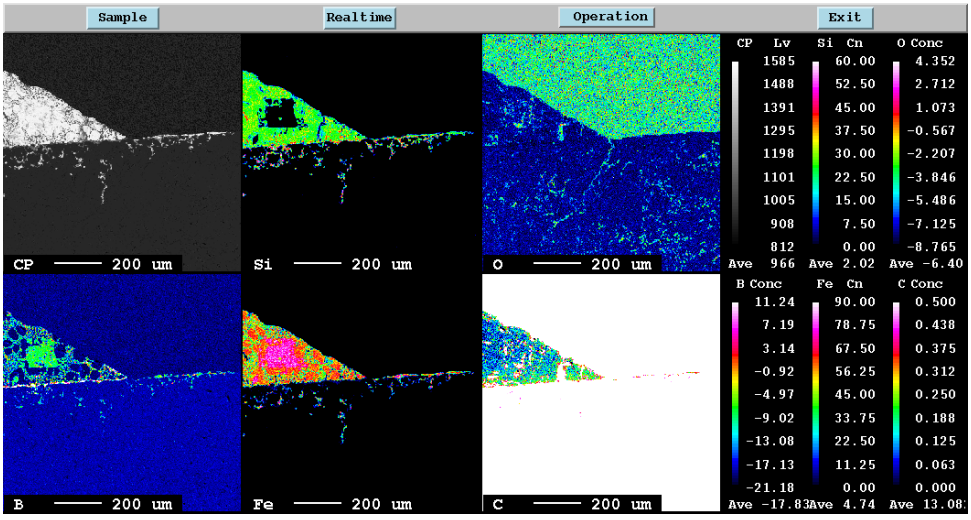

Figure 4-59 EPMA mapping image of the cross-section of the Fe-26Si-9B/graphite after solidification in the capillary purification process under 10^{-9} atm.

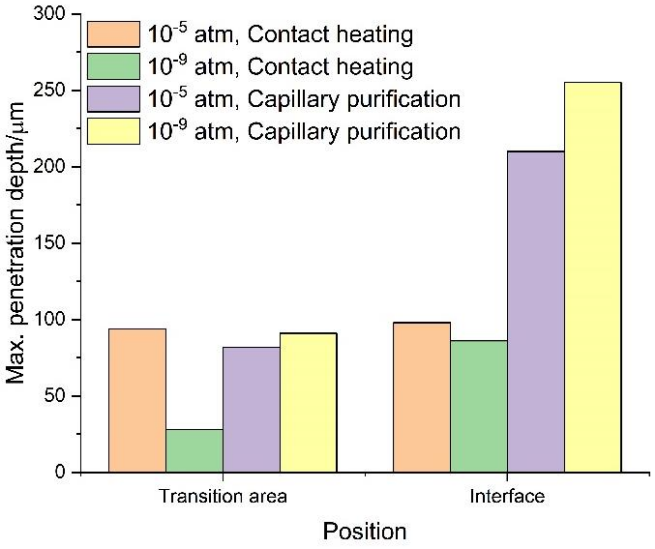

Figure 4-60 The comparison of the maximum penetration depth of liquid Fe-26Si-9B alloy in the transition and interface position.

The wetting kinetics curves calculated for the Fe-26Si-9B alloy with the graphite substrates under four conditions are shown in **Figure 4-61**a-d. **Figure 4-61**a shows the plots of the contact angle as a function of exposure time in the contact heating process under 10^{-5} atm. It is seen that the Fe-26Si-9B particle was completely melted at 1221 ºC with corresponding the initial contact angle of 138º, which was the contact angle on the unreacted graphite substrate. During further heating up to 1250 ºC, the contact angle values rapidly decreased to 89º. Then, in the first cycle, the contact angle had a continuous decrease. In the second cycle, the contact angle was maintained at the level of 48º at 1250 ºC. The chemical equilibrium between the liquid Fe-26Si-9B alloy and the formed SiC layer was achieved. If we move to the spreading kinetics obtained in the contact heating process under 10^{-9} atm (**Figure 4-61**c), it shows that the initial contact angle was decreased to ~ 90º after complete melting at 1240 ºC, compared to the initial value of 138º under 10^{-5} atm. The spreading time was similar under two different vacuum conditions in the heating process. The equilibrium state was obtained at the beginning of the second cycle. In addition, the relatively large scatter of the contact angles was measured in the wetting process under 10^{-5} atm and 10^{-9} atm.

Figure 4-61b and d show the kinetics curves obtained from the capillary purification under 10^{-5} atm and 10^{-9} atm. The initial contact angle was measured to be the same value of ~ 136º, regardless of the degree of vacuum. However, the spreading rate to the equilibrium state was faster under 10^{-9} atm at the cost of 15 min than under 10^{-5} atm at the cost of 20 min. The contact angles were relatively stable in the wetting process under the capillary purification. It indicates that the C to SiC transformation is faster to reach equilibrium in a high vacuum atmosphere.

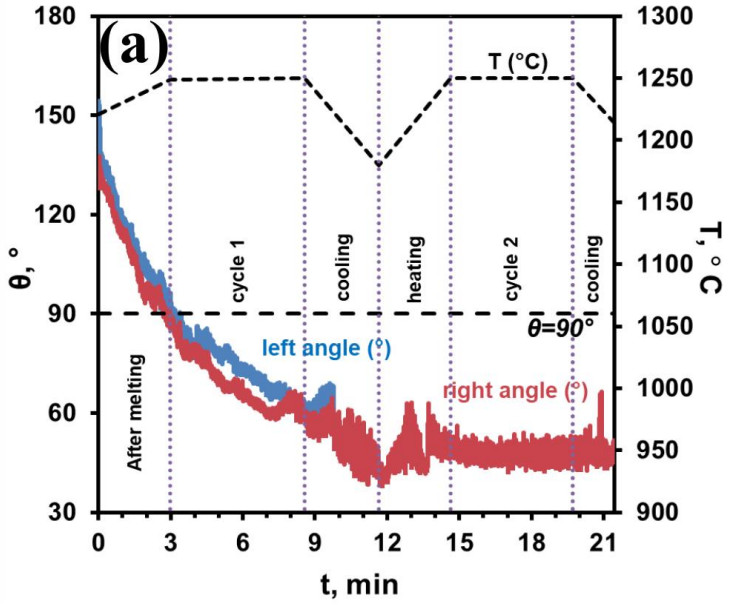
(a)
T (°C)
θ, °
T, °C
cycle 1
cooling
heating
cycle 2
cooling
After melting
θ=90°
left angle (°)
right angle (°)
t, min

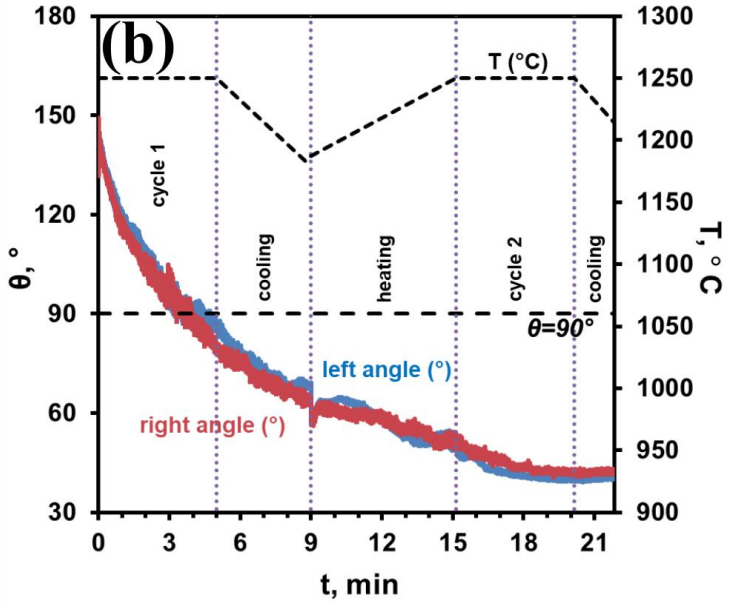
(b)
T (°C)
θ, °
T, °C
cycle 1
cooling
heating
cycle 2
cooling
θ=90°
left angle (°)
right angle (°)
t, min

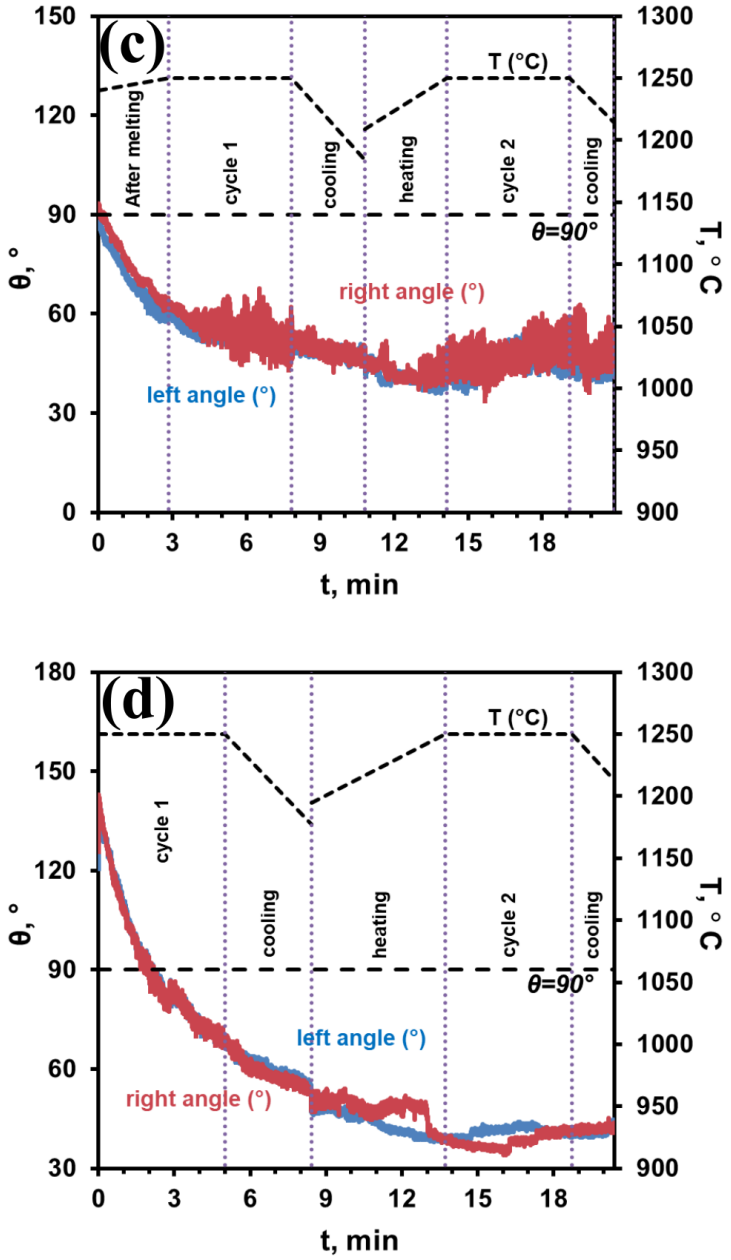

Figure 4-61 The relationship between the contact angle and time. (a) Contact heating, 10^{-5} atm; (b) Capillary purification, 10^{-5} atm; (c) Contact heating, 10^{-9} atm; (d) Capillary purification, 10^{-9} atm.

The following wetting tests of the Fe-26Si-9B alloys on the graphite substrates were performed in the SDF-1. **Figure 4-62** presents the wetting process of the Fe-26Si-9B alloy on the graphite substrate under

10^{-4} atm, in which the Fe-26Si-9B particle was milled to powder before the wetting test. It is seen that the Fe-26Si-9B powder started to melt at 1220 °C and was completely melted at 1350 °C. Then, the shape of the alloy was not changed with the increase of temperature to 1450 °C. It shows a good wetting with graphite. The equilibrium contact angle was measured to be 31°.

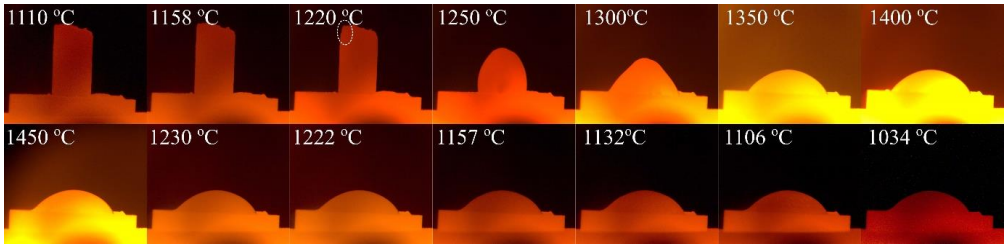

Figure 4-62 Images of the Fe-26.38Si-9.35B powder on the graphite substrate after heating to 1450 °C under 10^{-4} atm.

Some challenges were occurred at the beginning of the wetting tests, in which the maximum temperature and the atmosphere affected the wetting results. **Figure 4-63**a shows the Fe-26Si-9B alloy on the graphite substrate after heating to 1250 °C under Ar flow. It is seen that the shape of the Fe-26Si-9B particle was not changed. The particle was not melted at temperatures up to 1250 °C, which was higher than the measured melting point of 1220 °C. The morphology at the surface of the Fe-26Si-9B particle was studied by SEM, and the results are shown in **Figure 4-63**b. In the high magnification state, it is seen that two distinct areas were observed: needle-like and spherical crystals. Then, the chemical compositions were analyzed by EDS. The average results in area 1 and area 2 are listed in **Table 4-4**, in which area 1 represents the spherical area and area 2 represents the needle-like area. The analyzed results show that the composition of B and C were high in both areas. The phases formed in the top area might be B_4C. It might be caused by a leakage in the furnace, leading to small parts of O_2 present. Then, the O_2 would react with graphite to generate CO gas, which would react with the Fe-26Si-9B alloy to form the B_4C layer on the surface.

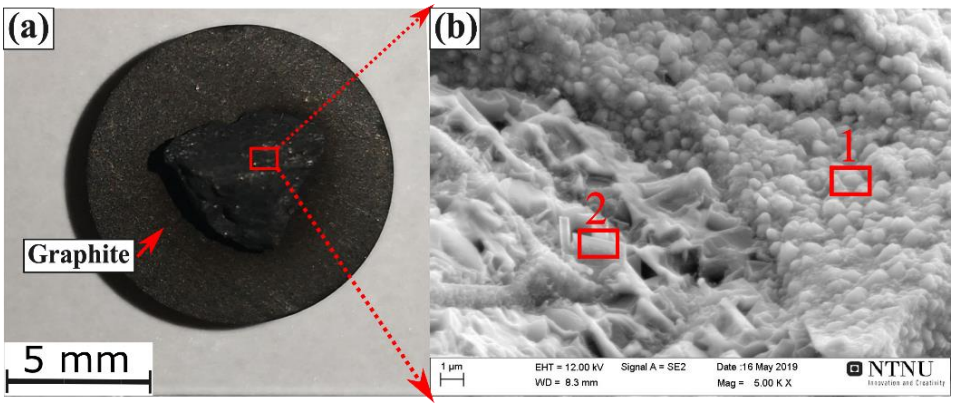

Figure 4-63 (a) The solidified Fe-26Si-9B droplet on the graphite substrate after heating to 1250 °C under Ar; (b) SEM image obtained from the surface of the solidified Fe-26Si-9B alloy. Red rectangle area of 1 and 2 represent the EDS point analysis area.

Table 4-4 EDS results of the 2 different areas at the surface of the Fe-Si-B/graphite system under Ar [at.%].

Area	B	C	O	Fe	Si
1	56	28	11.6	0.7	2.1
2	70	21	6.4	0.6	1.2

As the Fe-26Si-9B particle was not melted up to 1250 ºC, the maximum temperature was increased to 1550 ºC in the next wetting test under Ar flow. The wetting process is shown in **Figure 4-64**. It is seen from the figure that the particle started to melt at 1421 ºC. Then, the shape of the particle was changed with the increasing temperature. At the highest temperature of 1550 ºC, the Fe-26Si-9B alloy was wrapped by the formed layer. It showed a non-wetting behavior between the Fe-26Si-9B alloy and the graphite. Compared with **Figure 4-63**a and **Figure 4-64**, the formed layer might be the B_4C layer.

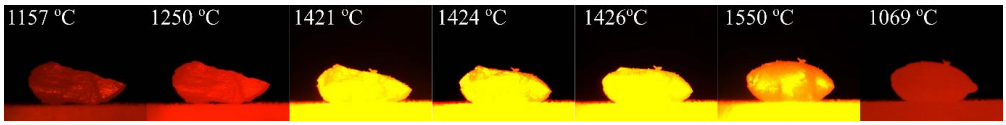

Figure 4-64 Images of Fe-26.38Si-9.35B particle on the SiC substrate after heating to 1550 ºC under Ar.

Al_2O_3

The wetting behavior of the Fe-26Si-9B alloy on the Al_2O_3 substrate was investigated by the present author and later reported by Grorud [15]. Two wetting tests were performed on Al_2O_3 substrates under 10^{-4} atm. One was heated to 1550 ºC on the Al_2O_3-1 substrate and another was heated to 1300 ºC on the Al_2O_3-2 substrate. The wetting processes are presented in **Figure 2-53**. The results show that the equilibrium contact angle between the Fe-26Si-9B alloy and Al_2O_3 was ~ 120º. At present, the wetting on Al_2O_3-1 is used to investigate the interaction between the Fe-26Si-9B alloy and Al_2O_3. The sample was oscillating in the temperature range 1450-1550 ºC during the wetting process, as shown in **Figure 4-65**. The liquid Fe-26Si-9B drop moved in the right direction on the Al_2O_3 from 1420 ºC to 1510 ºC, where the dotted curve lines present the original position at 1400 ºC. Simultaneously, the diameter of the liquid Fe-26Si-9B drop was decreased to $0.9d_0$ at 1510 ºC from the original value of d_0 at 1400 ºC. It shows that gas was released at the three phases contact area. At room temperature, a corrosion area was observed on the Al_2O_3 substrate, as shown in **Figure 4-66**a. Then, the microstructures in the cross-sectional part of the Fe-26Si-9B/Al_2O_3 droplet was observed by SEM, as shown in **Figure 4-66**b. No Al-based phase was detected in the Fe-26Si-9B alloy. Simultaneously, a line scan was performed from the Fe-26Si-9B alloy to the Al_2O_3 substrate based on the red line in **Figure 4-66**b. The result is shown in **Figure 4-67**. As the sample was C sputtered before the SEM characterization, the detection of C is negligible. What is interesting about the result in **Figure 4-67** is that no penetration was detected from the liquid Fe-26Si-9B alloy to the Al_2O_3 substrate.

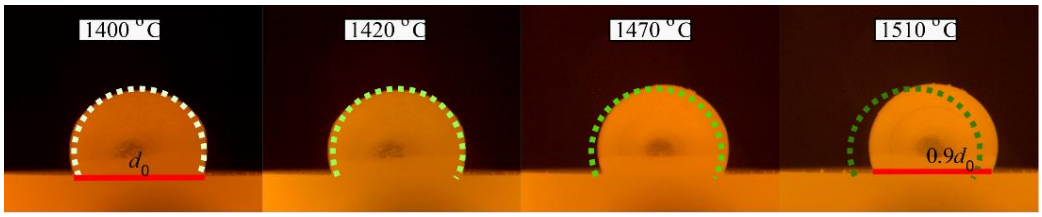

Figure 4-65 Images of the Fe-26Si-9B particle on the Al_2O_3 substrate in the heating process from 1400 °C to 1510 °C under 10^{-4} atm [15].

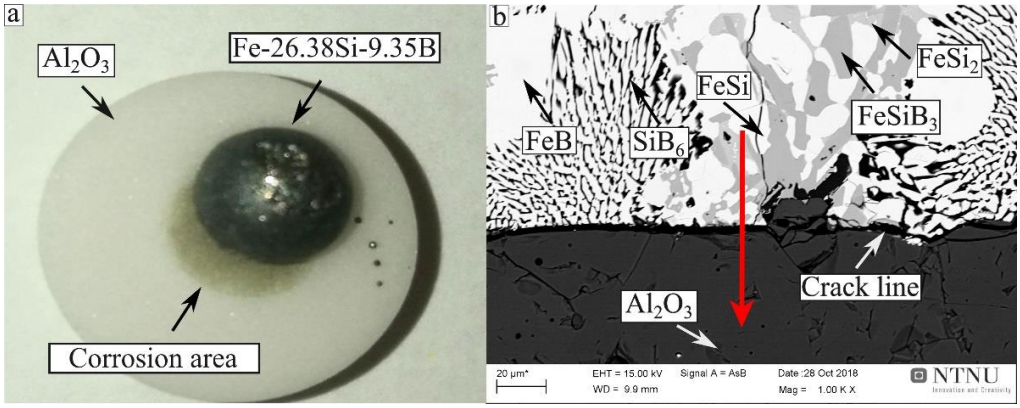

Figure 4-66 (a) Macroscopic images of the Fe-26.38Si-9.35B droplet/Al_2O_3 after the wetting test [15]; b) The interface between Fe-26.38Si-9.35B droplet and Al_2O_3 substrate.

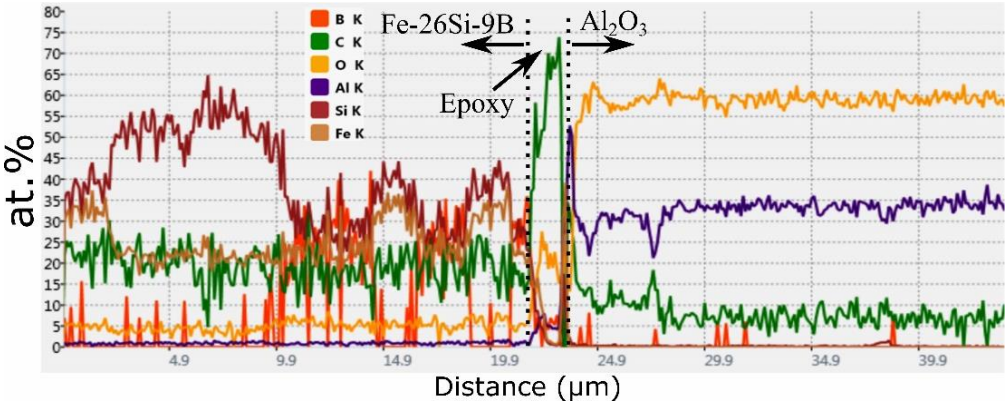

Figure 4-67 EDS line scan from Fe-26.38Si-9.35B droplet to Al_2O_3 substrate.

Figure 4-68 presents the wetting process of the Fe-26Si-9B alloy on the Al_2O_3 substrate with heating to 1350 °C under 10^{-4} atm, in which the Fe-26Si-9B powder was used in the wetting test. It is seen from the wetting process that the Fe-26Si-9B alloy started to melt at 1223 °C and was completely melted at 1227 °C. The equilibrium contact angle was measured to be 120°. The oscillation phenomenon was not observed in this wetting process. Moreover, in the wetting test of the Fe-26Si-9B alloy on the Al_2O_3-2 substrate (**Figure 2-53**), Grorud [15] also did not observe the oscillation phenomenon after heating to 1300 °C. Hence, it seems that the oscillation would happen at temperatures higher than 1450 °C.

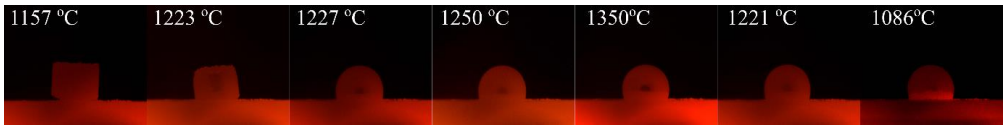

Figure 4-68 Wetting test of the Fe-26Si-9B powder on Al_2O_3 substrate under 10^{-4} atm.

Si_3N_4

The wetting behavior of the Fe-26Si-9B alloy on the Si_3N_4 substrate was investigated in the sessile drop furnace (SDF-1) under 10^{-4} atm. The pretreated Fe-26Si-9B particle was placed on the Si_3N_4 substrate and heated to 1350 °C. It is seen from **Figure 4-69** that the particle started to melt at ~1218 °C, and it was completely melted at 1250 °C. The function of the contact angle with time is plotted in **Figure 4-70**. The contact angle was constant within 20 min. Hence, the equilibrium contact angle was ~ 135°. The thermal cycle experiments of the Fe-26Si-9B alloy in Si_3N_4 crucibles have been described in subsection 4.2.2, in which the solidified Fe-26Si-9B alloy was easily taken out from the Si_3N_4 crucible. It corresponds well to the results obtained from the wetting test.

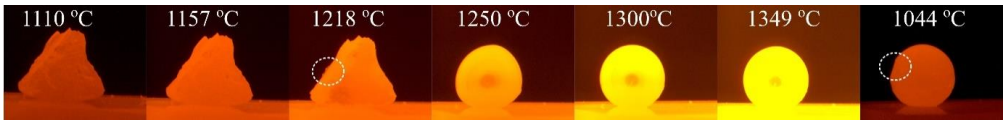

Figure 4-69 Images of Fe-26Si-9B particle on the Si_3N_4 substrate under 10^{-4} atm.

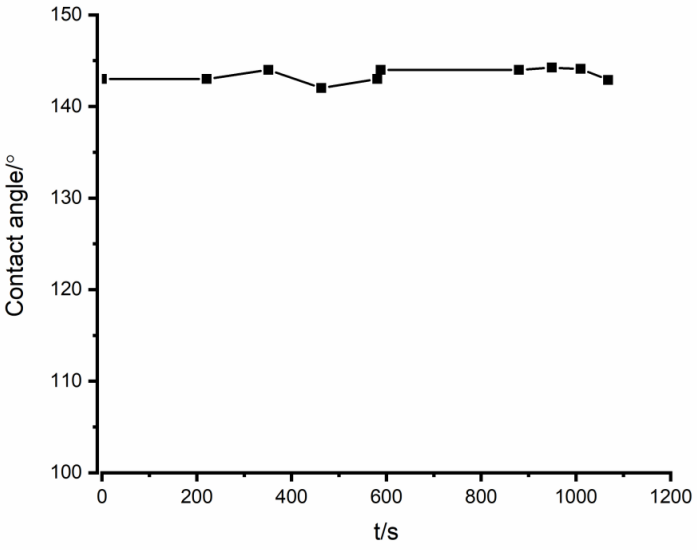

Figure 4-70 Contact angle as a function of time for the liquid Fe-26Si-9B alloy on the Si_3N_4 substrate after complete melting.

h-BN

Figure 4-71 provides the images of the Fe-26Si-9B alloy on the h-BN substrate that underwent three melting/solidification processes in the temperature range 1100-1550 ºC under 10^{-4} atm. It is seen that the Fe-26Si-9B particle started to melt at 1218 ºC and was completely melted at 1250 ºC in the first cycle. In the second cycle, it started to melt at 1221 ºC. **Figure 4-72** shows the contact angle as a function of temperature in the wetting process. The contact angle continued to be at ~ 142º in the first cycle. It was changed abruptly to 100º at 1468 ºC in the second cycle. Then, in the third cycle, it was again increased to 130º at 1477 ºC. Moreover, a slight vibration was observed in the whole process.

Figure 4-73 shows the images at 1446 ºC and 1447 ºC in the third cycle, where the contact angle was changed from 105º to 130º. Correspondingly, the contact area in the red rectangle at 1446 ºC was detached from the h-BN substrate. Then, the morphology of this contact area was analyzed by SEM, as shown in **Figure 4-74**. It is seen from the figure that the SiC particles were formed on the surface of the contact area.

BN

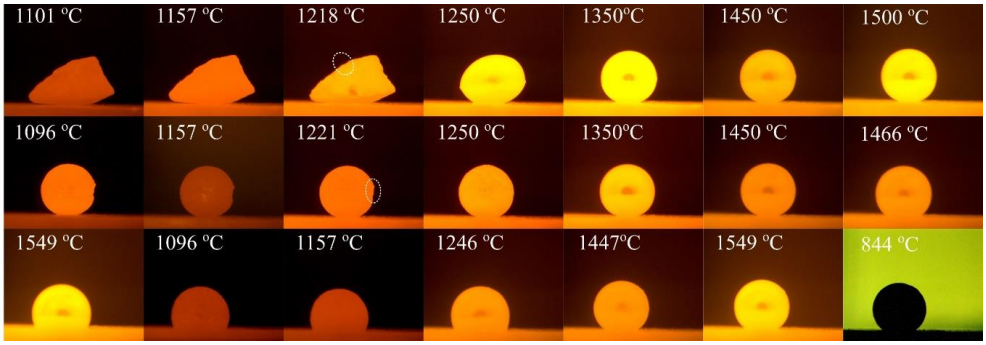

Figure 4-71 Images of Fe-26.38Si-9.35B alloy particle subjected to three thermal cycles on the h-BN substrate under 10^{-4} atm.

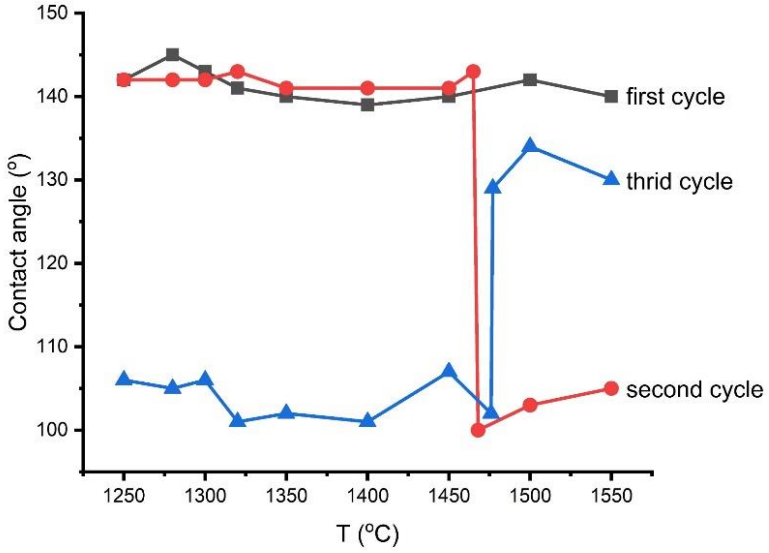

Figure 4-72 Contact angle as a function of temperature for the liquid Fe-26.38Si-9.35B alloy on the h-BN substrate in the three times melting/solidification process.

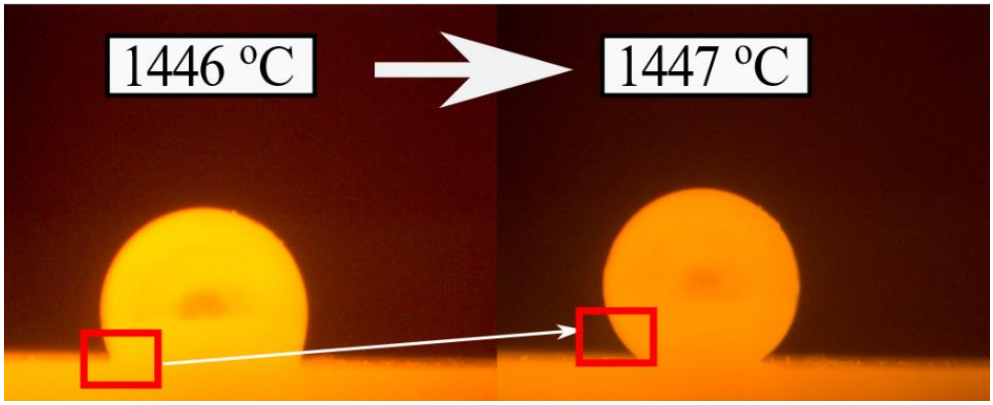

Figure 4-73 The images of the Fe-26Si-9B/h-BN system at 1446 °C and 1447 °C in the third cycle. Red rectangles represent the transition area.

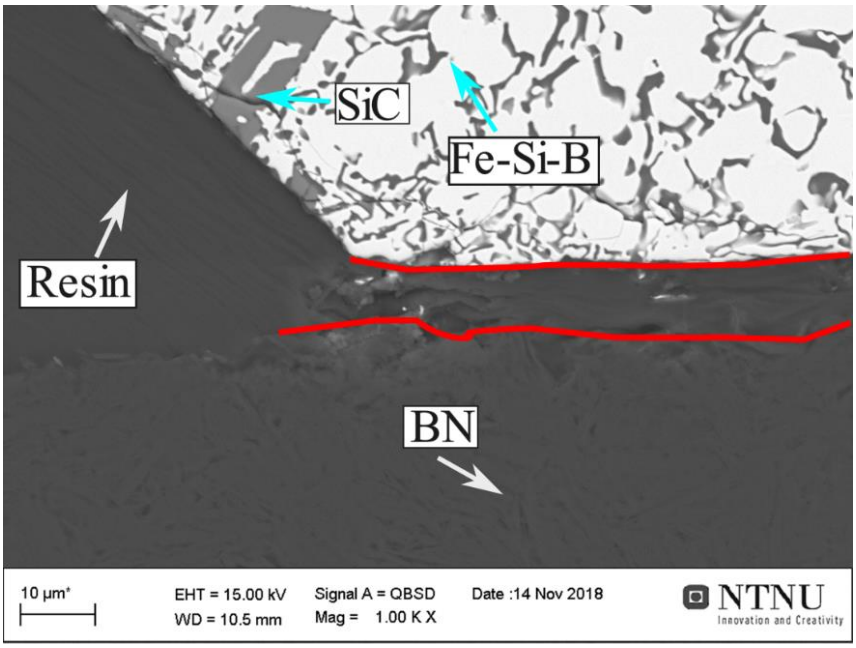

Figure 4-74 The interface between Fe-26.38Si-9.35B droplet and h-BN substrate.

Volume change in the Fe-26Si-9B alloys during solidification in the wetting tests

The relative area change of the cross section of the Fe-26Si-9B alloy was calculated based on the recorded images in the wetting tests during solidification, as shown in **Figure 4-75**. The black squares and gray triangles represent the relative area change during solidification on the Al_2O_3 (**Figure 4-68**) and Si_3N_4 (**Figure 4-69**), respectively. It should be noted that the measured melting temperature was ~ 1220 ºC in the wetting tests. To some extent, the area change represents the volume change in the wetting tests. It shows that the volume of the Fe-26Si-9B alloy continued to decrease with temperature drop in the solidification process. From 1350 ºC to 1220 ºC, the volume change was – 1.65 % on the Al_2O_3 and -0.89 % on the Si_3N_4. From 1220 ºC to ~ 1090 ºC, the volume change was ~ – 1.55 % on the Al_2O_3 and Si_3N_4. Considering the whole solidification process, the maximum volume change was in the range -2.44 - -3.2% from time reaching the liquidus point to the complete solidification. The calculated results show that the Fe-26Si-9B alloy would be shrink during solidification.

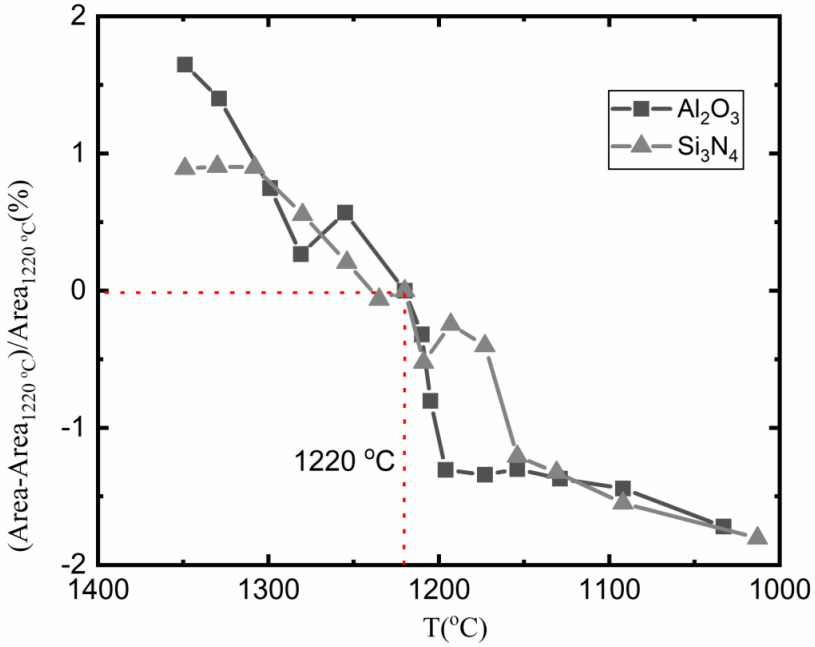

Figure 4-75 Relative area change (%) of the Fe-26Si-9B particle on the Al_2O_3 and Si_3N_4 substrates.

4.2.4. DSC measurements

In the DSC study, Fe-26Si-9B particles were pretreated in a 38% HF acid bath before the DSC tests to remove any possible oxide layer. Then, it was placed in an Al_2O_3 crucible and was heated to 1450 °C with a heating rate of 10 °C/min. A holding time of 5 min was kept at 1450 °C. Subsequently, it was cooled down to room temperature with 10 °C/min.

Figure 4-76-**Figure 4-78** provide the obtained DSC curve of the Fe-26Si-9B alloy, in which the relevant DSC tests were performed under Ar flow. It is seen from the three DSC curves that the measured liquidus and solidus temperatures in the heating step were similar. The onset of melting was ~ 1227 °C, while the end of melting was ~ 1270 °C.

The solidified samples are presented in **Figure 4-79** a-c. It is seen that the solidified Fe-26Si-9B alloy adhered to the Al_2O_3 wall in the DSC-57 test, while the alloys from the DSC-58 and DSC-59 tests were isolated in the Al_2O_3 crucible and these alloys were easily moved from the crucible. **Figure 4-80** a-d show the phases formed on the surface in the DSC-70 test. **Figure 4-80**a shows that the main phase was distributed to the grey area, which was confirmed to be FeSi (**Figure 4-80**b). The B_4C (black area) and oxide particles were also observed at the surface (**Figure 4-80**c and d). The Al_2O_3 particles were found in the large white particles, as shown in **Figure 4-80**d. However, the composition of the other oxide particles was complex. The average content of the oxide particles was 42 at.% O, 25at.% B, 11 at.% Fe, 20 at.% Al, and 3 at.% Si. It indicates that the oxide may consist of Fe_2O_3, Al_2O_3, and SiO_2. The results

show that a small number of oxide particles were formed at the surface of the Fe-26Si-9B particle. It indicates that oxides were formed on the surface of the Fe-26Si-9B alloys after DSC tests.

The value of heat of fusion was also measured based on the three DSC tests. The curve obtained from the DSC-69 test shows a lower heat of fusion at 536 J/g and lower heat of solidification at -546 J/g (**Figure 4-76**). However, the curves obtained from the DSC-70 and DSC-71 tests show the heat of fusion with 633 J/g and 551 J/g, and the heat of solidification with -696 J/g and -667 J/g. Moreover, it is found that the values of solidification heat were higher than the values of heat of fusion. This is lower than the theoretical value of 872 J/g calculated with FactSage based on the FTlite database (**Figure 4-85**).

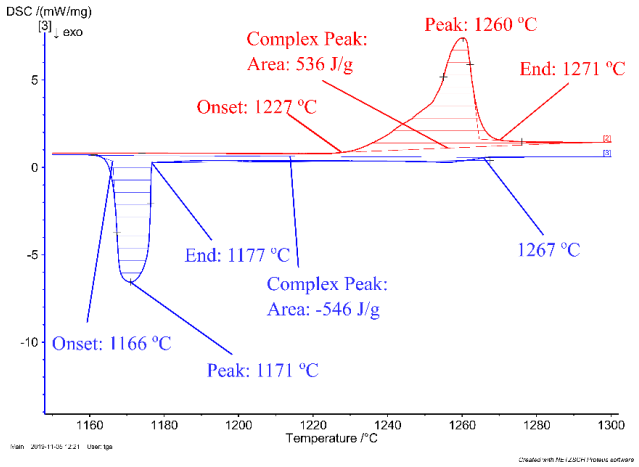

Figure 4-76 The part of the DSC curve for Fe-26Si-9B alloy under Ar. (**DSC-57**)

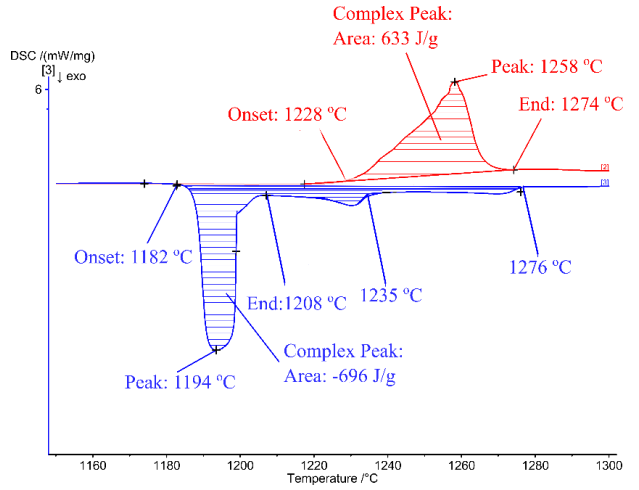

Figure 4-77 The part of the DSC curve for Fe-26Si-9B alloy under Ar. (**DSC-58**)

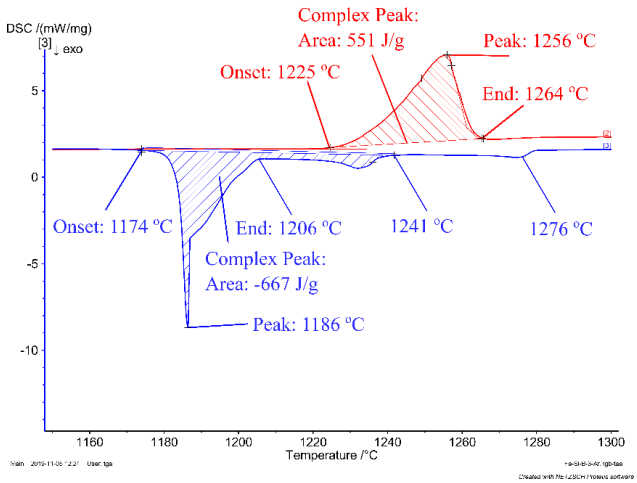

Figure 4-78 The part of the DSC curve for Fe-26Si-9B alloy under Ar. (**DSC-59**)

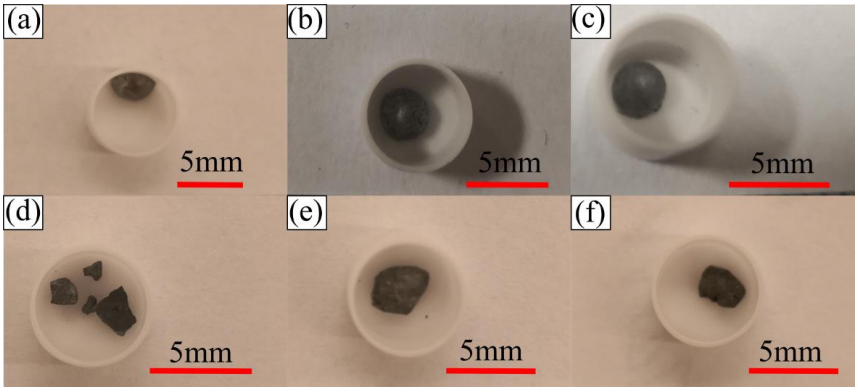

Figure 4-79 Views of Fe-26Si-9B samples after the DSC tests. (a) **DSC-57** under Ar; (b) **DSC-58** under Ar; (c) **DSC-59** under Ar; (d) **DSC-54** under N_2; (e) **DSC-55** under N_2; (f) **DSC-56** under N_2.

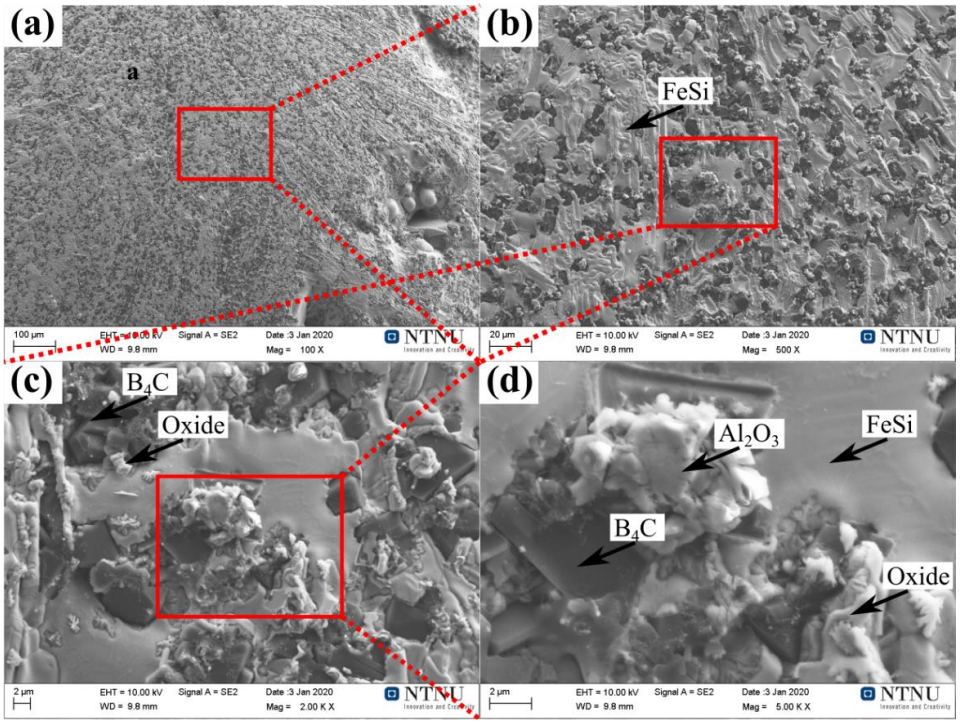

Figure 4-80 Top-view of the sample after **DSC-58** test under Ar. (a) 50X; (b) 500X; (c) 2000X; (d) 5000X.

Three DSC tests were first performed under N_2 flow. The solidified alloys were presented in **Figure 4-79** d-f. It is seen that the Fe-26Si-9B alloys were covered by a high temperature melting oxide layer, which blocked the complete melting of the alloy.

Figure 4-84 a and b show the microstructures at the surface in the DSC-56 test. A glass phase was formed and covered the surface. The chemical composition was analyzed in the three points and the results are listed in **Table 4-5**. It is seen that the glass phase consisted of the oxides, while the N content was not detected. Hence, the formed oxide layer resulted in the incomplete melting of the Fe-26Si-9B alloy in the wetting tests.

The obtained typical DSC curves are shown in **Figure 4-81**-**Figure 4-83**. It is seen that the onset of melting was ~ 1226 ºC and the end of melting was ~ 1266 ºC. In the cooling process, it started to solidify at ~ 1198 ºC and ended at ~ 1167 ºC. The melting temperature range of 1226-1266 ºC shows similar results in the DSC tests under Ar. When it turns to the fusion and solidification heat, it is seen that the measured heat of fusion was in the range 426-500 J/g in the heating process and the measured solidification heat was in the range -486 - -448J/g, which was lower than the measured values under Ar. It might be caused by the incomplete melting of the Fe-26Si-9B alloys.

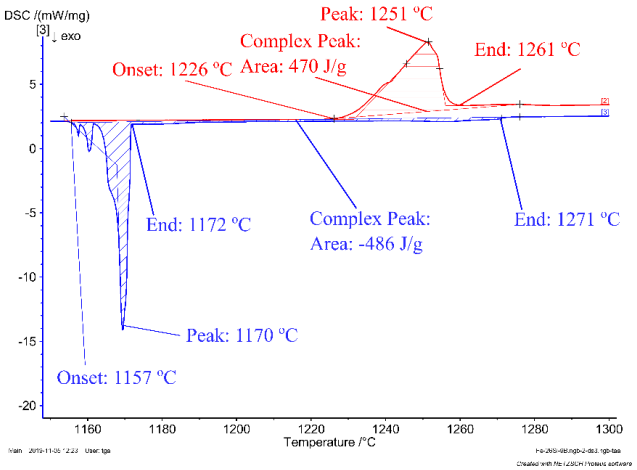

Figure 4-81 The part of the DSC curve for Fe-26Si-9B alloy under N_2. (**DSC-54**)

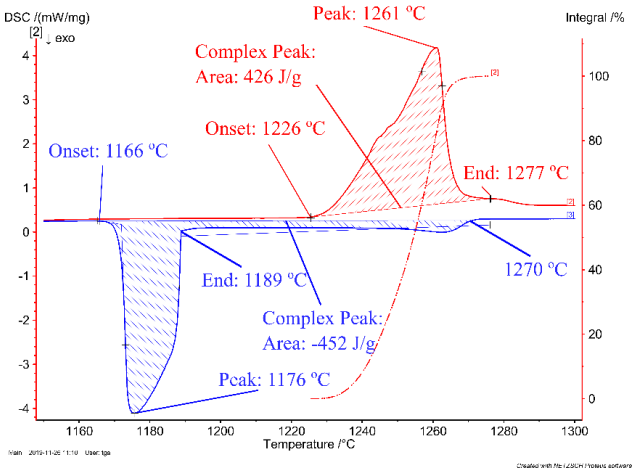

Figure 4-82 The part of DSC curve for Fe-26Si-9B alloy under N_2. (**DSC-55**)

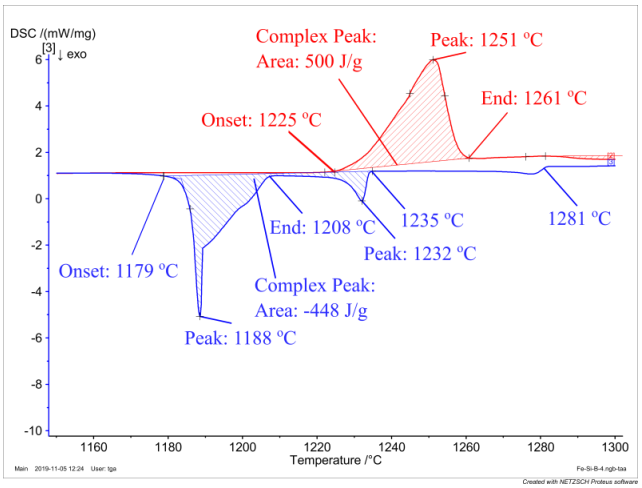

Figure 4-83 The part of DSC curve for Fe-26Si-9B alloy under N_2. (**DSC-56**)

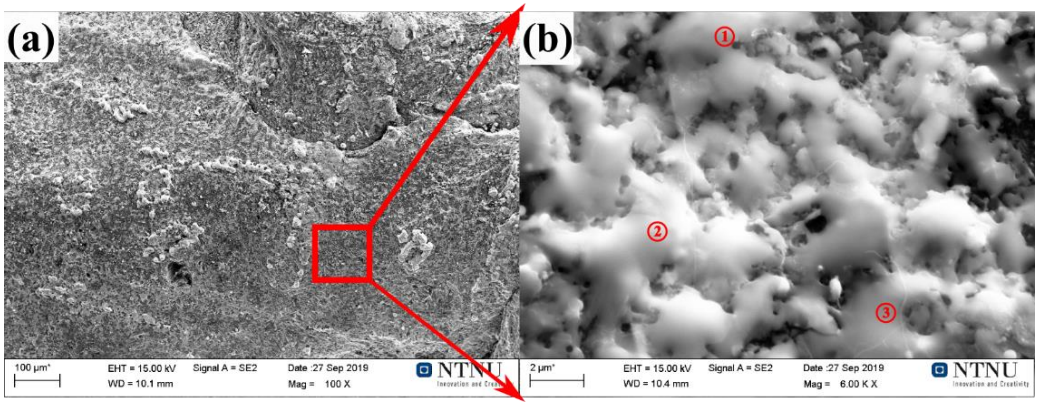

Figure 4-84 Top-view of the **DSC-56** under N_2. (a) 100X magnification; (b) 6000X magnification.

Table 4-5 EDS results of the 3 different points at the surface of the **DSC-56** under N_2 [at.%].

	N	O	Al	Si	Fe
1	2.1	46.8	14.9	22.2	14
2	0	59.5	15.4	16.9	5
3	0	63.6	14	12.4	0.6

Compared to the results obtained from the DSC-54 to DSC 59 test, the Fe-26Si-9B alloy started to melt at ~ 1226 ºC and completely melted at ~ 1268 ºC. The heat of fusion is in the range of 551-633 J/g and the heat of solidification is in the range of -696 - -667 J/g, which is lower than the predicted value of 872 J/g (**Figure 4-85**). The atmosphere was different in the calibration experiments (N_2) and in our DSC experiments (Ar) and may have affected the results. All the measured data are summarized in **Table 4-6**.

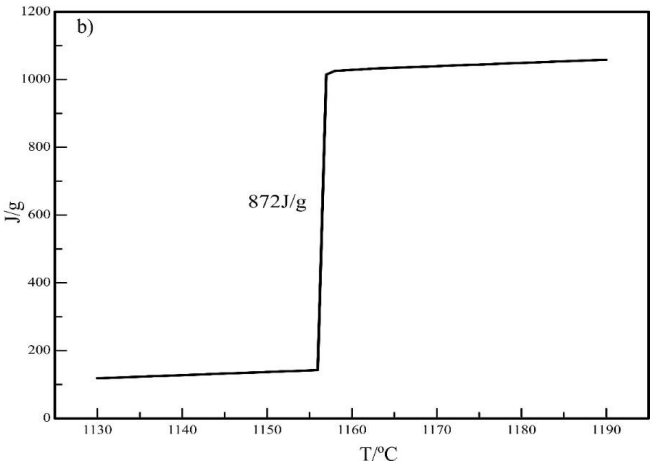

Figure 4-85 The predicted fusion of heat in Fe-26Si-9B alloy. Calculated with FactSage 7.2 based on the FTlite database.

Table 4-6 The DSC results of **Fe-26Si-9B** alloy during continuous heating in Al_2O_3 crucibles up to 1450 °C.

Sample	Heating, Exo					Cooling, Endo					Gas	Mass, mg	Remarks
	T_{onset}, °C	T_{max}, °C	T_{end}, °C	**Heat of fusion**		T_{onset}, °C	T_{max}, °C	T_{end}, °C	**Heat of solidiication**				
				J/g	**kJ/cm³**				**J/g**	**kJ/cm³**			
Fe-26Si-9B	1226	1251	1261	**470**	**2.62**	1157	1170	1172	**-486**	**-2.71**	N_2	30.03	Unmelted (**DSC-54**)
	1226	1261	1277	**426**	**2.37**	1166	1176	1189	**-452**	**-2.52**	N_2	54.95	Unmelted (**DSC-55**)
	1225	1251	1261	**500**	**2.79**	1179	1188	1208	**-448**	**-2.50**	N_2	30.16	Unmelted (**DSC-56**)
	1229	1260	1271	**536**	**2.99**	1166	1171	1177	**-546**	**-3.04**	Ar*	40.05	Melted, adhere (**DSC-57**)
	1228	1258	1274	**633**	**3.53**	1182	1194	1208	**-696**	**-3.88**	Ar*	50.31	Melted (**DSC-58**)
	1225	1256	1264	**551**	**3.07**	1174	1186	1206	**-667**	**-3.72**	Ar*	35.10	Melted (**DSC-59**)

*: The sensitivity and temperature calibrations were done under flow N_2.

4.3. Cr-43Si-5B alloy

Cr-43Si-5B eutectic alloy is another potential PCM that was investigated. Cr is added to the Si-B based alloy, aiming to decrease the volume expansion of Si-B alloys. Simultaneously, the latent heat should be similar or higher than Si-B eutectic alloy per unit volume. In the calculation process, the phase evolution of Cr-43Si-5B alloy during the solidification process is presented in **Figure 4-86**. It is seen that a eutectic reaction occurred at 1414 °C, liquid → CrB_2 + Cr_3B_4 + $CrSi_2$ and CrB_2, Cr_3B_4, and $CrSi_2$

phases are produced in the Cr-43Si-5B alloy. The heat of fusion is calculated to be 1240 J/g (4.27 kJ/cm^3) (**Figure 4-87**). Moreover, 3% volume expansion of Cr-43Si-5B alloy was calculated by Grorud based on the pure elements volume change in the liquid and solid-state [15]. Therefore, Cr-43Si-5B alloy is assumed to be a desirable PCM to be investigated by the present author and also reported by Sindland [17].

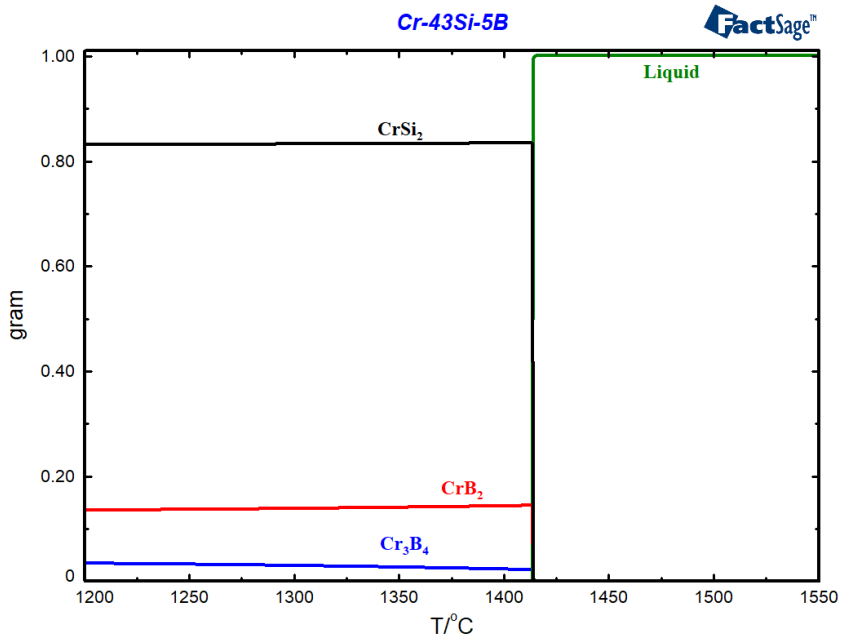

Figure 4-86 Phase evolution of Cr-43Si-9B alloy during solidification from 1550 ºC to 1200 ºC. Calculated with FactSage 7.2 based on the FTlite database.

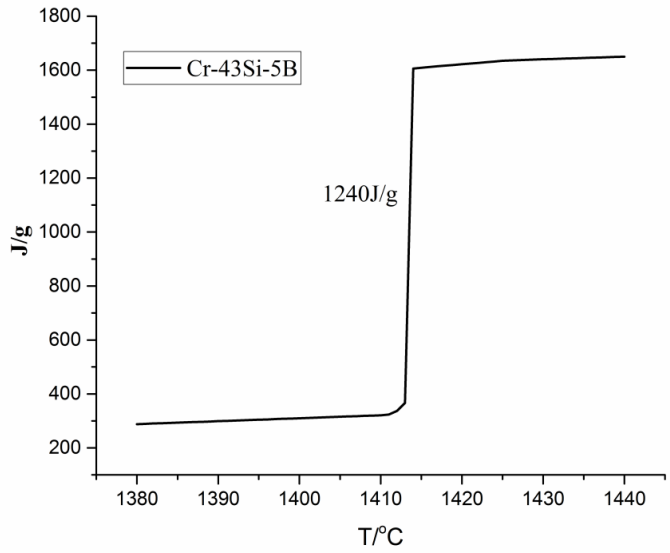

Figure 4-87 Latent heat of Cr-43Si-5B alloy. Calculated with FactSage 7.2 based on FTlite database.

To investigate the possibility of the use of Cr-43Si-5B alloy in the TES systems, Cr-43Si-5B alloy was first prepared in an Al_2O_3 crucible. Then, the thermal cycle experiments were performed in a resistance furnace, in which the master Cr-43Si-5B alloy was charged to the graphite crucible and subjected to 4 thermal cycles in the temperature range 1314-1514 ºC after holding of 1 h at 1600 ºC. 10 min holding time was kept at each temperature. The microstructures in the center of the Cr-43Si-5B alloy and at the interface between the alloy and graphite were characterized by SEM, as shown in **Figure 4-88**. It shows how Si, CrB_2, Cr_3B_4, $CrSi_2$ phases were produced in the Cr-43Si-5B alloy after 4 thermal cycles. **Figure 4-88**b shows that a continuous SiC layer was produced at the interface. In addition, Cr_3B_4 particles were found in the graphite. It indicates that Cr, B, and Si will penetrate the graphite in the thermal cycle experiments.

Images in **Figure 4-89**a-c show the penetration phenomenon of the Cr-43Si-5B alloy into graphite in the bottom, left, and corner positions. It is seen that the penetration was limited in the three different positions. The maximum penetration depth was ~ 200 µm in the left position. It shows that graphite was a desirable PCM container for the Cr-43Si-5B alloy. However, the substantial pores existed in the Cr-43Si-5B alloy after experiments. It was detected by the CT-scan with a 360º 2D rotation by Sindland [17], as shown in **Figure 4-90**. The existing pores are harmful if the Cr-43Si-5B alloy is used as PCM in the TES systems. It will especially affect the thermal conductivity of the Cr-43Si-5B alloy.

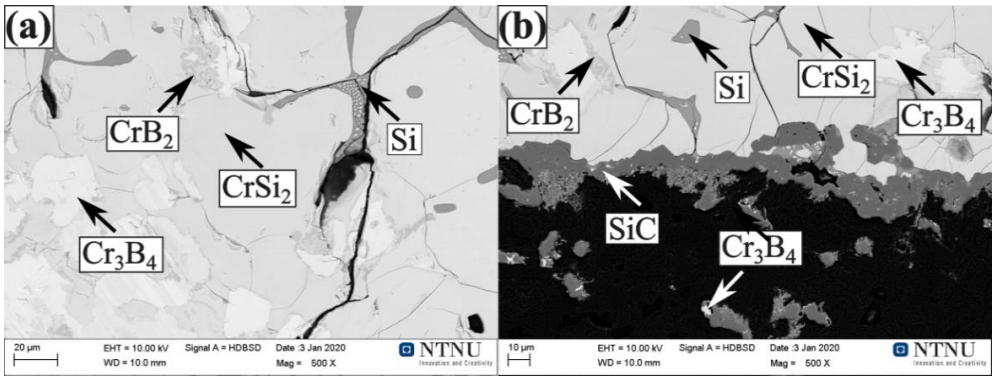

Figure 4-88 Phases formed in the Cr-43Si-5B alloy after 4 thermal cycles in the graphite crucible under Ar. (a) in the center of the alloy; (b) at the interface between the Cr-43Si-5B alloy and graphite.

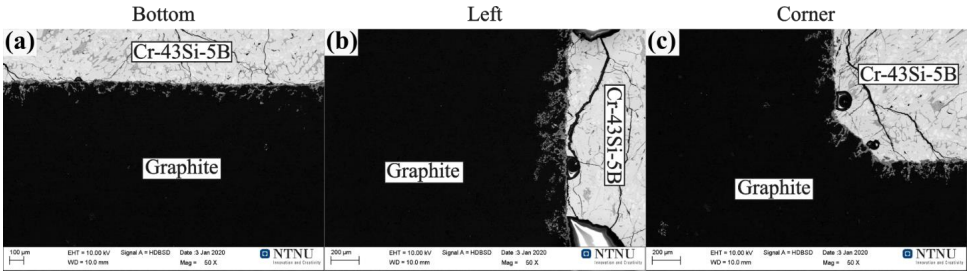

Figure 4-89 The interface between Cr-43Si-5B alloy and graphite in three different positions. (a) bottom position; (b) left position; (c) corner position.

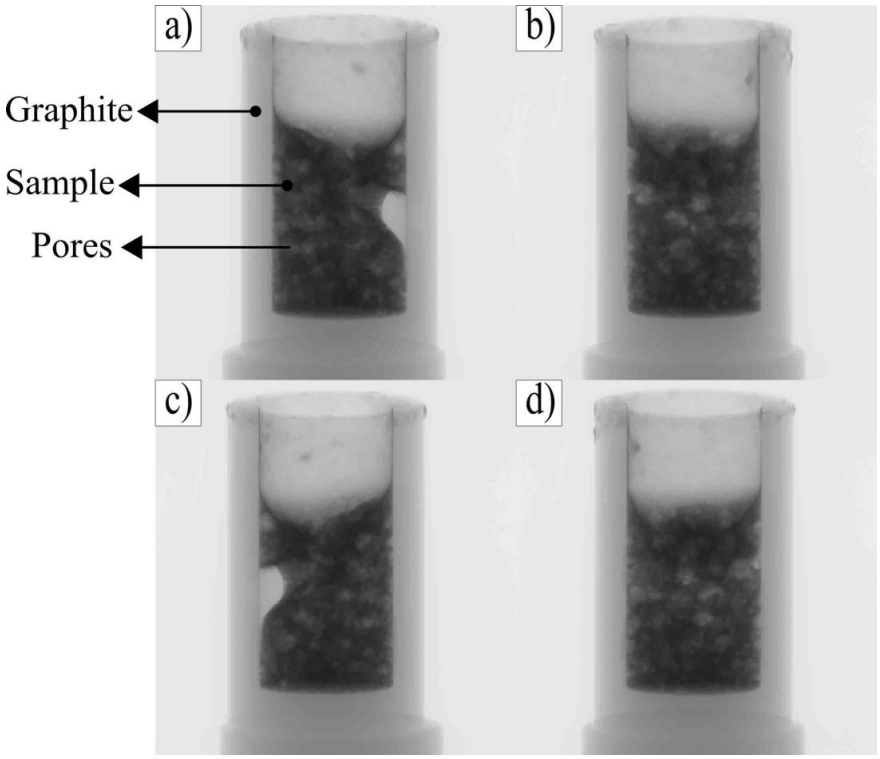

Figure 4-90 Images of the CT scan in the Cr-43Si-5B after 4 thermal cycles in the graphite crucible. (a) front view; (b) right side view; (c) rear view; (d) left side view. [17]

5. Discussion

The discussion is based on the results obtained from the experiments and modeling. The discussion is divided into three parts based on the investigated PCMs: Si-B, Fe-26Si-9B, and Cr-43Si-5B alloys. It mainly focuses on the influence of the formed phases in the PCMs and the adaptability of the PCMs for the containers in the TES systems.

5.1. Si-B alloys

5.1.1. Phase stability in the Si-B alloys

In the long-term energy storage process, Si-B alloys will store and release energy by the phase changes from solid phases to a liquid or from a liquid to solid phases. **Figure 5-1** shows the Si-B phase diagram in the B range 0-15 mass %. As shown, the Si-B alloys start to melt at 1385 °C by absorbing a high amount of energy at 1385 °C, while the complete melting temperature depends on the addition of B. Three different types of phase changes, going from temperatures below 1270°C to above the liquidus temperature, are summarized.

1. SiB_3 + Si ↔ SiB_6 + Si ↔ Liquid + Si(ss) ↔ Liquid in the B range 0-3.25 mass %;
2. SiB_3 + Si ↔ SiB_6 + Si ↔ Liquid at B content of 3.25 mass %;
3. SiB_3 + Si ↔ SiB_6 + Si ↔ Liquid + SiB_6 ↔ Liquid in the B range 3.25-15 mass %;

In our experiments, Si(ss) and Si(ss) + SiB_3 (eutectic structure) was detected in the Si-B alloys with the B addition of 0-3.25 mass %, while Si(ss), eutectic structure, and the larger crystals of SiB_3 particles were detected in the Si-B alloys with the B addition higher than 3.25 mass %. The SiB_6 was however only found in the Si-8B and Si-11B alloys in the use of Si_3N_4. **Table 5-1** summarizes the phases formed in the Si-B alloys.

Table 5-1 Comparison of the formed phases in the Si-B alloys.

Crucible	Expected structure	Si(ss)	SiB_3	Eutectic structure	SiB_6	*Impurity*		
Graphite	2-3.25 mass % B	Si(ss)		Si(ss) + SiB_3	-	*SiC*	*B_4C*	
	5-25 mass % B	Si(ss)	SiB_3	Si(ss) + SiB_3	-	*SiC*	*B_4C*	
Si_3N_4	2 mass % B	Si(ss)		Si(ss) + SiB_3	-	-	-	-
	5 mass % B	Si(ss)	SiB_3	Si(ss) + SiB_3	-	-	-	-
	8 and 11 mass % B	Si(ss)	SiB_3	Si(ss) + SiB_3	SiB_6	-	-	*BN*

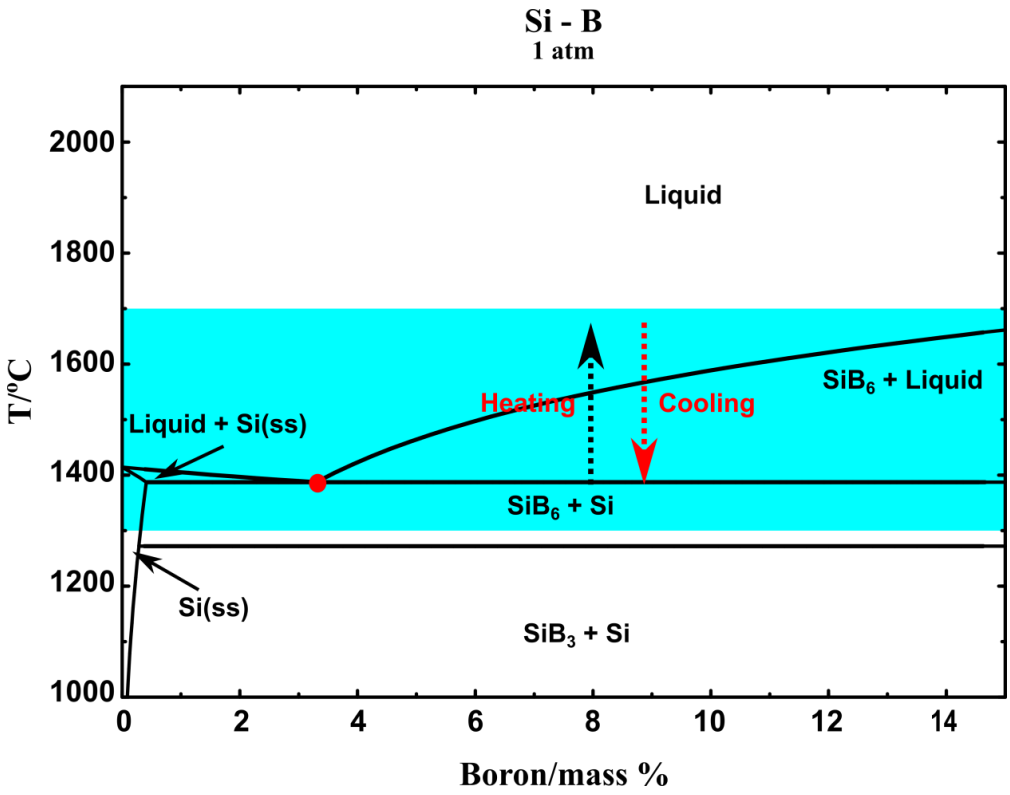

Figure 5-1 Description of the phase transformation in the Si-B alloys in the PCM. Calculated with FactSage 7.2 based on the FTlite database.

The phases found are independent on the cooling rate. Using graphite in the Si-B alloys' crucible, the cooling rate was ~ 50 °C/min in the induction furnace. On the other hand, the cooling rate cannot be measured in the resistance furnace, as we moved the sample from the heating area to a low temperature area after experiments. It is believed that the cooling rate should be faster than that in the induction furnace. However, the formed phases were the same in the graphite crucible, and no SiB_6 phase was observed in the Si-B alloys here either. It is hence believed that the phases seen at room temperature from these experiments would represent the phases seen at higher temperatures in a TES system (**Figure 4-14**-**Figure 4-16**). Therefore, in the use of the Si-B alloys for the long term energy storage, the choice of the operating temperature is important. The phases will be changed between the liquid and SiB_6 + Si when the lowest temperature is over 1270 °C. However, the phases will be changed between the liquid and SiB_3 + Si when the lowest temperature is lower than 1270 °C, due to the fast transformation rate from SiB_6 to SiB_3.

Si(ss) was formed in the Si-B alloys with the B addition higher than 3.25 mass %. **Figure 5-2**a shows the SEM images in the Si-5B alloy and **Figure 5-2**b shows the SEM images in the Si-5.7B alloy [95]. It is seen that the Si(ss) primary phase was formed in both alloys. This is not excpected from the phase diagram, as primary Si crystals should not be formed. Typically, the formed Si(ss) phases are close to the big SiB_3 particles. It is known from **Figure 5-1** that primary SiB_6 will precipitate in hypereutectic

Si-B alloy during cooling. When the temperature decreases to the eutectic point, SiB_6 and liquid phases coexist in Si-B alloy and the eutectic reaction occurs, liquid → Si(ss) + SiB_6. As the SiB_6 is already existing in the alloy, it can act as a nucleus for the new SiB_6 phase. Therefore, if the eutectic reaction occurs close to the SiB_6 particle, the new SiB_6 will be formed on the existing SiB_6 particles, and Si(ss) will surround the particle. Otherwise, the eutectic structures will appear in Si-B alloy. If the temperature is reduced further to the peritectic temperature, SiB_6 will be transformed into SiB_3.

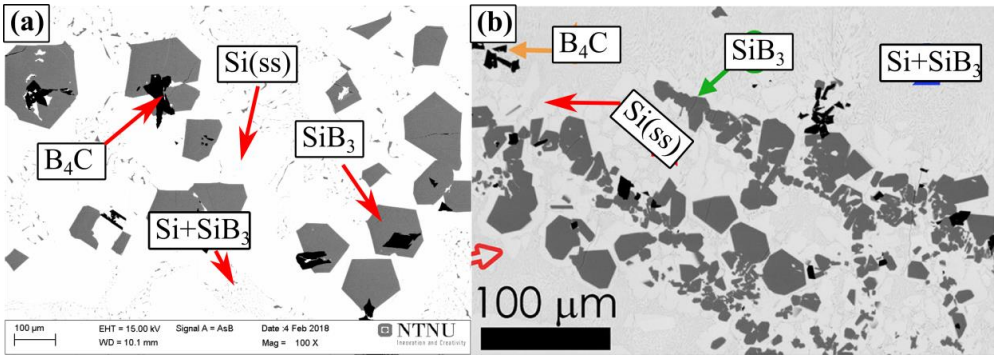

Figure 5-2 The microstructures in the Si-B alloys with the B addition higher than 3.25B mass %. (a) Si-5B alloys in the graphite crucible; (b) the Si-5.7 B alloy on the h-BN substrate [95].

Some minor carbide phases are found in the bulk alloy due to some C dissolved into the liquid Si-B alloys. In the graphite crucible experiments, the liquid Si-B alloys were C-saturated, and hence the B_4C and SiC particles were formed during cooling (**Figure 4-2**). In order to explain the influence of the C content on the phase formation in the Si-B-C system, the thermodynamic modeling of phase equilibria is calculated with FactSage 7.2 based on the FTlite database. **Figure 5-3** shows the phase evolution for the Si-2B alloys in the graphite crucible in the temperature range 1000–1800 °C. Two different conditions are considered in the calculation: a C content higher than the saturation level at 1750 °C (**Figure 5-3**c, d) and lower than the saturation level at 1750 °C (**Figure 5-3**a, b). At high C content, SiC will be in equilibrium with liquid alloy at high temperatures. Then, the B_4C will be formed during cooling, and finally, the SiC, B_4C, and Si(ss) will be formed in the Si-2B alloys. As the B will be precipitated as B_4C, no B is left to form the SiB_3 phase during cooling. At low C contents, that is in the bulk phase, during cooling the carbon solubility decreases and hence SiC will be precipitated. Similar to the high C content calculation, B_4C is formed in the solidification process. Moreover, SiB_6 is formed in the solidified Si-2B alloys, which is further transformed into SiB_3 with the descending temperature. Therefore, solid phases are B_4C, SiB_3, and Si(ss). In addition, it is possible that SiC is detached from SiC layer on the graphite crucible, and then moves to liquid Si-B alloys, leading to SiC particles found in the Si-B alloys. It is hence believed that at the holding temperature the alloy is C-saturated and that the carbides are mainly precipitated during cooling.

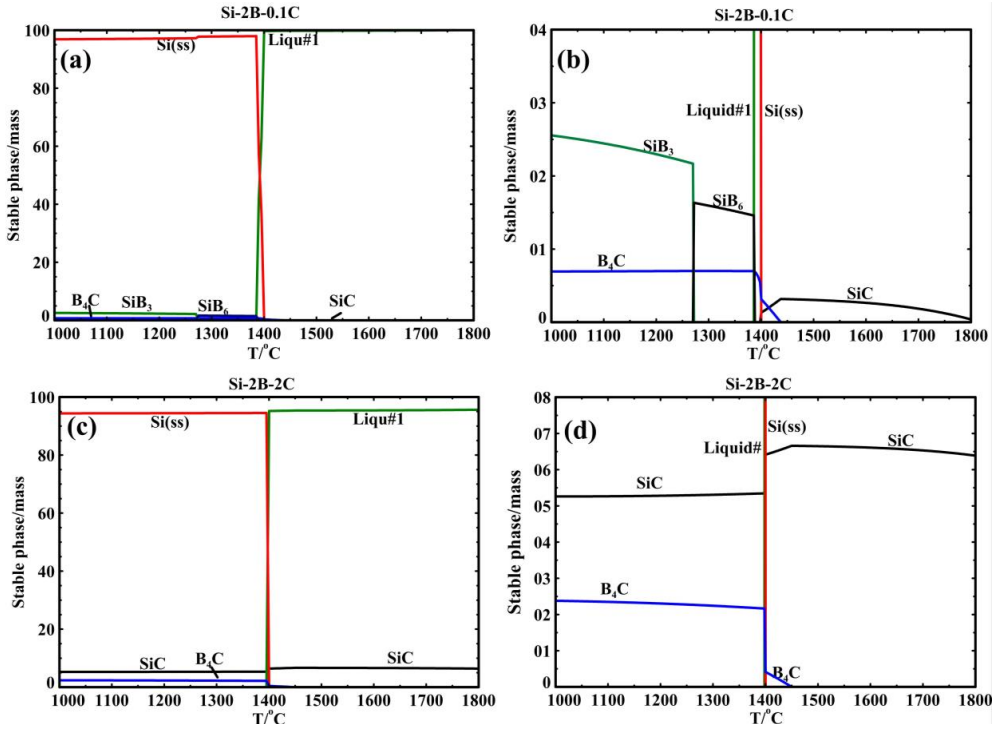

Figure 5-3 The phase evolution of the cooling process from 1800 °C, (**a**) Si-2B-0.1C; (**b**) magnification of the lower part in the Si-2B-0.1C system; (**c**) Si-2B-2C; (**d**) magnification of the lower part in the Si-2B-2C system. Calculated with FactSage 7.2 based on the FTlite database.

The number of SiC particles in the bulk phase is independent of the thermal cycles in the Si-3.25B alloys. The thermal cycle experiments of the Si-3.25B alloy were investigated in a graphite crucible by Grorud [58], in which 1, 2, 5, and 10 thermal cycles were conducted in the temperature range 1430-1550 °C after 1 h holding at 1550 °C. Moreover, one experiment was performed over 48 h, in which the liquid Si-3.25B alloy was held at 1550 °C. The formed phases were Si(ss), SiB_3, and SiC, which was not changed with increasing thermal cycles and holding times. This is in agreement with our experimental results. Besides, the amounts of SiC particles in the Si-3.25B alloys were independent of the thermal cycles and holding times. Hence, the use of graphite will not increase the number of carbides in the Si-B alloys after the long-term melting/solidification process.

SiB_6 was observed in the Si-8B and Si-11B alloys in the use of Si_3N_4 as the refractory material. It might be caused by the dissolved N content. **Figure 5-4** shows the projection of the Si-B-N phase diagram in the Si-rich area. The X and Y-axis represent the B and N content in the Si-B alloys. It is seen that the liquid Si-B alloy equilibrates with Si_3N_4 at lower B content, while it equilibrates with BN at higher B content. The dissolved N content decreases with the increasing B content in the liquid Si-B alloys, and it increases with the increasing temperature. Therefore, the dissolved N contents in the Si-8B and Si-11B alloys are lower than that in the Si-2B and Si-5B alloys in the Si_3N_4 crucible. It seems that the lower content of N in the Si-B alloys, the lower transformation rate from SiB_6 to SiB_3. However, no SiB_6 was found in the Si-8B and Si-11B alloys in the graphite crucible, in which the N content was

close to zero. It can hence not be explained why nitride crucibles and high B content will give a slow transformation from SiB_6 to SiB_3.

BN was found in the Si-B alloys (**Figure 4-23**), due to the dissolved N into the liquid Si-B alloys. The formation of BN was caused by the reaction, $\underline{N}$ + B(l) → BN(s). Therefore, the dissolved N results in the formation of BN in Si-B alloys. As seen in **Figure 5-4**, N content is lower than 10 ppm mass at 1750 °C in the liquid Si-B alloys with the 2-11 mass % B addition. Hence, the amount of BN is limited in the Si-B alloys.

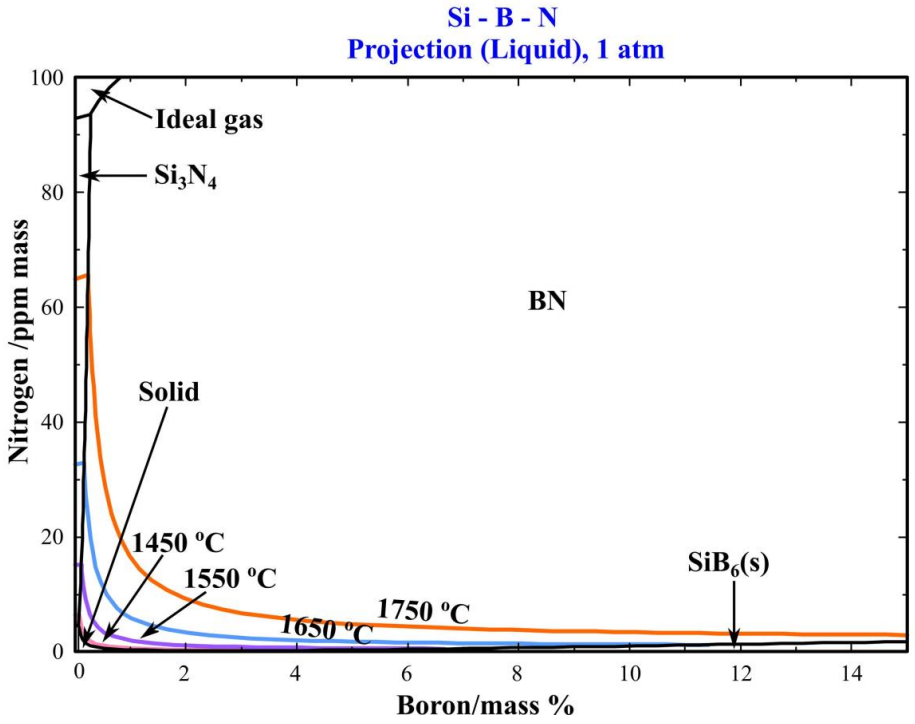

Figure 5-4 Liquidus projection of Si-B-N phase diagram. Calculated by Kai Tang (SINTEF) using FactSage based on the Sintef database.

When Si-B alloy is used as a PCM, the highest energy would be achieved when going from a liquid above liquidus temperature to a temperature just below the solidus temperature at 1385 °C. Just below the solidus Si(ss) and SiB_6 would coexist. Si(ss) and an eutectic structure will be formed in the Si-B alloys with the B addition of 0-3.25 mass %, while Si(ss), eutectic structure, and SiB_6 particle will be formed in the Si-B alloys with the B addition higher than 3.25 mass %. The phase transformation is fast from SiB_6 to SiB_3. Hence, it is believed that the phases will be changed to Si(ss) + SiB_3 if the Si-B alloy is cooled to lower than 1270 °C. Carbides will be precipitated in the Si-B alloys when graphite is used as the container, while the precipitated phase will be changed to BN when Si_3N_4 is used as the container. These carbides and BN will however be dissolved again when the temperature is increased. Hence, the influence of the C and N to the stability of the Si-B alloys is limited.

5.1.2. Volume change in the Si-B alloys

The volume change in the Si-3.25B alloys was roughly measured based on the recorded images in the wetting tests. It shows that the maximum volume change was ~ 9 % from the liquidus point to the complete solidification (**Figure 4-34**).

The ideal volume change of Si-B alloys during solidification from the liquidus point to room temperature was calculated based on the density of the formed phases. It should be noted that the solid volume is the sum of Si and SiB_6 phases and the solid Si has no B dissolved, while the liquid volume is the sum of Si(*l*) and B(*l*) phases with the assumption of an ideal solution. It is assumed that *a* mole B is mixed with *b* mole Si. Hence, the ideal volume expansion can be expressed as follows:

$$n_{Si(l)} = b,\ n_{B(l)} = a,\ n_{SiB_6} = a/6,\ n_{Si(s)} = b - a/6 \tag{5.1}$$

Where $n_{Si(l)}$, $n_{B(l)}$, n_{SiB_6}, and $n_{Si(s)}$ are the mole of the Si(*l*), B(*l*), SiB_6, and Si(*s*) in the Si-B alloys. Hence, the volume of the solidified Si-B alloys at 1270 °C, V_s and the volume of the liquid Si-B alloys, V_l can be expressed:

$$V_s = \frac{n_{SiB_3} \cdot M_{SiB_3}}{\rho_{SiB_3}} + \frac{n_{Si(s)} \cdot M_{SiB_3}}{\rho_{Si(s)}} \tag{5.2}$$

$$V_l = \frac{n_{Si(l)} \cdot M_{Si(l)}}{\rho_{Si(l)}} + \frac{n_{B(l)} \cdot M_{B(l)}}{\rho_{B(l)}} \tag{5.3}$$

In the end, the volume change ΔV is expressed as follows.

$$\Delta V = \frac{V_s - V_l}{V_s} \cdot 100\% \tag{5.4}$$

The ideal volume change of the Si-B alloys is calculated based on the above equations. The results are presented in **Figure 5-5**. There are two Y-axis in the figure, in which the left one represents the value of the liquidus temperature and the right represents the volume change. The X-axis represents the B addition in the Si-B alloys. The green triangle represents the experimental result obtained from the wetting test. It is seen that the ideal volume change of pure Si is 9.7 %. As shown, the volume expansion of the Si-B alloys decreases with the increase of B content. It might be caused by the contraction of the Si lattice in an alloy with B [24]. The measured volume change of the Si-3.25B alloy has a good agreement with the calculated result. Moreover, the volume change of Si-25B alloy is calculated to be ~ -0.8 %. Hence, the volume change will be eliminated in the Si-B alloys with the B addition of higher than 25 mass %. It is also verified by the macro behaviors of the Si-25B alloy (**Figure 4-12**), in which the alloy showed shrinkage in the solidified alloy.

Figure 5-6 shows the relationship between the value of heat and temperature in the Si-B alloys with B contents from 0 to 30 mass %. It is seen that the sum of the heat increases with the increase in the B content, in which the total heat includes the heat of fusion and the sensible heat. Si-3.25B eutectic alloy

can be completed melted at 1385 ºC with the heat of fusion value of 1992 J/g.

Using the Si-B alloys in the TES systems, the use of higher B content can decrease the volume expansion of the Si-B alloy. However, the liquidus temperature will be increased. For instance, if the Si-20B alloy is used as the PCM, the volume expansion is ~ 1.9 %, while the liquidus temperature is increased to ~ 1740 ºC. As the temperature increases to 1385 ºC, the Si-20B alloy starts to melt and transformed to the liquid + SiB_6 mixture phases, in which the heat of fusion capacity is lower than the eutectic Si-3.25B alloy, due to the point that more of the mass will be solid as one gets to the solidus temperature. With further increase of the temperature to the liquidus point (1740 ºC), the total heat of the Si-20B alloy is higher than that in the Si-3.25B eutectic alloys, due to the higher heat of fusion of SiB_6 (3240J/g) [119]. If we consider the heat of fusion capacity, Si-3.25B eutectic alloy is the optimal PCM over a small temperature area. However, if we consider the total heat capacity, over a larger temperature area, the higher B content Si-B alloy is the optimal PCM.

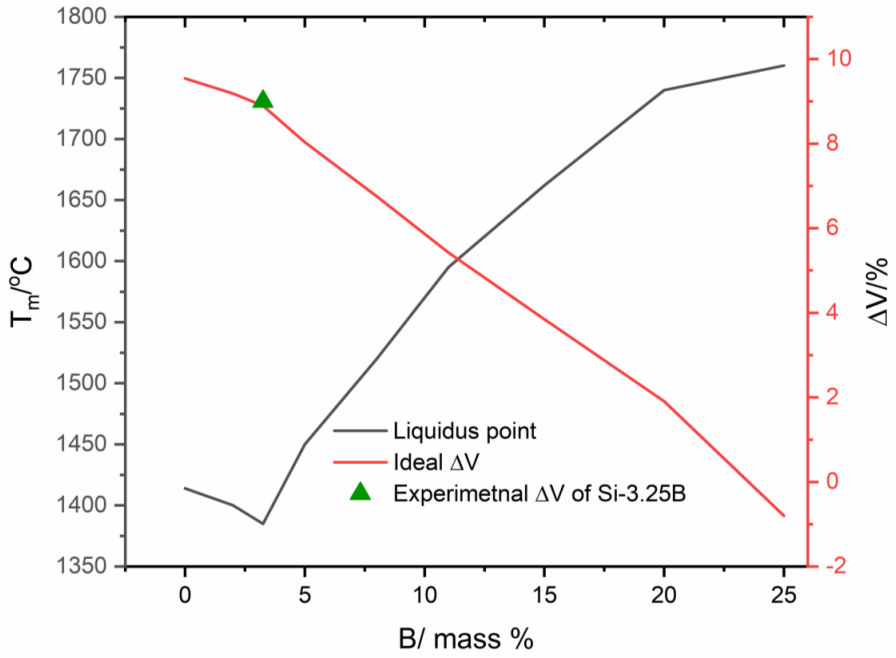

Figure 5-5 The volume expansion and the liquidus temperature of the Si-B melts as a function with B content.

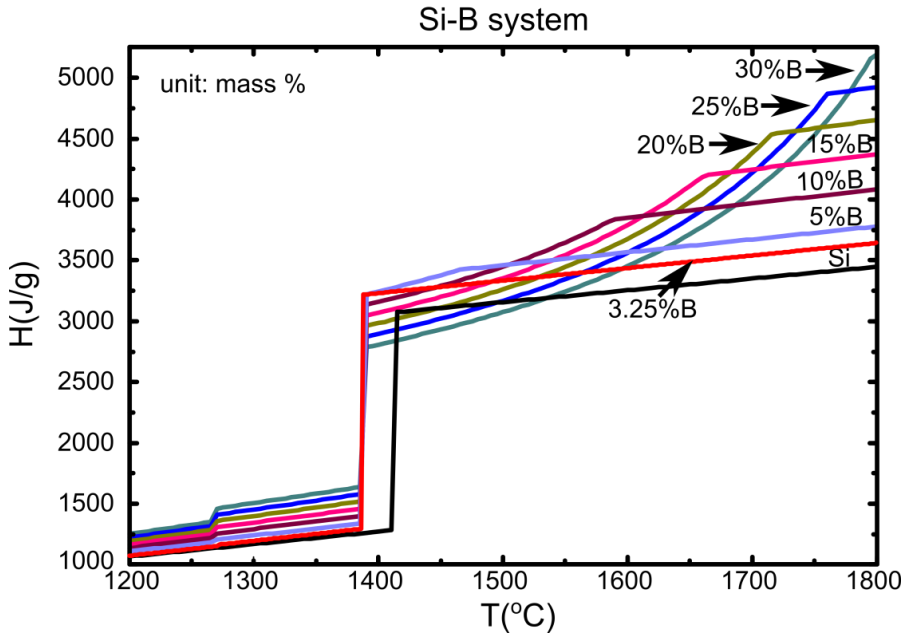

Figure 5-6 The function of the fusion enthalpy as the temperature in the Si-B alloys. Calculated with FactSage 7.2 based on the FTlite database.

5.1.3. Interaction between Si-B alloys and graphite

There will be some interaction between the graphite crucible and the Si-B alloy. A continuous SiC layer was produced along the interface between the Si-2B and Si-3.25B alloys and graphite. The SiC and B_4C layers were, however, formed between the graphite and the Si-B alloys with the B addition higher than 5 mass %. The formation of the SiC and B_4C layers was hence dependent on the B content of the Si-B alloys and temperature.

Figure 5-7 shows the isothermal section of the Si-B-C system at 1550 °C. The mechanism of the interface phase distribution at a constant temperature is explained as follows. In the heating process, the liquid Si-B alloy penetrates the graphite quickly, leading to B_4C and SiC produced in the graphite, as shown in the purple area in **Figure 5-7**. Then, the system is changed to the Si-B-SiC system from the Si-B-C system. There are four different phase areas existing in the system based on the B content. In a low B content Si-B alloy, the liquid Si-B alloy equilibrates with SiC, and only SiC will be formed at the interface during cooling (**Figure 5-8**(1)). If the B content is increased in the Si-B alloys, the system is changed to B_4C + SiC + liquid area, in which SiC and B_4C will be formed at the interface in the solidification process. Subsequently(**Figure 5-8**(2))with the further increase of the B content in the Si-B alloys, the liquid Si-B alloy will equilibrate with B_4C, and only B_4C will be formed at the interface

during cooling (Figure 5-8(3)). If the Si-B alloy is in the SiB_6 + B_4C + Liquid area, the SiB_6 phase will coexist with the liquid Si-B alloy and equilibrate with B_4C layer(Figure 5-8(4)). Therefore, the B content in the Si-B alloys determines the layer phase formation in the Si-B-C system.

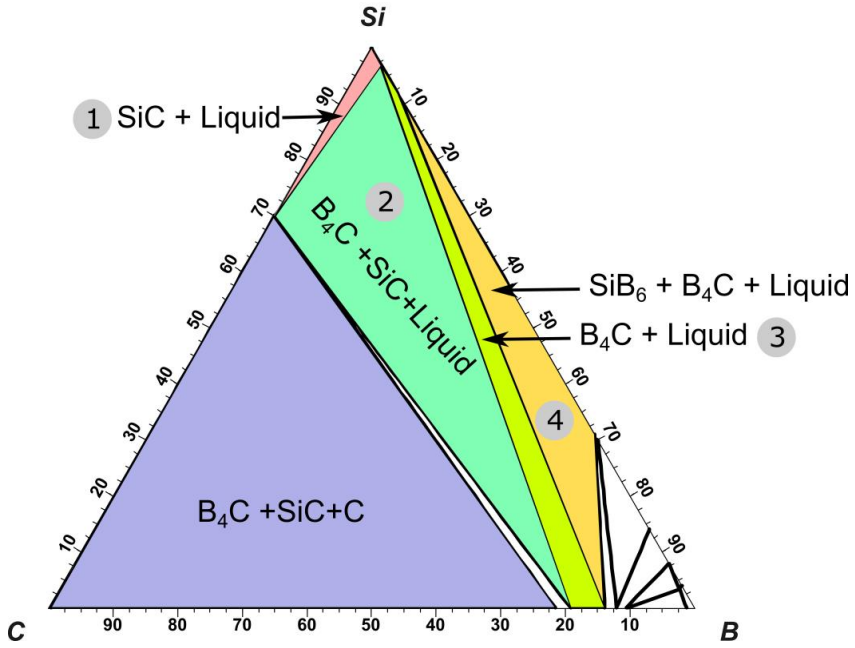

Figure 5-7 Isothermal section of the equilibrium phase diagram of the Si-B-C ternary system at 1550 °C (mass %). Calculated with FactSage 7.2 based on the FTlite database.

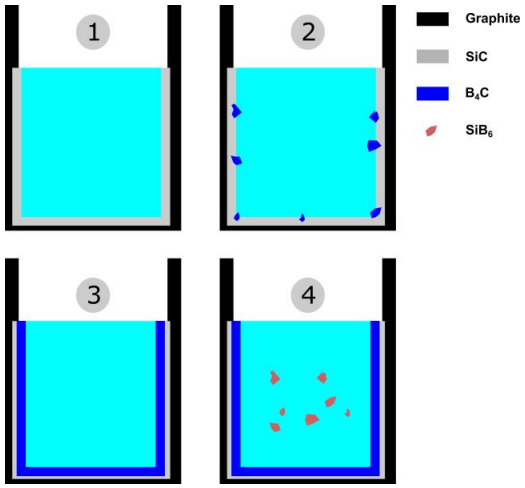

Figure 5-8 Illustration of the evolution of the reaction between the liquid Si-B alloys and graphite with the increase of B content at 1550 °C (1–4 correspond to the phase area in Figure 15).

Figure 5-9 illustrates the relationship between the B and C content in the Si-B-C system. The X and Y

axes represent the B and C content, respectively. The black boundary line divides the SiC and B_4C primary precipitation areas, in which the left region is the SiC phase area, and the right region is the B_4C phase area. Other colored lines show the liquidus temperature. It is known from the figure that C is in the form of the SiC at low B contents, while it is in the form of the B_4C at high B contents. At B content of 2 mass %, the liquid Si-2B alloy and SiC is in thermodynamic equilibrium at temperatures lower than 1750 °C. It supports the formation of the SiC layer in the interface. At B contents of 8 and 11 mass %, the liquid Si-B alloy equilibrates with B_4C at temperatures lower than 1750 °C. However, it changes to be more complicated at boron content of 5 mass %. As shown, the liquid Si-5B alloy equilibrates with SiC in the temperature range 1700 -1750 °C, while it equilibrates with B_4C below 1700 °C. It means that SiC will be transformed into B_4C at 1700 °C during cooling. At B content of 3.25 mass %, the liquid Si-3.25B alloy equilibrates with the B_4C at temperatures below ~ 1550 °C. However, Grorud [58] and the present experiments show that the SiC was the only phase formed at the interface at temperatures below 1750 °C. This may indicate that the phase transformation from SiC to B_4C is quite slow at lower temperatures.

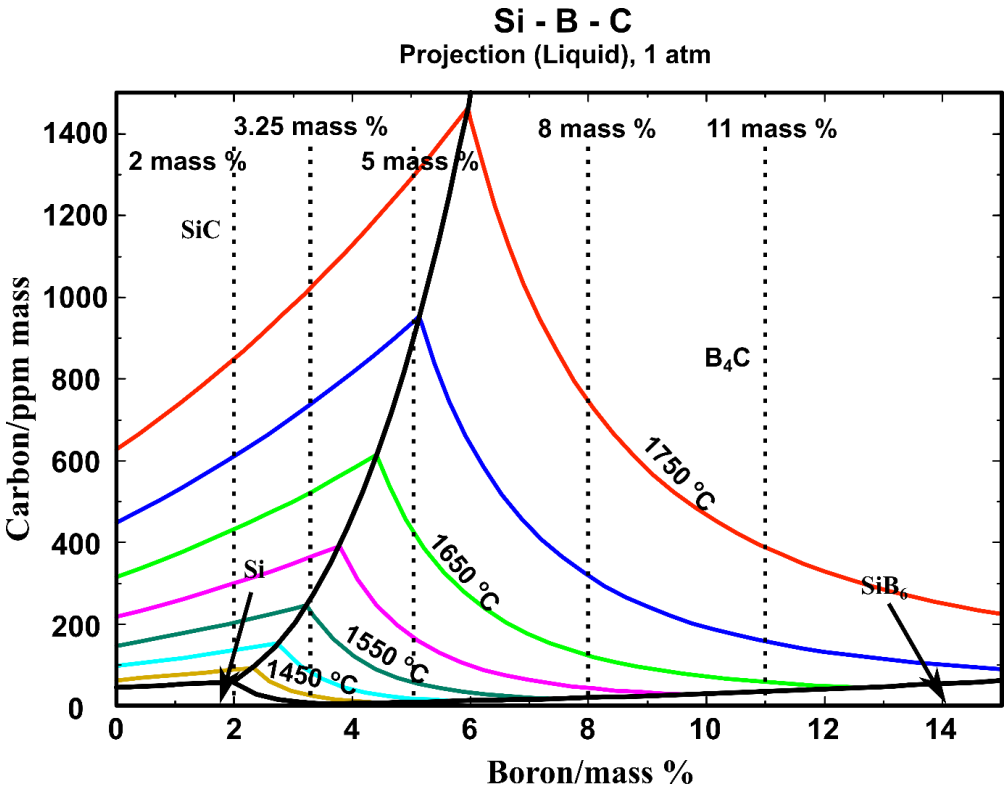

Figure 5-9 The function of C content with increasing B content in Si-B alloys at temperatures of 1450-1750 ºC. Calculated with FactSage 7.2 based on the FTlite database.

In order to determine the equilibrium B content in the liquid Si-B alloys in coexistence with SiC and B_4C, the Wagner model was used in the following equations. The reaction of liquid B and SiC can be expressed as follows:

$$4B(l) + SiC(s) = B_4C(s) + Si(l) \quad 5.5$$

The SiC(s) and $B_4C(s)$ are presented in the solid state, and hence the activities are assumed to be unity. The equilibrium constant (K) of the reaction is expressed.

$$K = exp^{\frac{-\Delta G^0}{RT}} = \frac{\alpha_{B_4C} \cdot \alpha_{Si(l)}}{\alpha_{SiC} \cdot \alpha_{B(l)}^{\ 4}} = \frac{\gamma_{Si(l)} \cdot x_{Si(l)}}{\gamma_{B(l)}^{\ 4} \cdot x_{B(l)}^{\ 4}} \quad 5.6$$

Where $\gamma_{Si(l)}$ and $\gamma_{B(l)}$ are the activity coefficients of the liquid Si and liquid B, $x_{Si(l)}$ and $x_{B(l)}$ are the mole fraction of the liquid Si and liquid B, in which $x_{Si(l)} + x_{B(l)} = 1$. The relationship between the equilibrium constant and the temperature is presented in **Figure 5-10**. It is worth noting that $\gamma_{Si(l)}$ is assumed to be 1. Hence, the equilibrium constant is rewritten as follows.

$$K = exp^{\frac{-\Delta G^0}{RT}} = \frac{\alpha_{B_4C} \cdot \alpha_{Si(l)}}{\alpha_{SiC} \cdot \alpha_{B(l)}^{\ 4}} = \frac{x_{Si(l)}}{\gamma_{B(l)}^{\ 4} \cdot x_{B(l)}^{\ 4}} = \frac{1 - x_{B(l)}}{\gamma_{B(l)}^{\ 4} \cdot x_{B(l)}^{\ 4}} \quad 5.7$$

This is combined with the dilute activity coefficient of B in pure Si [36]:

$$ln\gamma_{B(l)} = 289 / T + 1.19 \quad 5.8$$

Then the equilibrium B content is calculated and presented in **Figure 5-11**. The blue and red lines represent the predicted values from Wagner model and FactSage 7.2 based on the FTlite database. The pink points represent the experimental values (**Table 4-3**). It is seen that the predicted equilibrium B content increases with the increasing temperature. The experimental data is lower than the predicted values from Wagner model and higher than the predicted values from FactSage 7.2.

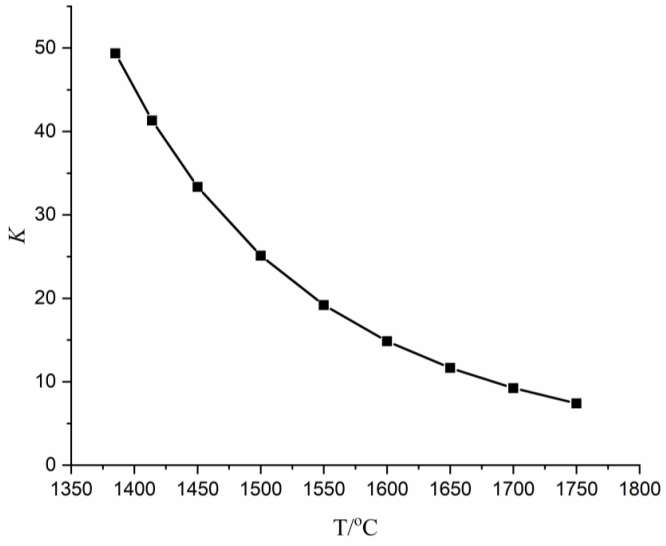

Figure 5-10 Equilibrium constant *vs* temperature. Calculated with FactSage 7.2 based on the FTlite database.

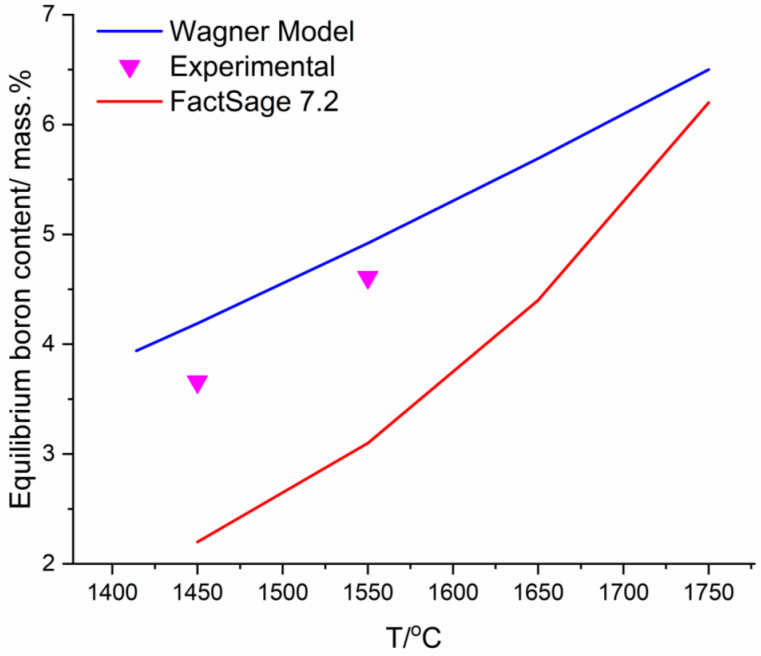

Figure 5-11 Equilibrium boron content in Si-B alloys at different temperatures.

The B content of 3.66 mass % is regarded as the equilibrium B content in the reaction between the liquid Si-B alloys and SiC and B_4C at 1450 °C. The following steps are proposed for the interaction of Si-B melts and graphite crucible in the solidification process (**Figure 5-12**). If the B content is lower than 3.66 mass %, the Si-B melts and the SiC has a thermodynamic equilibrium at 1450–1750 °C, and there is only a SiC layer produced between the Si-B alloy and graphite, as shown in **Figure 5-12**a. If the B content is higher than 3.66 mass %, there are two different situations. One is that the liquid Si-B alloy equilibrates with the SiC layer at high temperatures and the B_4C layer was produced at the descending temperatures (**Figure 5-12**b). Another is that the liquid Si-B alloy equilibrates with the B_4C in the whole temperatures range, as shown in **Figure 5-12**c.

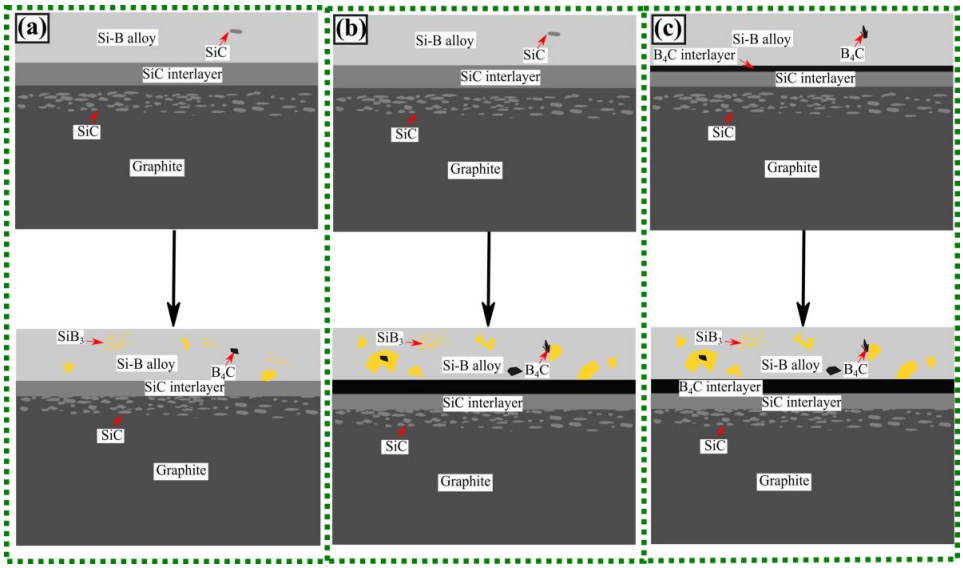

Figure 5-12 Illustration of the interaction of the graphite crucible and Si-B melt. (a) at B content lower than 3.66 mass %; (b-c) at B content higher than 3.66 mass %, in which (b) equilibrates with SiC layer and (c) equilibrates with B_4C layer at the holding temperature.

In the previous discussion, the formation of B_4C layer was caused by the reaction between the liquid B and SiC layer, $4SiC(s) + 4B(l) \rightarrow B_4C(s) + 4Si(l)$. However, it also might be caused by the reaction between the dissolved C and B components during the solidification process, $\underline{C} + B(l) \rightarrow B_4C(s)$. The C solubilities in the Si-2B, Si-3.25B, and Si-5B alloys had been measured in the experiments, and hence, the thickness of the formed SiC and B_4C layer can be calculated as follows.

The mass of the B_4C layer can be obtained by the C solubility in the Si-B alloys:

$$m_{B_4C} = \frac{m_C * M_{B_4C}}{M_C} \tag{5.9}$$

Hence, the volume of the B_4C can be obtained.

$$V_{B_4C} = \frac{m_{B_4C}}{\rho_{B_4C}} \tag{5.10}$$

Moreover, **Figure 5-13** shows the size of the graphite crucible. Therefore, the volume of the B_4C can also be expressed as follows.

$$V_{B_4C} = \pi\left(\frac{D}{2}\right)^2 x + \pi D(H - x)x \tag{5.11}$$

Where m_{B_4C}, m_C are the mass of the B_4C and C. M_{B_4C}, M_C are the molar mass of the B_4C and C. V_{B_4C}, ρ_{B_4C} are the volume and density of the B_4C. D is the diameter of the crucible.H is the hight of the formed B_4C layer.

It is known that the layer of the B_4C is on the scale of the micrometer. (H-x) is assumed to be H. Hence, the last equation can be rewritten.

$$V_{B_4C} = \pi\left(\frac{D}{2}\right)^2 x + \pi DHx \qquad 5.12$$

The value of D is 15 mm. The value of H is assumed to be 20 mm based on the macrostructure of the Si-B alloys (**Figure 4-12**). Hence, the thickness of the B_4C layer can be obtained.

Similarly, the thickness of the SiC layer can be calculated using the same method.

Figure 5-14 presents the calculated thicknees of the SiC and B_4C layer, which were caused by the dissolved C in the liquid Si-B alloys. It is seen that the thickness of the SiC layer was within 1.4 μm and the thickness of the B_4C layer was within 4.5 μm. However, the average value of the measured SiC layer was in the range of 6.3-35 μm in the Si-2B alloys. The measured thickness of the B_4C layer was in the range of 8-26 μm. It indicates that the thickness of the SiC layer does not have an obvious increase during cooling and the formation of B_4C layer is mainly caused by the reaction between the B in liquid and SiC layer, $4SiC(s) + 4B(l) \rightarrow B_4C(s) + 4Si(l)$.

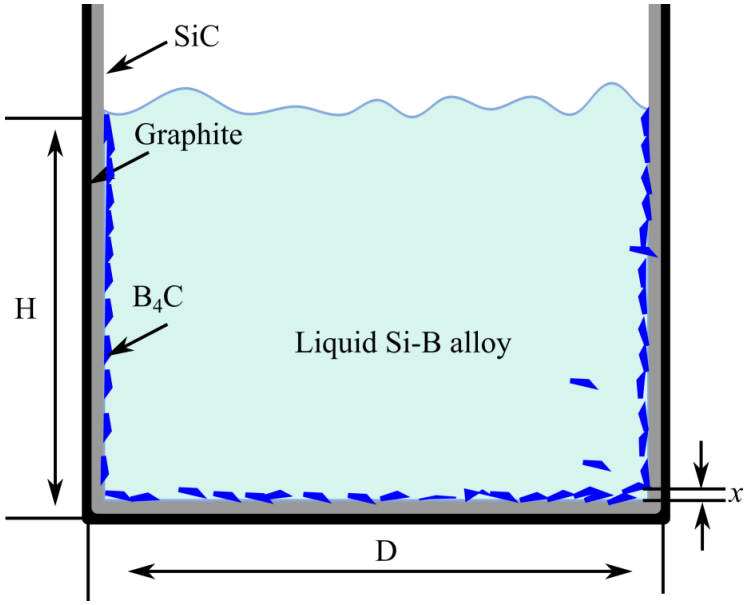

Figure 5-13 Illustration of the calculation for the B_4C layer thickness, which was caused by the reaction between the dissolved C and B.

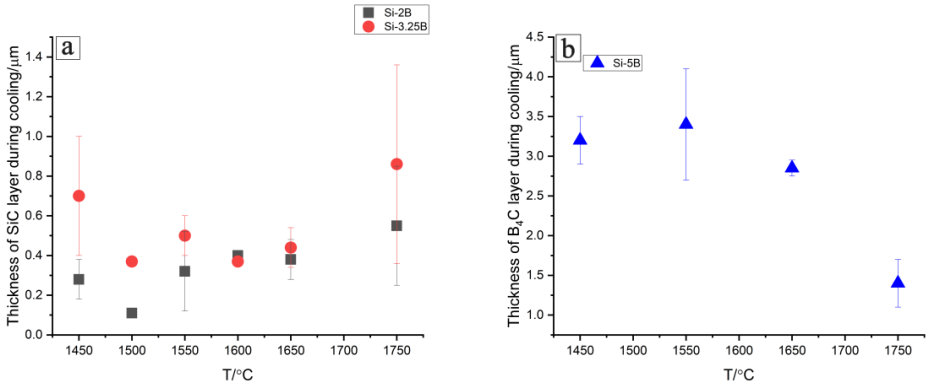

Figure 5-14 The calculated layer thickness, which was caused by the dissolved C in the liquid Si-B alloys. (a) SiC; (b) B_4C.

To sum up, using graphite as the PCM container the interface phase formation is dependent on the B addition in the Si-B alloys. A single SiC layer is formed at the interface in a low B Si-B alloys, while SiC and B_4C layers are formed at the interface in a high B Si-B alloys. Both SiC and B_4C layers can serve as protection layers for the graphite holder during their long term use in a TES system. However, the formation of the B_4C layer will consume some B in the Si-B alloys. It further decreases the energy storage capacity of the Si-B alloys. Hence, if we want to form the SiC and B_4C layers, the added B content should be higher than what is desired.

5.1.4. The solubility of C in liquid Si and Si-B alloys

Liquid Si

The relationship between the C solubility and the temperature in the liquid Si in the temperature range 1450-1750 °C was found to be:

$$Cc(T) = 0.596 \cdot \exp(\frac{-16452}{T}) \ (T = 1723\text{-}2023\ K) \qquad 4.1$$

Figure 5-15 shows the Si-C phase diagram in the Si-rich area, in which the red circle points represent the measured C content and other points represent the reported C content in the liquid Si. Compared to the reported results, the present work shows a good agreement with Scace et al. [43] and Oden et al. [46] in the temperature range 1450-1750 °C. However, it is lower than the values obtained from Ottem [47], Dalaker et al. [52], Iguchi et al. [53], and Hall [42].

Hall [42] measured the C content in liquid Si in a fused quartz container, and the C solubility was determined to be 61 ppmm at the melting point. Dalaker et al. [52] used the quartz tube to extract sample from the liquid Si, and the C solubility was measured to be 65 ppmm at the melting point. In the use of quartz in the experiments, O would dissolve into the Si sample and react with liquid Si to form CO or

CO_2 gas, which might underestimate the C solubility in the liquid Si. However, the results obtained by Hall [42] and Dalaker et al. [52] had similar results with Ottem [47] and Iguchi et al. [53].

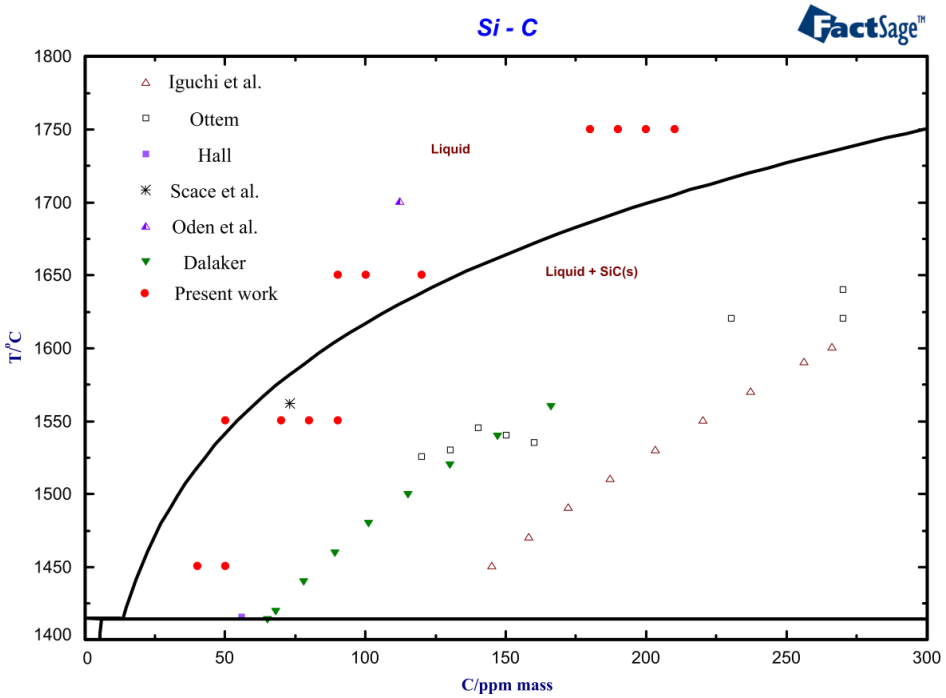

Figure 5-15 Si-C phase diagram in the Si-rich part. The points represent the experimental and literature data. Calculated with FactSage 7.3 based on the FTlite database.

Liquid Si-B alloys

The C contents in the liquid Si-B alloys were measured in the temperature range 1450-1750 °C. The results are presented in **Figure 4-20**. It shows that the C content was in the range 120–585 ppm mass in the liquid Si-2B alloy, 390–915 ppm mass in the liquid Si-3.25B alloy, and 835–2090 ppm mass in the liquid Si-5B alloy. The C content was increased with the increase of the B addition in the Si-B alloys.

The residue B content in the liquid Si-B alloys was calculated at different temperatures, as shown in **Figure 5-16**. The dotted lines represent the added B content, and the points with their standard deviation represent the residual B content in the extracted Si-B alloys after solidification. It is seen that the B loss is negligible in the Si-2B and Si-3.25B alloys at temperatures of 1450–1750 °C. However, the retained B contents are 3.66 mass % at 1450 °C and 4.61 mass % at 1550 °C. They are lower than the added boron content of 5 mass %. It means that some B was lost in the B_4C layer in the Si-5B alloys at 1450 °C and 1550 °C. Hence, the C content in the liquid Si-5B alloy was affected by the formation of the B_4C layer at the interface.

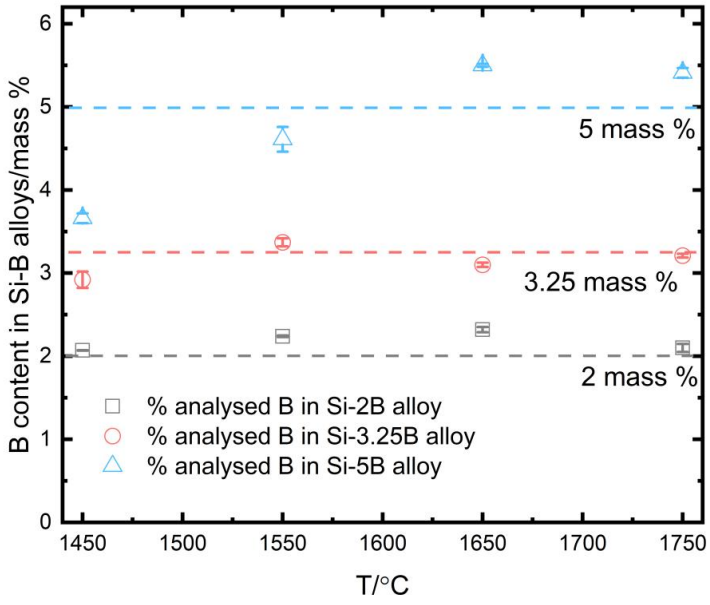

Figure 5-16 The residue B content in Si-B melts at different temperatures.

Figure 5-17-**Figure 5-19** shows the Si-B-C phase diagram in the Si-rich parts, in which 2, 3.25, and 5 mass % B is fixed in the system, respectively. As seen in **Figure 5-17**, the measured C contents in the liquid Si-2B alloy are compared with the reported values. The measured C increases with the increase of temperature. Besides, the use of graphite and SiC does not affect the results as expected. Yanaba *et al.* [48] and Dalaker [52] reported the C content in the Si-2B alloys. It is found that the measured C contents are higher than those obtained by Yanaba *et al.* [48] and Dalaker [52] at lower temperatures, while it is in good agreement at higher temperatures. The Si-3.25B-C system is presented in **Figure 5-18**. The measured C contents are in good agreement with the predicted values at 1650 °C and 1750 °C. It is seen that the C content has not an apparent increase with increasing temperature in the temperature range 1450-1650 °C. The Si-5B-C system is presented in **Figure 5-19**. It has been calculated that the B_4C layer will be formed between the liquid Si-5B alloy and graphite at 1450 °C. When the temperature increases to a higher temperature, only a SiC layer is formed at the interface. As seen in the figure, the measured C contents kept constant in the temperature range 1450-1650 °C, and then, it decreased at 1750 °C. No correlation was found between the measured C content and temperature in the Si-5B alloys.

According to our experiments, a single SiC layer was formed between the graphite and the Si-2B and Si-3.25B alloys in the temperatures range 1450-1750 °C. Hence, these liquid Si-B alloys equilibrate with SiC in the extraction process. The extraction sample state in the Si-B alloys is illustrated in **Figure 5-20**a. As the experiments were carried out in an induction furnace, the liquid Si-B alloy was continuously stirred by the electromagnetic force, as seen by the green circle in the figure. The

continuous electromagnetic stirring might bring the detached SiC particles to the center of the liquid Si-B alloys from the SiC layer. Then, the detached SiC particles were extracted to the Si-B alloys, which would result in overestimating the C solubility in the Si-B alloys. The microstructures of the extracted Si-B alloys were observed by SEM (**Figure 4-18**) and SiC particle was not found in the sample. However, we can not exclude the possibility of the influence by the SiC particles, as the measured C contents had wide scatter at a constant temperature. For instance, the measured C content was from 450 ppm mass to 1080 ppm mass in the Si-3.25B alloys at 1450 ºC. Similarly, the liquid Si-5B alloy equilibrated with the B_4C layer at 1450 ºC, as shown in **Figure 5-20**b. The detached B_4C particles would overestimate the C content in the Si-5B alloys at 1450 ºC.

For the Si-3.25B-C system, as shown in **Figure 5-18**, it shows that the liquid Si-3.25B alloy equilibrates with B_4C at temperatures lower than 1580 ºC. However, the experimental results show that only a SiC layer was formed between the liquid Si-3.25B alloy and graphite [58]. As no reference literature was found in the research of the C solubilities in the Si-3.25B and Si-5B alloys, the phase diagram of the Si-3.25B-C and Si-5B-C systems may not be reliable.

For the Si-5B-C system, it is believed that the B_4C layer was formed between the liquid Si-5B alloy and SiC at 1450 ºC. Therefore, the B content in the Si-5B alloys would be lower than the added B content of 5 mass %. The calculated equilibrium B content was 3.66 mass %. It means that the Si-5B alloy was changed to Si-3.66B alloy at 1450 ºC. The C solubility should be similar with that in the Si-3.25B alloys at 1450 ºC. However, the average value of 1955 ppm mass in the Si-3.66B alloy was much higher than the average value of 757 ppm mass in the Si-3.25B alloy at 1450 ºC. The formation of the B_4C layer had a great influence on the C solubility in the Si-B alloys.

In conclusion, the C content increased with the increase of B content in the Si-B alloys with the B content of lower than 5 mass %. In the Si-2B and Si-3.25B alloys, the C content increased with the increase in temperature.

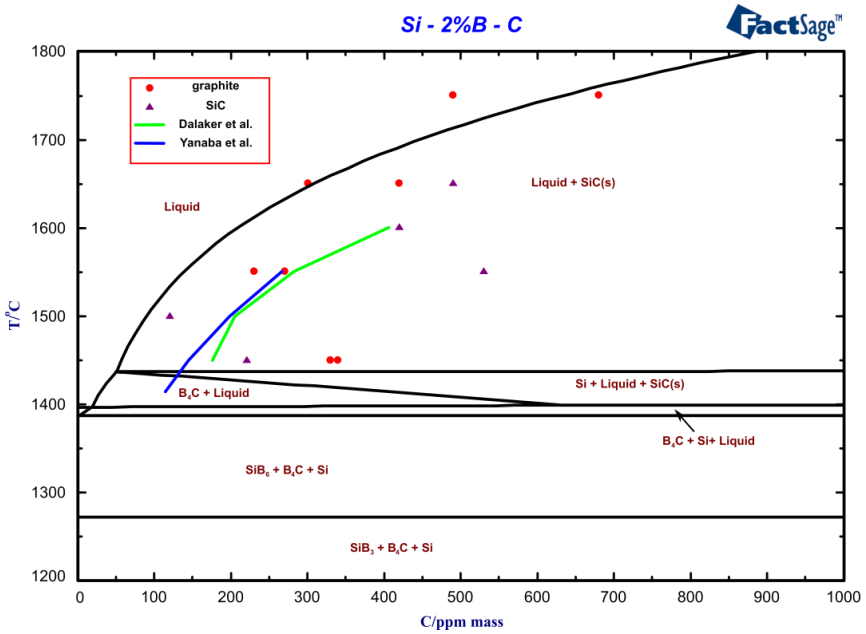

Figure 5-17 Si-2B-C phase diagram in the Si-rich part. The points represent the experimental and literature data. Calculated with FactSage 7.3 based on the FTlite database.

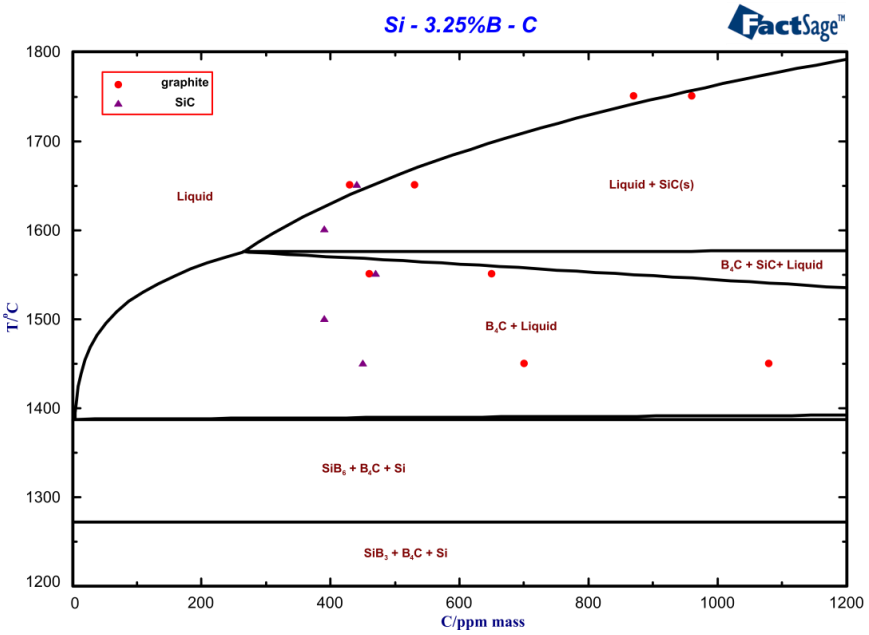

Figure 5-18 Si-3.25B-C phase diagram in the Si-rich part. The points represent the experimental data. Calculated with FactSage 7.3 based on the FTlite database.

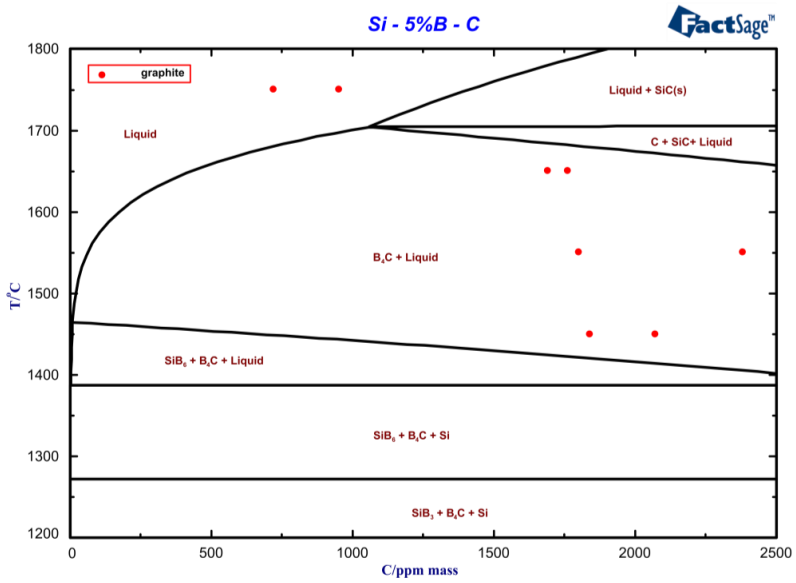

Figure 5-19 Si-5B-C phase diagram in the Si-rich part. The points represent the experimental data. Calculated with FactSage 7.3 based on the FTlite database.

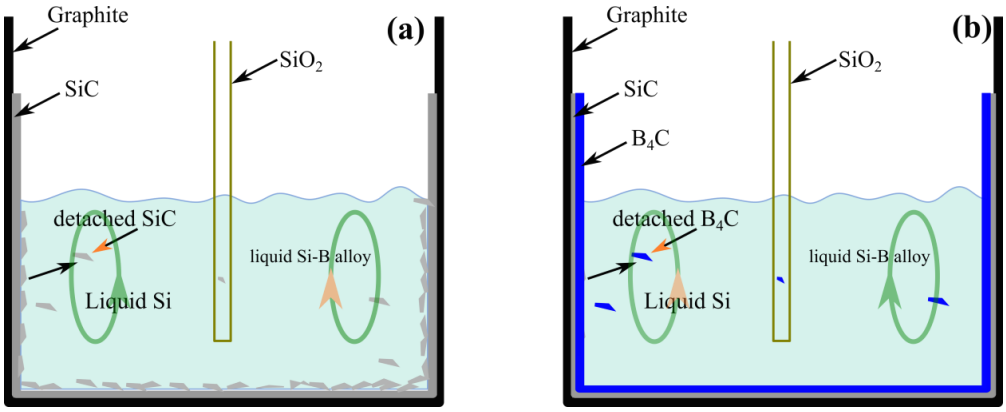

Figure 5-20 Sketch of the extraction sample state in the Si-B alloys. (a) equilibrating with SiC; (b) equilibrating with B_4C.

5.1.5. The interaction between the Si-B alloys and Si_3N_4

There will be some interaction between the Si_3N_4 crucible and the Si-B alloy. A continuous BN layer was formed at the interface between the Si-8B alloys and Si_3N_4 crucible (**Figure 4-25**). Hence, the liquid B would react with the Si_3N_4 at 1750 °C. On the other hand, the formation of the BN layer might also be caused by the dissolved N, due to the reaction $\underline{N} + B(l) = BN(s)$. However as the BN is at the

Si_3N_4 surface, it is believed that the reaction will happen between the dissolved B and Si_3N_4.

Figure 5-21 shows the interaction between the Si-B alloys and Si_3N_4 at 1750 °C. The X-axis represents the content of the Si-B alloys, in which X = 0 shows the Si_3N_4 position and X = 1 shows the Si-B alloys position. The Y-axis represents the mass percent of the formed phase. As it is expected, the formation of BN is possible from the reaction of Si-B alloy and Si_3N_4 at 1750 °C. The amount of the BN increases with the increase of B content in the Si-B alloys.

The formation of BN at the Si/Si_3N_4 interface is resulting from the following reaction.

$$\underline{B} + \tfrac{1}{4} Si_3N_4(s) = BN(s) + \tfrac{3}{4} Si(l) \qquad 5.13$$

The Gibbs energy, ΔG, of the formation of BN is given as

$$\Delta G = \Delta G^0 + RT \ln \frac{a_{Si}^{3/4} \cdot a_{BN}}{a_B \cdot a_{Si_3N_4}^{1/4}} \qquad 5.14$$

Where R is the gas constant. T is the absolute temperature. a_{BN} and $a_{Si_3N_4}$ are the activities of BN and Si_3N_4 at solid state, which are assumed to be unity. a_{Si} and a_B are the activities of Si and B at liquid state. ΔG^0 is the standard Gibbs energy of the formation of BN. The calculated results are shown in **Figure 5-22**.

As shown in **Figure 5-22**, the Gibbs energy, ΔG, shows a negative value in the B range 2-11 mass % at 1750 °C, and it decreases with the increase in the B content in the Si-B alloys. The negative Gibbs energy indicates that the formation of BN is possible. Simultaneously, the BN layer hinders the B penetration to the Si_3N_4 crucible.

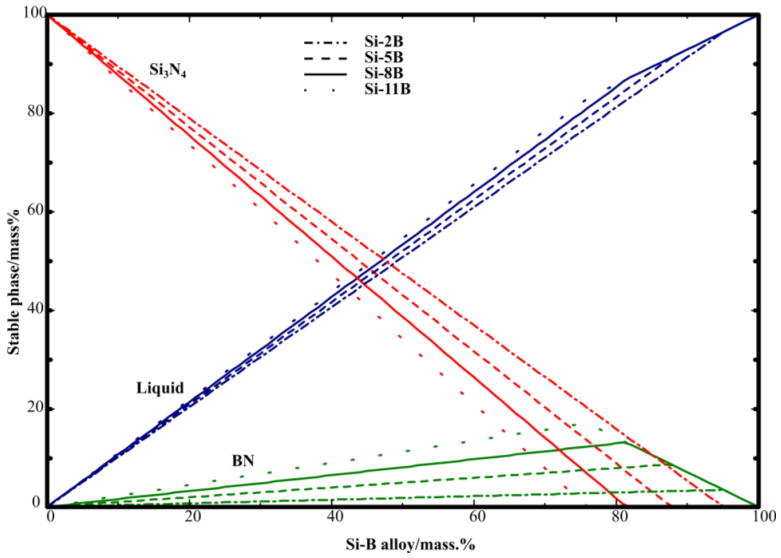

Figure 5-21 The interaction between Si_3N_4 crucible and Si-B alloys (2-11 mass % of boron) at 1750 °C. Calculated with FactSage 7.2 based on the FTlite database.

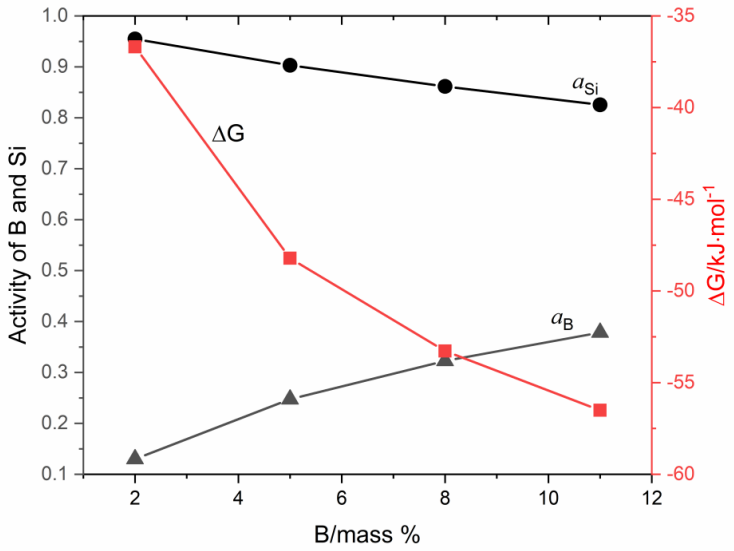

Figure 5-22 The function of Gibbs energy and activity with B content at 1750 ºC. Calculated with FactSage 7.2 based on the FTlite database.

The equilibrium contact angle was 134 ± 1º between the Si-3.25B alloy and Si_3N_4. The value of the contact angle in the Si-3.25B/Si_3N_4 system is higher than the contact angles measured in the Si/Si_3N_4 systems (0 to 90º) in the literature [14], [90]–[92]. According to [17] at the surface of the Si_3N_4 substrate, a thin layer of oxynitride (SiN_xO_y) was formed. Therefore, in the Si/ Si_3N_4 system, the initial angle of 85º was contributed to the SiN_xO_y layer. Then, the contact angle was decreased with time and tended to 49º, which was close to the contact angle between the liquid Si and Si_3N_4. However, in the Si-3.25B/Si_3N_4 system in this work, the contact angle was measured to be 134 º ± 1º, close to the wetting angle in the Si/BN system (90-145º) [88], [89], [92], [93], [120] and in the Si-3.2B/BN system (144-151º) [96]. Hence, it is believed that a BN layer was formed between the Si-3.25B alloy and Si_3N_4.

In the use of the Si_3N_4 as the PCM container at high temperatures, the surface of the Si_3N_4 will be transformed to BN, and hence it shows non-wetting behavior with Si-B alloys. A small amount of BN particles is produced in the Si-B alloys. However, the N solubility is lower than 10 ppm mass. The produced BN is negligible and will not degrade the Si-B alloys. It shows the possibility of using the Si_3N_4 refractory material for building the Si-B alloys' container.

5.1.6. The interaction between the Si-B alloys and h-BN

The equilibrium contact angle between the Si-3.25B alloy and h-BN was 120-135º based on the wetting tests. The formed phases were stable in the Si-3.25B alloys after three thermal cycles. Moreover, no

reaction occurs at the interface. **Figure 5-24** shows the theoretical interaction between Si-3.25B alloy and BN at 1450 ºC, in which X = 0 represents the BN, and X = 1 represents the Si-3.25B alloy. No new phases is expected to form in the Si-3.25B/BN system, which is in accordance with the experimental results.

In the use of BN as the refractory material, the decomposition of BN should be paid attention to the Si-3.25B/BN system. The decomposition of BN can be expressed as follow.

$$2BN(s) = \underline{2B} + N_2(g) \quad 5.15$$

At equilibrium,

$$\Delta G^0 = -RT \ln \frac{P_{N_2} \cdot a_B^2}{a_{BN}^2} \quad 5.16$$

Where a_{BN} is the activity of BN at a solid state, which is assumed to be 1. P_{N2} is the partial pressure of N_2 in the system. a_B is the activity of B in the liquid Si-3.25B alloy. ΔG^0 is the standard Gibbs energy of the decomposition of BN. It is worth noting that ΔG^0 and a_B were calculated by FactSage 7.3 based on the FTlite database.

Figure 5-23 presents the equilibrium partial pressure of N_2 as a function of temperature in the BN decomposition process. It increases with the increase of temperature. The red line shows the equilibrium partial pressure of N_2 is 3.4×10^{-5} atm at 1550 ºC, which means that BN will decompose at a partial pressure of N_2 lower than that in the system. Hence, the control of the partial pressure of N_2 is important in the use of h-BN as the refractory material at high temperatures. In the present wetting test, the value of vacuum is 10^{-4} atm, and hence the partial pressure of N_2 was ~ 7.9×10^{-5} atm, which is higher than the equilibrium partial pressure at 1550 ºC. Therefore, BN is stable in the interaction with the Si-3.25B alloy.

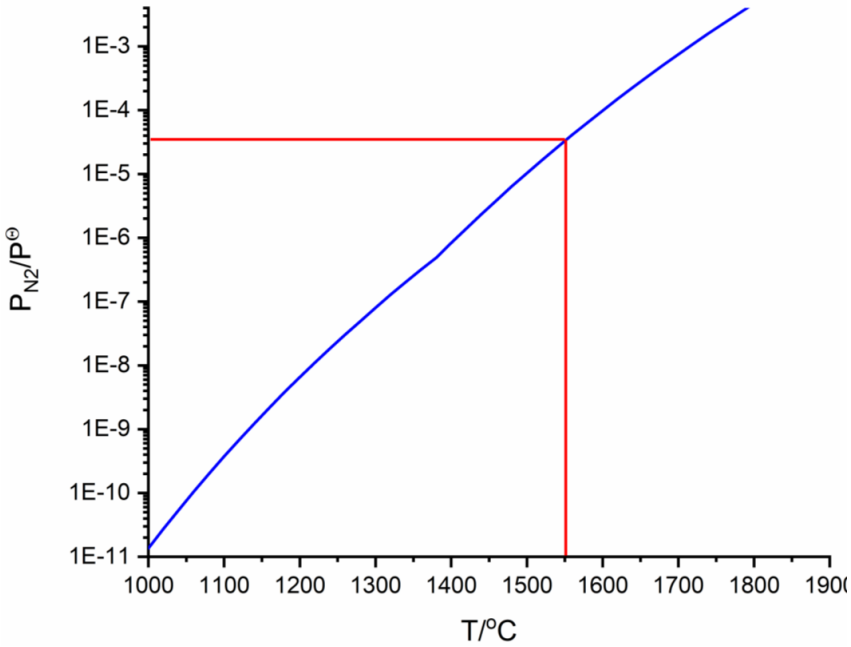

Figure 5-23 The equilibrium partial pressure of N_2, P_{N2} as a function of temperature in the BN decomposition process. Calculated with FactSage 7.3 based on the FTlite and the FactPS databases.

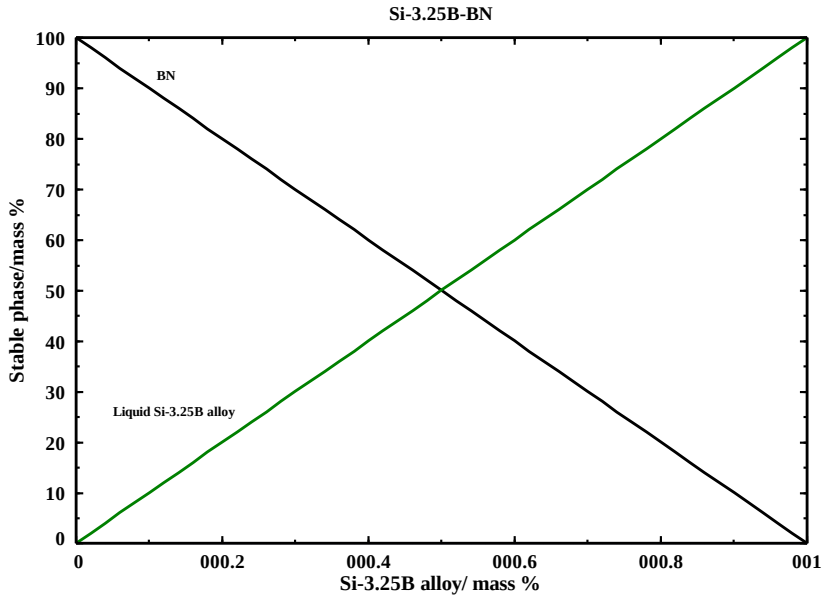

Figure 5-24 The interaction between BN and Si-3.25B alloy at 1450 °C. Calculated with FactSage 7.2 based on the FTlite database.

The contact angle of Si on h-BN was reported to be in the range 90-144° [88]–[90], [92], [93]. Moreover, the wetting behavior of the Si-B alloys on the h-BN substrate was investigated in the B range of 1-5.7 mass %. The equilibrium contact angle was between 131-152° [95]. The equilibrium contact angle of the Si-3.25B alloy on h-BN was measured to 120 and 135°, which is in accordance with the literature. The variations might be caused by the roughness of the substrate surface, type, and the content of impurities in the Si-B/BN system, and the partial pressure of O_2.

In the thermal cycle experiment, the equilibrium contact angle was decreased to 85° in the second thermal cycle and decreased to 63° in the third thermal cycle. The wetting behavior was transformed from non-wetting to good wetting. A SiO_2 layer was observed to be formed at the h-BN surface in the triple point (**Figure 4-33**), which resulted in the continuous decrease of the contact angle. The SiO_2 formation is believed to be caused by the leakage in the sessile drop furnace (SDF-1).

Figure 5-25 shows a schematic presentation of the wettability and reactivity in the Si-3.25B/h-BN system. Due to the leakage there will be some oxygen in the furnace. During heating, CO(g) is produced in the chamber due to the reaction of O_2 and graphite. Then, CO(g) is dissolved into the liquid Si-3.25B alloy, which will increase the O content in the liquid phase. When oxygen is dissolved, SiO(g) will be release to the chamber, as shown in **Figure 5-25**a. As well as the formation of SiO_2, it may be formed at the triple point due to the reaction, $3Si(l) + 2CO \rightarrow SiO_2(s) + SiC(s)$ (**Figure 5-25**b). In the second and third thermal cycles, the liquid Si-3.25B alloy will contact SiO_2 in the triple point, which leads to the decrease of the wetting angle (**Figure 5-25**c).

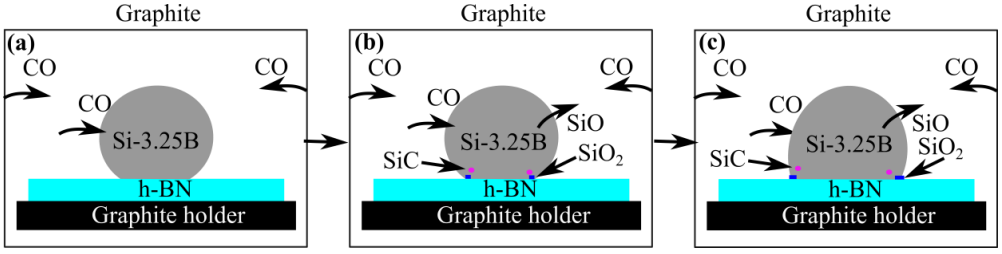

Figure 5-25 A schematic presentation of wettability and reactivity in the Si-3.25B/h-BN system in the thermal cycle experiments. When SiO_2 is formed from the CO in the furnace, the wetting will be changed.

h-BN refractory material, as the PCM container in the TES system, is inert toward the Si-3.25B alloys at high enough N_2 pressures. Hence, only minor amount of dissolved N is introduced to the Si-3.25B alloys, which will not change the chemical composition of the Si-3.25B alloy in the long-term energy storage process. A non-wetting behavior was observed in the Si-3.25B/h-BN system, and it would avoid the liquid Si-3.25B alloy penetrating the h-BN wall and avoid its degradation. The use of BN as the Si-B alloys' container has also been reported by Wojciech et al. [93]–[96], and this shows that h-BN is a potential refractory material to be used in the LHTES system. However, the atmosphere in the TES system is very important. It is better to operate in an N_2 atmosphere, as the equilibrium partial pressure of N_2 is high at temperatures higher than 1800 °C.

5.2. Fe-26Si-9B alloys

5.2.1. Phase stability in the Fe-26Si-9B alloy

Thermodynamic calculations were carried out in order to determine the Fe-Si-B eutectic composition and its melting temperature. **Figure 5-26**-**Figure 5-28** shows the projection of the Fe-Si-B system calculated by FactSage 7.2 based on the FTlilte, FTstel, and Sintef database, respectively. The blue point represents the eutectic point in the Fe-Si-B system and the three red points represent the chemical composition of the master alloys produced and analyzed by ICP-MS, used in the experiments. **Figure 5-26** shows that the eutectic chemical composition is 65 mass % Fe, 26 mass % Si, and 9 mass % B. A eutectic reaction occurs at 1157 ºC, Liquid = FeSi + FeB + SiB_6, in which FeSi, FeB, and SiB_6 will be formed below the melting temperature. However, the eutectic chemical composition is changed to 63 mass % Fe, 26 mass % Si, and 11 mass % B when the FTstel database is used in the FactSage 7.2 (**Figure 5-27**). Moreover, the eutectic reaction happens at 1086 ºC, Liquid = FeSi + FeB + B, which is different with the FTlite database.

As seen in **Figure 5-26** and **Figure 5-27**, no ternary phase is found in the Fe-Si-B phase diagram calculated based on the FTlite and FTstel database. It does not correspond to the published results that the Fe_5SiB_2, $Fe_{14}Si_6B_3$, and $Fe_{10}Si_2B_5$ ternary phases had been determined [69]. In order to deeply understand the Fe-Si-B phase diagram, Kai Tang (Sintef) established a Sintef database based on the published thermodynamic parameters in the Fe-Si-B system [72]. The calculated Fe-Si-B phase diagram is presented in **Figure 5-28**. It is seen that the eutectic point is changed to 63 mass % Fe, 28 mass % Si, and 9 mass % B and the formed phases were the same as in the FTlite database, while the melting temperature of 1082 ºC is lower compared to the results obtained from the FTlite and FTstel databases. The detailed information of the eutectic Fe-Si-B alloy is summarized in **Table 5-2**.

It is known from the FactSage calculations that the chemical compositions are similar in the three different Fe-Si-B phase diagrams, while the melting point is in the range 1082-1157 ºC. FeB, FeSi, SiB_6, and B may be formed under the melting temperature.

For illustrating the phase formation in the solidification process, the cooling path of the Fe-26Si-9B alloy from 1450 °C to 200 °C is calculated based on the FTlite database, as shown in **Figure 5-29**. It is seen from the figure that FeSi, FeB, and SiB_6 are formed at a temperature below 1157 ºC. Then, SiB_3 will be formed at 412 ºC, due to $3FeSi + 4SiB_6 \rightarrow 3FeB + 7SiB_3$. Thus, the formed phases in the solidified alloy should be FeSi, FeB, and SiB_3 at room temperature.

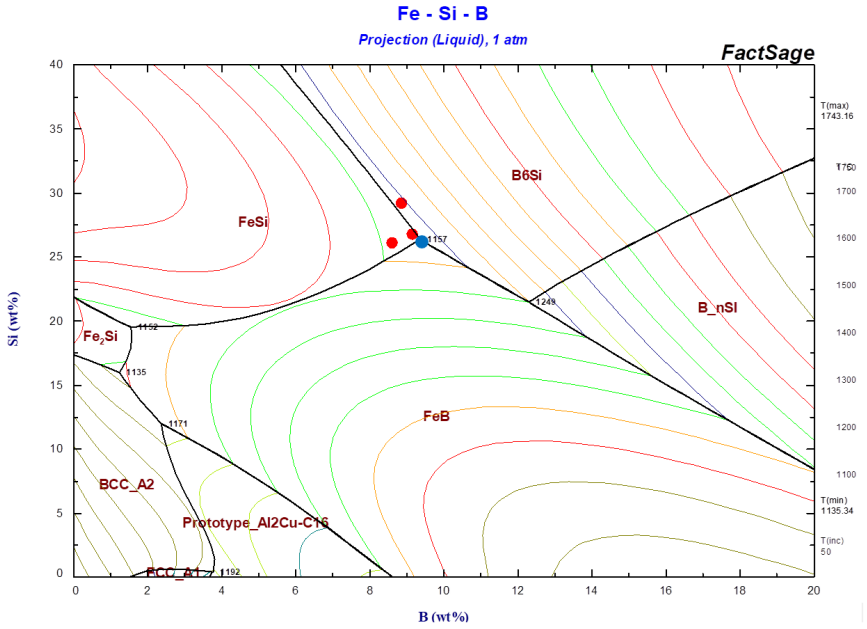

Figure 5-26 Projection of Fe-Si-B system, where red points represent the composition of the prepared master Fe-26Si-9B alloy. Calculated with FactSage 7.2 based on the FTlite database.

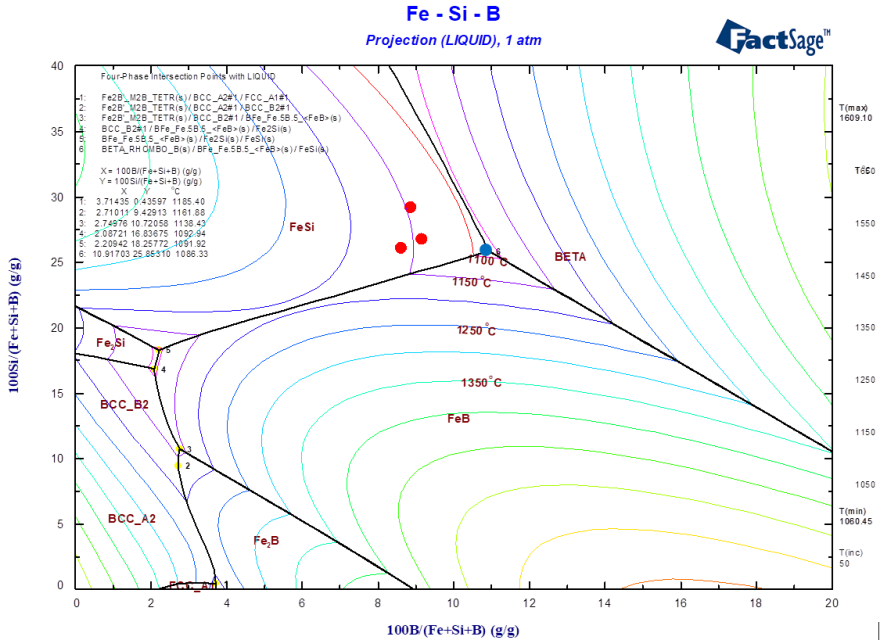

Figure 5-27 Projection of Fe-Si-B system, where red points represent the composition of the prepared master Fe-26Si-9B alloy. Calculated with FactSage 7.2 based on the FTstel database.

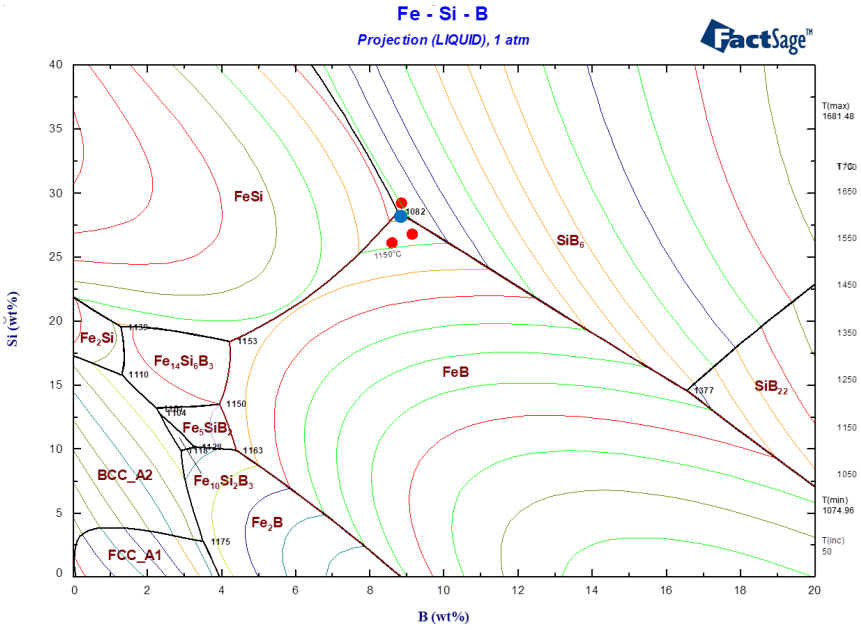

Figure 5-28 Projection of Fe-Si-B system, where red points represent the composition of the prepared master Fe-26Si-9B alloy. Calculated by Kai Tang with FactSage 7.2 based on the Sintef database.

Table 5-2 Comparison of the calculated phases in the Fe-Si-B eutectic alloy in different databases.

	Fe/mass%	Si/mass%	B/mass%	T_m/°C	Eutectic equation
FTlite	65	26	9	1157	Liquid = FeSi + FeB + SiB_6
FTstel	63	26	11	1086	Liquid = FeSi + FeB + B
Sintef*	63	28	9	1082	Liquid = FeSi + FeB + SiB_6

**: Calculated by Kai Tang by FactSage 7.2.*

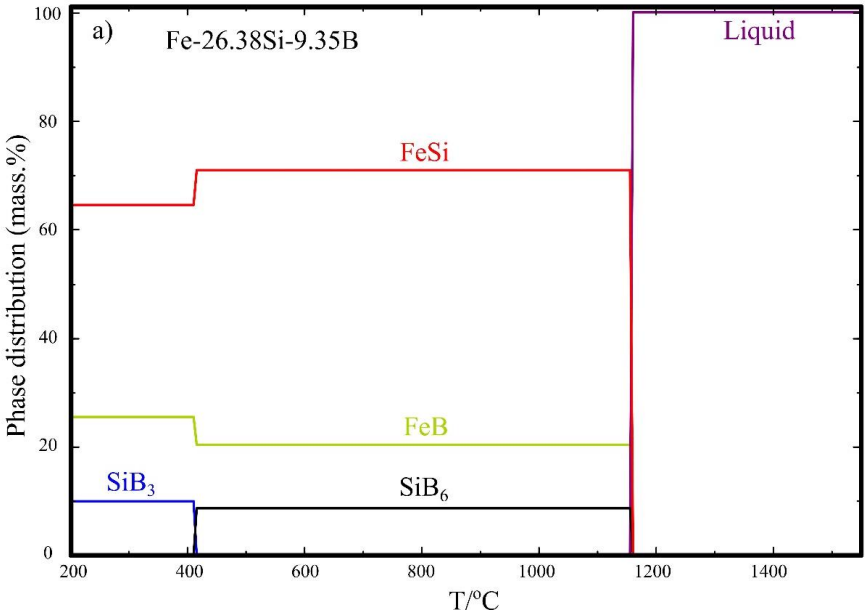

Figure 5-29 Cooling path of the Fe-26.38Si-9.35B alloy. Calculated with FactSage 7.2 based on the FTlite database.

FeSi, FeB, SiB_6, and $FeSiB_3$ were detected in the Fe-26Si-9B alloys after the thermal cycle experiments in the Si_3N_4 crucible. The formed phases in the Fe-26Si-9B alloy were also investigated by Grorud [15], Sindland [17], Jayakumari [121] and Sellevoll [16] in this project. The observed phases in the bulk Fe-26Si-9B alloys are summarized in **Table 5-3**. The average chemical composition of the detected phases accompanied by the standard deviations is summarized in **Table 5-4**. It is worth noting that all the analyzed results were obtained by WDS. It is seen from **Table 5-3** that FeB, Fe_4Si_4B, and $FeSiB_3$ were detected in all samples.

The Fe_4Si_4B is believed to be the FeSi phase. As seen by the XRD pattern in **Figure 5-30**, the offset of the FeSi peak towards left, which was caused by the B dissolution in the FeSi phase. Besides, the Fe_4Si_4B phase showed the same lattice parameter with the FeSi phase (**Figure 4-48**). Hence, ~ 11 at.% B would be dissolved into the FeSi phase in the Fe-26Si-9B alloy.

For the SiB_x phase, SiB_9 was found by Sellevoll [16]. However, the chemical composition of the SiB_9 phase was similar to the SiB_6 phase with ~ 90 at. % B. The measured B content was beyond the reported B range of 85.1-85.9 at. % in the SiB_6 phase, which might be caused by the influence of the C coated at the surface. In addition, the SiB_3 phase was found in the wetting tests on the graphite substrates in FRI. due to a slower cooling rate (30 °C/min). It is known that the phase transformation from SiB_6 to SiB_3 occurs at 1270 °C in the Si-B alloys during cooling, which is very fast. However, this transformation starts at 412 °C in the Fe-26Si-9B alloy. The low temperature may lead to the slow transformation from SiB_6 to SiB_3. Hence, SiB_6 is produced in the bulk alloys.

$FeSiB_3$ is not expected from the calculated phase diagram. The measured average chemical composition of the $FeSiB_3$ phase was 22.0 at % Fe, 20.6 at% Si, and 57.3 at % B, which was different from the other ternary compounds, Fe_5Si_2B, $Fe_{4.7}SiB_2$, and $Fe_2Si_{0.4}B_{0.6}$ described by Aronsson [69]. Therefore, XRD

and TEM analysis was performed to confirm this new ternary phase. As shown in **Figure 4-42**b, the unidentified peaks were detected in the XRD pattern. Moreover, the lattice structure was measured by TEM, and an orthorhombic lattice structure was first detected in the Fe-Si-B system with the following unit cell parameters: a = 4.88 Å, b = 10.22 Å, and c = 5.91 Å.

Table 5-3 Comparison of the formed phases in the Fe-26Si-9B alloys.

Expected phases	FeSi	FeB	-	-	SiB_6	-	-
Grorud [15]	-	FeB	Fe_4Si_4B	$FeSiB_3$	SiB_6	-	-
Sellevoll [16]	-	FeB	Fe_4Si_4B	$FeSiB_3$	-	SiB_9	-
Jayakumari [121]	-	FeB	Fe_4Si_4B	$FeSiB_3$	SiB_6	-	-
The author	-	FeB	Fe_4Si_4B	$FeSiB_3$	SiB_6		SiB_3*

*: Wetting tests at the FRI, Krakow.

Table 5-4 The detected phases in the Fe-26Si-9B alloys after experiments. All the values are obtained by the WDS analysis and have been normalized (at %). [15], [16], [121]

Phase	**Fe**	**Std. Dev.**	**Si**	**Std. Dev.**	**B**	**Std. Dev.**
Fe_4Si_4B	45.5	± 1.2	43.2	± 1.1	11.3	± 1.7
$FeSiB_3$	22.0	± 1.0	20.6	± 1.4	57.3	± 0.4
$FeSiB_2$	27.5	±1.3	26.8	±2.0	45.7	±5.8
FeB	47.7	± 0.9	0.23	± 0.9	52.0	± 0.1
SiB_6	0.31	± 0.1	10.6	± 0.2	89.3	± 0.2
SiB_9	0.49	±0.1	8.9	±0.7	90.6	±0.6
SiB_3	1.5	±0.6	26.0	±1.6	72.5	±2.3

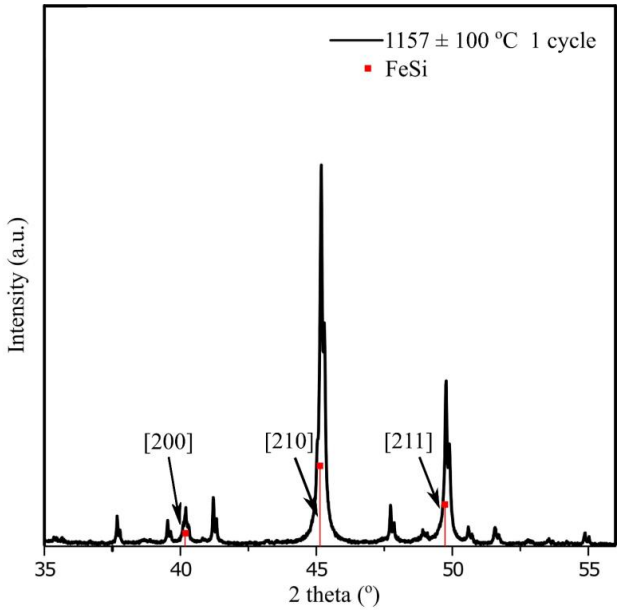

Figure 5-30 An expanded view of the FeSi XRD spectra at the scan range of 35-55°, showing a clear peak shift towards left.

It is seen from **Figure 4-53**b that FeSi and FeB were the primary phases during cooling. With the temperature decreasing, the eutectic structure was formed in the Fe-26Si-9B alloys. According to **Figure 4-36**, the eutectic structure consisted of 40 % $FeSiB_3$ and 60 % FeSi in the low magnification and 44 % $FeSiB_3$ and 56 % FeSi in the high magnification. Combining this with the chemical composition in **Table 5-4**, the chemical composition in the eutectic structure can be calculated. The results are shown in **Table 5-5**. Hence, the eutectic point was calculated to be about 36 at. % (61 mass %) Fe, 34 at. % (29 mass %) Si, and 31 at. % (10 mass %) B. It is not so different from the theoretical eutectic point of 39 at. % (64 mass%) Fe, 32 at. % (26 mass %) Si, and 29 at. % (9 mass %) B.

Figure 5-31 shows the obtained DSC curve of the Fe-26Si-9B alloy under Ar flow. It is seen from the cooling curve that the liquid Fe-26Si-9B alloy started to be solidified at 1276 ºC following the first precipitated phase formed in the alloy. When the temperature descending to 1235 ºC, the second precipitated phase was formed in the alloy. With the further decrease to 1208 ºC, the eutectic reaction occurred. It is in good accordance with our experimental results that there is some primary phases formed (FeB and FeSi) before the eutectic point.

Table 5-5 The chemical composition in the eutectic structure. [at. %]

$FeSiB_3$	FeSi	Fe	Si	B
40	60	36	34	30
44	56	35	33	32
Average		36	34	31

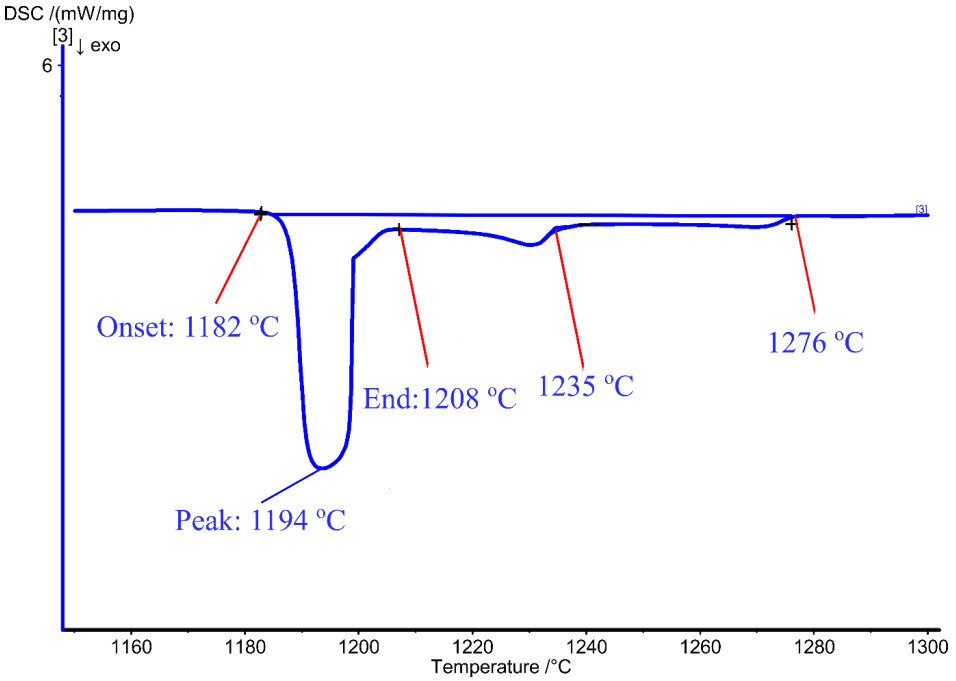

Figure 5-31 The part of the DSC curve for Fe-26Si-9B alloy under Ar.

The liquidus and solidus temperature of the Fe-26Si-9B alloy in the heating and cooling steps were summarized in **Figure 5-32**, in which the values on the left of the blue dotted line were obtained from the wetting tests and on the right were obtained from the DSC tests. It is seen that the Fe-26Si-9B alloy started to melt at ~ 1223 ºC, while it was completely melted at ~ 1254 ºC. There is scatter for the measured liquidus temperature, from 1228 ºC to 1280 ºC. The outlayer at 1350 ºC is believed to be due to some melting issues that will be discussed later. In the cooling steps, the liquid Fe-26Si-9B alloy started to solidify at ~ 1193 ºC and completely solidified at ~ 1171 ºC. This might be caused by the undercooling effect in the solidification process, due to the fast cooling rate of 10 ºC/min in the DSC tests.

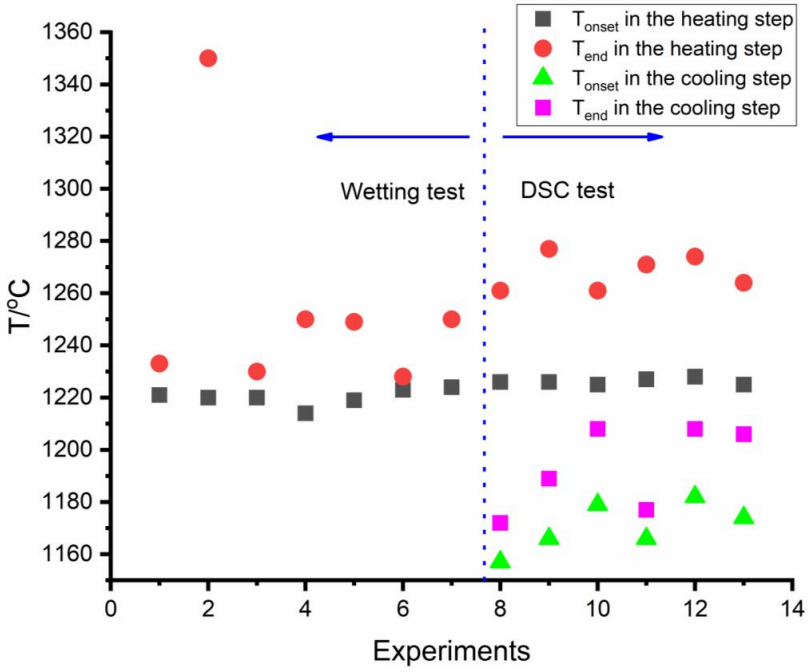

Figure 5-32 Summary of the measured liquidus and solidus point in the Fe-26Si-9B alloys in the heating process.

Figure 5-33 shows the formed phases in the bulk Fe-26Si-9B alloy after thermal cycle experiments. It is seen from **Figure 5-33**a that FeSi, FeB, and $FeSiB_3$ were formed in the bulk alloys after 6 thermal cycles at 1100-1300 ºC in the Si_3N_4 crucible, in which the main morphology was the eutectic structure. A small amount of SiB_6 was found in this area. Grorud [15] performed the thermal cycle experiments in the graphite crucible during the solidification and melting process, in which 1 thermal cycle was run at 1157 ± 20 °C, the detected formed phases are presented in **Figure 5-33**b. Later, Sellevoll [16] investigated the interaction of the Fe-26Si-9B alloy with graphite under long-term thermal cycles. The Fe-26Si-9B master alloy was subjected to the temperature range of 1137-1550 ºC for thermal cycles, in which a holding time of 3h was kept at the highest and lowest temperatures. 16 thermal cycles were conducted in the running of one experiment over 5 days. The observed microstructure is shown in **Figure 5-33**c. Moreover, in the production of the Fe-26Si-9B prototypes, the thermal cycle experiments were carried out in an induction furnace, in which three temperature cycles from 1120-1375 ºC was

performed by Jayakumari [121], the detected phases are shown in **Figure 5-33**d. Compared with **Figure 5-33**a-d, it is found that the formed phases did not change, which is independent of the thermal cycle times, the refractory materials, and the size of the containers.

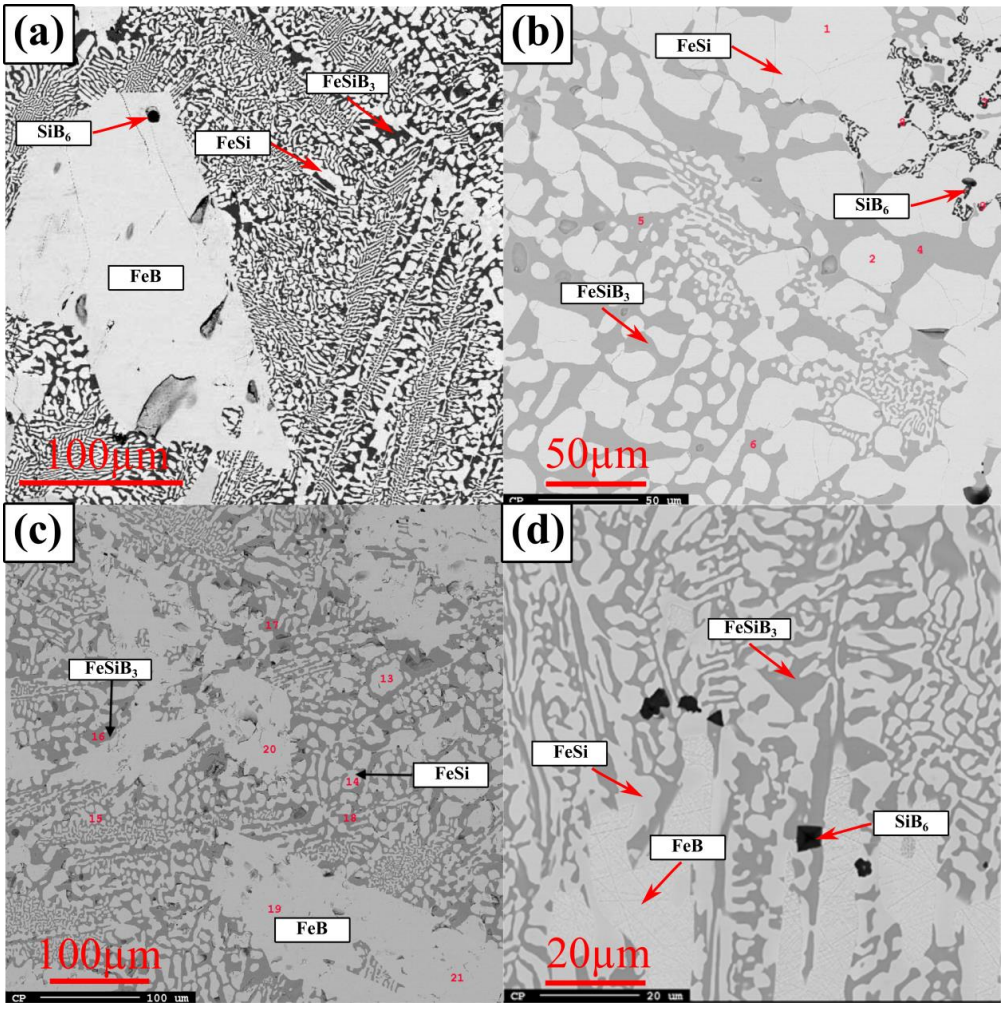

Figure 5-33 Images of the formed phases in the bulk Fe-26Si-9B alloys after thermal cycle experiments. (a) 6 cycles at 1100-1300 ºC in the Si_3N_4 crucible; (b) 1 cycle at 1137-1177 ºC in the graphite crucible [15]; (c) 5 days cycles at 1137-1550 ºC in the graphite crucible [16]; (d) 3 cycle in the Fe-Si-B prototype in the graphite crucible [121].

In the use of the resistance furnace, C was introduced to the Fe-26Si-9B alloy, which leads to the formation of B_4C and SiC at the top position of the alloy. **Figure 5-34** shows the microstructures of Fe-26Si-9B alloy at the top position. **Figure 5-34**a was obtained from the experiment in the Si_3N_4 crucible. **Figure 5-34** b and c were obtained from the experiments in the graphite crucible [17]. The formed SiC and B_4C particles were not detected in the bulk of the samples. This phenomenon might be explained by the fact that the density of the liquid Fe-26Si-9B alloy, B_4C, and SiC are 4.38 g/ml, 2.52 g/ml, and 3.217g/ml [122]. Hence, the B_4C and SiC particles would float to the top of the liquid alloy in the

cooling process due to their lower density. Moreover, it is found that the number of SiC and B_4C particles were not increased with increasing thermal cycles and holding times. The pollution of C, forming carbides, is believed to be due to the pollution from other graphite parts in the furnace as discussed for the Si-B alloys.

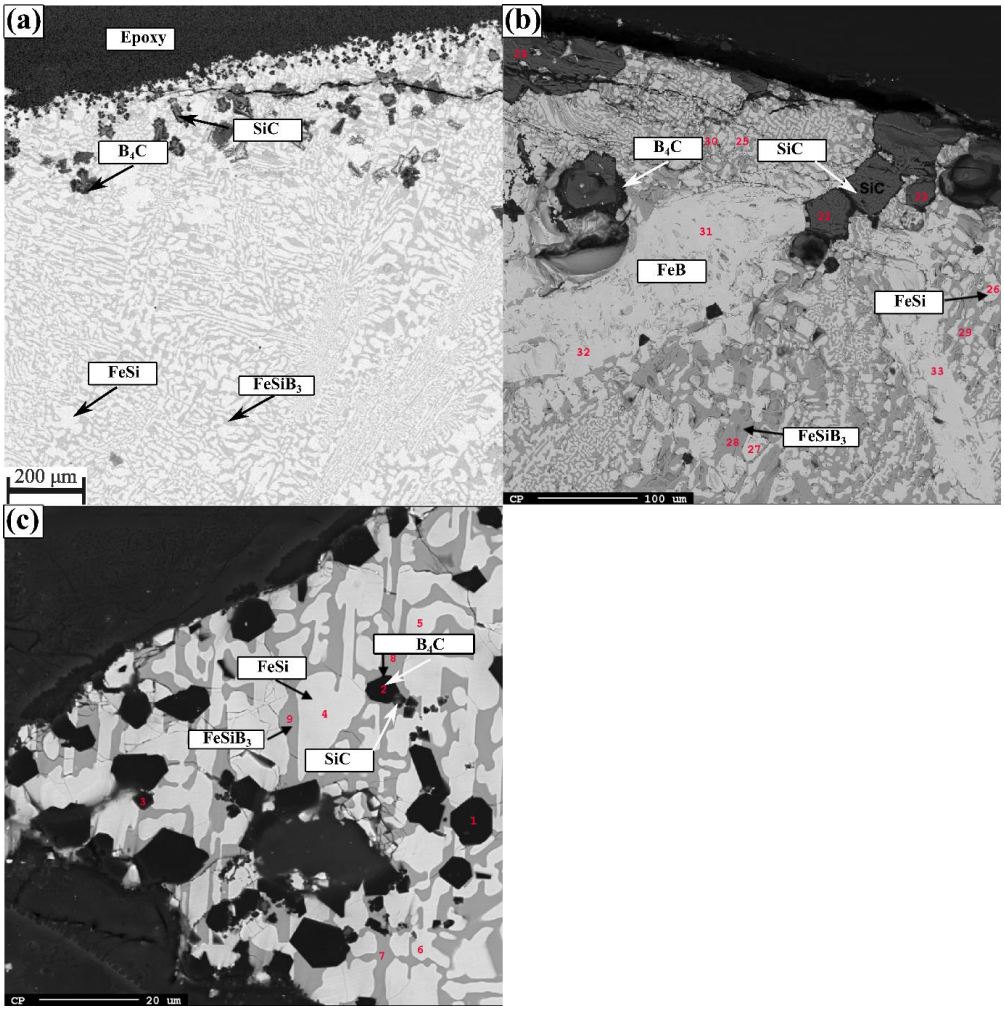

Figure 5-34 Images at the top position of the Fe-26Si-9B alloys. (a) 6 cycles at 1100-1300 ºC; (b) holding of 1 h at 1250 ºC [16]; (c) 5 days thermal cycles in the temperature varies between 1137 ºC and 1550 ºC [16].

In the use of the Fe-26Si-9B alloys in the TES systems, the formed phases are stable in the long- term energy storage process. Moreover, the liquid Fe-26Si-9B alloy shrunk during cooling, which is considered to be a desirable property. It shows the possibility of using the Fe-Si-9B alloy as the PCM. The Fe-Si-B eutectic alloy was calculated to be Fe-29Si-10B and its eutectic melting temperature is believed to be ~ 1223 ºC. Hence, the Fe-29Si-10B is suggested to be used as the PCM in the TES systems.

5.2.2. The interaction between Fe-26Si-9B alloy and graphite

In the interaction between the Fe-26Si-9B alloy and graphite substrate, a continuous SiC layer was formed close to the graphite and a continuous B_4C layer was formed close to the Fe-26Si-9B alloy. **Figure 5-35** illustrates the phase evolution upon heating the (Fe-26Si-9B)-99 mass % C alloy, in which only 1 mass % Fe-26Si-9B alloy is added to the system. It shows the phase formation in the graphite part in the heating process. At low temperatures, FeSi, C, FeB, SiC are present in the system, and then FeB and FeSi are transformed into a liquid phase at high temperatures. As shown, SiC is the only formed carbide close to the graphite. The calculated result has good accordance with the experimental results, in which graphite and SiC will coexist in the graphite part.

Figure 5-36 illustrates the phase evolution upon heating the (Fe-26Si-9B)-0.01 mass % C alloy illustrating the surface of the graphite crucible. As shown, B_4C will be formed in the Fe-26Si-9B alloy in the heating step. Moreover, the amount of B_4C decreases with the increasing temperature, and then it disappears at temperatures over 1450 °C. **Figure 5-37** shows the interface between the Fe-26Si-9B alloy and graphite substrate after two thermal cycles at 1175 ± 50 °C under 10^{-5} atm. It is seen that a continuous B_4C layer was formed close to the Fe-26Si-9B alloy.

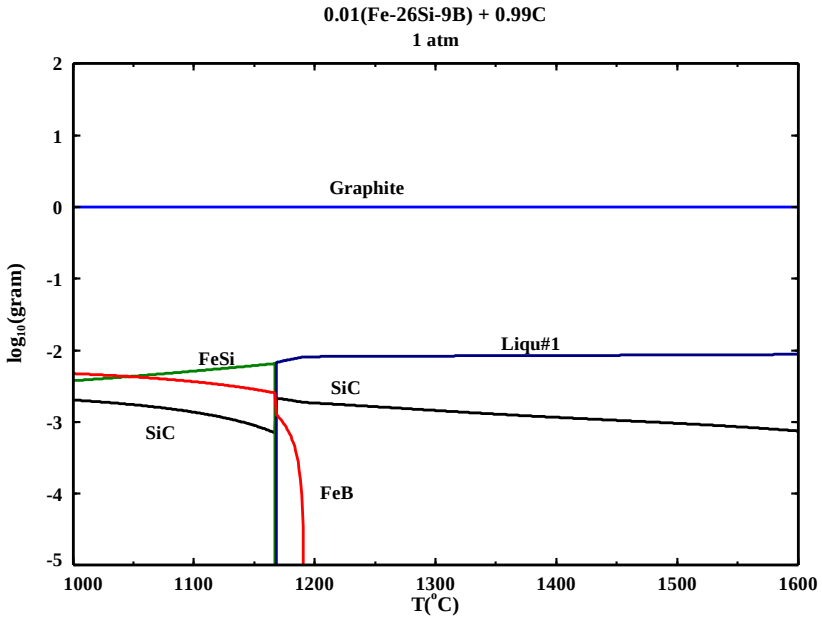

Figure 5-35 Calculated phase evolution upon heating the (Fe-26Si-9B)-99 mass % C system. Calculated with FactSage 7.3 based on the FTlite database.

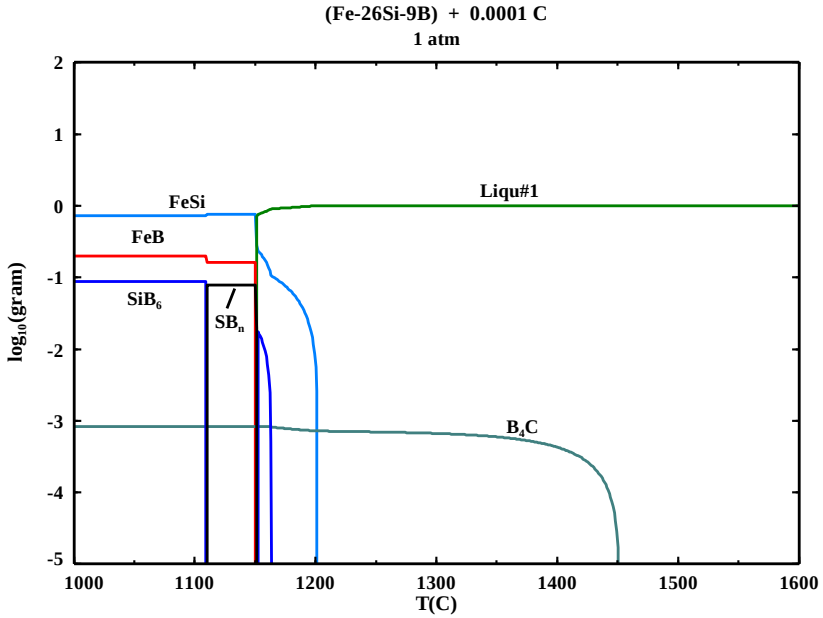

Figure 5-36 Calculated phase evolution upon heating the (Fe-26Si-9B)-0.01 mass % C system. Calculated with FactSage 7.3 based on the FTlite database.

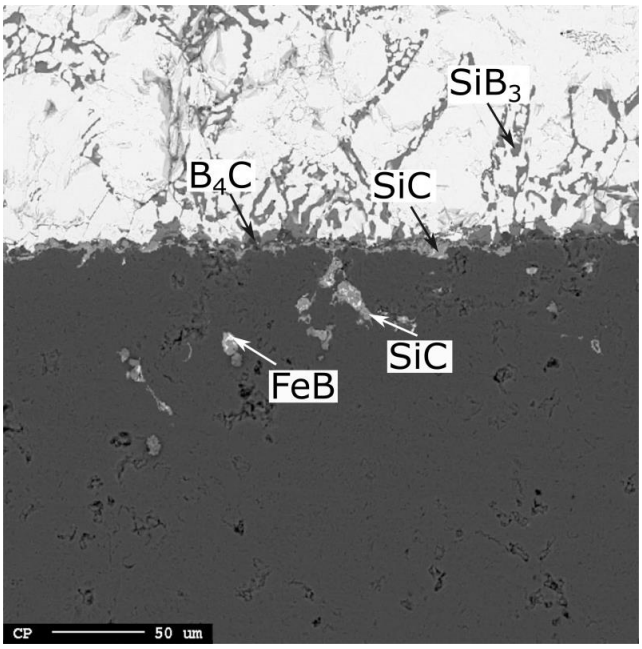

Figure 5-37 The distribution of phases at the interface between the Fe-26Si-9B alloy and graphite substrate after two thermal cycles at 1175 ± 50 °C under 10^{-5} atm.

The equilibrium contact angle was in the range 31-48°, which shows a good wetting between the liquid

Fe-26Si-9B alloy and the formed SiC layer. It is known that the wetting angle of pure Fe on graphite exhibited good wetting at 1300–1500 °C, with 0–66° under different atmospheres [97]–[100]. For the Fe-Si/graphite system, the contact angle was less than 40° in the Si range 25-98.5 mass % [88], [102], which shows a good agreement with our results. Gao et al. [37] measured the contact angles of the Fe-5.3Si-3B alloy on the SiC substrate under vacuum. The contact angle was measured to be ~ 100° on the SiC substrate at 1150–1360 °C. The value of the contact angle had a considerable difference with our experimental result. Firstly, it might be caused by the chemical composition in the Fe-Si-B alloys. However, the content of Si and B in the Fe-5.3Si-3B alloy was lower than in the Fe-26Si-9B alloy and higher than in the pure Fe metal. Hence, the contact angle might be between the valued obtained from the Fe-26Si-9B alloy and pure Fe, which was in the range 0-66°. Secondly, it might be caused by the C content in the alloys. Sun et al. [99] reported that the wetting was highly affected by the C content in the liquid Fe, in which the value of the contact angle would be increased from 60° to ~ 120° at 1400 °C when the initial C content was increased from 0 to 4.8 mass %. The contact angle of 100° might be caused by the high C content in the Fe-5.3Si-3B alloy. Lastly, it also might be caused by the roughness of the substrate, and the atmospheres.

The formation of SiC is dependent on the activity of Si. The wetting tests showed that the eutectic Fe-26Si-9B alloy displayed good wetting on the graphite substrate. The contact angle was changed from the initial contact angle of ~ 138° to the equilibrium contact angle of ~ 31°, in which the layer phase was changed from graphite to SiC. In the Si-based alloys, the formation of SiC was caused by the reaction of Si and C at the interface.

$$Si(l) + C(s) = SiC(s) \tag{5.17}$$

Therefore, the Gibbs energy can be expressed as follow:

$$\Delta G = \Delta G^0 + RT \ln \frac{a_{SiC(s)}}{a_{C(s)} \cdot a_{Si(l)}} \tag{5.18}$$

Where, ΔG^0, $a_{SiC(s)}$, and $a_{C(s)}$ are constant at a given temperature. Hence, the activity of Si ($a_{Si(l)}$) affects the formation of SiC. The higher Si activity, the lower ΔG, and hence it is easier to form SiC phase in the alloys.

Figure 5-38 shows the activity of Si in the Si-3.25B alloy and Fe-26Si-9B alloy in the temperature range of 1000-1600 °C, in which the blue line represents the equilibrium activity of Si for the formation of SiC. It is seen that the activities of Si in the Si-based alloys are higher than the equilibrium activities of Si in coexistence with SiC. Therefore, SiC will be formed in the use of graphite as the crucible for both the Si-3.25B and the Fe-26Si-9B alloy. Moreover, the activity of Si in the Si-3.25B alloy is higher than that in the Fe-26Si-9B alloy, the formation of SiC is easier in the Si-3.25B alloy and it explains that the Fe-26Si-9B alloy have almost no SiC in the bulk area.

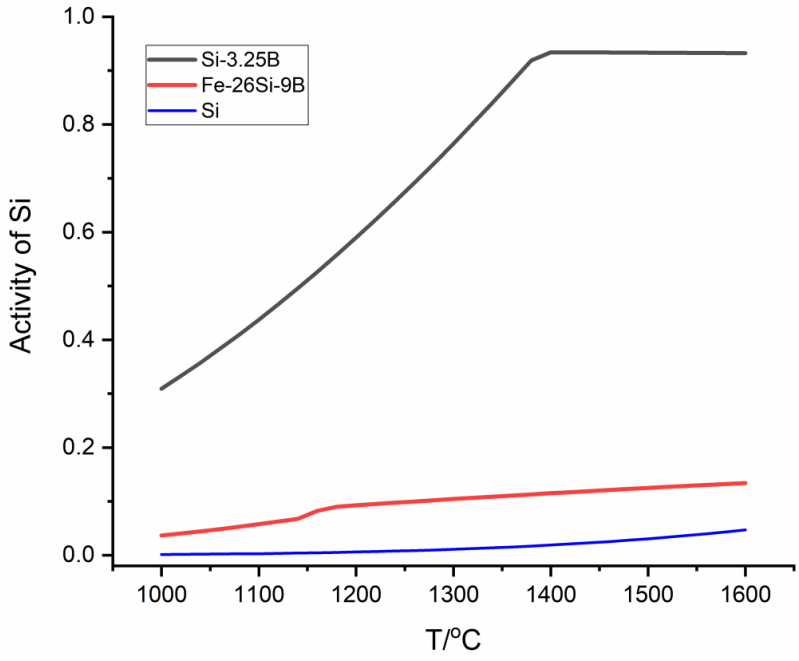

Figure 5-38 Activities of Si in Si-3.25B and Fe-26Si-9B alloys compared to the equilibrium activities of Si in coexistence with SiC. Calculated with FactSage 7.3 based on the FTlite database.

In the use of graphite as the Fe-26Si-9B PCM's container in the TES systems, the protective layer of SiC and B_4C were formed between the Fe-26Si-9B alloy and graphite, which could be a protective layer to hinder the penetration from the PCM to graphite wall. The chemical wear or dissolution of the crucible is negligible. Moreover, it displays a good wetting behavior on the graphite, which makes the liquid alloy adhering to the graphite. It demonstrates the viability of graphite as the refractory material in the Fe-26Si-9B PCM.

5.2.3. The interaction between Fe-26Si-9B alloy and Al_2O_3

The equilibrium contact angle was ~ 120° between the Fe-26Si-9B alloy and Al_2O_3, which shows a non-wetting behavior. No Al-based phases was formed in the Fe-26Si-9B alloy and no penetration was observed in the Al_2O_3 side. However, the Fe-26Si-9B alloy adhered to the Al_2O_3 after solidification and an oscillation phenomenon occurred at a temperature higher than 1450 °C.

Figure 5-39 illustrates the phase evolution in the (Fe-26Si-9B)-Al_2O_3 system, in which 1g Fe-26Si-9B alloy is mixed with 0.5g Al_2O_3 and 0.1g Ar. **Figure 5-40** shows the magnification area for the

$(Al_2O_3)_9(B_2O_3)_2$, Mullite ($Al_6Si_2O_{13}$), and the gas phases. It is seen that the $(Al_2O_3)_9(B_2O_3)_2$ is formed at ~ 1170 °C and disappeared at ~ 1240 °C. Subsequently, the Mullite ($Al_6Si_2O_{13}$) is produced in the system. Hence, it shows that Al_2O_3 will react with the Fe-26Si-9B alloy at temperatures higher than 1170 °C. It is in accordance with our finding that the oxides were formed at the surface of the Fe-26Si-9B alloy after heating to 1450 °C in the Al_2O_3 crucible (**Figure 4-80**). The adherence between the alloy and Al_2O_3 crucible might be caused by the formation of Mullite.

The gas content is constant at temperatures below 1410 °C, and then it increases with the increase of temperature. It is caused by the formation of SiO gas, due to the reaction: $SiO_2(s) + Si(l) = 2SiO(g)$. This explains the oscillation phenomenon that occurred at high temperatures.

In the use of Al_2O_3 as the Fe-26Si-9B alloy's container in the TES systems, Al_2O_3 will react with Fe-26Si-9B alloy to form $Al_6Si_2O_{13}$. With a long-term melting/solidification process, the chemical composition of the Fe-26Si-9B alloy will be changed. SiO gas will be formed at temperatures higher than 1410 °C. Hence, Al_2O_3 cannot be used as the refractory material for the Fe-26Si-9B alloy. It can also be mentioned that Al_2O_3 has a high volume expansion (5.5×10^{-6}-7.5×10^{-6} K^{-1} [123]) and may break during heating and solidification.

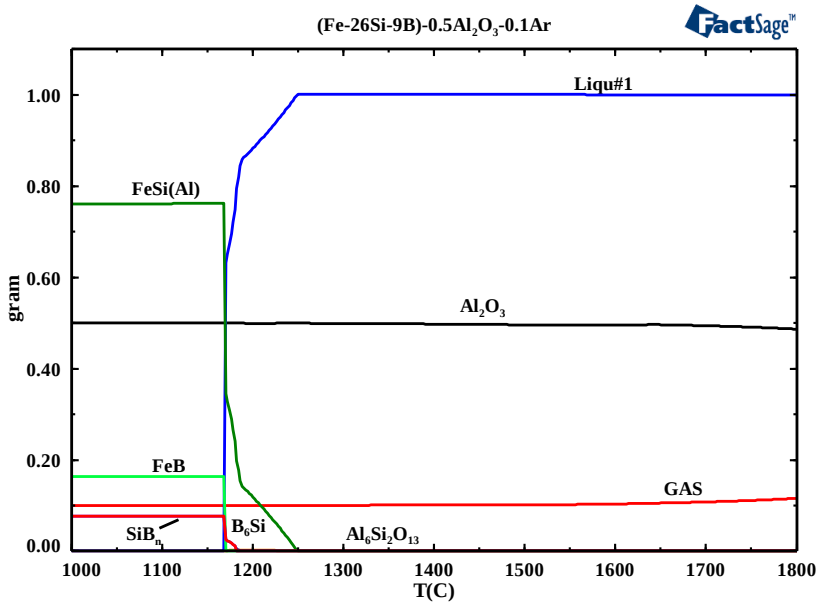

Figure 5-39 Calculated phase evolution in the (Fe-26Si-9B) + 0.5C+0.1Ar system. Calculated with FactSage 7.3 based on the FactPS and the FTlite database.

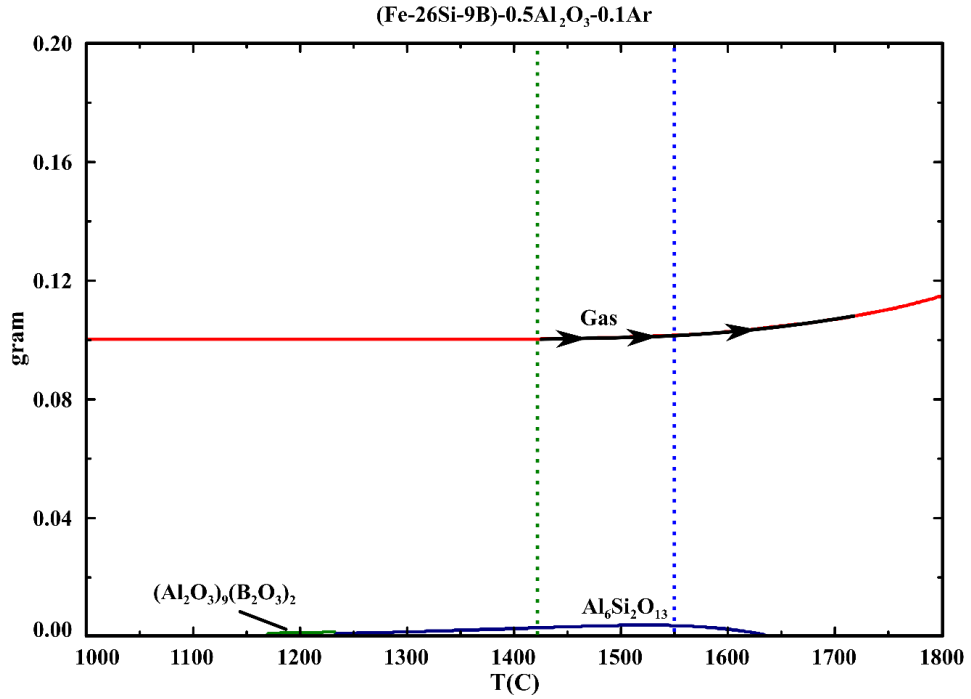

Figure 5-40 Calculated phase evolution in the (Fe-26Si-9B) + 0.5C+0.1Ar system in the magnification state. Calculated with FactSage 7.3 based on the FactPS and the FTlite database.

5.2.4. The interaction between Fe-26Si-9B alloy and h-BN

In the thermal cycle experiment of the Fe-26Si-9B alloy on h-BN, the equilibrium contact angle was measured to be ~ 142° in the first thermal cycle. No nitride phase was detected in the Fe-26Si-9B alloy. Moreover, the penetration from the liquid alloy into the h-BN was limited.

Figure 5-41 shows the theoretical interaction between the Fe-26Si-9B alloy and BN at 1550 °C, in which X = 0 presents the BN and X = 1 represents the Fe-26Si-39B alloy. It is seen that no reaction will occur in the Fe-26Si-9B/BN system. Gao *et al.* [103] measured the contact angles of the liquid Fe-5.3Si-3B on the h-BN under vacuum. The contact angle of 140°-147.5° was observed in the temperature range 1160-1360 °C. Moreover, the contact angle of the liquid Si on the h-BN was measured by Drevet *et al.* [92] lying between 114° and 136° under vacuum. Both of them are in accordance with our experimental results. Significantly, the formation of Si_3N_4 was found at the interface in the Si/BN and Fe-5.3Si-3B/BN systems, while it was not found in our experiment. Besides, Wojciech *et al*. [93] investigated the wetting behavior between the liquid Si and h-BN. The Si_3N_4 was not detected at the interface in the Si/h-BN system, while the SiC particle was found at the interface. What they claimed is that the formation of the SiC was caused by the C pollution of the h-BN substrate, which was dissolved into the liquid Si from

the h-BN substrate in the heating process.

In the present Fe-26Si-9B/BN system, the BN may decompose into the dissolved B in the alloy and N_2 gas. The equation of the decomposition of the BN has been expressed earlier. Hence, the equilibrium partial pressure of N_2 as a function of temperature in the Fe-26Si-9B/BN system can be calculated based on the following equation. $\Delta G^0 = -RT \ln \frac{P_{N_2} \cdot a_B^2}{a_{BN}^2}$ 5.16

Figure 5-43 presents the equilibrium partial pressure of N_2 as a function of temperature in the BN decomposition process in the Fe-26Si-9B/BN system. It shows a similar tendency with that in the Si-3.25B/BN system. As shown, the equilibrium partial pressure of N_2 increases with the increase of the temperature. The red line shows that the equilibrium partial pressure of N_2 is 3.6×10^{-5} atm at 1550 ºC, which means that the BN will be decomposed at a partial pressure of N_2 lower than that in the system. In our experiment, the wetting test was performed under the vacuum of 10^{-4} atm. Hence, the partial pressure of N_2 was ~ 7.9×10^{-5} atm in the chamber, which is higher than the equilibrium partial pressure of 3.6×10^{-5} atm. Therefore, the BN will not be decomposed in the wetting test.

A slight vibration was observed in the whole wetting process, which indicates that the gas was released at the three phases contact area. As has been described in the Si-3.25B/h-BN system, CO(g) is produced in the wetting test due to the reaction of O_2 and graphite. The behavior for the Fe-26Si-9B/h-BN system can be explained as follows. CO(g) will be dissolved into the liquid Fe-26Si-9B alloy and the C and O content will be increased (**Figure 5-42**(a)). When oxygen is dissolved, SiO(g) will be release to the chamber (**Figure 5-42**(b)), which causes the vibration of the drop. The SiC was formed at the surface of the h-BN during cooling (**Figure 5-42**(b)). In the second cycle, the formed SiC was moved to the triple point, leading to the contact angle decrease. Then, in the third cycle, the equilibrium state was broken, causing an abrupt increase in the contact angle again.

In conclusion, h-BN is a potential refractory material to be used as the container for Fe-26Si-9B alloy in the TES system. The operating system should be at high enough N_2 pressure, as the BN will be decomposed at low N_2 pressure. The non-wetting behavior of the Fe-26Si-9B alloy on h-BN was observed, and it would avoid the penetration of the liquid Fe-26Si-9B alloy and avoid the h-BN's degradation.

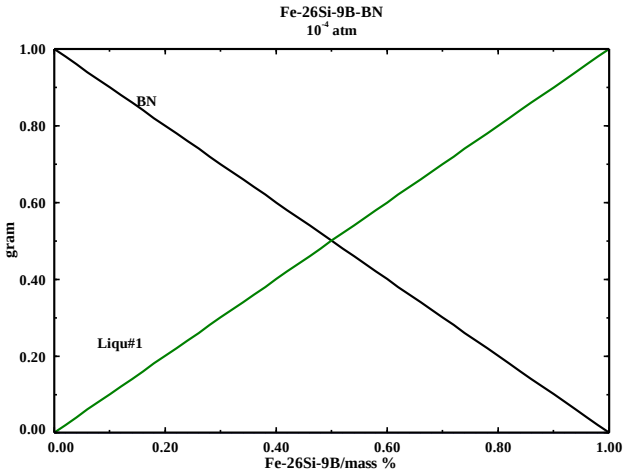

Figure 5-41 The interaction between BN and Fe-26Si-9B alloy at 1550 °C under 10^{-4} atm. Calculated with FactSage 7.3 based on the FTlite database.

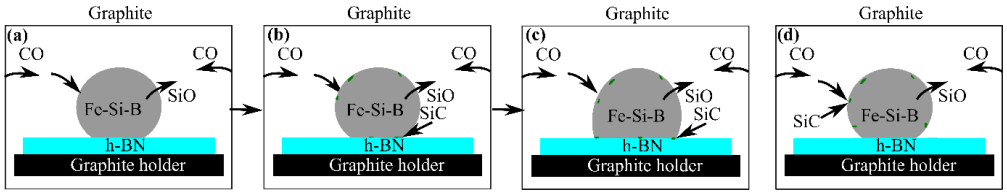

Figure 5-42 A schematic presentation of wettability and reactivity in the Fe-26Si-9B/h-BN system in the thermal cycle experiments.

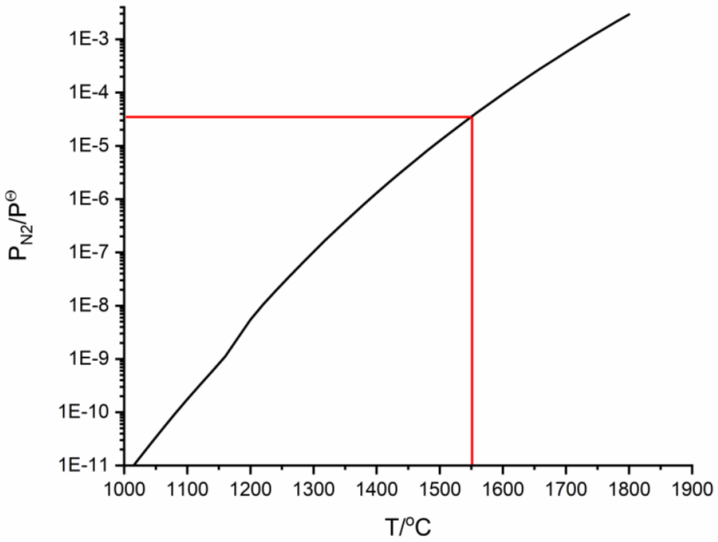

Figure 5-43 The equilibrium partial pressure of N_2, P_{N2} as a function of temperature in the BN decomposition process in the Fe-26Si-9B/BN system. Calculated with FactSage 7.3 based on the FTlite and the FactPS databases.

5.2.5. The melting issues of the Fe-26Si-9B alloy

In the investigation of the Fe-26Si-9B alloy, there was a challenge melting the Fe-26Si-9B particles. The Fe-26Si-9B master alloy seems to be not completely melted above its melting temperature (1220 °C) under Ar flow, while it was melted well under the vacuum of 10^{-4} atm, 10^{-5} atm, and 10^{-9} atm.

The melting issues might be caused by the formed carbides layer at the surface of the Fe-26Si-9B alloy. **Figure 5-44** a and b show the SEM images at the surface of the Fe-226Si-9B alloy after the experiments under Ar flow. The Fe-26Si-9B alloys seem not to be melted at temperatures up to 1250 °C. It is seen that the formed B_4C and SiC particles were covering the surface, which blocked the free surface movement of the alloy. **Figure 5-44** c shows the SEM image at the surface of the Fe-26Si-9B alloy after the wetting test in the SDF-1 furnace under 10^{-4} atm. Moreover, **Figure 5-44** d shows the SEM image at the surface of the Fe-26Si-9B alloy after the wetting test in the SDF-2 furnace under 10^{-5} atm. These alloys started to melt at 1220 °C. It is seen that FeSi, FeB, and $FeSiB_3$ were formed at the surface. In addition, SiC was found at the surface in **Figure 5-44** c, due to the C pollution from the SDF-1 furnace. However, it did not affect the melting of the alloy as the mass of it was much lower compared to the experiments under Ar flow. According to the observation of the microstructure in **Figure 5-44** a-d, it indicates that the carbide layer was formed at the surface in the heating process, and then it hindered the free surface movements. From a visual point of view it then seems like the sample was not molten.

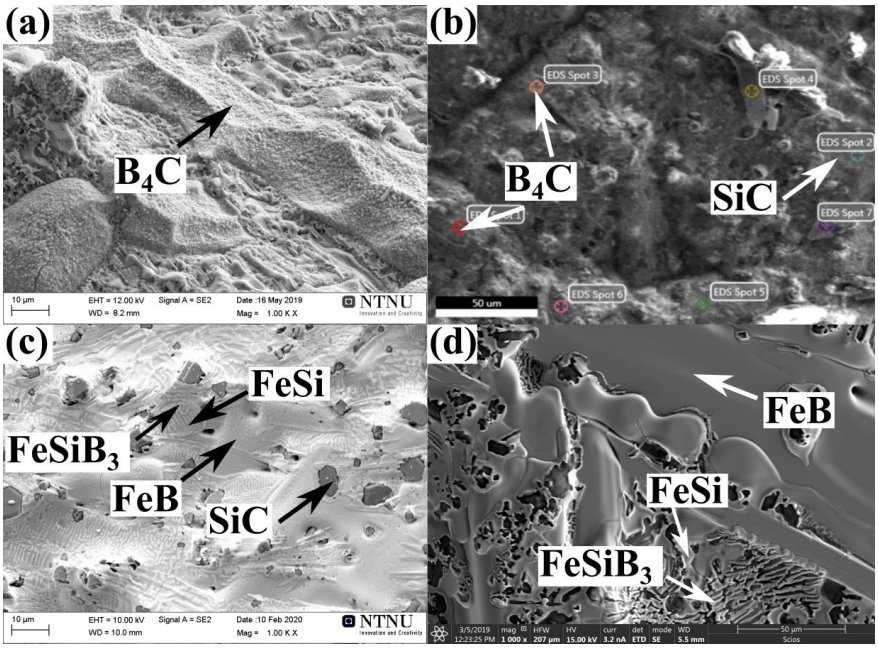

Figure 5-44 SEM images at the surface of the Fe-26Si-9B alloy. (a) heating to 1250 °C on the graphite substrate under Ar; (b) heating to 1250 °C in the graphite crucible under Ar [16]; (c) heating to 1450 °C on the graphite substrate under 10^{-4} atm; (d) heating to 1250 °C on the graphite substrate under 10^{-5} atm.

Formed oxides might also result in the melting issue for the Fe-26Si-9B alloy. **Figure 5-45** and **Figure 5-46** show the calculated phase evolution in the Fe-26Si-9B/CO system under 1 atm and 10^{-4} atm, respectively. It is seen from the figures that SiO_2 and B_4C phases were formed at low temperatures. At high temperatures, the formed SiO_2 phase was still in the system at the atmosphere of 1 atm, while it was transformed into SiO gas at the vacuum of 10^{-4} atm. It indicates that SiO_2 could also be the reason that hindered the melting of the Fe-26Si-9B alloy. The O content was measured to be lower than 12 at. % at the surface of the solidified Fe-26Si-9B alloy (**Table 4-4**). However, O belongs to the light element group that is not easy to be detected by EDS. Hence, any quantification of phases involving O has huge uncertainties. To sum up, the challenge melting of the Fe-26Si-9B particles might be caused by both the carbides and oxides formed at the surface.

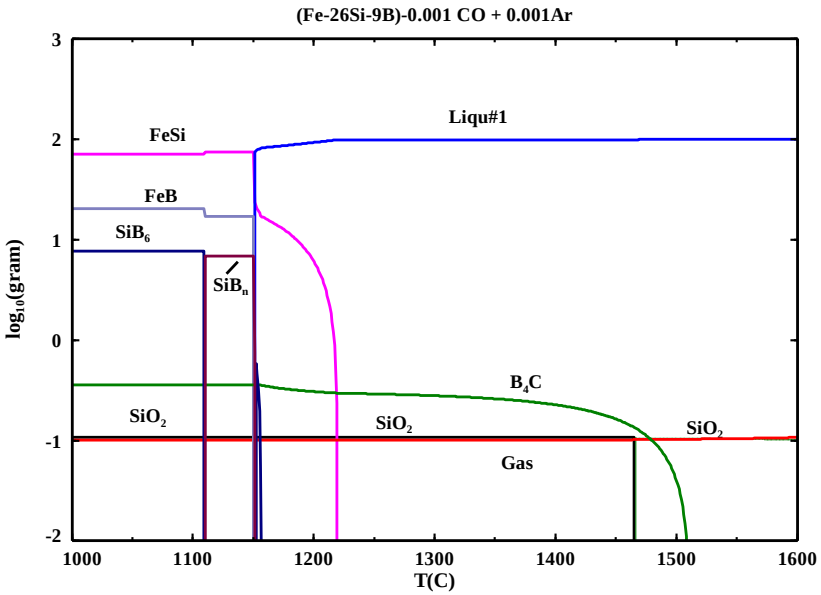

Figure 5-45 Calculated phase evolution in the (Fe-26Si-9B) + 0.001CO system under 1 atm. Calculated with FactSage 7.3 based on the FactPS and the FTlite database.

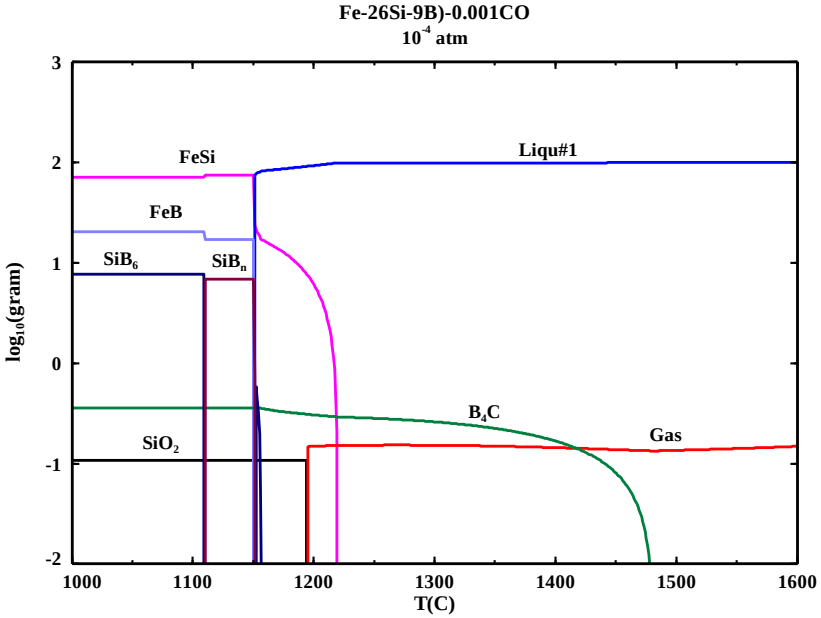

Figure 5-46 Calculated phase evolution in the 1g (Fe-26Si-9B) + 0.001CO system under 10^{-4} atm. Calculated with FactSage 7.3 based on the FactPS and the FTlite database.

5.3. Cr-43Si-5B alloys

5.3.1. Phases stability in the Cr-43Si-5B alloys.

$CrSi_2$, CrB_2, Cr_3B_4, and Si were formed in the Cr-43Si-5B alloy after the thermal cycle experiment in a graphite crucible. The projection of the Cr-Si-B ternary system is shown in **Figure 5-47**, which is calculated in FactSage 7.2 based on the FTlite database. The colored lines correspond to the isothermal curves in the temperature range 1000-2000 °C. Twelve four-phase invariant points are labeled in the figure. It is seen that no ternary compound is formed in the Cr-Si-B system. Experimentally, a ternary phase identified as $D8_8$ with a stoichiometric composition of Cr_5Si_3B was reported by Nowotny et al. [124]. Later, Chad et al. [125] investigated the Cr-rich region of the Cr-Si-B system and did not find this ternary phase in their experimental results. Hence, it is believed that no ternary phase was formed in the Cr-Si-B system.

Of particular, point 9 (red circle) represents a eutectic reaction at 1414 °C with the chemical composition of 52.2 mass % Cr. 43.1 mass % Si, and 4.7 mass % B.

$$liquid \rightarrow CrB_2 + Cr_3B_4 + CrSi_2 \qquad 5.19$$

It is seen from **Figure 5-48** that $CrSi_2$, CrB_2, and Cr_3B_4 are formed in the Cr-43Si-5B alloy. However, the observed morphology was not formed by the eutectic phases. Instead, $CrSi_2$ was the matrix, while CrB_2 and Cr_3B_4 were the precipitates. Besides, Si was formed in the alloy. It is seen from **Figure 5-47** that $CrSi_2$ and CrB_2 formed close to the Si phase due to the eutectic reaction at 1306 °C (green point).

$$Liqud \rightarrow Si + CrSi_2 + CrB_2 \qquad 5.20$$

The eutectic structure was not found in the solidified Cr-Si-B alloy. It is difficult to say if the calculated phase diagram can represent the formed phases in the real experiments. It could be interesting to investigate the formed phases in different compositions of the Cr-Si-B alloys and see if it fits well with the calculated phase diagram.

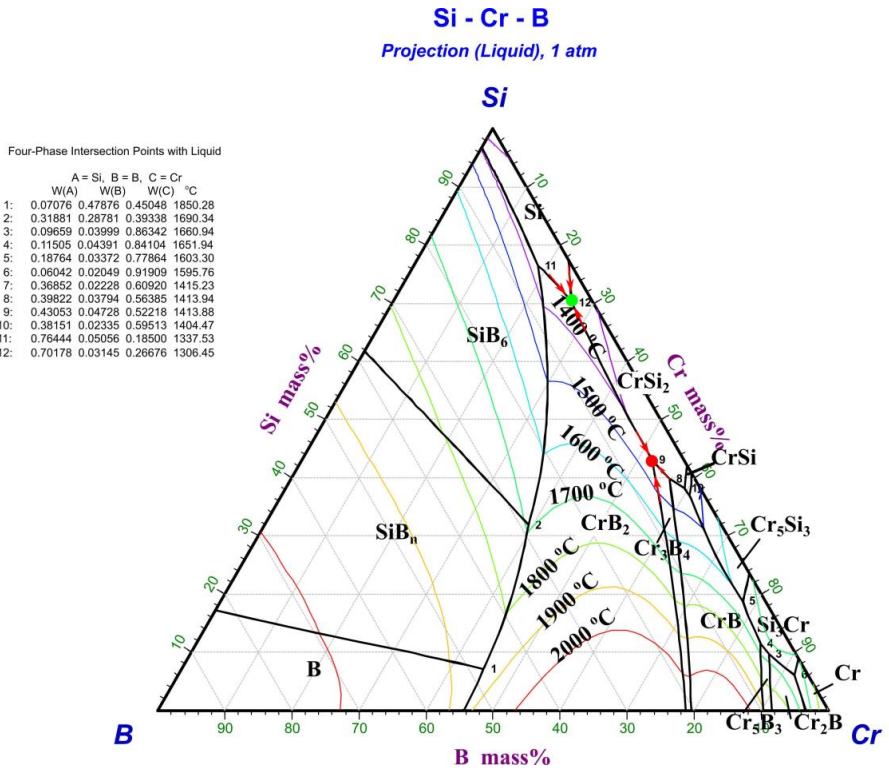

Figure 5-47 Projection of the Cr-Si-B ternary system. Calculated with FactSage 7.2 based on FTlite database.

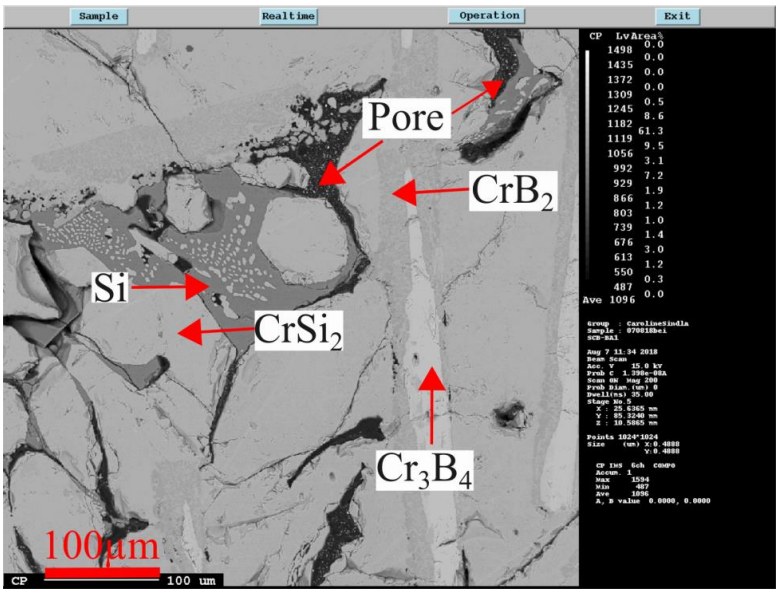

Figure 5-48 Microstructures in the Cr-Si-B alloy. [17]

5.3.2. The interaction between Cr-43Si-5B alloys and graphite

There will be some interaction between the graphite crucible and the Cr-43Si-5B alloy. A continuous SiC layer was formed at the interface between the Cr-43Si-5B alloy and graphite, and the penetration from the liquid Cr-43Si-5B alloy to the graphite was limited.

Figure 5-49 illustrates the phase evolution upon heating the (Cr-43Si-5B)-99 mass % C alloy, in which only 1 mass % Cr-43Si-5B alloy was added to the system. It shows the phase formation in the graphite part in the heating process. At low temperatures, Cr_3C_2, C, CrB, and SiC are present in the system. the modeling results show good accordance with the experimental results, with the exemption of the Cr_3C_2 phase. As has been discussed earlier in the Fe-26Si-9B/graphite system, the activity of Si affects the formation of SiC. Hence, the activity of Si in Cr-43Si-5B alloy is calculated in the temperature range 1000-1600 ºC and the results are compared with the Si-3.25B alloy and Fe-26Si-9B alloy, as shown in **Figure 5-50**. The blue line represents the equilibrium activity of Si for the formation of SiC. It is seen that the activities of Si in the Si-based alloys are higher than the equilibrium activity of Si. Hence, SiC will be formed in the graphite crucible using a Cr-43Si-5B alloy. The activity of Si in the Cr-43Si-5B alloy is higher than in the Fe-26Si-9B alloy and lower than in the Si-3.25B alloy. Therefore, the formation of SiC in the alloy decreases in the order Si-3.25B alloy > Cr-43Si-5B alloy > Fe-26Si-9B alloy.

In the use of graphite as the Cr-43Si-5B alloy's container in the TES systems, a protective layer of SiC was formed between the Cr-43Si-5B alloy and graphite, which could be a protective layer to hinder the

reaction between the PCM and graphite wall. It shows the possibility of using graphite as the refractory material in the Cr-43Si-5B PCM.

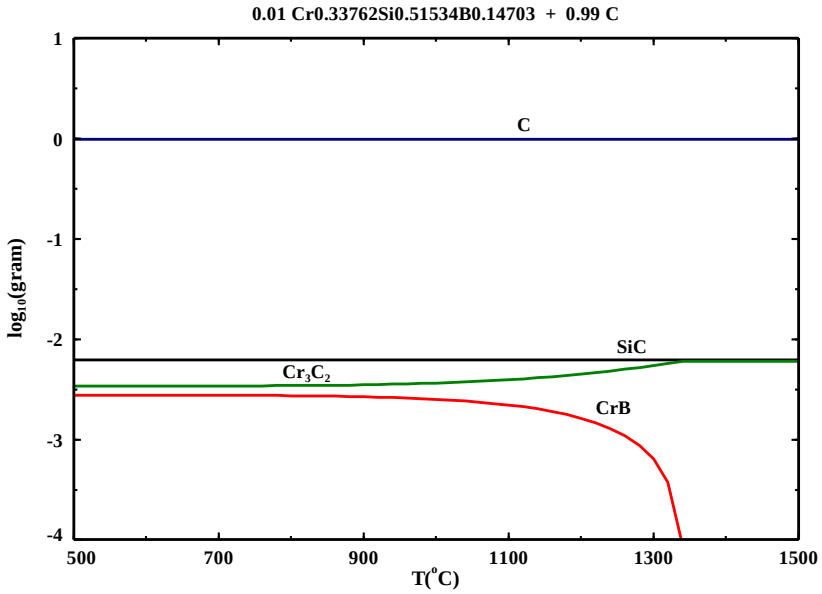

Figure 5-49 Calculated phase evolution upon heating the (Cr-43Si-5B)-99 mass % C system. Calculated with FactSage 7.3 based on the FTlite database.

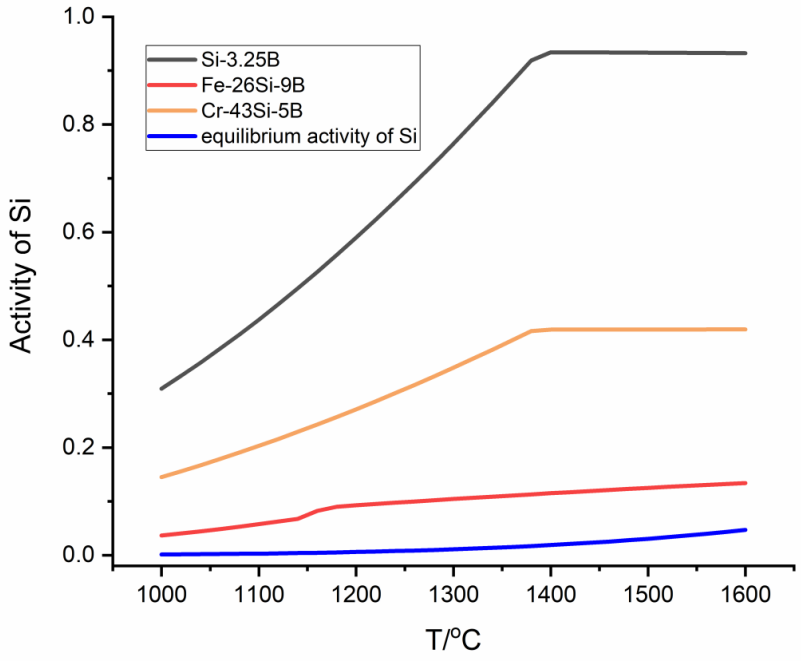

Figure 5-50 Activity of Si in Si-3.25B, Fe-26Si-9B, and Cr-43Si-5B alloys. Calculated with FactSage 7.3 based on the FTlite database.

6. Conclusions and future work

In this thesis, the work aimed at finding a desirable material as new PCM in the TES systems and compatible refractory material for PCM containers at high temperatures. In this regard, Si-B, Fe-26Si-9B, and Cr-43Si-5B alloys were proposed to be potential PCM candidates for the intended application. These were mainly chosen due to their eutectic composition. Correspondingly, graphite, Al_2O_3, Si_3N_4, and h-BN were tested with PCMs. The present experiments of PCMs were performed to study the stability of phases during applied thermal cycles, volume changes, liquidus temperatures, heat of fusion, and compatibility with refractory materials.

Combined with the experimental and theoretical results, it is suggested that Si-3.25B and Fe-26Si-9B alloys are suitable PCMs in the TES systems. Si-3.25B alloy has the advantages of low liquidus temperature (1386-1400 ^oC), high storage density (4.3 kJ/cm^3, in theory), and stable phase during thermal cycles. The volume change is, however, still very high (9%) during solidification. Dense graphite, Si_3N_4, and h-BN are recommended to be the compatible materials for Si-3.25B alloy's container at high temperatures. Fe-26Si-9B alloy also has the advantages of low liquidus temperature ((~1250 ^oC), high storage density (4.5 kJ/cm^3, in theory), and stable phase during thermal cycles. Moreover, it has a slight shrinkage during cooling, which is expected for PCM. Graphite, Si_3N_4, and h-BN are recommended to be the compatible materials for Fe-26Si-9B alloy's container at high temperatures. The more detailed conclusions will here be summarized and some recommendations are put forward for future work.

6.1. Si-B alloys

1. Si solid solution (Si(ss)) and Si(ss) + SiB_3 (eutectic structure) were detected in the Si-B alloys with the B addition lower than 3.25 mass %, while Si(ss), eutectic structure, and the larger crystals of SiB_3 particles were detected in the Si-B alloys with the B addition higher than 3.25 mass %. The B content of 3.25 mass % was regarded to be the optimal B content in the Si-B alloys due to its eutectic composition.
2. The liquidus temperature of Si-3.25B alloy was measured to be in the range 1386-1400 ^oC based on the wetting tests. It is close to the theoretical melting point of 1385 ^oC.
3. The volume change in Si-3.25B alloys was measured to be ~ 9 %. It still has a high volume expansion during cooling and up to 25 mass % B must be added to obtain no volume change during solidification.
4. In the interaction between graphite and Si-B alloys, B_4C and SiC particles were formed in Si-B alloys. A continuous SiC layer was produced along the interface between graphite and Si-B alloys with the B addition lower than 3.66 mass %. SiC and B_4C layers were, however, formed between graphite and Si-B alloys with the B addition higher than 3.66 mass %. The formation of the SiC and B_4C layers was hence dependent on the B content of Si-B alloys and temperatures.

5. C content was increased with the increasing temperature in liquid Si in the temperature range 1450-1750 °C. Moreover, C content as a function of temperature is described as follows.

$$Cc(T, mass\%) = 59.6 \cdot \exp(\frac{-16452}{T}) \qquad (T: 1723\text{-}2023K)$$

6. C content was in the range 120–585 ppm mass in liquid Si-2B alloy, 390–915 ppm mass in liquid Si-3.25B alloy, and 835–2090 ppm mass in liquid Si-5B alloy. C content was increased with the increase of the B addition in Si-B alloys.
7. In the interaction between Si_3N_4 and Si-B alloys, a continuous BN layer was formed at the interface between Si-8B alloy and Si_3N_4 crucible. Moreover, BN particles were found in Si-8B alloy. In the wetting test, the equilibrium contact angle was measured to be 134° between Si-3.25B alloy and Si_3N_4.
8. In the interaction between h-BN and Si-3.25B alloy, no new phases was formed in Si-3.25B alloy and at their interface. The equilibrium contact angle was measured to be in the range 120°-135°. Besides, h-BN should be used at high enough N_2 pressure in case of decomposition of h-BN at high temperatures.

6.2. Fe-26Si-9B alloy

1. FeSi, FeB, SiB_6, and $FeSiB_3$ were formed in Fe-26Si-9B alloy after thermal cycle experiments. FeB was in the form of large crystals. However, FeSi and $FeSiB_3$ were in the form of eutectic structures.
2. $FeSiB_3$ was confirmed to be a new phase formed in Fe-26Si-9B alloy, which was never reported in the literature. In TEM characterization, $FeSiB_3$ was analyzed to be an orthorhombic unit cell with the following unit cell parameters: a = 4.88 Å, b = 10.22 Å, and c = 5.91 Å.
3. Fe-26Si-9B alloy started to melt at ~ 1223 °C, while it was completely melted at ~ 1254 °C. It shows that Fe-26Si-9B alloy was not a eutectic alloy. The eutectic point was calculated to be about 61 mass % Fe, 29 mass % Si, and 10 mass % B (Fe-29Si-10B) in Fe-Si-B system.
4. The maximum volume change was measured to be in the range -2.44 - -3.2 % from the liquidus point to the complete solidification, which shows that Fe-26Si-9B alloy shrunk during solidification.
5. In the interaction between graphite and Fe-26Si-9B alloy, the equilibrium contact angle was measured to be in the range 31°-48°. B_4C and SiC particles were formed at the top of Fe-26Si-9B alloy. However, no carbides were formed in the bulk Fe-26Si-9B alloy, even after long-term thermal cycles. At the interface, SiC and B_4C layers were formed. The penetration from liquid Fe-26Si-9B alloy into graphite was limited.
6. In the interaction between the Al_2O_3 and Fe-26Si-9B alloy, the equilibrium contact angle was measured to be 120-124°. No Al-based phases was formed in Fe-26Si-9B alloy, and no penetration was observed in Al_2O_3 side. However, oxides were found at the surface of Fe-26Si-9B particle, and the oscillation phenomenon occurred at a temperature higher than 1450 °C.
7. In the interaction between Si_3N_4 and Fe-26Si-9B alloy, the equilibrium contact angle was measured to be ~ 135°. No nitride phases were present in Fe-26Si-9B alloy and at their interface. It shows the possibility of using Si_3N_4 refractory material as Fe-26Si-9B alloy's container at high temperatures.
8. In the interaction between h-BN and Fe-26Si-9B alloy, the equilibrium contact angle was measured

to be ~ 142°. No nitride phases was detected in Fe-26Si-9B alloy, and the penetration from the liquid alloy into h-BN was limited. Besides, h-BN should be used at high enough N_2 pressures in case of decomposition of h-BN at high temperatures.

6.3. Cr-43Si-5B alloy

1. $CrSi_2$, CrB_2, Cr_3B_4, and Si were formed in Cr-43Si-5B alloy after the thermal cycle experiment in a graphite crucible, in which the formation of Si was not consistent with FactSage calculation. Moreover, eutectic structure was not found in Cr-Si-B alloy. Hence, it is believed that Cr-43Si-5B alloy was not a eutectic alloy. In addition, a considerable number of pores existed in Cr-43Si-5B alloy, which would affect the thermal conductivity of Cr-43Si-5B alloy as PCM.
2. In the interaction between graphite crucible and Cr-43Si-5B alloy, a continuous SiC layer was formed at the interface between Cr-43Si-5B alloy and graphite, and penetration from the liquid Cr-43Si-5B alloy to the graphite was limited.

6.4. Future work

In the research of the Si-based PCMs for the application in the TES systems, thermal cycle experiments in the graphite crucible have been performed by Grorud [58] for Si-3.25B alloy and by Grorud [58], Sindland [17], Jayakumari [121], and Sellevoll [16], [108] for Fe-26Si-9B alloy. The students were all co-supervised by the author. The following recommendations are pointed out based on the achieved experimental results in this thesis and in the published reports:

1. The heat of fusion is an important parameter for PCMs. Some preliminary measurements of the heat of fusion of Fe-26Si-9B alloys were measured in DSC test. This is an important variable for PCM, and it is hence suggested to improve DSC tests to measure the heat of fusion of Si-3.25B, Fe-26Si-9B, and Cr-43Si-5B alloys.
2. Thermal conductivity is another important parameter for PCMs. Further investigation should be carried out in the measurement of thermal conductivity of Si-3.25B, Fe-26Si-9B, and Cr-43Si-5B alloys.
3. Volume changes in the Si-3.25B and Fe-26Si-9B alloys were measured based on the recorded images in wetting tests. However, the recorded images were only two dimensions, and physical volume should be calculated based on three-dimensional images. It might affect the calculated results. Other, more accurate, techniques should be used to investigate Si-based alloys' volume change. This could for example be high temperature electrostatic levitator method.
4. Si_3N_4 was suggested to be a potential refractory material for Si-3.25B and Fe-26Si-9B alloys. It would be interesting to do long-term thermal cycle experiments in Si_3N_4 container to investigate the chemical stability of Si-3.25B and Fe-26Si-9B alloys, in which the operating time can last more than five days.
5. The challenge of melting Fe-26Si-9B alloy was caused by the formation of B_4C and oxides layer at

the surface under Ar. It is important to find the solution to prevent the formation of the high melting layers in the heating process.

6. The eutectic composition of Fe-Si-B system was calculated to be Fe-29Si-10B. Hence, its melting point, latent heat of fusion, and stable phases in the solid state should be investigated.
7. $FeSiB_3$ was confirmed to be a new ternary phase in Fe-Si-B system. Therefore, the thermodynamic modeling of the Fe-Si-B system should be improved. Furthermore, the properties of this phase should be investigated more in detail, as this material may be suited for other applications as well.
8. The present research was carried out in the form of small scale experiments. The results in the pilot-scale are unknown and should be tested. This work is in progress at the University of Madrid, the coordinator of the Amadeus project.

Reference

[1] Wikipedia, "2019-20 Australian bushfire season," 2020. [Online]. Available: https://en.wikipedia.org/wiki/2019–20_Australian_bushfire_season#cite_note-5. [Accessed: 10-Jan-2020].

[2] G. Sylte, "Svalbard has experienced warming of 4°C the last 50 years," *Bjerknes centre for climate research*, 2019. [Online]. Available: https://www.bjerknes.uib.no/en/article/news/svalbard-have-experienced-warming-4c-last-50-years. [Accessed: 10-Jan-2020].

[3] C. Gramling, "Here's how climate change may make Australia's wildfires more common," *ScienceNews*, 2020. [Online]. Available: https://www.sciencenews.org/article/how-climate-change-may-make-australia-wildfires-more-common. [Accessed: 10-Jan-2020].

[4] W. J. Ripple, C. Wolf, T. M. Newsome, P. Barnard, and W. R. Moomaw, "World Scientists' Warning of a Climate Emergency," *Bioscience*, Nov. 2019.

[5] H. Murdock, D. Gibb, T. André, F. Appavou, and A. Brown, "Renewables 2019 Global Status Report," 2019.

[6] M. Liu, W. Saman, and F. Bruno, "Review on storage materials and thermal performance enhancement techniques for high temperature phase change thermal storage systems," *Renew. Sustain. Energy Rev.*, vol. 16, no. 4, pp. 2118–2132, May 2012.

[7] M. M. Kenisarin, "High-temperature phase change materials for thermal energy storage," *Renew. Sustain. Energy Rev.*, vol. 14, no. 3, pp. 955–970, Apr. 2010.

[8] N. Kumar and D. Banerjee, "Phase change materials," in *Handbook of Thermal Science and Engineering*, Cham: Springer International Publishing, 2018, pp. 2213–2275.

[9] A. Datas, A. Ramos, A. Martí, C. del Cañizo, and A. Luque, "Ultra high temperature latent heat energy storage and thermophotovoltaic energy conversion," *Energy*, vol. 107, pp. 542–549, 2016.

[10] M. R. Gilpin, *High Temperature Latent Heat Thermal Energy Storage To Augment*, no. August. 2015.

[11] AMADEUS *et al.*, "Next generation materials and solid state devices for ultra high temperature energy storage and conversion," *SolarPACES (Solar Power and Chemical Energy Systems) Conference*, 2017. [Online]. Available: http://amadeus-project.eu/.

[12] A. Datas, "Hybrid thermionic-photovoltaic converter," *Appl. Phys. Lett.*, vol. 108, no. 14, 2016.

[13] A. I. Fernández, C. Barreneche, M. Belusko, M. Segarra, F. Bruno, and L. F. Cabeza, "Considerations for the use of metal alloys as phase change materials for high temperature applications," *Sol. Energy Mater. Sol. Cells*, vol. 171, no. October 2016, pp. 275–281, Nov. 2017.

[14] B. Drevet and N. Eustathopoulos, "Wetting of ceramics by molten silicon and silicon alloys: A review," *J. Mater. Sci.*, vol. 47, no. 24, pp. 8247–8260, Dec. 2012.

[15] B. Grorud, "Interaction of Eutectic Fe-Si-B Alloy with Graphite Crucibles," Master thesis, Norwegian University of Science and Technology, Trondheim, 2018.

[16] K. Sellevoll, "Interactions of Eutectic Fe-Si-B Alloy with Graphite Crucibles," Norwegian University of Science and Technology, Trondheim, Specialization project report, 2018.

[17] C. Sindland, “Production of Eutectic Si-Fe-B and Si-Cr-B alloy and their Interaction with Graphite Crucibles,” Norwegian University of Science and Technology, Trondheim, Summer job report, 2018.

[18] K. Tang, E. J. Øvrelid, G. Tranell, and M. Tangstad, “A thermochemical database for the solar cell silicon materials,” *Mater. Trans.*, vol. 50, no. 8, pp. 1978–1984, 2009.

[19] E. T. TURKDOGAN, *Physical chemistry of high temperature technology: Physical Chemistry of Ironmaking and Steelmaking.* Metals Society, 1980.

[20] T. Iida and R. I. L. Guthrie, *The physical properties of liquid metals*. 1988.

[21] A. I. Zaitsev and A. A. Kodentsov, “Thermodynamic properties and phase equilibria in the Si-B system,” *J. Phase Equilibria*, vol. 22, no. 2, pp. 126–135, 2001.

[22] W. K. Rhim and K. Ohsaka, “Thermophysical properties measurement of molten silicon by high-temperature electrostatic levitator: Density, volume expansion, specific heat capacity, emissivity, surface tension and viscosity,” *J. Cryst. Growth*, vol. 208, no. 1, pp. 313–321, 2000.

[23] G. V Samsonov and V. M. Sleptsov, “Investigation of the solubility of boron in silicon,” *ZhNH*, vol. 8, pp. 2009–2011, 1963.

[24] R. W. Olesinski and G. J. Abbaschian, “The B-Si (Boron-Silicon) system,” *Bull. Alloy Phase Diagrams*, vol. 5, no. 5, pp. 478–484, 1984.

[25] G. L. Vick and K. M. Whittle, “Solid Solubility and Diffusion Coefficients of Boron in Silicon,” *J. Electrochem. Soc.*, vol. 116, no. 8, p. 1142, Aug. 1969.

[26] C. F. Cline and D. E. Sands, “A new silicon boride, SiB4,” *Nature*, vol. 185, no. 4711, p. 456, 1960.

[27] C. Brosset and B. Magnusson, “The silicon-boron system,” *Nature*, vol. 187, no. 4731, p. 54, 1960.

[28] M. Vlasse, G. A. Slack, M. Garbauskas, J. S. Kasper, and J. C. Viala, “The crystal structure of SiB6,” *J. Solid State Chem.*, vol. 63, no. 1, pp. 31–45, 1986.

[29] B. Armas, G. Male, D. Salanoubat, C. Chatillon, and M. Allibert, “Determination of the boron-rich side of the B-Si phase diagram,” *J. Less-Common Met.*, vol. 82, no. C, pp. 245–254, Nov. 1981.

[30] R. F. Giese, J. Economy, and V. I. Matkovich, “Kurze originalmittelungen interstitial derivatives of 8 boron,” *Zeitschrift fur Krist. - New Cryst. Struct.*, vol. 122, no. 1–2, pp. 144–147, 1965.

[31] A. T. Dinsdale, “SGTE data for pure elements,” *Calphad*, vol. 15, no. 4, pp. 317–425, 1991.

[32] Landolt and Börnstein, “Thermodynamic Properties of Inorganic Materials: PureSubstances,” *Sci. Gr. Thermodata Eur. (SGTE), Springer-Verlag, Berlin Heidelb.*, 2002.

[33] A. I. Zaitsev, N. E. Shelkova, N. P. Lyakishev, and B. M. Mogutnov, “Thermodynamic properties and phase equilibria in the Na2O-SiO2 system,” *Phys. Chem. Chem. Phys.*, vol. 1, no. 8, pp. 1899–1907, 1999.

[34] R. Noguchi, K. Suzuki, F. Tsukihashi, and N. Sano, “Thermodynamics of boron in a silicon melt,” *Metall. Mater. Trans. B*, vol. 25, no. 6, pp. 903–907, 1994.

[35] T. Mitsuru, F. Toshiharu, and C. Yamauchi, “Activity of Boron in Molten Silicon,” *JOURNAL-MINING Mater. Process. Inst. JAPAN*, vol. 114, pp. 807–812, 1998.

[36] G. Inoue, T. Yoshikawa, and K. Morita, “Effect of Calcium on Thermodynamic Properties of Boron in Molten Silicon,” *High Temp. Mater. Process.*, vol. 22, no. 3–4, pp. 221–226, 2004.

[37] T. Yoshikawa and K. Morita, “Thermodynamic property of B in molten Si and phase relations in

the Si-Al-B system," *Mater. Trans.*, vol. 46, no. 6, pp. 1335–1340, 2005.

[38] L. T. Khajavi, K. Morita, T. Yoshikawa, and M. Barati, "Thermodynamics of boron distribution in solvent refining of silicon using ferrosilicon alloys," *J. Alloys Compd.*, vol. 619, pp. 634–638, 2015.

[39] H. Chen, K. Morita, X. Ma, Z. Chen, and Y. Wang, "Boron removal for solar-grade silicon production by metallurgical route:A review," *Sol. Energy Mater. Sol. Cells*, vol. 203, p. 110169, Dec. 2019.

[40] R. W. Olesinski and G. J. Abbaschian, "The C-Si (Carbon-Silicon) system," *Bull. Alloy Phase Diagrams*, vol. 5, no. 5, pp. 486–489, 1984.

[41] K. P. Trumble, "Spontaneous infiltration of non-cylindrical porosity: Close-packed spheres," *Acta Mater.*, vol. 46, no. 7, pp. 2363–2367, Apr. 1998.

[42] R. N. Hall, "Electrical contacts to silicon carbide," *J. Appl. Phys.*, vol. 29, no. 6, pp. 914–917, 1958.

[43] R. I. Scace and G. A. Slack, "Solubility of carbon in silicon and germanium," *J. Chem. Phys.*, vol. 30, no. 6, pp. 1551–1555, 1959.

[44] T. Nozaki, Y. Yatsurugi, and N. Akiyama, "Concentration and Behavior of Carbon in Semiconductor Silicon," *J. Electrochem. Soc.*, vol. 117, no. 12, p. 1566, 1970.

[45] A. R. Bean and R. C. Newman, "The solubility of carbon in pulled silicon crystals," *J. Phys. Chem. Solids*, vol. 32, no. 6, pp. 1211–1219, 1971.

[46] O. L.L. and M. R.A., "Phase equilibria in the Al-Si-C system," *Metall. Trans. A*, vol. 18, no. A, pp. 2005–2014, 1987.

[47] L. Ottem, "Løselighet og termodynamiske data for oksygen og karbon i flytende legeringer av silisium og ferrosilisium," *Sintef, Stf34 F*, 1993.

[48] K. Yanaba, Y. Matsumura, T. Narushima, and Y. Iguchi, "Effect of alloying elements on carbon solubility in liquid silicon equilibrated with silicon carbide," *Mater. Trans. JIM*, vol. 39, no. 8, pp. 819–823, 1998.

[49] F. Durand and J. C. Duby, "Carbon solubility in solid and liquid silicon - A review with reference to eutectic equilibrium," *J. Phase Equilibria*, vol. 20, no. 1, pp. 61–63, 1999.

[50] B. O. Kolbesen and A. Mühlbauer, "Carbon in silicon: Properties and impact on devices," *Solid State Electron.*, vol. 25, no. 8, pp. 759–775, Aug. 1982.

[51] F. Durand and J. C. Duby, "Solid-liquid equilibria in the silicon-rich corner of the Si-O-C system," *J. Phase Equilibria*, vol. 21, no. 2, pp. 130–135, 2000.

[52] H. Dalaker and M. Tangstad, "Time and temperature dependence of the solubility of carbon in liquid silicon equilibrated with silicon carbide and its dependence on boron levels," *Mater. Trans.*, vol. 50, no. 5, pp. 1152–1156, 2009.

[53] Y. Iguchi and T. Narushima, "Solubility of oxygen, nitrogen and carbon in liquid silicon," in *First International Conference on Processing Materials for Properties*, 1993, pp. 437–440.

[54] H. Kleykamp and G. Schumacher, "Constitution of the silicon-carbon system," *Berichte der Bunsengesellschaft/Physical Chem. Chem. Phys.*, vol. 97, no. 6, pp. 799–805, Jun. 1993.

[55] R. Voytovych, R. Israel, N. Calderon, F. Hodaj, and N. Eustathopoulos, "Reactivity between liquid Si or Si alloys and graphite," *J. Eur. Ceram. Soc.*, vol. 32, no. 14, pp. 3825–3835, Nov. 2012.

[56] R. Deike and K. Schwerdtfeger, "Reactions Between Liquid Silicon and Different Refractory

Materials," *J. Electrochem. Soc.*, vol. 142, no. 2, pp. 609–614, 1995.

[57] A. Favre, H. Fuzellier, and J. Suptil, "An original way to investigate the siliconizing of carbon materials," *Ceram. Int.*, vol. 29, no. 3, pp. 235–243, 2003.

[58] B. Grorud, "Interaction of liquid Si-B alloys with graphite crucibles," NTNU, Trondheim, Summer job report, 2017.

[59] A. Hoseinpur and J. Safarian, "Mechanisms of graphite crucible degradation in contact with Si–Al melts at high temperatures and vacuum conditions," *Vacuum*, vol. 171, p. 108993, Oct. 2020.

[60] V. Domnich, S. Reynaud, R. A. Haber, and M. Chhowalla, "Boron carbide: Structure, properties, and stability under stress," *J. Am. Ceram. Soc.*, vol. 94, no. 11, pp. 3605–3628, Nov. 2011.

[61] K. Y. Xie *et al.*, "Microstructural characterization of boron-rich boron carbide," *Acta Mater.*, vol. 136, pp. 202–214, 2017.

[62] S. H. Jürgen and F. Aldinger, "Phase equilibria in the Si-B-C-N system," in *High Performance Non-Oxide Ceramics I*, Berlin/Heidelberg: Springer, 2002, pp. 1–58.

[63] S. Berlin *et al.*, *Landolt-Börnstein / New Series*. 2000.

[64] U. R. Kattner and B. P. Burton, "Phase diagrams of binary iron alloys," in *ASM international*, 1993, pp. 12–28.

[65] M. G. Poletti and L. Battezzati, "Assessment of the ternary Fe-Si-B phase diagram," *Calphad Comput. Coupling Phase Diagrams Thermochem.*, vol. 43, pp. 40–47, 2013.

[66] K. Tang and M. Tangstad, "A thermodynamic description of the Si-rich Si-Fe system," *Acta Metall. Sin. (English Lett.*, vol. 25, no. 4, pp. 249–255, 2012.

[67] T. Van Rompaey, K. C. Hari Kumar, and P. Wollants, "Thermodynamic optimization of the B-Fe system," *J. Alloys Compd.*, vol. 334, no. 1–2, pp. 173–181, Feb. 2002.

[68] V. Raghavan, "B-Fe-Si (boron-iron-silicon)," *J. Phase Equilibria Diffus.*, vol. 28, no. 4, pp. 380–381, 2007.

[69] I. Aronsson, Bertil; Engström, "X-Ray Investigations on M-Si-B Systems (M = Mn, Fe, Co). II. Some Features of the Fe-Si-B and Mn-Si-B Systems," *Acta Chem. Scand.*, no. 14, pp. 1403–1413, 1960.

[70] B. V. Neamţu, T. F. Marinca, I. Chicinaş, O. Isnard, F. Popa, and P. Păşcuţă, "Preparation and soft magnetic properties of spark plasma sintered compacts based on Fe-Si-B glassy powder," *J. Alloys Compd.*, vol. 600, pp. 1–7, Jul. 2014.

[71] H. Y. Tong, J. T. Wang, B. Z. Ding, H. G. Jiang, and K. Lu, "The structure and properties of nanocrystalline Fe78B13Si9 alloy," *J. Non. Cryst. Solids*, vol. 150, no. 1–3, pp. 444–447, Nov. 1992.

[72] T. Tokunaga, H. Ohtani, and M. Hasebe, "Thermodynamic evaluation of the phase equilibria and glass-forming ability of the Fe–Si–B system," *Suppl. Sci. Rep. RITU.*, pp. 136–142, 1980.

[73] M. Nagumo and Takashi Sato, "Glass forming ability of Fe-based alloys," *Scr. Mater.*, vol. 36, no. 7, pp. 783–787, 1997.

[74] Y. Du and J. C. Schuster, "Experimental reinvestigation of the CrSi-Si partial system and update of the thermodynamic description of the entire Cr-Si system," *J. Phase Equilibria*, vol. 21, no. 3, pp. 281–286, May 2000.

[75] H. Chen, Y. Du, and J. C. Schuster, "On the melting of Cr5Si3 and update of the thermodynamic description of Cr-Si," *Calphad Comput. Coupling Phase Diagrams Thermochem.*, vol. 33, no. 1, pp. 211–214, Mar. 2009.

[76] A. B. Gokhale and G. J. Abbaschian, “The Cr-Si (Chromium-Silicon) system,” *J. Phase Equilibria*, vol. 8, no. 5, pp. 474–484, Oct. 1987.

[77] P. K. Liao and K. E. Spear, “The B-Cr (Boron-Chromium) System,” *J. Phase Equilibria*, vol. 7, no. 3, pp. 232–237, 1986.

[78] A. Datta and S. Mukherjee, *Structural and morphological evolution in metal-organic films and multilayers*. CRC Press, 2015.

[79] S. Seetharaman, *Fundamentals of metallurgy*. 2005.

[80] T. J. Whalen and A. T. Anderson, “Wetting of SiC, Si3N4, and Carbon by Si and Binary Si Alloys,” *J. Am. Ceram. Soc.*, vol. 58, no. 9–10, pp. 396–399, 1975.

[81] J.-G. G. Li and H. Hausner, “Wetting and infiltration of graphite materials by molten silicon,” *Scr. Metall. Mater.*, vol. 32, no. 3, pp. 377–382, Feb. 1995.

[82] O. Dezellus, S. Jacques, F. Hodaj, and N. Eustathopoulos, “Wetting and infiltration of carbon by liquid silicon,” *J. Mater. Sci.*, vol. 40, no. 9–10, pp. 2307–2311, 2005.

[83] A. Ciftja, T. A. Engh, and M. Tangstad, “Wetting properties of molten silicon with graphite materials,” *Metall. Mater. Trans. A Phys. Metall. Mater. Sci.*, vol. 41, no. 12, pp. 3183–3195, Dec. 2010.

[84] J. F. White, L. Ma, K. Forwald, and D. Sichen, “Reactions between silicon and graphite substrates at high temperature: In situ observations,” in *Metallurgical and Materials Transactions B: Process Metallurgy and Materials Processing Science*, 2014, vol. 45, no. 1, pp. 150–160.

[85] R. Israel, R. Voytovych, P. Protsenko, B. Drevet, D. Camel, and N. Eustathopoulos, “Capillary interactions between molten silicon and porous graphite,” *J. Mater. Sci.*, vol. 45, no. 8, pp. 2210–2217, Apr. 2010.

[86] M. Naikade, B. Fankhänel, L. Weber, A. Ortona, M. Stelter, and T. Graule, “Studying the wettability of Si and eutectic Si-Zr alloy on carbon and silicon carbide by sessile drop experiments,” *J. Eur. Ceram. Soc.*, vol. 39, no. 4, pp. 735–742, Apr. 2019.

[87] A. Casado, J. M. Torralba, and S. Milenkovic, “Wettability and infiltration of liquid silicon on graphite substrates,” *Metals (Basel).*, vol. 9, no. 3, Mar. 2019.

[88] J. A. Champion, B. J. Keene, and S. Allen, “Wetting of refractory materials by molten metallides,” *J. Mater. Sci.*, vol. 8, no. 3, pp. 423–426, Mar. 1973.

[89] Y. Maeda, T. Yokoyama, I. Hide, T. Matsuyama, and K. Sawaya, “Releasing material for the growth of shaped silicon crystals,” *J. Electrochem. Soc.*, vol. 133, no. 2, pp. 440–443, Feb. 1986.

[90] Z. Yuan, W. L. Huang, and K. Mukai, “Wettability and reactivity of molten silicon with various substrates,” *Appl. Phys. A Mater. Sci. Process.*, vol. 78, no. 4, pp. 617–622, 2004.

[91] J. G. Li and H. Hausner, “Influence of oxygen partial pressure on the wetting behaviour of silicon nitride by molten silicon,” *J. Eur. Ceram. Soc.*, vol. 9, no. 2, pp. 101–105, Jan. 1992.

[92] B. Drevet, R. Voytovych, R. Israel, and N. Eustathopoulos, “Wetting and adhesion of Si on Si3N4 and BN substrates,” *J. Eur. Ceram. Soc.*, vol. 29, no. 11, pp. 2363–2367, 2009.

[93] W. Polkowski *et al.*, “Wetting Behavior and Reactivity of Molten Silicon with h-BN Substrate at Ultrahigh Temperatures up to 1750 °C,” *J. Mater. Eng. Perform.*, no. 7, pp. 1–14, 2017.

[94] W. Polkowski, N. Sobczak, A. Polkowska, G. Bruzda, A. Kudyba, and D. Giuranno, “Silicon as a Phase Change Material: Performance of h-BN Ceramic During Multi-Cycle Melting/Solidification of Silicon,” *JOM*, vol. 71, no. 4, pp. 1492–1498, Apr. 2019.

[95] W. Polkowski *et al.*, "The Effect of Boron Content on Wetting Kinetics in Si-B Alloy/h-BN System," *J. Mater. Eng. Perform.*, pp. 1–7, Dec. 2018.

[96] W. Polkowski, N. Sobczak, M. Tangstad, and J. Safarian, "Silicon and silicon-boron alloys as phase change materials in thermal energy storage units," *Silicon Chem. Sol. Ind. XIVSilicon Chem. Sol. Ind. XIV*, no. June, 2018.

[97] M. HUMENIK and W. D. KINGERY, "Metal-Ceramic Interactions: III, Surface Tension and Wettability of Metal-Ceramic Systems," *J. Am. Ceram. Soc.*, vol. 37, no. 1, pp. 18–23, Jan. 1954.

[98] C. Wu and V. Sahajwalla, "Influence of melt carbon and sulfur on the wetting of solid graphite by Fe-C-S melts," *Metall. Mater. Trans. B Process Metall. Mater. Process. Sci.*, vol. 29, no. 2, pp. 471–477, 1998.

[99] H. Sun, K. Mori, V. Sahajwalla, and R. D. Pehlke, "Carbon solution in liquid iron and iron alloys," *High Temp. Mater. Process.*, vol. 17, no. 4, pp. 257–270, Jan. 1998.

[100] L. Zhao and V. Sahajwalla, "Interfacial phenomena during wetting of graphite/alumina mixtures by liquid iron," *ISIJ Int.*, vol. 43, no. 1, pp. 1–6, 2003.

[101] L. Zhao and V. Sahajwalla, "Interfacial phenomena during wetting of graphite/alumina mixtures by liquid iron," *ISIJ Int.*, vol. 43, no. 1, pp. 1–6, 2003.

[102] P. J. Y. Rubio, L. Hong, N. Saha-Chaudhury, R. Bush, and V. Sahajwalla, "Dynamic Wetting of Graphite and SiC by Ferrosilicon Alloys and Silicon at 1550 C," *ISIJ Int.*, vol. 46, no. 11, pp. 1570–1576, 2006.

[103] H. Gao, B. S. Dong, J. Zhong, Z. Z. Li, M. Xu, and S. X. Zhou, "The influence of substrate and atmosphere on the properties of FeSiB(Cu,Nb) alloy melts," *Sci. China Technol. Sci.*, vol. 59, no. 12, pp. 1892–1898, 2016.

[104] I. Jim Bo and A. W. Cramb, "Computer Aided Interfacial Measurements," *ISIJ Int.*, vol. 32, no. 1, pp. 26–35, 1992.

[105] K. Nakashima, K. Mori, K. Takihira, and N. Shinozaki, "Wettability of Al2O3 Substrate by Liquid Iron—Effects of Oxygen in Liquid Iron and Purity of Al2O3 Substrate," *Mater. Trans. JIM*, vol. 33, no. 10, pp. 918–926, 1992.

[106] W. Yan *et al.*, "Wettability phenomena of molten steel in contact with alumina substrates with alumina and alumina-carbon coatings," *J. Eur. Ceram. Soc.*, vol. 38, no. 4, pp. 2164–2178, Apr. 2018.

[107] G. A. Yasinskaya, "The wetting of refractory carbides, borides, and nitrides by molten metals," *Sov. Powder Metall. Met. Ceram.*, vol. 5, no. 7, pp. 557–559, Jul. 1966.

[108] K. Sellevoll, "Interactions of FeSi Alloys with Graphite Crucibles," Master thesis, Norwegian University of Science and Technology, Trondheim, 2019.

[109] J. Jiao *et al.*, "The use of eutectic Fe-Si-B alloy as a phase change material in thermal energy storage systems," *Materials (Basel).*, vol. 12, no. 14, 2019.

[110] L. Jakobsson, "Distribution of Boron Between Silicon and CaO-SiO2, MgO-SiO2, CaO-MgO-SiO2 and CaO-Al2O3-SiO2 Slags at 1600 C," 2013.

[111] N. Sobczak, R. Nowak, W. Radziwill, J. Budzioch, and A. Glenz, "Experimental complex for investigations of high temperature capillarity phenomena," *Mater. Sci. Eng. A*, vol. 495, no. 1–2, pp. 43–49, 2008.

[112] Netzsch, "Differential scanning calorimetry." [Online]. Available: www.netzsch.com.

[113] "FactSage." [Online]. Available: http://www.factsage.com/fs_general.php.

[114] K. Tang, E. J. Øvrelid, G. Tranell, and M. Tangstad, "Thermochemical and Kinetic Databases for the Solar Cell Silicon Materials," 2009, pp. 219–251.

[115] R. Telle, "Structure and Properties of Si-Doped Boron Carbide," in *The Physics and Chemistry of Carbides, Nitrides and Borides*, Springer Netherlands, 1990, pp. 249–267.

[116] T. Narushima, A. Yamashita, C. Ouchi, and Y. Iguchi, "Solubilities and Equilibrium Distribution Coefficients of Oxygen and Carbon in Silicon.," *Mater. Trans.*, vol. 43, no. 8, pp. 2120–2124, 2002.

[117] P. Franke, D. Neuschütz, H. Landolt, and R. Börnstein, *Binary systems. Part 2: Elements and Binary Systems from B – C to Cr – Zr*, vol. 19B2. Berlin/Heidelberg: Springer Berlin Heidelberg, 2004.

[118] P. Villars and K. Cenzual, Eds., "FeSi Crystal Structure," *SpringerMaterials (online database)*, 2012. [Online]. Available: https://materials.springer.com/isp/crystallographic/docs/sd_1100697. [Accessed: 25-Jan-2020].

[119] B. Landolt, R. Börnstein, and SGTE, "Thermodynamic Properties of Inorganic Materials," *Sci. Gr. Thermodata Eur. (SGTE), Springer-Verlag, Berlin Heidelb.*, 1999.

[120] J. V. Naidich, "The Wettability of Solids by Liquid Metals," in *Elsevier*, 2013, pp. 353–484.

[121] S. Jayakumari, "Making of prototypes: Fe-Si, Fe-Si-B alloys and SiC-crucibles for Phase Change Materials (PCMs)," Trondheim, technical report, 2019.

[122] C. W. Bale *et al.*, "FactSage thermochemical software and databases, 2010-2016," *Calphad Comput. Coupling Phase Diagrams Thermochem.*, vol. 54, pp. 35–53, 2016.

[123] F. P. Fernández, "Ultra High Temperature Refractories and Coatings," Nov. .

[124] H. Nowotny, E. Piegger, R. Kieffer, and F. Benesovsky, "Das Dreistoffsystem: Chrom-Silizium-Bor - Mit 4 Abbildungen," *Monatshefte für Chemie*, vol. 89, no. 4–5, pp. 611–617, Jul. 1958.

[125] V. M. Chad, N. Chaia, T. F. Villela, C. A. Nunes, and G. C. Coelho, "Experimental determination of liquidus projection in the Cr rich region of the Cr-Si-B system," *J. Alloys Compd.*, vol. 772, pp. 735–739, Jan. 2019.